PREPARATION OF AN OPTICALLY-TRAPPED DEGENERATE FERMI GAS OF ^{6}LI: FINDING THE ROUTE TO DEGENERACY

by

Michael Eric Gehm

Department of Physics
Duke University

Date:_____
Approved:

_____
Dr. John E. Thomas, Supervisor

_____
Dr. Robert P. Behringer

_____
Dr. Glenn Edwards

_____
Dr. Daniel J. Gauthier

_____
Dr. Joshua E. S. Socolar

Dissertation submitted in partial fulfillment of the
requirements for the degree of Doctor of Philosophy
in the Department of Physics
in the Graduate School of
Duke University

2003

ABSTRACT

(Physics)

PREPARATION OF AN OPTICALLY-TRAPPED DEGENERATE FERMI GAS OF ^{6}LI: FINDING THE ROUTE TO DEGENERACY

by

Michael Eric Gehm

Department of Physics
Duke University

Date: _____
Approved:

_____
Dr. John E. Thomas, Supervisor

_____
Dr. Robert P. Behringer

_____
Dr. Glenn Edwards

_____
Dr. Daniel J. Gauthier

_____
Dr. Joshua E. S. Socolar

An abstract of a dissertation submitted in partial fulfillment of
the requirements for the degree of Doctor of Philosophy
in the Department of Physics
in the Graduate School of
Duke University

2003

Abstract

This thesis describes the first all-optical production of a degenerate Fermi gas of atoms. In the experiment, a Magneto-Optical-Trap (MOT) containing $\simeq 1-3\times10^8$ atoms of ^{6}Li at a temperature of 150 μK is used to load an optical trap formed by the focus of a 65 W CO_2 laser beam. The optical potential has a depth of 700 μK and trap oscillation frequencies of 6.6 kHz in the radial direction and 275 Hz in the axial. Approximately 3×10^6 atoms are transferred to the optical trap and the MOT is extinguished. A uniform magnetic field of 100 G is applied to the atoms, tuning the s-wave scattering length to $\simeq$ -100 a_0. This initiates free evaporative cooling in the sample. After 6 s, evaporation has stagnated and 1.3×10^6 atoms remain at a temperature of 50 μK. The intensity of the CO_2 laser is then lowered to drive forced evaporative cooling. After 60 s of forced evaporative cooling, 1×10^5 atoms remain at a temperature $\leq 4\,\mu$K. For this number of atoms, the Fermi temperature, T_F =8 μK. With $T/T_F \leq 0.5$, the sample is clearly degenerate.

In addition to the experimental work, this thesis presents three theoretical results of note: 1) The development of a Monte-Carlo model for simulating a classical or near-classical gas in a Gaussian well. This model extends previous techniques for harmonic wells to a case which approximates the potential well of an optical trap. The application of the model to temperature measurement, trap frequency measurement, and cloud size in an anharmonic potential is presented. 2) The development of a Fokker-Planck approach to studying the evolution dynamics of trap

populations in response to fluctuations in the trapping potential. The heating that results from such fluctuations was a primary factor in early failures of optical traps. Understanding these heating processes allowed our group to construct the first optical trap capable of storing atoms for more than a few seconds. 3) The development of an analytical treatment which relates the signal-to-noise ratio of atomic imaging techniques to the physical characteristics of the imaging equipment and the specific imaging technique. This treatment was used to design the imaging system used in the aforementioned experiments.

Acknowledgments

It has been much harder to write these acknowledgements than it has been to write any other portion of this thesis. As I have struggled to write these comments over many months, I have come to realize that whatever I write here will not adequately convey the magnitude of the debt that I owe to the people who have made this accomplishment possible, nor will it successfully convey the gratitude and love that I feel towards them.

I must begin with my parents, Vern and Barbara Gehm. They have been a constant source of love and support throughout my life. Looking back on my childhood, I now recognize what magnificent sacrifices they made in order to give me every opportunity that they could possibly manage. Though they have taught me much with their words, they have taught me more by their actions. In myself I see much of them: my mother's love of teaching, inquisitiveness, and seriousness; my father's natural mechanical ability, dedication, and joviality. But perhaps the greatest thing they taught me is the pride that can come from a job well done, no matter how small the task. I fervently hope that I can meet the challenges of parenthood with the same wisdom, humor, and love that they have always shown me.

Dr. Pat Laverty was my first technical mentor. I worked for Pat as part of my first job after receiving my engineering degree. He had been John's first student at Duke, and always spoke very highly of John and of the program. He supported

my intellectual growth at work, and when I decided to pursue a Ph.D. in physics, he encouraged me to get in touch with John. I am grateful for his friendship and support, both then and now.

I am deeply indebted to Dr. John Thomas for his support and advice throughout the years. He has been a fantastic mentor and a true friend. I spent many years trying to find a way to accurately describe John to my friends and family, and the closest I ever came to success was calling him "the Yogi Berra of Physics." Like Yogi, John is a world-class talent at his chosen profession, yet easily avoids the self-importance that so often accompanies such prominence. He makes friends easily, is good-natured, and has a wry and playful sense of humor. And, of course, both he and Yogi are known for generating quotations that are mind-bending combinations of sense and nonsense. It has become traditional for students in our group to include quotations from John in their acknowledgements. Here are some of my favorites:

- "H-bar ain't small if you're an atom!"
- "In the limit of infinite approximation, we have ultimate simplicity."
- "It's a little bit tricky, but it's extremely straightforward."
- "The beauty of this is that you can make 100 pages of algebra out of something you could have written on one line if you'd been on the ball. But we don't let that bother us."
- "Now a physicist says that infinity isn't really infinity. I mean, we can't have a frequency corresponding to the mass of the universe or anything. Infinity is just a formality."

My work on cold atoms has spanned a number of experiments and has given me the pleasure of working closely with a number of outstanding people. Tom Savard was the lead student when I joined the group. He was always very friendly and supportive, and tolerated my many questions. I fondly remember the many gatherings he and his wife, Lynda, had at their house. Samir Bali joined the group as a post-doc about the time we began our first work with the FORT. Samir was the first AMO-physicist from outside our research group that I spent a lot of time with. As such, his stories were invaluable in helping me to place my own experiences into perspective with the rest of the field. He was always willing to lend a hand or share a bit of knowledge. Ken O'Hara was one of the two people I worked with most closely in graduate school. Ken is an amazing scientist with dedication beyond anything I have ever encountered. All of the cold atom work in our lab builds in one way or another off his ideas and hard work. I have no doubt he will be a fantastic professor of physics. I owe a great debt to Stephen Granade, my coworker on the degeneracy experiment. Stephen has been a wonderful friend and a great colleague. Besides being a gifted physicist, he is very skilled at interfacing computer hardware and software. The computer control system and data analysis infrastructure we have is due, almost entirely, to his ingenuity and hard work. I am very excited that he and his wife Misty have moved to my hometown—as that means I will have an opportunity to see them frequently. Staci Hemmer joined our group a little over two years ago, and it has been a lot of fun working with her. She has a positive attitude that is quite infectious and is skilled beyond her years. She is going to do a great job as the head student on the experiment. Joe Kinast joined the group this past summer, but we are already picking on him like he has been around forever. It

is clear that he is a great addition to the group. I look forward to working closely with Staci and Joe in my new role as post-doc.

In addition, I am also indebted to former group memebers Hongzhi Zhao, Chris Baird, Adam Wax, and Zehuang Lu. While we never worked on the same experiment, they always made me feel a part of the group. Frank Reil and Kim Fook Lee joined the group a few years after I did. Again, our work did not overlap directly, but it is been a lot of fun sharing an office with them. I have greatly enjoyed our discussions on physics, sports, and politics, as well as just joking around with them. I wish them the best of luck in their upcoming endeavors.

My committee members, Dr. Robert Behringer, Dr. Daniel Gauthier, Dr. Glenn Edwards, and Dr. Joshua Socolar provided many thoughtful and constructive comments on this thesis. It is far better now than it would have been without their input. I thank them for their assistance.

Perhaps not surprisingly, there are a number of bureaucratic hurdles that must be cleared in graduate school. I would like to specifically thank Donna Ruger and Maxine Stern for always helping me to untangle the maze of red-tape. I also would like to express my appreciation to Richard "Dickie" Poole, formerly of the Instrument Shop. He was a patient machining instructor, and taught me many useful tricks. I have also received invaluable advice and assistance on numerous occasions from the manager of the Instrument Shop, Robert Timberlake.

Graduate school is a challenging experience. In the absence of friendship, it would have been a a bleak one as well. Luckily, I have been blessed with a number of close friends throughout my years at Duke. My earliest years were spent in the near-constant company of Stephen Granade, Dan Howell, Glen Doki, John Eaton,

and Lester Chen. As classwork transitioned into research, I continued to benefit from their friendship, while being lucky enough to also add Michael Stenner, Seth Vidal, and Konstantin "Icon" Riabitsev to my list of compatriots. Graduate school has been the most intellectually stimulating period of my life. In many ways, it has also been the most fun. These gentlemen are largely responsible for both.

In the past year or so, Wendy and I have become good friends with a number of people from her Doctor of Physical Therapy class: Holly Turbyfill, Anna and Shawn Ratkus, Tasha Kulka, and Nikki Reader. I am extremely indebted to them for their friendship and for their kindness. They also provided a much needed escape from physics, especially during the latter phases of the experiment and the writing of this thesis. Any credit (or blame) for my continued sanity can be laid squarely at their feet.

Finally, I come to Wendy, my wife, to whom I owe everything. Without her, I surely would not be writing this thesis. It is through her love and support that I had the courage to leave a well-paying job and enter graduate school. It is through her love and support that I had the perseverance to finish this thesis. Words cannot express how much she means to me, how much I am looking forward to our life together, and how thankful I am for the time we have already had. Thanks, sweetheart, I love you.

For Wendy

Contents

List of Figures

List of Tables

Chapter 1

Introduction

1.1 Overview

Quantum-mechanical effects typically exhibit themselves only on microscopic scales as a result of the extremely small size of Planck's constant, h. Systems where quantum effects are manifest on mesoscopic or macroscopic scales tend to be quite rare, and yet are some of the most intriguing systems in all of physics. Lasers, neutron stars, and superconductors are all examples of such macroscopic quantum ensembles.

One of the first, if not the first, proposal for a macroscopic quantum system was Albert Einstein's paper in which he discovers the quantum-mechanical phase transition we know today as *Bose-Einstein Condensation* [1]. This paper, written during the transition period between the "old" and "new" quantum mechanics expands on his earlier paper where he develops *Bose-Einstein statistics* [2]. A Bose-Einstein Condensate, or BEC results when a non-interacting gas of particles that obey BE-statistics are cooled below a transition temperature. At this point, a quantum mechanical phase transition occurs, and there arises a macroscopic occupation of the ground state. In 1995, seventy years after the original proposal, physicists succeeded in producing BECs [3–5]. The following years have seen a phenomenal burst

of experimental and theoretical exploration of condensates. In 2001, in recognition of their tremendous scientific accomplishment, Eric Cornell, Wolfgang Ketterle, and Carl Weiman were awarded the centennial Nobel Prize in physics "for the achievement of Bose-Einstein condensation in dilute gases of alkali atoms, and for early fundamental studies of the properties of the condensates."

Of course, we know that there are two types of quantum statistics. Not long after Einstein expanded Satyendra Nath Bose's work [6] into BE-statistics, Enrico Fermi and P.A.M. Dirac were simultaneously formulating *Fermi-Dirac statistics* [7,8]. BE-statistics apply to particles with integer spin, called *bosons*, while FD-statistics apply to particles with half-integer spin, called *fermions*.

Just as it is possible to create a macroscopic quantum state of bosons, it is possible to create a macroscopic quantum state of fermions. Unfortunately, the nature of FD-statistics, namely that fermions obey the Pauli exclusion principle [9], means that the systems evolve smoothly from classical to quantum behavior and lack a dramatic hallmark of entry to the quantum regime. Further, quantum statistics dictate that it is much more difficult to create a degenerate Fermi gas (DFG) than it is to create a BEC. As a gas of bosons is cooled, bosonic enhancement [10] makes it *more* likely that an atom in the thermal component is scattered into the ground state. In contrast, as a gas of fermions is cooled, the lower lying states fill, and the Pauli exclusion principle then *slows* any cooling process as fewer and fewer low-lying states are available.

It then seems natural to ask: If it is so difficult to produce DFGs, and if they lack much of the dramatic behavior of BECs, why attempt to study them? The answer is threefold. First, they are the natural counterpart to BECs. Physicists are obviously interested in thoroughly exploring *both* quantum statistical regimes.

Second, the physics of DFGs appears in many important physical systems (*e.g.* superconductors). By studying a new DFG system, especially one where many interaction parameters are widely-tunable, physicists hope to gain insights into broad classes of fermionic behavior. Third, it has recently been realized that in the limit of strong interactions, Fermi systems become *universal* [11,12]. All important physical parameters become proportional to the Fermi energy with different constants of proportionality, which are independent of the nature of the interaction. Thus tabletop experiments in a strongly-interacting atomic DFG can determine the proportionality constants, which also apply to systems such as nuclear matter and compact stellar objects. This is a tremendously exciting development.

It is interesting to note that our motivation for studying DFGs has progressed through all three of these rationales. When we began our cooling and trapping experiments, we settled on a fermionic isotope primarily because so much of the field was focused on BECs. We felt that we could contribute more by striking out into relatively unexplored territory rather than following the crowd. Quickly, we recognized the analogies between an atomic DFG and other DFG systems, and focused on the creation of an atomic superfluid via the Bardeen-Cooper-Schrieffer (BCS) pairing mechanism [13] as the most interesting analog. Production of a fermionic atomic superfluid [14] became our primary long-term goal.

Our interest in the superfluid remained, even as further analysis showed that a true BCS pairing interaction would require exceedingly low temperatures. Attention in the field focused on the use of Feshbach resonances [15] to magnetically tune the interatomic interaction to extremely large and attractive values, where the superfluid transition temperature would become experimentally attainable. A number of groups developed detailed theories of superfluidity in this strongly-interacting

regime, under the name *resonance superfluidity* [16–18]. Even in this modified form, superfluidity was deemed interesting because of the general analogies that could be drawn between the atomic system and other fermionic systems.

In the past few months, we have succeeded in creating degenerate samples in this strongly-interacting regime [19]. As we did so, we began to appreciate the import of the theoretical predictions of universality in strongly-interacting Fermi systems. While superfluidity still remains a major goal of our group, we now view exploration of this universal behavior as the most compelling rationale for studying DFGs.

1.2 Significance of Current Work

This thesis presents the first all-optical production of a degenerate Fermi gas, and the fourth degenerate atomic Fermi gas ever created. While this makes the experimental effort significant in its own right, degeneracy has never been the ultimate goal of our research. Degeneracy is instead a significant milestone in our efforts and an excellent starting point for our further explorations of the physics of Fermi gases.

Reaching this point has taken many years and the efforts of many people. The path to degeneracy was not clear, however, and required the sustained development of broad concepts as well as analytical and experimental techniques. In addition to the experimental results presented within, this thesis attempts to document the development of the many ideas that were central to our eventual achievement of degeneracy—in essence, documenting the route to degeneracy.

A more detailed characterization of the degenerate Fermi gas produced in this experiment is contained in the concurrent thesis of my coworker, Stephen Granade [20].

Both of our theses build on the tremendous foundation laid down previously by Ken O'Hara [21]. A discussion of the primary results of this thesis are contained in the sections below.

1.2.1 All-Optical Production and Detection of a Degenerate Fermi Gas of ^{6}Li

The primary experimental result of this thesis is the first all-optical production of a degenerate Fermi gas of ^{6}Li atoms. With this experiment, we have shown that it is possible to create a degenerate Fermi gas of atoms without using a magnetic trap.

Evaporative cooling in a spin-polarized sample of fermions is not possible. For this reason, most groups [22–24] have attempted to create a degenerate Fermi gas by confining both bosons and fermions in a magnetic trap. Thermal equilibrium between the two species then ensures that evaporatively cooling the bosons results in cooling of the fermions. This approach is known as *sympathetic cooling*. It is relatively simple to remove the bosons at the end of the cooling process, leaving a spin-polarized degenerate Fermi gas. However, the most interesting physics of fermion systems require multiple spin states; specifically mixtures that cannot be contained in a magnetic trap. These other groups must then transfer their degenerate gases to optical traps and use some form of state preparation to create the desired mixture.

By working directly in an optical trap, we avoid the need for this complexity. We directly create the desired mixture and evaporatively cool that mixture in the optical trap. The experiment begins with $\simeq 1 - 3 \times 10^8$ ^{6}Li atoms confined in a Magneto-Optical-Trap (MOT) at a temperature of $\simeq 150\,\mu$K. In the center of the MOT, a 65 W CO_2 laser beam is focused to a spot with a $1/e^2$ intensity radius of

$\simeq$47 μm. The focused CO_2 laser beam creates an additional trap potential for the ^{6}Li atoms The optical trap has a depth $\simeq$700 μK and trap frequencies of 6.6 kHZ in the radial direction and 275 Hz in the axial direction. We tune the MOT laser fields into resonance with the ^{6}Li cycling transition and transfer $\simeq 3{\times}10^6$ atoms into the optical potential, after which, we extinguish the MOT laser fields and magnetic gradient. We then apply a 100 G magnetic field to the atoms, tuning their scattering length to $\simeq$-100 a_0, initiating evaporative cooling in the sample. After 6 s, evaporative cooling has stagnated and the CO_2 laser trap contains $\simeq 1.3 \times 10^6$ atoms at a temperature of $\simeq$50 μK. We then initiate forced evaporative cooling by adiabatically lowering the CO_2 laser intensity. After 60 s of forced evaporative cooling, the atomic sample contains $\simeq 1 \times 10^5$ atoms at a temperature $\leq 4\,\mu$K. For this number of atoms, the Fermi temperature, $T_F = 8\,\mu$K. With $T/T_F < 0.5$, the sample is clearly in the degenerate regime.

At this point, we have the exact atomic system required for future experiments, with no need for transfer or further state preparation. We are therefore in the ideal situation for moving forward in the exploration of atomic DFGs.

1.2.2 Monte-Carlo Model

This thesis describes a numerical computer model for simulating a classical gas trapped in a (possibly time-dependent) three-dimensional Gaussian confining potential. The model uses standard Monte-Carlo techniques to generate a random atomic ensemble, which is then evolved forward in time according to the technique known as *Bird's method* [25], an approach for applying Newton's laws in Monte-Carlo simulations.

Through this model we gained some of our first insights into the general behavior

of trapped atomic gases. It has allowed us to rapidly simulate ideas to test their worth. The model played a direct analytical role during the experiments of Ken O'Hara's thesis [21], where it formed the heart of our temperature measurement technique.

Perhaps the greatest contribution of the model has been that it has allowed us to investigate the effect that an anharmonic trapping potential has on the atomic cloud. Initially, we believed that the anharmonic nature of the trap would not play a big role, since the cold atoms would reside primarily at the bottom of the well where it is close to harmonic. While this is certainly true in the limit of extremely cold temperatures, we found that the effects of the anharmonicity were more significant than we expected. This directly led to our rejection of *in situ* imaging as a temperature measurement technique. Further, the anharmonicity leads to a notable shift between measured trap frequencies and the "true" trap frequency—a shift which we must account for in our analysis.

1.2.3 Fokker-Planck Treatment of Noise-Induced Heating

Motivated by the early failure of optical traps, our group proposed the mechanism of noise-induced heating, whereby fluctuations in the trapping potential heat the atoms contained within. A previous publication of ours provides the basic physics of this mechanism [26], and a subsequent one develops a Fokker-Planck equation approach for more accurately modelling the resulting heating and trap loss [27].

This thesis provides a detailed discussion of the development of the Fokker-Planck equation relevant to this effect and presents a previously unpublished analytical treatment of the equation. As part of this treatment, the long-time behavior of the equation is studied in two important limits. Further, in these two limits, the

equation is converted to a form suitable for numerical solution and a full stability analysis of the numerical technique is performed. The results of the numerical solution are discussed and the long-time behavior is shown to be consistent with the analytical predictions.

The most striking result of these studies is the fact that in the long time limit, the system evolves into a state where the trap population continues to decay while the mean energy of the trapped atoms remains constant (the system has evolved into an single eigenmode). This behavior is qualitatively identical to that reported by early optical trap researchers [28]—a fact which strengthened our conjecture that it was noise-induced heating which limited the performance of early optical traps.

1.2.4 Signal-To-Noise Analysis of Imaging Techniques

When we began investigating the possibility of using direct imaging of the atomic cloud as our means of data collection, it became necessary to develop a quantitative technique for evaluating potential cameras, imaging techniques, and optical designs. To that end, we developed a simple signal-to-noise model that relates the physical parameters of the camera, optical characteristics of the imaging system, and the details of the imaging technique to the signal-to-noise ratio produced in the data.

We used the model to evaluate prospective cameras and to design the imaging system. The development of the model is presented in this thesis and an imaging system similar to ours is analyzed.

1.3 Organization

Chapter 2 introduces the reader to the basic physics of cooling and trapping. MOTs, FORTs, and evaporative cooling are discussed from both theoretical and practical contexts. Evaporative cooling in an optical trap differs in a number of particulars from evaporative cooling in a magnetic trap. This chapter looks at the problem of evaporative cooling in an optical trap and culminates with a derivation of how to optimally lower the intensity of an optical trap to produce a DFG.

Chapter 3 derives the equilibrium spatial and momentum distributions of atoms in the Maxwell-Boltzmann and Fermi-Dirac regimes. In addition, the effect of ballistic expansion on the spatial distributions is examined, and the resulting time-dependent distributions are derived. These results will prove important during the analysis of the experimental data.

Chapter 4 introduces the Monte-Carlo model. We developed a computer program which uses Monte-Carlo techniques to numerically simulate the behavior of a classical gas trapped in a three-dimensional Gaussian potential. Over the years, the program has allowed us to quickly simulate many experiments, gaining valuable insight into the general behavior of trapped gases and the complications introduced by an anharmonic confining potential.

When we initiated our cooling and trapping efforts, optical traps were not suitable for work with degenerate gases. All previous optical traps suffered from unexplained heating and trap loss. We formulated a simple model of noise-induced heating where fluctuations in the trapping potential heat the trapped atoms. Chapter 5 presents the physics of these mechanisms and the details of a Fokker-Planck approach we developed to more accurately study the evolution of the population distributions. Analysis of the Fokker-Planck equation as well as computer simula-

tion show evolution characteristics very similar to those reported in early studies of optical traps—supporting our conjecture that noise-induced heating limited the performance of early traps.

Chapter 6 describes the experiment used to create a degenerate gas of ^{6}Li. This chapter provides detailed descriptions of the apparatus (focusing especially on upgrades to the equipment developed during the course of the experiments presented in this thesis), as well as step-by-step descriptions of the procedure.

Every experimental run culminates in an absorption image of an expanding atomic cloud. Chapter 7 introduces the physics of atomic imaging in general and the details of the specific case used in this experiment in particular. The chapter concludes with a signal-to-noise analysis which relates image quality to physical imaging parameters. This analysis was particularly useful in evaluating cameras and imaging systems when we were designing that portion of the experiment.

Combining the imaging physics of Chapter 7 with the theoretical atomic distributions of Chapter 3, Chapter 8 develops a technique for analyzing the experimental images to determine the number, temperature, and degeneracy parameter of the experimental trials. The chapter demonstrates conclusively that the experiment succeeded in producing a degenerate gas of ^{6}Li.

Chapter 9 is the conclusion of the thesis. This chapter summarizes the major results of the thesis as well as potential (and completed) upgrades to the apparatus and the future outlook for research on degenerate fermi gases.

There are several appendices to this thesis. Appendix A is a detailed presentation of the physical, optical, and collisional properties of ^{6}Li, and how these change with applied external fields. The appendix is written at an introductory level, and includes properties not directly related to this thesis in the hopes that it may be

excerpted to serve as a general reference to ^{6}Li within our research group.

Appendix B discusses the techniques for generating random numbers from non-uniform probability distributions given a source of uniformly-distributed random numbers. This topic is central to implementation of the Monte-Carlo code of Chapter 4. The specific details of the Monte-Carlo implementation are presented in this chapter.

Appendix C provides listings of all the computer codes used in this thesis.

Chapter 2

Basic Cooling and Trapping Techniques

For thou wilt mark here many a speck, impelled
By viewless blows, to change its little course,
And beaten backwards to return again,
Hither and thither in all directions round.

—Lucretius (c. 50 BCE)

2.1 Overview

This thesis is ultimately concerned with atomic cooling and trapping. An atomic *trapping* technique confines atoms in a small spatial region, while an atomic *cooling* technique confines atoms in a small region of momentum space. The benefits of working with trapped and cooled atoms are manyfold, but the two primary gains are long interaction times as a result of the atoms being trapped and reduced thermal fluctuations as a result of the atoms being cooled. This thesis is concerned with creating and investigating a degenerate Fermi gas—a system which forms at extremely low temperatures. Thus, our choice of trapping and cooling techniques are constrained by the stringent requirements of our goal.

This chapter addresses the basic physics of the trapping and cooling techniques utilized in this thesis. For greater detail, the reader is advised to consult earlier

theses by students from this group [21, 29, 30].

2.2 Magneto Optical Traps (MOTs)

2.2.1 Characteristics

Our experiment begins with a Magneto-Optical Trap [31] (MOT). The MOT is the workhorse of the cooling and trapping field. It both traps and cools the atoms, and is comparably easy to implement. A typical MOT contains a relatively large number of atoms ($\simeq 10^6$-10^9) at relatively low temperatures ($\simeq$ 3-150 μK).

The MOT operates via strong optical interactions with the atoms (as described in the next section). The result of this interaction is that the atoms are constantly "jostled" by the optical fields. As a result, while a MOT produces relatively low temperatures and relatively high densities, it falls far short of the requirements for quantum degeneracy. It is useful as a first-stage in the experimental process, where it excels as a source of atoms for the subsequent cooling and trapping techniques used in this thesis.

2.2.2 Physics

As mentioned above, the MOT acts both as a trap and as a cooling technique. The cooling capability is provided by *Doppler cooling*—a method first observed in a MOT precursor known as *optical molasses* [32].

Doppler Cooling

To understand Doppler cooling, we consider the system known as one-dimensional optical molasses. In this system, an atom is placed in a pair of counterpropagating

laser beams, each of which is detuned slightly below an optical resonance in the atom ($\omega < \omega_0$). A schematic of the process is shown in Figure 2.1. If the atom has a velocity to the left, the Doppler shift induced by its motion tunes the beam propagating to the right closer into resonance, while tuning the beam propagating to the left farther out of resonance. As a result, the radiation pressure force is imbalanced between the two beams, and the atom feels a net force to the right—opposing its initial velocity. A similar argument holds if we assume the atom has an initial velocity to the right. In either case, the net force on the atoms serves to decelerate the atom. The atom acts as if it is moving through a viscous fluid (hence the name "optical molasses"). A plot of the net force on the atom as a function of velocity is given in Figure 2.1.

A three-dimensional version can be created by producing three pairs of mutually-orthogonal, red-detuned counterpropagating beams with a common intersection. The velocity of an atom can always be described in terms of components along the three orthogonal beam-pairs. At the intersection of the beams, all three velocity components experience doppler cooling.

While Doppler cooling effectively reduces the momentum (and hence the temperature) of the atoms, it is effectively a random walk in momentum space (albeit one where the probabilities are biased in terms of motion towards the momentum origin). This has two immediate consequences which we must address.

First, although the momentum is kept near zero, there is no spatial confinement for the atoms. It is possible for the atoms to random-walk out of the beams, and hence to leave the viscous-damping region. This lack of confinement is what led to the development of the MOT. The MOT superimposes a spatial confinement mechanism on top of Doppler cooling. The next section addresses this confinement

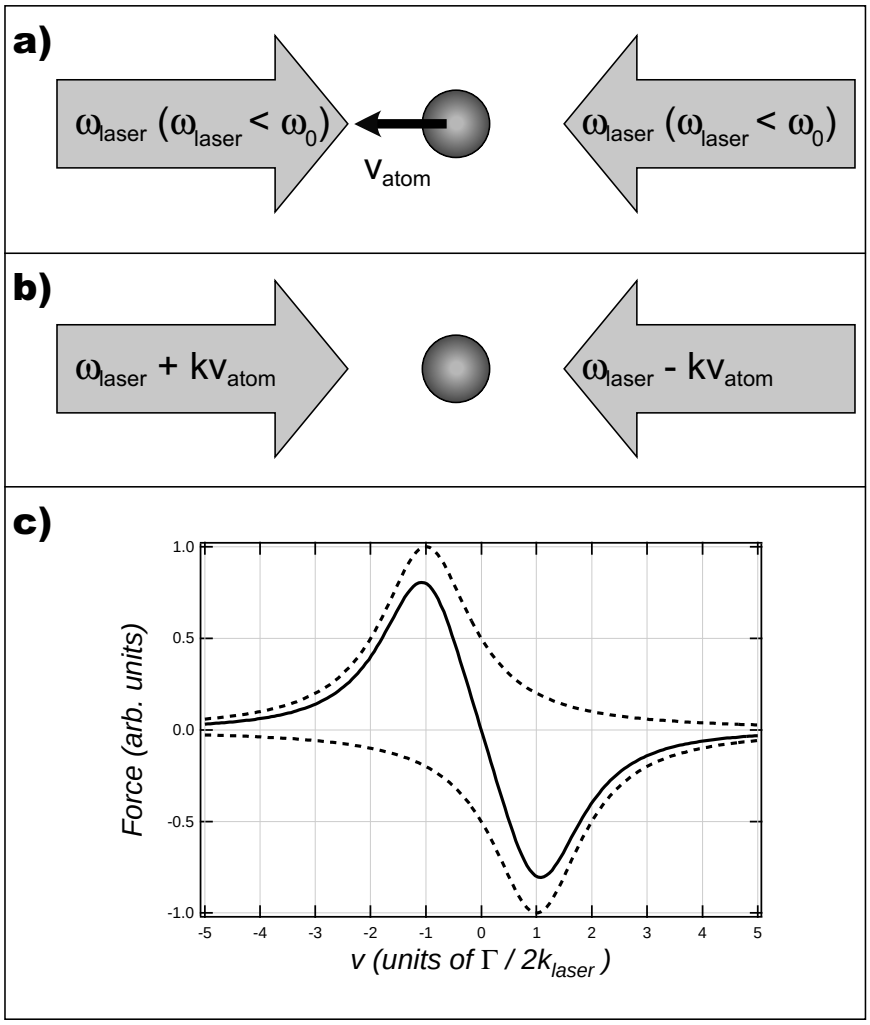

Figure 2.1: Physical basis of Doppler cooling. a) One-dimensional Doppler cooling as seen in the laboratory frame. The atom has an initial velocity to the left, and the beams are detuned to the red of the atomic transition, ω_0. b) The same situation in the reference frame of the atom. Here, the atom is at rest, and the two beams appear to have different frequencies as a result of the Doppler effect. The left beam is shifted towards resonance, while the right beam is shifted away from resonance. Thus, the atom preferentially interacts with the left beam, and the light pressure applies a force which decelerates the atom. c) Here we see a plot of the force on the atom as a function of its velocity. This plot is for the specific detuning value $\Delta = -\Gamma/2$, but the characteristics are fairly general. The two dashed lines show the forces from the two individual beams, while the solid curve shows the total force. Note that for a range of velocities near the origin, the total force is linear. This represents viscous damping.

mechanism.

Second, like any random-walk process, Doppler cooling can be viewed as diffusion. The biasing in favor of steps towards the origin means the atom does not diffuse arbitrarily far away, but it also means that the atom cannot sit precisely on the origin. The net effect is a balancing between the cooling effect produced by the optical molasses, and the diffusion effect produced by the random momentum kicks. The result is a limiting temperature, known as the *Doppler cooling limit*. It is given by

$$T_{\text{Doppler}} = \frac{\hbar\Gamma}{2k_B}, \tag{2.1}$$

where Γ is the natural linewidth of the optical transition. For ^{6}Li, $\Gamma/2\pi = 5.872\,\text{MHz}$ (see Table A.4) and $T_{\text{Doppler}} = 140\,\mu\text{K}$. It is the existence of this sizable, non-zero limit which makes the MOT suitable only for the first-stage of quantum degeneracy studies

Spatial Confinement: The Quadrupole Field

Doppler cooling works by introducing a force that is linear in the atom velocity

$$F_{\text{Doppler}} = -\alpha v. \tag{2.2}$$

The MOT differs from optical molasses by adding another force—one that is linear in the atom position

$$F_{\text{confine}} = -\beta x. \tag{2.3}$$

It does this by using an applied magnetic field gradient. The gradient itself exerts a negligible force in comparison to the optical beams, however, the presence of a field gradient causes a spatially dependent Zeeman shift that is also state dependent.

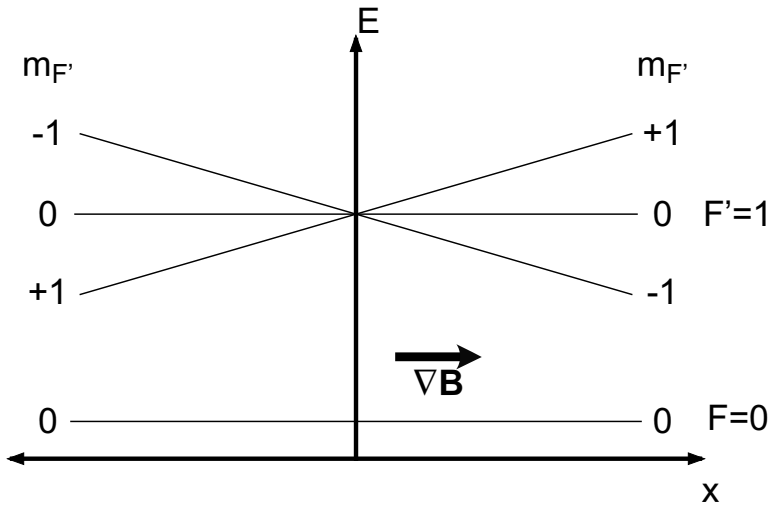

Figure 2.2: Zeeman tuning of the levels. The applied magnetic field gradient splits the magnetic sublevels of the excited state and tunes them as shown.

This spatially-dependent tuning affects the optical force balance in an analogous manner to the velocity-dependent tuning supplied by the Doppler effect.

In analyzing this situation, we consider a one-dimensional system for simplicity. Further, we consider an atom with a total ground state angular momentum of $F = 0$, and a total excited state angular momentum of $F' = 1$. A fully three-dimensional model which includes the actual level structure of ^{6}Li is well beyond the scope of this section, and adds no important insights. In Figure 2.2, we see a schematic of how the levels tune as a result of the field gradient.

By applying a pair of red-detuned, counterpropagating laser beams of specific polarizations, we can use the spatial tuning of the energy levels to cause a linear restoring force. In Figure 2.3, we show a $\hat{\boldsymbol{\sigma}}_-$-polarized beam from the right and a $\hat{\boldsymbol{\sigma}}_+$-polarized beam from the left. Since the ground state has $F = 0$, the $\hat{\boldsymbol{\sigma}}_-$ beam can only drive transitions to the $m_{F'} = -1$ sublevel of the excited state, while the $\hat{\boldsymbol{\sigma}}_+$ beam can only drive transitions to the $m_{F'} = 1$ sublevel of the excited state. An atom in the ground state sees a spatially-varying detuning with respect to the

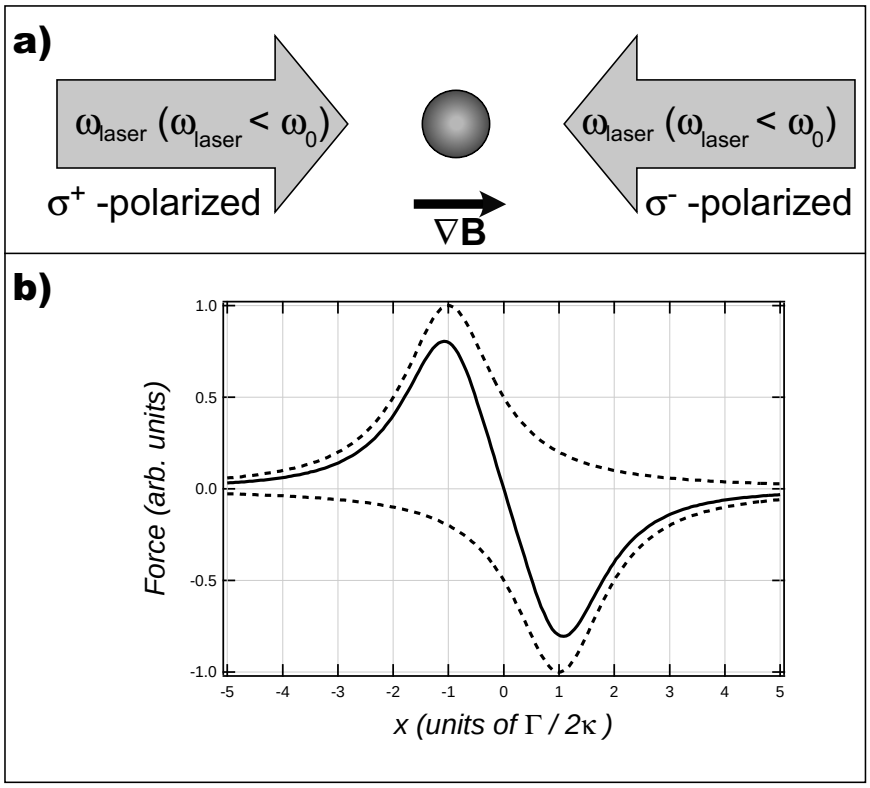

Figure 2.3: Physical basis of spatial confinement. a) One-dimensional spatial confinement. The atom has an initial position to the right of the origin, and the beams are detuned to the red of the unshifted atomic transition, ω_0, and have the polarizations shown. Because of the Zeeman tuning of the levels, the atom is tuned into resonance with the $\hat{\boldsymbol{\sigma}}_-$ beam and out of resonance with the $\hat{\boldsymbol{\sigma}}_+$ beam. The atom interacts preferentially with the $\hat{\boldsymbol{\sigma}}_-$ beam and feels a net force to the left (towards the origin). b) Here we see a plot of the force on the atom as a function of its position. This plot is for the specific detuning value $\Delta = -\Gamma/2$, but the characteristics are fairly general. The two dashed lines show the forces from the two individual beams, while the solid curve shows the total force. The position is given in units of $\Gamma/2\kappa$, where Γ is the natural linewidth of the transition and $\kappa = (\mu_B g/\hbar)(\partial|\mathbf{B}|/\partial x)$, with g the gyromagnetic ratio. Note that for a range of positions near the origin, the total force is linear. This represents a harmonic restoring force.

two beams. If the atom is to the right of the origin, it is closer into resonance with the $\hat{\boldsymbol{\sigma}}_-$ beam, and the atom preferentially interacts with it. The net radiation force pushes the atom back towards the origin. A similar argument holds if the atom is to the left of the origin.

A three dimensional system can be arranged by providing a magnetic field gradient in three orthogonal directions. A pair of anti-Helmholtz coils produces a quadrupole magnetic field with the desired properties. It has a field zero at the center of the coil pair, and has a linear gradient in the field magnitude $|\mathbf{B}|$ in all three directions. If we center the anti-Helmholtz coil pair on the common intersection of optical molasses beams, we can use these beams as the counterpropagating beam pairs in the confinement scheme (the requirement of specific polarizations has no effect on the Doppler cooling).

2.2.3 Final MOT Configuration

A MOT, then, is a pair of anti-Helmholtz coils, centered on the common intersection of three, red-detuned, mutually-orthogonal, pairs of counterpropagating, oppositely-circularly-polarized laser beams. This configuration results in a spatial restoring force and a viscous damping force. The net effect is to produce a ball-shaped atomic gas at or below the Doppler limit (additional effects in three-dimensional MOTs can produce temperatures below the Doppler limit for some atoms—alas, ^{6}Li is not one of these atoms). A schematic of a MOT setup is shown in Figure 2.4.

2.2.4 Real World Complications

Unfortunately, the real world is not quite as simple as the system we have considered here. Alkali atoms (the favorite choice for cooling and trapping experiments), by

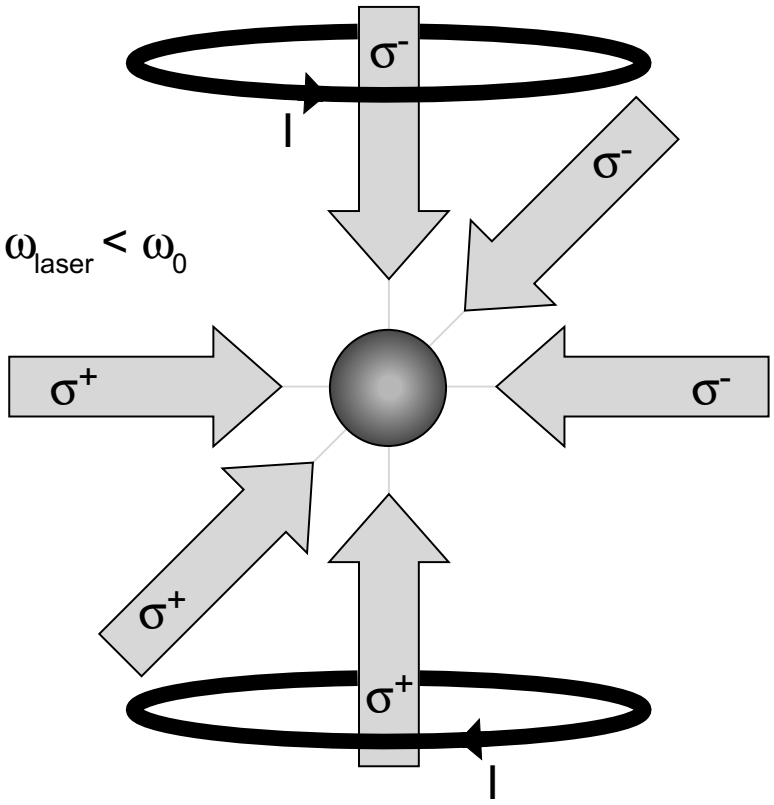

Figure 2.4: Configuration of a MOT. The full geometry of a MOT. The anti-Helmholtz coils are centered on the common intersection of the three, mutually-orthogonal beam pairs.

virtue of their single, unpaired electron, have a ground state that is split into a hyperfine doublet (see Section A.4). As a result, a MOT designed as described above would lose spatial confinement over time as the branching ratio for decays from the excited state eventually moved the population into the hyperfine groundstate that is *dark*—that is, unconnected to the excited state by the optical transition. The problem can be avoided by making the MOT beams bi-chromatic. The addition of a second laser frequency (termed the *repumper*), detuned from the first by the hyperfine splitting of the groundstate, couples the former dark state to the same excited state as the MOT frequency. A small amount of repumper power is sufficient, in most cases, to keep the unwanted hyperfine groundstate empty.

^{6}Li, however, is not one of those cases. The short lifetime of the excited state means that its hyperfine splitting is unresolvable (see Section A.4). As a result, the rate at which atoms decay to the dark state is greatly enhanced and therefore we must apply a correspondingly greater amount of repumper power to keep the MOT operating. In fact, the powers of the two frequencies must be of same order of magnitude. In such a system, the "repumper" is providing a non-negligible force and the system is more accurately viewed as using two MOT transitions rather than the MOT and repumper transitions of other alkali systems.

2.3 Dipole Force Trap

2.3.1 Characteristics

For the primary trap of our experiment, we rely on a *dipole-force* trap [33, 34]. A dipole-force trap uses one or more laser beams to provide spatial confinement for the atoms, but does not cool them. In fact, dipole-force traps optically *heat* the

atoms they contain, although the heating rate can be reduced by using laser beams that are detuned far from resonance. A dipole-force trap of this type is known as a *Far Off-Resonance Trap* [35] (FORT).

We use a special case of the FORT, where the laser beams are so far from the resonance frequency of the atoms that the interaction between the atoms and the electric field of the laser can be treated as quasi-electrostatic. The result is sometimes referred to as a *QUasi-ElectroStatic Trap* [36] (QUEST). We use this terminology only in this chapter—where it is important to make the distinction between dipole-force traps, FORTs, and QUESTs. In all other parts of this thesis, we refer to our apparatus as an optical trap, a CO_2 laser trap, or a FORT.

To a good approximation, the trapping potential of a QUEST is independent of the internal state of the atom. Further, the detuning from resonance is so great that the interaction between the atoms and the optical field is purely coherent scattering. In this regime, the optical scattering rate is just proportional to the cube of the laser frequency. With the infrared laser frequencies used in QUESTs, the scattering rate is so low, and the energy of a scattered photon is so small, that the optical heating is completely negligible. As a result, a QUEST is a purely conservative potential. It is the ideal, state-independent bowl for experiments with ultracold atoms.

2.3.2 Physics

The Dipole Force

The trapping potential arises from the interaction between the electric field of a optical field and the dipole moment that the electric field induces in an electrically-neutral object like an atom. For this reason, the interaction is sometimes referred to as the AC *Stark effect*, in analogy to the DC Stark effect (see Section A.5.2). The

interaction potential for the induced dipole is

$$U = -\frac{1}{2}\overline{\mathbf{p} \cdot \mathbf{E}}. \tag{2.4}$$

Here, $\mathbf{p}$ is the dipole moment induced in an atom of polarizability α ($\mathbf{p} = \alpha\mathbf{E}$). The bar indicates an average over a number of optical cycles. Finally, the factor of one half represents the fact that it is an *induced* dipole moment rather than a fixed dipole moment. Inserting the expression for $\mathbf{p}$ gives us

$$U = -\frac{1}{2}\alpha\overline{\mathbf{E}^2}. \tag{2.5}$$

For an optical field, $\mathbf{E}$ is sinusoidal and the average of $\mathbf{E}^2$ over a number of cycles is of course $\mathcal{E}^2/2$, where $\mathcal{E}$ is the slowly-varying field amplitude. Thus we can write the potential as

$$U = -\frac{1}{4}\alpha\mathcal{E}^2 \quad = -\frac{2\pi}{c}\alpha I \text{ (CGS-Gaussian)} \quad = -\frac{1}{2\epsilon_0 c}\alpha I \text{ (MKS)}, \tag{2.6}$$

where I is the optical intensity. Note that the sign of α will determine whether an atom is attracted to or repelled from maxima in the optical field. We treat the atoms as a two-level atomic system interacting with a classical electric field. The interaction is given by $\boldsymbol{\mu} \cdot \mathbf{E}$, with $\boldsymbol{\mu} = e\mathbf{r}$ the electric dipole moment operator (see Section A.6.1). First-order time-dependent perturbation theory allows us to calculate $\langle\boldsymbol{\mu}\rangle$, the expectation value of the dipole moment operator. Rewriting $\mathbf{p} = \alpha\mathbf{E}$ as $\langle\boldsymbol{\mu}\rangle = \alpha\mathbf{E}$ we find

$$\alpha = \frac{\mu^2}{\hbar}\left[\frac{1}{\omega_0 - \omega} + \frac{1}{\omega_0 + \omega}\right]. \tag{2.7}$$

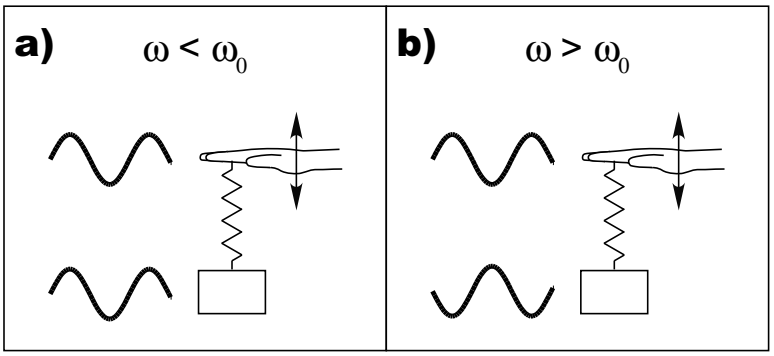

Figure 2.5: Heuristic model of polarizability. The detuning-dependence of the sign of the atomic polarizability can be heuristically determined by considering the atom as a driven oscillator. Considering a familiar driven oscillator system we see that: a) For driving below the natural frequency of the oscillator, the driven system follows the forcing function, and the polarizability is positive. b) For driving above the natural frequency of the oscillator, the driven system is 180° out of phase with the driving, and the polarizability is negative.

In the above, μ is the dipole moment matrix element for a transition between the two levels.

From this result, we can see that the sign of α is determined by the sign of the first term in the brackets. The polarizability is positive when the driving frequency is below the resonance frequency ($\omega < \omega_0$) and negative when the driving frequency is above the resonance frequency ($\omega > \omega_0$). Another way of expressing this is that the dipole oscillates in phase with the driving field when the excitation is below resonance and out of phase with the driving field when the excitation is above resonance. We can intuitively understand this behavior by recognizing that the atom is acting as a driven harmonic oscillator. Thinking of a mass-spring system driven by a supporting hand (see Figure 2.5), we immediately realize that the mass moves with the hand for slow driving, while the mass moves in opposition to the hand for fast driving.

Our two-level model is, of course, an oversimplification. In general, the ground

and excited states have fine and hyperfine structure (see Section A.4). The polarizability of the ground state for this more complicated system is a sum of terms of the form (2.7),

$$\alpha = \frac{1}{\hbar} \sum_{|g\rangle,|e\rangle} \mu_{eg}^2 \left[\frac{1}{\omega_{eg} - \omega} + \frac{1}{\omega_{eg} + \omega} \right], \tag{2.8}$$

where $\mu_e g$ is the dipole moment transition matrix element between a specific hyperfine ground state $|g\rangle$ and a specific hyperfine excited state $|e\rangle$ and ω_{eg} is the associated transition frequency.

In a QUEST, however, the extreme detuning simplifies matters greatly. The frequency-dependent terms in (2.8) become equal for all transitions. Effectively, the fine and hyperfine structure cannot be resolved as a result of the extreme detuning. As a consequence, the two-level approximation is once again valid. The net effect is a completely hyperfine state-independent polarizability, and hence hyperfine state-independent trapping potential.

In this limit, the trap potential is given by

$$U = -\frac{1}{4}\alpha_0 \mathcal{E}^2 \quad = -\frac{2\pi}{c}\alpha_0 I \text{ (CGS-Gaussian)} \quad = -\frac{1}{2\epsilon_0 c}\alpha_0 I \text{ (MKS)}, \tag{2.9}$$

where α_0 is the static polarizability of the atom as used in the DC Stark Effect (see Section A.5.2).

For the case of ^{6}Li, the $2P$ excited state dominates, and the sum can be simplified even further. Ignoring all other excited states leads to the expression

$$\alpha = \frac{2\mu_0^2}{\hbar\omega_0}, \tag{2.10}$$

where μ_0 is the dipole moment of the $2S - 2P$ cycling transition, and ω_0 is the

corresponding frequency (see Section A.6.3). For ^{6}Li, this expression agrees with the more complicated result (2.8) to within a few percent.

Optical Scattering Rate

As briefly mentioned earlier, dipole-force traps heat the atoms they contain. This is a result of optical scatter, and the heating process is identical to the momentum-space diffusion discussed in the context of optical molasses and the MOT (Section 2.2.2).

We can again use first-order time-dependent perturbation theory to calculate the photon scattering rate. Fermi's Golden Rule gives us

$$\Gamma_{\text{scat}} = \frac{3\pi c^2}{2\hbar\omega_0^3}\left(\frac{\omega}{\omega_0}\right)^3 A^2 \left[\frac{1}{\omega_0-\omega}+\frac{1}{\omega_0+\omega}\right]^2 I, \tag{2.11}$$

with A the Einstein A-Coefficient

$$A = \frac{4\omega_0^3\mu^2}{3\hbar c^3}\ (\text{CGS-Gaussian}) \quad = \frac{\omega_0^3\mu^2}{3\pi\epsilon_0\hbar c^3}\ (\text{MKS}). \tag{2.12}$$

Again, for a real atom, we need to consider a sum of contributions of the form (2.11)

$$\Gamma_{\text{scat}} = \sum_{|g\rangle,|e\rangle} \frac{3\pi c^2}{2\hbar\omega_0^3}\left(\frac{\omega}{\omega_{eg}}\right)^3 A_{eg}^2 \left[\frac{1}{\omega_{eg}-\omega}+\frac{1}{\omega_{eg}+\omega}\right]^2 I. \tag{2.13}$$

This equation also simplifies dramatically in the limit of extreme detuning. In a QUEST,

$$\Gamma_{\text{scat}} = \frac{2A}{\hbar\omega_0}\left(\frac{\omega}{\omega_0}\right)^3 U_0, \tag{2.14}$$

where U_0 is the well-depth (the reader should note that an identical result can be

achieved in terms of the Larmor power). The factor of $(\omega/\omega_0)^3$ is what makes the QUEST so useful. Extremely low photon scattering rates are possible. For our system (^{6}Li in a CO_2-laser based QUEST), the scattering rate is 2 photons per atom per hour. The recoil energy of a CO_2-laser photon at 10.6 μm is 14 nK in temperature units. At our scattering rate, this produces a heating rate on the order of 10 pK/s. With the energy scale of the system on the order of 1 μK, this is a completely negligible heating rate. Thus, the trapping potential is perfectly conservative.

2.3.3 Trap Geometry

Dipole-force traps fall naturally into two classes: blue-detuned and red-detuned [37]. A blue-detuned trap repels atoms from the region of highest intensity, while a red-detuned trap attracts them. Spatial confinement in a blue-detuned trap requires surrounding the atoms with regions of high intensity. As a result, the trap geometries tend to be rather complicated—involving multiple beams or hollow beams. However, blue detuned traps have the natural advantage of very low scattering rates, as the atoms spend little time in regions of high optical intensity. This practical advantage of a blue-detuned trap has lessened, however, as a result of the development of red-detuned QUESTs, which can also avoid optical scatter as described above.

Red-detuned traps need only to have a local intensity maximum to spatially confine atoms. The simplest geometry, and the one we use in our experiments, is a simple, focussed beam. The transverse Gaussian profile provides a radial maximum on the axis, while the focus provides a longitudinal maximum. A schematic of the potential well generated by a single, focused-beam red-detuned trap is shown in Figure 2.6.

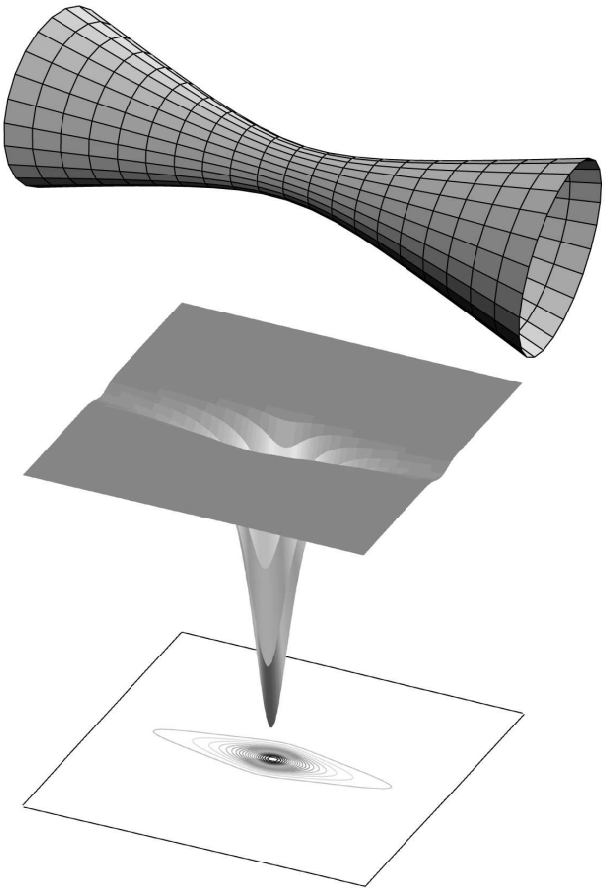

Figure 2.6: Trapping potential of a single-beam FORT. The top image shows a focussed Gaussian beam. The middle image is the trapping potential in a horizontal plane through the axis of the beam. The bottom image is the corresponding contour plot of the trapping potential. Note a common feature of single-beam FORTs:the confinement in the radial direction is significantly stronger than the confinement in the axial direction. This results in elongated, "cigar-shaped" clouds.

For a focused Gaussian beam, the intensity is [38]

$$I(r,z) = \frac{I_0}{1+(z/z_0)^2}\ \exp\left[\frac{-2r^2}{a^2}\right]. \tag{2.15}$$

Here I_0 is the peak intensity in the beam, z_0 is the Rayleigh range ($z_0 = \pi a^2/\lambda$), and a is the $1/e^2$ intensity radius of the beam at the focus. Inserting this intensity profile in the expression for the potential well of a QUEST (2.9) yields

$$U(r,z) = -\frac{U_0}{1+(z/z_0)^2}\ \exp\left[\frac{-2r^2}{a^2}\right], \tag{2.16}$$

where

$$U_0 = \frac{2\pi}{c}\alpha_0 I_0 \text{ (CGS-Gaussian)} \quad = \frac{1}{2\epsilon_0 c}\alpha_0 I_0 \text{ (MKS)}. \tag{2.17}$$

To determine the oscillation frequencies of the trap, we Taylor expand the trap potential about the center

$$U(r,z) \simeq -U_0 + \frac{U_0}{z_0^2}z^2 + 2\frac{U_0}{a^2}r^2 + \dots\ . \tag{2.18}$$

The second and third terms must be equivalent to the standard harmonic oscillator potential energy terms

$$\frac{U_0}{z_0^2}\,z^2 \equiv \frac{1}{2}\,m\omega_z^2 z^2, \tag{2.19}$$

$$2\frac{U_0}{a^2}\,r^2 \equiv \frac{1}{2}\,m\omega_r^2 r^2. \tag{2.20}$$

From this we can determine

$$\omega_z = \sqrt{\frac{2U_0}{mz_0^2}}, \tag{2.21}$$

$$\omega_r = \sqrt{\frac{4U_0}{ma^2}}. \tag{2.22}$$

2.3.4 Real World Complications

An actual QUEST does not differ dramatically from the simplified view presented in this section. The experimenter must, of course, attempt to minimize distortions to the beam as a result of abberations, vignetting (the clipping of the beam from apertures that are too small), etc. Any distortions not only affect the minimum focus size, and hence the deepest well that can be achieved with a laser of a given power, but also change the intensity profile at and near the focus, resulting in deviations to the potential shape discussed above.

For a long time, groups were unable to construct FORTs or QUESTs with long storage times. Trap lifetimes were limited to at most a few seconds—far shorter than expected based on optical scattering rates or loss rates due to background gas collisions. Eventually, we postulated that the atoms were being heated by fluctuations in the trapping potential caused by fluctuations in the trapping laser. We developed a simple formalism which relates the fluctuation spectrum to the resulting heating rate (see Chapter 5). As a result, we built our QUEST using an *ultrastable* CO_2 laser. The result was a storage time in excess of 300 s [21, 39]—a full two orders of magnitude longer than previous FORTs and QUESTs. It is now accepted that an effective FORT or QUEST must utilize an ultrastable trapping laser.

Loading the trap brings additional challenges. The two lasers most often used

for quests are the CO_2 and the Nd:YAG. Both lasers emit radiation that is out of the visible range. The Nd:YAG produces near-infrared light at λ=1064 nm and the CO_2 produces infrared light at λ=10.6 μm. Using these lasers as the source of a QUEST necessarily involves very high laser powers. Working with high-powered, invisible beams requires extreme care from the experimenter.

Further, the initial alignment of the system is quite difficult. The challenge is to place the focus of an invisible beam, roughly 50 μm in radius and extending for about 0.5 mm, into the center of a MOT of radius 3 mm. To make this even more difficult, both the focus and the MOT occur inside a vacuum system, away from direct access. The first time that our group attempted this, it took almost six months before we succeeded. We ultimately relied on a technique utilizing visible beams to place the optics as close to the correct position as possible and a spectroscopic technique to detect the minute effect which the misaligned CO_2 beam had on the atoms (see [21] for a detailed discussion). Once we had a signal, of course, we could peak it up. Further, once the system was aligned the first time, we gained valuable knowledge on the precise location of the MOT within the vacuum system—information that makes subsequent alignment simpler.

2.4 Evaporative Cooling

2.4.1 Characteristics

Most, if not all, experiments involving degenerate atomic gases use evaporative cooling as the cooling technique. Evaporative cooling gets its name from the conceptual similarity it shares with the cooling process experienced by a bowl of hot soup or a cup of hot coffee. Collisions in the trap preferentially eject high-energy atoms from

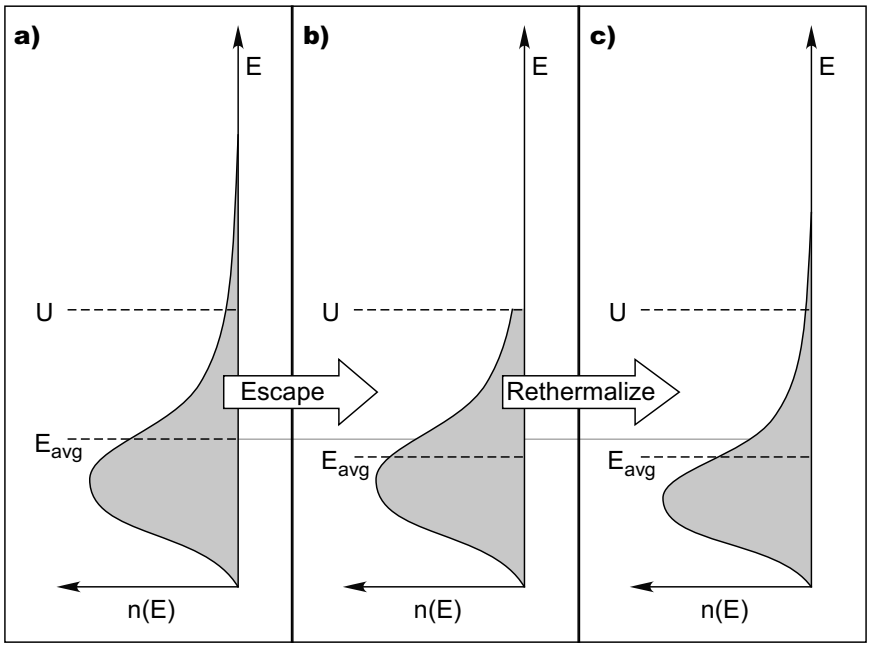

Figure 2.7: Evaporative cooling process. a) Collisions in the gas have produced a "thermal tail" of atoms which extends above the well depth. These atoms are unbound. b) The unbound atoms leave the system, each carrying much more than the mean atomic energy $E_{\rm avg}$. c) Collisions between the atoms rethermalize the cloud, reducing the temperature, and producing another thermal tail. At this point, the system begins over at a). Note that, while the effect is portrayed as a discrete process, in reality the escape and rethermalization happen continuously. When the cloud has cooled to a point where a negligible faction of the thermal tail extends above the well, the evaporation stagnates. Some additional technique (*e.g.* RF-knife, continuous lowering) is then required for evaporation to continue.

the trap (in fact, the ejected atom necessarily will have an energy greater than the mean energy of the trapped cloud). Further collisions in the trap rethermalize the remaining atoms. The new mean energy and energy spread are lower than before the ejection of the "hot" atoms—hence the cloud is now at a lower temperature. A schematic of this process is shown in Figure 2.7.

The success of evaporative cooling hinges on elastic collisions between atoms dominating the inelastic collisions. At the temperatures characteristic of cooling and trapping experiments, the kinetic energies of the atoms are insignificant compared

to the energy differences between atomic states. Inelastic collisions in ultracold systems are then almost exclusively exothermic and release tremendous amounts of energy into the system (in ^{6}Li, the release would be on the order of 10 mK, some 3-4 orders of magnitude larger than the temperature scales we work with). This release either ejects the atoms directly from the trap, heats the cloud through secondary collisions, or a combination of the two effects. Any of these three possibilities are inimicable to work at ultracold temperatures. For evaporative cooling to succeed, the elastic collision rates in the system must dominate the inelastic collision rates. By working with the two lowest hyperfine ground states of ^{6}Li, we dramatically suppress all inelastic rates in the system, making it an excellent candidate for evaporative cooling.

Eventually, as the cloud gets cooler and cooler, the likelihood of a collision producing an atom capable of escaping the well becomes smaller and smaller (in fact, evaporation rate scales as $e^{-U/T}$, where U is the well depth in temperature units, and T is the cloud temperature). When the evaporation rate is highly-suppressed by this exponential, the system is said to have *stagnated*. In previous work on BECs, researchers enabled continued evaporation in their magnetic traps by employing an RF-knife technique. This approach utilizes the fact that the internal state energies of the atoms tune spatially in the magnetic trap as a result of the Zeeman effect. By applying an RF-field that matched the splitting between trapped and untrapped states *for atoms in a specific field magnitude on the periphery of the atomic cloud*, they could eject only the hottest atoms from the trap. By slowly tuning the RF-field to match splittings at positions closer and closer to the center of the trap, the experimenters were able to effectively have a time-dependent well depth. With a suitable lowering curve, the problem of stagnation could be avoided.

In our optical trap, the atoms escape from the well without the help of an RF-transition. How would we avoid stagnation? Simple. By continuously lowering the intensity of the CO_2 laser beam, we can easily lower the depth of the well. The situation differs slightly from the time-dependent well depth in the RF-knife scenario, however. In our scheme, lowering the intensity also "loosens" the trap—it lowers the oscillation frequencies. The elastic collision scattering rates scale with the oscillation frequencies of the trap. Hence, lowering the well could have a dramatic effect on the evaporation rate. This effect does not happen with the RF-knife technique, as the underlying potential is not being modified—a manufactured "leak" in the well is being lowered. Any technique that avoids stagnation is a *forced evaporation* process. The difference between these two methods of forced evaporation is illustrated in Figure 2.8.

Because of this difference, we could not simply lower our well according to the schemes developed by the BEC researchers. We had to develop our own understanding of evaporative cooling in a continuously-lowered optical potential.

2.4.2 Physics

As part of a prior thesis by this group [21], Ken O'Hara developed a full s-wave Boltzmann-equation model of evaporative cooling. This model fully treated evaporation of a two-state mixture of fermionic atoms in a time-dependent Gaussian well. The results were quite encouraging. The calculations showed that evaporation to degeneracy in such a system should be possible. The calculations and model were quite complex, however, and took an extremely long time to complete. We have since developed simple scaling-law expressions for evaporation in the system [40]. These scaling laws, based on simple physical principles and heuristic arguments,

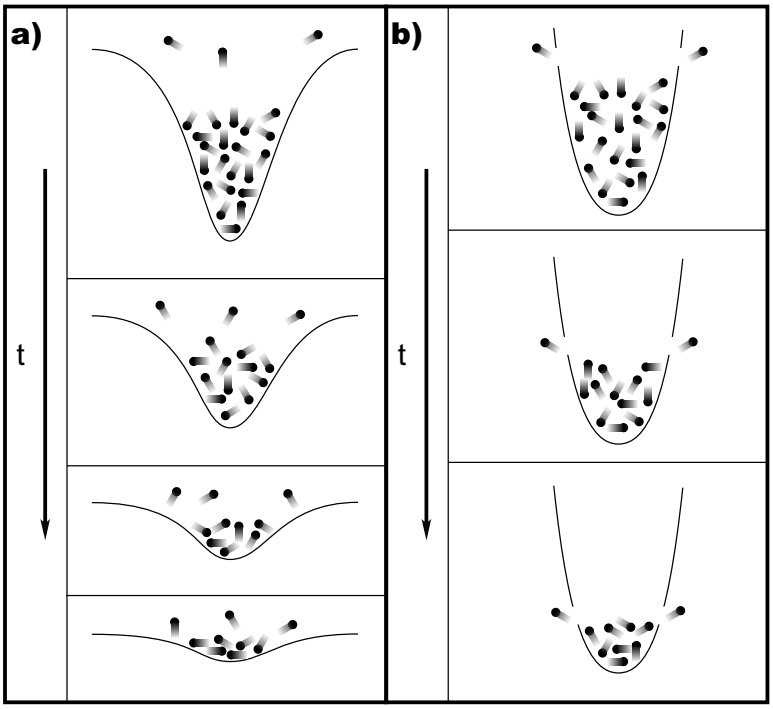

Figure 2.8: Methods of forced evaporation. a) The continuous-lowering method used in this thesis. Stagnation is avoided by lowering the well-depth in a manner that remains below a portion of the thermal tail. Note the loosening of the trap as it is lowered. This arises because the oscillation frequencies of the trap are functions of the well depth ($\nu \propto \sqrt{U}$). b) The RF-knife technique used in magnetic trapping. An applied RF-field combines with the spatial Zeeman tuning of the trapping field to produce a "leak" on the periphery of the cloud. The RF-frequency is adjusted over time to move the spatial location of the leak and keep it on the periphery of the cloud.

match the Boltzmann-equation model to an uncanny degree of accuracy. Below we reproduce the derivation of the scaling laws. They provide a quite accurate model of evaporative cooling in a continuously-lowered optical potential.

Evaporative Cooling Scaling Laws

We begin by writing an expression for the change of energy of the trapped gas as the well depth is changed. We must include not only the energy taken out by evaporation, but (what differs from RF-knife techniques) the work done by the gas on the potential as the gas expands in the loosening trap. We write the energy loss due to evaporation as

$$\Delta E_{\text{total}} = \Delta N \, \overline{\Delta E}_{\text{atom}}. \tag{2.23}$$

In the above, $\overline{\Delta E}_{\text{atom}}$ is the average energy carried away by an evaporating atom. From studying the s-wave Boltzmann equation, we find that for any trap potential that is harmonic at the bottom,

$$\overline{\Delta E}_{\text{atom}} = U + \frac{(\eta - 5)}{(\eta - 4)} k_B T = U + \alpha k_B T, \tag{2.24}$$

for $U \gg k_B T$, where U is the trap depth, T is the cloud temperature, and $\eta = U/(k_B T) \gg 1$.

To get an expression for the work done by the gas on the potential, we make the assumption that the evaporation process is carried out near stagnation, where the efficiency of evaporation is very high. This implies that $\eta \gg 1$, and the atoms see a nearly harmonic potential. In a harmonic potential, the average potential energy of a cloud with total energy E is $E/2$. We can then write the work done in responding

to a change in the potential of ΔU as

$$W = \frac{\Delta U}{U}\frac{E}{2}. \tag{2.25}$$

Combining (2.24) and (2.25), and writing the result in differential form, we find the differential equation for the energy of the gas

$$\dot{E} = \dot{N}(U + \alpha k_B T) + \frac{\dot{U}}{U}\frac{E}{2}. \tag{2.26}$$

We then make the assumption that we are dealing with a classical gas. In this limit, the total energy of of the cloud is $E = 3Nk_BT$. This implies $\dot{E} = 3\dot{N}k_BT + 3Nk_B\dot{T}$. Inserting these relations into (2.26) yields

$$3\dot{N}k_BT + 3Nk_B\dot{T} = \dot{N}(U + \alpha k_B T) + \frac{\dot{U}}{U}\frac{3Nk_BT}{2}. \tag{2.27}$$

To eliminate one of the three system variables (N, U, T), we make the further assumption that we will lower the well in a manner that maintains η as a constant (an approach which ensures thermal equilibrium). From this we find the relationships

$$T = \frac{1}{k_B\eta}U, \tag{2.28}$$

$$\dot{T} = \frac{1}{k_B\eta}\dot{U}. \tag{2.29}$$

Inserting these in (2.27), and collecting terms gives the differential equation

$$\frac{\dot{N}}{N} = \left(\frac{3}{2\left(\eta' - 3\right)}\right)\frac{\dot{U}}{U}\,, \tag{2.30}$$

where we have defined $\eta' = \eta + \alpha$ for simplicity.

Of course, $U(t)$ is an arbitrary function at this point (subject only to the constraint that it maintains η as a constant). Thus we cannot derive an explicit solution to (2.30). However, we can find an implicit solution. The form of (2.30) allows us to immediately write

$$\ln\left(\frac{N}{N_0}\right) = \left(\frac{3}{2\left(\eta' - 3\right)}\right) \ln\left(\frac{U}{U_0}\right), \tag{2.31}$$

where N_0 and U_0 are the trap population and well depth at some convenient time origin. This expression can, of course be rewritten as our desired scaling law

$$\frac{N}{N_0} = \left(\frac{U}{U_0}\right)^{\frac{3}{2\left(\eta' - 3\right)}}. \tag{2.32}$$

While it is useful to have a scaling law that relates the trap population to the well depth, it does not address the most important question we would like answered, namely: How far do we have to lower the well to approach the degenerate regime? For this, we need to develop a relationship between the phase-space density of the atoms and the well depth. The phase-space density of a classical gas is

$$\rho = N\left(\frac{h\overline{\nu}}{k_B T}\right)^3. \tag{2.33}$$

Here, $\overline{\nu}$ is the geometric mean of the trap oscillation frequencies. This parameter varies as the well depth changes

$$\overline{\nu} \propto \sqrt{U}. \tag{2.34}$$

Inserting this result in (2.32) and making use of (2.28) and (2.29) leads to the

new scaling laws

$$\frac{\rho}{\rho_0} = \left(\frac{U_0}{U}\right)^{\frac{3(\eta'-4)}{2(\eta'-3)}}, \tag{2.35}$$

$$= \left(\frac{N_0}{N}\right)^{\eta'-4}. \tag{2.36}$$

This is the primary result we seek. It allows us to estimate how far we must lower the FORT in order to achieve a desired increase in the phase-space density. There is one more scaling law worth deriving. If we assume that the elastic collision cross-section is energy-independent (*i.e.* the collision cross-sections are not unitarity-limited (see Section A.7.2)), the collision rate, γ is proportional to

$$\gamma \propto \frac{N\overline{\nu}^3}{k_B T}. \tag{2.37}$$

Using this relationship, we can derive the final scaling law

$$\frac{\gamma}{\gamma_0} = \left(\frac{U}{U_0}\right)^{\frac{\eta'}{2(\eta'-3)}}. \tag{2.38}$$

These scaling laws reveal one very striking feature. The form of (2.36) is identical to that for an RF-knife technique [41] where the knife is lowered to maintain η as a constant! Evaporation in a continuously lowered potential is just as efficient in terms of trap population as an RF-knife. This answers one of the major objections to this form of evaporation. Many researchers had intuitively believed that forced evaporation based on a continuous lowering of the well would be an inherently "wasteful" approach. In hindsight, we can now clearly see that this is not true, *provided that the well is lowered slowly so the atoms only leave via evaporation.* In such a situation, the only change to the phase-space density comes from evaporation,

as adiabatic lowering of a potential well cannot affect the phase-space density of the trapped cloud. Thus, in both approaches, we see that the only loss of atoms and the only change in phase space density arise from the evaporation process. It is therefore not surprising that the two techniques have the same efficiency. The reader should note, however, that this assumes a *given value of* η. In reality, optical traps naturally achieve values of η that are significantly higher than in magnetic traps. As a result, while they share the same *expression* for efficiency, the higher η in optical traps means that, practically, they are much more efficient than magnetic traps.

One place where the two techniques differ significantly is in the elastic collision rate. In an RF-knife approach, as mentioned previously, the oscillation frequencies of the trap do not change. Viewing (2.37) in light of the constant value of $\overline{\nu}$ and a slow scaling of N with U in an RF-knife technique, we see that it is possible for the collision rate to actually increase as the evaporation process advances and the temperature of the cloud decreases. This situation is known as *runaway evaporation* and plays a significant role in many BEC experiments. Because of the loosening of the trap in the continuous lowering approach, runaway evaporation cannot occur. Many researchers believed that this would make the approach unfit for reaching degeneracy. This is incorrect. Runaway evaporation is never *required* to achieve degeneracy. Without runaway evaporation, the evaporation process is merely slowed. Provided that the system has a low loss rate due to background gas collisions and inelastic processes, as well as low optical (see Section 2.3.2) and noise heating rates (see Chapter 5), there is no limit to how long the experimenter can wait to reach degeneracy (subject only to the patience of the experimenter). All of these conditions apply in our experiment. Further, optical traps are typically tighter than

magnetic traps—their initial values of $\overline{\nu}$ are larger, and hence, so are the collision rates. Finally, the exceedingly large scattering lengths available in the ^{6}Li system [42] produce correspondingly large scattering rates. Thus, it is not a foregone conclusion that forced evaporative cooling via a continuously-lowered potential well cannot produce degeneracy.

We now use the scaling laws to determine if degeneracy is possible in our system. It is quite easy for our system to produce $\eta = 10$ via evaporation in a well of constant depth. If we choose this value for our lowering process, we find $\eta' = 10.8$. Inserting this in the general scaling laws above we get the scaling laws for this particular lowering approach

$$\frac{N}{N_0} = \left(\frac{U}{U_0}\right)^{0.19}, \tag{2.39}$$

$$\frac{\rho}{\rho_0} = \left(\frac{U}{U_0}\right)^{-1.3}, \tag{2.40}$$

$$\frac{\gamma}{\gamma_0} = \left(\frac{U}{U_0}\right)^{0.69}. \tag{2.41}$$

After free evaporation at a constant well depth, our trap produces values of $\eta \simeq$10-20, with a phase-space density in the range $\rho \simeq$0.003-0.008. Using the lower value of phase space density in (2.40), we find that we should have to lower the well by a factor of no more than 85 to achieve degeneracy at $\rho = 1$. Taking this as our target, (2.39) and (2.41) tell us that we should expect to have at least 43% of the atoms remaining and that the collision rate should have slowed by a factor of no more than 22. These results appear promising. But how long would it take to lower the trap by this factor? This is the topic of the next section.

Derivation of the Lowering Curve

In our derivation of the scaling laws, we made the assumption that we lower the well in a manner that maintains η as a constant. With that assumption, we derived the differential equation (2.30). We were able to solve this equation implicitly to determine our first scaling law. If we had the evaporation rate equation for $\dot{N}/N$, we could substitute into the differential equation to find an explicit solution for U.

Luckily, the s-wave Boltzmann equation allows us to get exactly such an expression for $\dot{N}/N$. To lowest order, the Boltzmann equation is [21, 40]

$$\dot{N} = -2(\eta - 4)\, e^{-\eta} \gamma N. \tag{2.42}$$

We rewrite this equation as

$$\frac{\dot{N}}{N} = -\left(\frac{3}{\eta'}\right)\left(\frac{1}{\tau}\right)\frac{\gamma}{\gamma_0}, \tag{2.43}$$

where we have defined

$$\frac{1}{\tau} = \frac{2}{3}\eta'(\eta - 4)\exp[-\eta]\gamma_0 \tag{2.44}$$

for a reason that will become clear soon. We then insert the scaling law in (2.38) to write

$$\frac{\dot{N}}{N} = -\left(\frac{3}{\eta'}\right)\left(\frac{1}{\tau}\right)\left(\frac{U}{U_0}\right)^{\frac{\eta'}{2\,(\eta'-3)}}. \tag{2.45}$$

Inserting the differential equation (2.30) yields

$$\frac{\dot{U}}{U} = -\frac{2\,(\eta' - 3)}{\eta'}\left(\frac{1}{\tau}\right)\left(\frac{U}{U_0}\right)^{\frac{\eta'}{2\,(\eta'-3)}}. \tag{2.46}$$

Making the simplifying definition $b = \eta'/(2\,(\eta' - 3))$, this becomes

$$\frac{\dot{U}}{U} = -\frac{1}{b\tau}\left(\frac{U}{U_0}\right)^b. \tag{2.47}$$

This equation yields the desired solution

$$U(t) = U_0\left(\frac{1}{1 + t/\tau}\right)^{\frac{2\,(\eta' - 3)}{\eta'}}. \tag{2.48}$$

We can specialize to the case we considered previously. There we assumed $\eta = 10$ and $\rho_0 = 0.003$. This information alone is not enough to specify the lowering curve. We must also know γ_0. In the classical regime, we can write the collision rate as [40]

$$\gamma_0 = \frac{8\pi^2 N_0 M \overline{\nu}^3 a^2}{k_B T_0}, \tag{2.49}$$

where M is the mass of the atoms and a is the scattering length.

Taking reasonable values for our system ($\overline{\nu} = 1300$, $a = -300a_0$, $N = 4\times10^5$, T_0 =30 μK), we find that the proper lowering curve is

$$U(t) = U_0\left(\frac{1}{1 + t/1.2}\right)^{1.446}. \tag{2.50}$$

From this lowering curve, we can see that we need to lower for approximately 25 s to reach the $U/U_0 = 85$ level where we expect to reach degeneracy. On a timescale this short, the system will not decay significantly as a result of background-gas collisions, nor will optical or noise heating have significantly affected the temperature of the cloud. Finally, it is within the "patience limit" of the experimenter. Therefore, based on the scaling law analysis, forced evaporation via continuous lowering of the trapping potential is a viable technique for producing degenerate samples in our

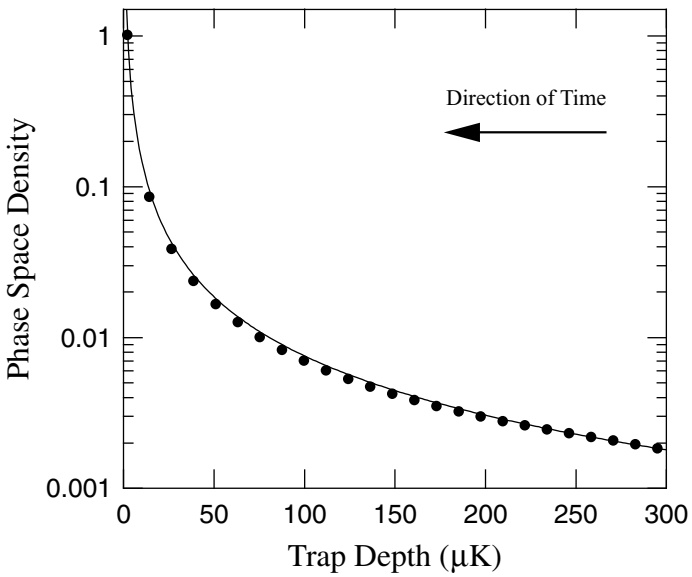

Figure 2.9: Comparison of scaling law and Boltzmann equation: phase-space density. For the system parameters in the text, the solid curve shows the phase-space density prediction of the scaling law (2.35), while the circles show the output of the s-wave Boltzmann equation. (From [40]).

system.

Comparison With the s-Wave Boltzmann Equation

With this lowering curve, how well do the scaling laws compare to the results of the s-wave Boltzmann equation? In Figure 2.9 and Figure 2.10, we see figures from [40] which compare the two approaches for the specific system parameters and lowering curve defined above. In each graph, the solid curves are the scaling law prediction while the symbols show the result of the Boltzmann equation. The first graph shows how the phase-space density of the cloud changes as the well is lowered, while the second shows the change in the trap population and in the collision rate as the well is lowered.

Clearly the two approaches agree extremely well. The scaling laws match the

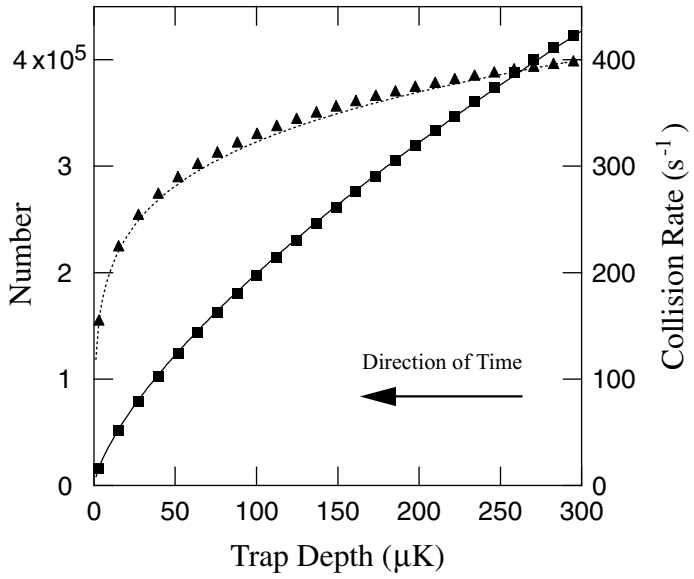

Figure 2.10: Comparison of scaling law and Boltzmann equation: number and collision rate. For the system parameters in the text, the dashed curve shows the trap-number prediction of the scaling law (2.32), while the triangles show the output of the s-wave Boltzmann equation. The solid curve shows the collision rate prediction of the scaling law (2.38), while the squares show the output of the s-wave Boltzmann equation. (From [40]).

full Boltzmann equation all the way to $\rho = 1$ despite all of the classical assumptions made in their derivations! Further, the results of the Boltzmann equation confirm that a lowering curve of the form given in (2.48) does indeed approximately maintain η as a constant (during the Boltzmann simulation η varied between 9.6 and 10. The computational difficulty of the two methods easily differs by several orders of magnitude—making the scaling laws the clear choice for "everyday" calculations in the classical regime and up to the onset of degeneracy.

2.4.3 Real World Complications

The greatest experimental challenge of implementing this technique is to perform the lowering curve in a manner that does not introduce additional trap fluctuations and associated noise (see Chapter 5). The simplest method for lowering the well-depth is to use an acousto-optic (AO) modulator. There are a number of methods for modulating the power of an AO, but they all rely on a voltage signal with the shape of the desired modulation. The challenge, then, is to create a quiet voltage signal of the form (2.48). The requirements are quite stringent. The methodology we used is discussed in Chapter 6.

The reality of working with a physical beam and physical devices as opposed to mathematical abstractions adds another complication. We are, in reality, not free to lower the well to an arbitrary level. Nonlinearities in drive electronics, thermal responses in the AO, and other effects all conspire to make it difficult to lower the well in a controlled manner by more than a factor of approximately 250. Thus, there is a limit on the phase-space increase which can be achieved by this technique. Luckily, our initial phase-space density is such that we need to lower the well by less than this factor to achieve degeneracy.

Chapter 3

Trapped Atomic Clouds: Equilibrium Distributions and Ballistic Expansion

How 'tis that, while the seeds of things are all
Moving forever, the sum yet seems to stand
Supremely still, except in cases where
A thing shows motion of its frame as whole.

—Lucretius (c. 50 BCE)

3.1 Overview

This chapter addresses two important questions about the atomic clouds produced in atomic cooling and trapping experiments: "How is their shape related to the shape of the trapping potential?" and "When released and allowed to expand ballistically, how does their shape vary with time?" In the experiment presented in this thesis, the data were collected by imaging the atomic cloud after ballistic expansion. In order to extract useful information from the images, it is imperative to have an answer to the two questions listed above.

3.2 3-D Spatial and Momentum Distributions

In general, the probability of a particle occupying a particular choice of coordinates is proportional to the product of the occupation number and the density of states [43]

$$P(\mathbf{q}) \propto f(\mathbf{q})\, g(\mathbf{q}). \tag{3.1}$$

Here, $\mathbf{q}$ represents the coordinates of interest, f is the occupation number for a state at those coordinates, and g is the density of states at $\mathbf{q}$.

For a gas of atoms at equilibrium, the generalized density of the cloud is proportional to this probability

$$n(\mathbf{q}) \propto P(\mathbf{q}) \propto f(\mathbf{q})\, g(\mathbf{q}). \tag{3.2}$$

As is typical, the proportionality constant is chosen such that the density normalizes to the total number of atoms

$$n(\mathbf{q}) = \frac{N f(\mathbf{q})\, g(\mathbf{q})}{\int d\mathbf{q}\, f(\mathbf{q})\, g(\mathbf{q})}. \tag{3.3}$$

If we work in Cartesian coordinates in $\mathbf{x}$-$\mathbf{p}$ phase-space, the density of states is a constant and cancels in (3.3), leaving the expression

$$n(\mathbf{x}, \mathbf{p}) = \frac{N f(\mathbf{x}, \mathbf{p})}{\int d\mathbf{x}\, d\mathbf{p}\, f(\mathbf{x}, \mathbf{p})}. \tag{3.4}$$

Generating expressions for the spatial and momentum distributions is then as

simple as integrating out the appropriate dimensions:

$$n(\mathbf{x}) = \frac{N}{\int d\mathbf{x}\, d\mathbf{p}\, f(\mathbf{x},\mathbf{p})} \int d\mathbf{p}\; f(\mathbf{x},\mathbf{p}) \tag{3.5}$$

$$n(\mathbf{p}) = \frac{N}{\int d\mathbf{x}\, d\mathbf{p}\, f(\mathbf{x},\mathbf{p})} \int d\mathbf{x}\; f(\mathbf{x},\mathbf{p}). \tag{3.6}$$

Proceeding further requires us to specify a form for the occupation number f.

3.2.1 The Classical Gas

In a classical gas at temperature T, the occupation number f is given by a term proportional to the standard Boltzmann factor [10]

$$f(\mathbf{x},\mathbf{p}) = \lambda\, e^{-H(\mathbf{x},\mathbf{p})/k_B T}\, \Theta[-H(\mathbf{x},\mathbf{p})]. \tag{3.7}$$

Here, $\lambda = \exp[\mu/(k_B T)]$ incorporates the chemical potential μ [10], $H(\mathbf{x},\mathbf{p})$ is the Hamiltonian for the system, and $\Theta[-H(\mathbf{x},\mathbf{p})]$ is a theta function that accounts for the effects of a finite well-depth U_0. For the remainder of this chapter, we will assume $U_0 \gg T$ so that we can neglect the theta function. The high-temperature case where the effects of this term cannot be neglected is explored in Section 4.4.2. Expanding (3.5) and (3.6), gives

$$n(\mathbf{x}) = \frac{N}{\int d\mathbf{x}\, d\mathbf{p}\, e^{-H(\mathbf{x},\mathbf{p})/k_B T}} \int d\mathbf{p}\; e^{-H(\mathbf{x},\mathbf{p})/k_B T} \tag{3.8}$$

$$n(\mathbf{p}) = \frac{N}{\int d\mathbf{x}\, d\mathbf{p}\, e^{-H(\mathbf{x},\mathbf{p})/k_B T}} \int d\mathbf{x}\; e^{-H(\mathbf{x},\mathbf{p})/k_B T} \tag{3.9}$$

Writing the Hamiltonian as

$$H(\mathbf{x},\mathbf{p}) = \frac{\mathbf{p}\cdot\mathbf{p}}{2m} + V(\mathbf{x}), \tag{3.10}$$

with m the atomic mass and $V(\mathbf{x})$ the trapping potential, we find another important simplification. Since the Hamiltonian appears in a simple exponential, we can separate $\exp(-H/k_BT)$ into the product of two exponentials, one incorporating the kinetic energy and one incorporating the potential energy. Making this substitution, we find the general expressions for a classical gas:

$$n(\mathbf{x}) = \frac{Ne^{-V(\mathbf{x})/k_BT}}{\int d\mathbf{x}\, e^{-V(\mathbf{x})/k_BT}} \tag{3.11}$$

$$n(\mathbf{p}) = \frac{Ne^{-\mathbf{p}\cdot\mathbf{p}/(2mk_BT)}}{\int d\mathbf{p}\, e^{-\mathbf{p}\cdot\mathbf{p}/(2mk_BT)}} = \frac{N}{(2m\,k_BT)^{3/2}\,\pi^{3/2}}\, e^{-\frac{p_x^2+p_y^2+p_z^2}{2mk_BT}}. \tag{3.12}$$

The momentum distribution is independent of the shape of the trapping potential (and is also independent of its depth in the low-temperature case we are considering), and simply reproduces the standard Maxwell-Boltzmann result [10]. The spatial distribution, however, *is* dependent on the trapping potential. Below we investigate two important trapping potentials.

3-Dimensional Gaussian Potential

We typically approximate the trapping potential of the FORT as a 3-Dimensional Gaussian. We then take the trapping potential as

$$V(\mathbf{x}) = -U_0 \exp\left[-\left(\frac{x^2}{a_x^2} + \frac{y^2}{a_y^2} + \frac{z^2}{a_z^2}\right)\right], \tag{3.13}$$

where U_0 is the trap depth, and a_x, a_y, and a_z are the $1/e$-widths of the trapping

potential. Inserting this expression in (3.11), we find

$$n(\mathbf{x}) = \frac{N \exp\left[\frac{U_0}{k_B T} \exp\left[-\left(\frac{x^2}{a_x^2} + \frac{y^2}{a_y^2} + \frac{z^2}{a_z^2}\right)\right]\right]}{\int d\mathbf{x} \exp\left[\frac{U_0}{k_B T} \exp\left[-\left(\frac{x^2}{a_x^2} + \frac{y^2}{a_y^2} + \frac{z^2}{a_z^2}\right)\right]\right]}. \tag{3.14}$$

Further analytical simplification is not possible, hence any further work with this expression must utilize numerical techniques. Indeed, investigating the cloud shapes in this trapping potential was one of the initial motivations for the creation of the Monte-Carlo code which is the subject of Chapter 4.

Harmonic Potential

For low enough temperatures, almost any trapping potential appears harmonic. If we Taylor-expand the 3-D Gaussian potential, we find the harmonic approximation

$$V(\mathbf{x}) = -U_0 \left[1 - \frac{x^2}{a_x^2} - \frac{y^2}{a_y^2} - \frac{z^2}{a_z^2}\right]. \tag{3.15}$$

Inserting this result in (3.11), the overall constant in the potential cancels, and we are left with the expression

$$n(\mathbf{x}) = \frac{N e^{\frac{-U_0}{k_B T}\left(\frac{x^2}{a_x^2} + \frac{y^2}{a_y^2} + \frac{z^2}{a_z^2}\right)}}{\int d\mathbf{x}\, e^{\frac{-U_0}{k_B T}\left(\frac{x^2}{a_x^2} + \frac{y^2}{a_y^2} + \frac{z^2}{a_z^2}\right)}} = \frac{N}{b_x b_y b_z\, \pi^{3/2}}\, e^{-\left(\frac{x^2}{b_x^2} + \frac{y^2}{b_y^2} + \frac{z^2}{b_z^2}\right)}, \tag{3.16}$$

where we have defined $b_x = a_x \sqrt{k_B T / U_0}$, and similarly for b_y and b_z.

We therefore conclude that a trapped classical gas in a harmonic potential forms a cloud that is a 3-D Gaussian. Further, the $1/e$-widths of the cloud are dependent on the temperature of the cloud. This observation led us to initially consider the size of a trapped cloud as a viable thermometer for a classical gas. This notion was

later rejected for reasons detailed in Section 4.5.3.

3.2.2 The Fermi-Dirac Gas

The treatment of a Fermi-Dirac gas necessarily complicates our calculations. For the temperatures accessed in this experiment, we can make the semiclassical Thomas-Fermi approximation [44]. In this case, we can still ignore the discrete nature of the oscillator states and may continue to use the continuum density of states formalism used above. Of course, for the Fermi-Dirac gas, we must use the Fermi-Dirac distribution for the occupation number [10] (again we assume $U_0 \gg T$ so that we need not include a theta function incorporating the effects of a finite well-depth)

$$f(\mathbf{x},\mathbf{p}) = \frac{1}{\lambda^{-1}e^{H(\mathbf{x},\mathbf{p})/k_BT}+1}, \tag{3.17}$$

where $\lambda = e^{\mu/k_BT}$ with μ the chemical potential.

Inserting this into (3.5) and (3.6) yields integrals of the form

$$I_1 = \int \frac{d\mathbf{p}}{\lambda^{-1}\exp\left[\frac{H(\mathbf{x},\mathbf{p})}{k_BT}\right]+1} \tag{3.18}$$

$$I_2 = \int \frac{d\mathbf{x}}{\lambda^{-1}\exp\left[\frac{H(\mathbf{x},\mathbf{p})}{k_BT}\right]+1} \tag{3.19}$$

To calculate I_1, we note that the momentum contribution to the Hamiltonian is isotropic and convert to spherical coordinates to find

$$I_1 = \int_0^\infty \frac{dp\ 4\pi p^2}{\lambda^{-1}\exp\left[\frac{H(\mathbf{x},p^2)}{k_BT}\right]+1}. \tag{3.20}$$

Equations of this form are expressible in terms of the *polylogarithm function* [45].

The polylogarithm function has its primary definition in terms of a series

$$\mathrm{Li}_\nu[z] = \sum_{l=1}^{\infty} \frac{z^l}{l^\nu}, \quad |z| < 1. \tag{3.21}$$

However, for our immediate purposes, we require the integral representation

$$\mathrm{Li}_\nu[z] = \frac{z}{\Gamma(\nu)} \int_0^\infty \frac{dt\ t^{\nu-1}}{e^t - z}, \quad \mathrm{Re}(\nu) > 0. \tag{3.22}$$

From this, we find that I_1 can be expressed as

$$I_1 = -(2\pi m k_B T)^{3/2}\, \mathrm{Li}_{3/2}\left[-\lambda\, e^{\frac{-V(\mathbf{x})}{k_B T}}\right]. \tag{3.23}$$

In the above, we have taken $H(\mathbf{x}, p^2) = p^2/2m + V(\mathbf{x})$. Further progress, as well as any progress on I_2 requires us to choose a form of the confining potential. Given the temperature ranges for which use of Fermi-Dirac statistics is necessary, it is reasonable to treat the potential in the harmonic limit.

Harmonic Potential

Now that we have specialized to the harmonic potential, we can write the final form of I_1. Inserting our expression for the harmonic potential (3.15) into our prior result (3.23), yields

$$I_1 = -(2\pi m k_B T)^{3/2}\, \mathrm{Li}_{3/2}\left[-\lambda \exp\left[\frac{U_0}{k_B T}\left(1 - \frac{x^2}{a_x^2} - \frac{y^2}{a_y^2} - \frac{z^2}{a_z^2}\right)\right]\right]. \tag{3.24}$$

However, before we can apply a similar technique to I_2, we must first deal with

the anisotropy of $V(\mathbf{x})$. If we make the transformations

$$x' = \frac{x}{a_x}, \quad y' = \frac{y}{a_y}, \quad z' = \frac{z}{a_z}, \tag{3.25}$$

we can scale out the anisotropy. In this case, I_2 is

$$I_2 = a_x a_y a_z \int \frac{d\mathbf{x'}}{\lambda^{-1} \exp\left[\frac{H(\mathbf{x'},\mathbf{p})}{k_B T}\right] + 1}. \tag{3.26}$$

In this scaled coordinate system, we can write the potential as

$$V(\mathbf{x'}) = V(r') = -U_0(1 - r'^2). \tag{3.27}$$

A similar approach to that used on I_1 then gives us the expression for I_2

$$I_2 = -a_x a_y a_z \left(\frac{\pi k_B T}{U_0}\right)^{3/2} \mathrm{Li}_{3/2}\left[-\lambda \exp\left[\frac{1}{k_B T}\left(U_0 - \frac{p_x^2 + p_y^2 + p_z^2}{2m}\right)\right]\right]. \tag{3.28}$$

Inserting the results for I_1 and I_2 into (3.5) and (3.6) and converting the remaining integrals to spherical coordinates yields

$$n(\mathbf{x}) = \frac{N \,\mathrm{Li}_{3/2}\left[-\lambda \exp\left[\frac{U_0}{k_B T}\left(1 - \frac{x^2}{a_x^2} - \frac{y^2}{a_y^2} - \frac{z^2}{a_z^2}\right)\right]\right]}{a_x a_y a_z \, 4\pi \int_0^\infty dr' \, r'^2 \, \mathrm{Li}_{3/2}\left[-\lambda \exp\left[\frac{U_0}{k_B T}\left(1 - r'^2\right)\right]\right]} \tag{3.29}$$

$$n(\mathbf{p}) = \frac{N \,\mathrm{Li}_{3/2}\left[-\lambda \exp\left[\frac{1}{k_B T}\left(U_0 - \frac{p_x^2 + p_y^2 + p_z^2}{2m}\right)\right]\right]}{4\pi \int_0^\infty dp \, p^2 \, \mathrm{Li}_{3/2}\left[-\lambda \exp\left[\frac{1}{k_B T}\left(U_0 - \frac{p^2}{2m}\right)\right]\right]}. \tag{3.30}$$

The remaining integrals can be evaluated by expressing the polylogarithms as infinite sums using (3.21), and switching the order of the sum and integral. Since we will be using this trick repeatedly, an example is in order. Taking the denominator

of (3.30) as I_3, we find:

$$\begin{aligned}
I_3 &= 4\pi \int_0^\infty dp\, p^2 \, \mathrm{Li}_{3/2}\left[-\lambda \exp\left[\frac{1}{k_B T}\left(U_0 - \frac{p^2}{2m}\right)\right]\right] \\
&= 4\pi \int_0^\infty dp\, p^2 \sum_{j=1}^{\infty} \frac{\left(-\lambda \exp\left[\frac{1}{k_B T}\left(U_0 - \frac{p^2}{2m}\right)\right]\right)^j}{j^{3/2}} \\
&= 4\pi \sum_{j=1}^{\infty} \frac{\left(-\lambda \exp\left[\frac{1}{k_B T}\left(U_0\right)\right]\right)^j}{j^{3/2}} \int_0^\infty dp\, p^2 \, \exp\left[\frac{-jp^2}{2mk_B T}\right] \\
&= (2\pi m k_B T)^{3/2} \sum_{j=1}^{\infty} \frac{\left(-\lambda \exp\left[\frac{1}{k_B T}\left(U_0\right)\right]\right)^j}{j^3} \\
&= (2\pi m k_B T)^{3/2} \, \mathrm{Li}_3\left[-\lambda \exp\left[\frac{U_0}{k_B T}\right]\right]. \qquad (3.31)
\end{aligned}$$

We can then rewrite the distributions in (3.29) and (3.30) in their final form

$$n(\mathbf{x}) = \frac{N}{b_x b_y b_z \pi^{3/2}} \frac{\mathrm{Li}_{3/2}\left[-\lambda\, e^{\frac{U_0}{k_B T}}\; e^{-\left(\frac{x^2}{b_x^2}+\frac{y^2}{b_y^2}+\frac{z^2}{b_z^2}\right)}\right]}{\mathrm{Li}_3\left[-\lambda\, e^{\frac{U_0}{k_B T}}\right]} \qquad (3.32)$$

$$n(\mathbf{p}) = \frac{N}{(2mk_B T)^{3/2}\,\pi^{3/2}} \frac{\mathrm{Li}_{3/2}\left[-\lambda\, e^{\frac{U_0}{k_B T}}\; e^{-\frac{p_x^2+p_y^2+p_z^2}{2mk_B T}}\right]}{\mathrm{Li}_3\left[-\lambda\, e^{\frac{U_0}{k_B T}}\right]}. \qquad (3.33)$$

Here $b_x = a_x\sqrt{k_B T/U_0}$ as before, and similarly for b_y and b_z.

The astute reader will have realized that this derivation has overdetermined the normalization. Typically, in Fermi systems, the value of the chemical potential μ is chosen such that

$$\int d\mathbf{x}\, d\mathbf{p} f(\mathbf{x},\mathbf{p}) \equiv N. \qquad (3.34)$$

The derivation above does not preclude such a choice. However, the forms in (3.32)

and (3.33) remain normalized for any value of μ. The benefit of the above approach is that it produces a high degree of symmetry between the Fermi-Dirac results and the classical results of (3.12) and (3.16).

3.3 2-D and 1-D Spatial and Momentum Distributions

In our experiment, we will be extracting information in the form of absorption images of the atomic cloud. Such a technique necessarily integrates out information in the direction of the probe laser. The resulting 2-D distribution is known as the *column density* [46]. Further, in analyzing the data, we will often find it useful to integrate the measured distributions in one direction to produce 1-D profiles which can be least-squares-fit to theory. This section derives the 2-D and 1-D distributions from the 3-D results of the preceding section. The trapping potential is always taken to be harmonic

3.3.1 2-D Distributions

We take the y-axis as the direction of propagation of the probe laser. Thus we need to integrate our prior results in this direction.

The Classical Gas

Integrating the classical results of (3.12) and (3.16) is straightforward. We find:

$$\tilde{n}(x,z) = \frac{N}{b_x b_z\,\pi}\; e^{-\left(\frac{x^2}{b_x^2}+\frac{z^2}{b_z^2}\right)} \tag{3.35}$$

$$\tilde{n}(p_x,p_z) = \frac{N}{(2m\,k_BT)\,\pi}\; e^{-\frac{p_x^2+p_z^2}{2mk_BT}} \tag{3.36}$$

The Fermi-Dirac Gas

In this case, we must integrate the results in (3.32) and (3.33). To do the integrals, we make use of the trick of writing the polylogarithms as sums (see (3.31)). We find:

$$\tilde{n}(x,z) = \frac{N}{b_x b_z \pi}\; \frac{\mathrm{Li}_2\left[-\lambda\, e^{\frac{U_0}{k_BT}}\; e^{-\left(\frac{x^2}{b_x^2}+\frac{z^2}{b_z^2}\right)}\right]}{\mathrm{Li}_3\left[-\lambda\, e^{\frac{U_0}{k_BT}}\right]} \tag{3.37}$$

$$\tilde{n}(p_x,p_z) = \frac{N}{(2mk_BT)\,\pi}\; \frac{\mathrm{Li}_2\left[-\lambda\, e^{\frac{U_0}{k_BT}}\; e^{-\frac{p_x^2+p_z^2}{2mk_BT}}\right]}{\mathrm{Li}_3\left[-\lambda\, e^{\frac{U_0}{k_BT}}\right]}. \tag{3.38}$$

3.3.2 1-D Distributions

The 1-D distributions are derived by integrating along the z-axis, using the same techniques as before. The symbol $\check{n}$ has been used to represent the 1-D distributions.

The Classical Gas

The distributions are:

$$\check{n}(x) = \frac{N}{b_x\sqrt{\pi}}\, e^{-\frac{x^2}{b_x^2}} \tag{3.39}$$

$$\check{n}(p_x) = \frac{N}{\sqrt{2m\,k_BT}\,\sqrt{\pi}}\, e^{-\frac{p_x^2}{2mk_BT}} \tag{3.40}$$

The Fermi-Dirac Gas

The distributions are:

$$\check{n}(x) = \frac{N}{b_x\sqrt{\pi}}\, \frac{\mathrm{Li}_{5/2}\left[-\lambda\, e^{\frac{U_0}{k_BT}}\; e^{-\frac{x^2}{b_x^2}}\right]}{\mathrm{Li}_3\left[-\lambda\, e^{\frac{U_0}{k_BT}}\right]} \tag{3.41}$$

$$\check{n}(p_x) = \frac{N}{\sqrt{2mk_BT}\sqrt{\pi}}\, \frac{\mathrm{Li}_{5/2}\left[-\lambda\, e^{\frac{U_0}{k_BT}}\; e^{-\frac{p_x^2}{2mk_BT}}\right]}{\mathrm{Li}_3\left[-\lambda\, e^{\frac{U_0}{k_BT}}\right]}. \tag{3.42}$$

In Figure 3.1, the classical gas distribution of (3.39) is compared to the Fermi-Dirac gas distribution in a variety of temperature ranges.

3.4 Ballistic Expansion

It is an easy task to determine how these distributions are affected by ballistic expansion of duration, τ. Gravity has a negligible effect for the expansion times used in our experiments (although the following treatment can easily be extended if necessary). Hence, during ballistic expansion, the atoms undergo non-accelerated

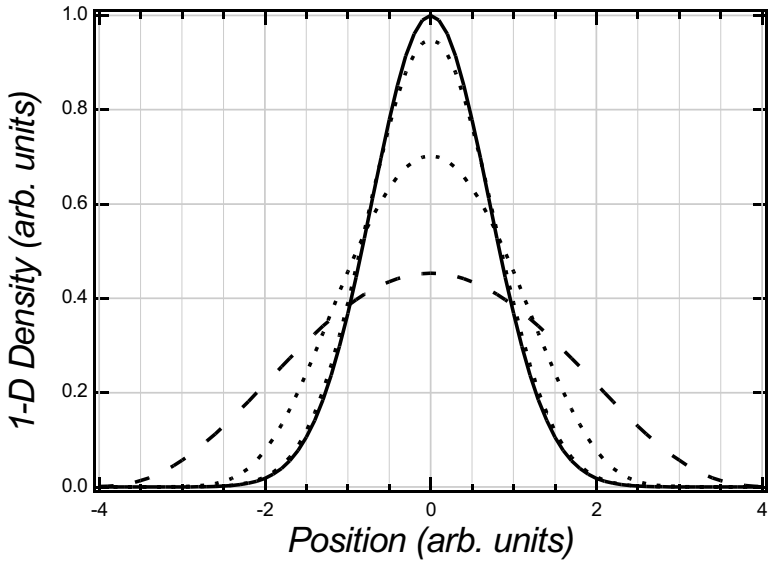

Figure 3.1: Comparison of classical and quantum 1-D density distributions. The 1-D spatial distributions, $\check{n}(x)$, are plotted for the classical gas (solid line) and the Fermi-Dirac gas. In the high-temperature limit, the Fermi-Dirac gas is indistinguishable from the classical gas. As the temperature decreases (dotted lines) the distributions flatten and spread as the Fermi pressure begins to manifest itself. In the zero-temperature limit (dashed line) the Fermi-Dirac gas exhibits a shape which is dramatically different from the classical gas.

motion, and their coordinates evolve according to

$$x = x_0 + v_x\tau, \tag{3.43}$$

where v_x is the x-velocity of the atom (and similarly in y and z).

We then reorder this equation to give an expression for x_0

$$x_0 = x - \frac{p_x}{m}\tau. \tag{3.44}$$

Here, we have also chosen to work in terms of p_x, the x-momentum, for a reason which will become clear.

3.4.1 The Classical Gas

For the classical gas we know that, at the time of release, the atomic spatial distribution is given by (3.16). We replace the variables x, y, and z in this distribution with our expressions for x_0, y_0, and z_0 to convert this distribution into the spatial distribution at time τ for atoms with momenta p_x, p_y, and p_z. To generalize from a specific momentum, we must integrate out the momentum variables. All momenta are not equally represented in our initial distribution, however. To properly account for this fact, we must include a weighting function that is given by our previously-derived momentum distribution in (3.12) (but with its normalization set to 1 instead of N),

$$n(\mathbf{x},\tau) = \frac{N}{b_x b_y b_z (2mk_BT)^{3/2}\pi^{3/2}} \int d\mathbf{p}\, e^{-\frac{\mathbf{p}\cdot\mathbf{p}}{2mk_BT}}\, e^{-\left(\frac{(x-\frac{p_x}{m}\tau)^2}{b_x^2}+\frac{(y-\frac{p_y}{m}\tau)^2}{b_y^2}+\frac{(z-\frac{p_z}{m}\tau)^2}{b_z^2}\right)}. \tag{3.45}$$

We can complete the square to generate Gaussians in the momenta. After

completing the integral, we find that we can write the answer as

$$n(\mathbf{x},\tau) = \frac{N}{c_x c_y c_z \, (2mk_BT)^{3/2} \, \pi^{3/2}} \, e^{-\left(\frac{x^2}{c_x^2}+\frac{y^2}{c_y^2}+\frac{z^2}{c_z^2}\right)}, \tag{3.46}$$

where we have made the definition

$$c_x = b_x\sqrt{1+\frac{2k_BT}{mb_x^2}\tau^2} = b_x\sqrt{1+\omega_x^2\tau^2}, \tag{3.47}$$

and similarly for y and z. Here ω_x is the initial trap frequency in the x-direction in circular units. Note that the form of (3.46) is identical to the distribution in (3.16), except for the scalings of the form

$$b_x \to b_x\sqrt{1+\omega_x^2\tau^2} = c_x. \tag{3.48}$$

This is known as *ballistic scaling*. It is a general scale transformation which holds for any freely expanding system with an initial Maxwell-Boltzmann momentum distribution. Applying it to the lower-dimensional results of (3.35) and (3.39), we find

$$\tilde{n}(x,z,\tau) = \frac{N}{c_x c_z \, \pi} \, e^{-\left(\frac{x^2}{c_x^2}+\frac{z^2}{c_z^2}\right)} \tag{3.49}$$

$$\check{n}(x,\tau) = \frac{N}{c_x \sqrt{\pi}} \, e^{-\frac{x^2}{c_x^2}}. \tag{3.50}$$

3.4.2 The Fermi-Dirac Gas

Although we discovered the scale transformation in (3.48) based on classical arguments, it has recently been shown to hold for quantum systems as well [47]. Thus, the strong symmetry between the classical and Fermi-Dirac results continues

to hold. Applying the scale transformation to the previously derived Fermi-Dirac results in the expressions

$$n(\mathbf{x},\tau) = \frac{N}{c_x c_y c_z \pi^{3/2}} \frac{\mathrm{Li}_{3/2}\left[-\lambda\, e^{\frac{U_0}{k_B T}}\; e^{-\left(\frac{x^2}{c_x^2}+\frac{y^2}{c_y^2}+\frac{z^2}{c_z^2}\right)}\right]}{\mathrm{Li}_3\left[-\lambda\, e^{\frac{U_0}{k_B T}}\right]}, \tag{3.51}$$

$$\tilde{n}(x,z,\tau) = \frac{N}{c_x c_z \pi} \frac{\mathrm{Li}_2\left[-\lambda\, e^{\frac{U_0}{k_B T}}\; e^{-\left(\frac{x^2}{c_x^2}+\frac{z^2}{c_z^2}\right)}\right]}{\mathrm{Li}_3\left[-\lambda\, e^{\frac{U_0}{k_B T}}\right]}, \tag{3.52}$$

$$\check{n}(x,\tau) = \frac{N}{c_x \sqrt{\pi}} \frac{\mathrm{Li}_{5/2}\left[-\lambda\, e^{\frac{U_0}{k_B T}}\; e^{-\frac{x^2}{c_x^2}}\right]}{\mathrm{Li}_3\left[-\lambda\, e^{\frac{U_0}{k_B T}}\right]}. \tag{3.53}$$

Chapter 4

The Monte-Carlo Model

> *If God has made the world a perfect mechanism, He has at least conceded so much to our imperfect intellects that in order to predict little parts of it, we need not solve innumerable differential equations, but can use dice with fair success.*
>
> —Max Born

4.1 Overview

In Chapter 3, we derived the *static* spatial distributions of a classical atomic gas in harmonic and gaussian confining potentials. The gaussian result, however, was expressible only as an integral. In addition, predicting the *dynamics* of the gas in a static or time-varying potential is well beyond the analytical machinery used in the prior chapter.

To attempt to address these issues, even if only for the classical gas, we developed a *Monte-Carlo* computer model (sometimes referred to as a *molecular dynamics* model in other fields). In this model a number of "atoms" are placed probabilistically in a mathematical representation of the confining potential. The number of simulated atoms is often less than the number of physical atoms we are attempting to simulate, but is large enough that the statistical nature of the ensemble becomes evident. Once the atoms are placed in the well, the simulation proceeds forward in

small time-steps, updating the state of all the simulated atoms at each step.

Since we have complete knowledge of the state of the atoms at all times, we can easily extract any data we wish: spatial distributions, velocity distributions, temperatures, trap population, etc.

4.2 Bird's Method

The algorithm used to evolve the state of the system in time is known as *Bird's Method* [25]. The algorithm involves the following steps:

1. Generate an appropriate initial condition
2. Update the position of the particle, according to its velocity
3. Update the velocity of the particle, according to the forces acting on it *at its previous position*
4. Treat interparticle collisions
5. Repeat steps 2-4 for the duration of the simulation

The astute reader will note that steps two and three are merely a numerical integration of the equations of motion. We can decouple the effect of collisions from the equations of motion by recognizing that, for a dilute gas, the mean-free-path is quite large compared to the distance a particle propagates in a time-step. This means that collisions are exceedingly rare on the time scales we are dealing with and can be treated as occurring "between" time-steps without materially affecting the result.

Collisions are handled by randomly selecting pairs of particles to collide. The probabilities are weighted such that the number of collisions at any time-step is

appropriate for the collision cross-section involved. If a particle is selected for collision, its collision partner is selected from nearby atoms. The collision is simulated by giving one atoms a random velocity (direction and speed), while the velocity of the other atom is updated to conserve energy and momentum of the pair. Inelastic collisions are not treated.

This algorithm is essentially a numerical integration of Newton's laws. This means that, for suitably small time-steps, the output of the algorithm converges to the correct physical behavior.

4.3 Implementation

This algorithm has been implemented in the *C* programming language. Details of the program change slightly depending on the specific experiment which is being simulated. A representative version is included in Section C.4.

As implemented, the code *does not include collisions*. This was done for a practical reason—inclusion of collisions dramatically increases the length of the computation for a given number of simulated atoms. We are free to make this simplification since the mixture of atoms we work with are collisionless at zero magnetic field (in this thesis the atoms undergo collisions *only* during evaporative cooling—all other portions of the experiments are performed at zero field where collisions are not possible). Further, even if we were to work in a system that is not collisionless (for example the $|1\rangle - |3\rangle$ mixture of an earlier thesis by this group [21]), often the effects we are interested in are *single-particle* effects and the lack of thermalization and damping in our simulation does not affect the result.

The most difficult portion of the implementation lies in properly generating the initial conditions. For each atom, the program tracks the three spatial and three

velocity components.

The confining potential is technically gaussian in two dimensions and lorentzian in the third, but we approximate this as a three-dimensional gaussian well,

$$U = -U_0 \, e^{-((\frac{x}{a_x})^2+(\frac{y}{a_y})^2+(\frac{z}{a_z})^2)}. \tag{4.1}$$

In the above, U_0 is the well-depth and the a_i are the $1/e$-radii of the potential in the ith-direction. The well *is* isotropic if viewed in a scaled coordinate system where the distance along each axis is measured in units of the a_i. In this system, the well is given by

$$U = -U_0 \, e^{-r'^2}. \tag{4.2}$$

Since the confining potential is isotropic in this coordinate system, the spatial distribution of the atoms is as well. The kinetic energy of the particles is isotropic in the original, unscaled coordinate system, implying isotropy of velocity in that coordinate system. We can then assume Maxwell-Boltzmann statistics to write the probability distributions for the velocity in the original coordinates and the radial position in the scaled coordinates,

$$p(v) \propto v^2 \exp\left[-\frac{mv^2}{2kT}\right], \tag{4.3}$$

$$p(r) \propto r^2 \exp\left[\frac{U_0 \, e^{-r^2}}{kT}\right]. \tag{4.4}$$

Note that the above expressions are similar in form. Both contain a Jacobian factor that is the square of the "radial" variable and an exponential function of that variable which is of the form of a Boltzmann factor of the appropriate (kinetic or

potential) energy.

When generating the initial conditions, a radius and a velocity are randomly chosen according to the probability distributions in (4.3) and (4.4). The details of how to generate random variables according to arbitrary distributions is discussed in Appendix B. The corresponding potential and kinetic energies are then calculated, and their sum is computed. If the sum is greater than or equal to zero, the atom is unbound and we reject the values of v and r, and begin again. If the total is less than zero, the atom is bound and we convert the radial coordinates into Cartesian by randomly choosing values of θ and ϕ and using the standard spherical to Cartesian conversion. The spatial coordinates are then scaled by the a_i values to convert into physical space and the coordinates and velocity components are recorded for the atom. We then repeat the process as necessary to generate the desired number of atoms.

4.4 Validation

Before we can begin to trust the predictions of the program, it must be validated. To validate the program, we test the major algorithms on known cases to see if the output reproduces the expected results. There were three tests run on the program. In the first, the output of the random number generators was tested to see if the output obeyed the expected distribution functions. In the second, the resulting atomic distribution was tested to see if it had the expected energy distribution. In the final test, the motion of a single atom was tracked to see if it followed the expected equations of motion.

4.4.1 Random Number Generation

In Appendix B, I discuss how to generate random numbers according to arbitrary probability distributions. The first test of the program is to see whether these routines do, in fact, produce random numbers that are distributed in the expected manner.

For this test, the 100,000 random radii and speeds were generated for a number of test cases. In all cases the depth of the potential well was $700\,\mu$K. The three different cases involved temperatures of $700\,\mu$K, $150\,\mu$K, and $35\,\mu$K, respectively. In each case, the values were converted into a 500-bin histogram, the shape of which should be proportional to probability distribution of the random numbers. This shape was then fit to the functions (4.3) and (4.4). The only free parameters in the fit were the overall constant of proportionality and the temperature of the distribution. The results are shown in Figure 4.1. The extracted temperature was, in every case, within approximately 1% of the expected temperature. From this, we conclude that the random-number-generation algorithms are performing as expected.

4.4.2 Atomic Ensemble Generation

Of course, the generation of random numbers according to the probability distributions given in (4.3) and (4.4) are not the whole of the algorithm for generating a simulated atom. Once a velocity/radius pair is generated, the total energy for the pair (kinetic plus potential) is calculated. Only if the total energy is negative, and hence the atom bound in the well, do we keep the pair. For this portion of the validation, 100,000 simulated atoms were generated for the same three cases ($700\,\mu$K, $150\,\mu$K, and $35\,\mu$K atoms in a $700\,\mu$K-deep well) and their radii and speeds were

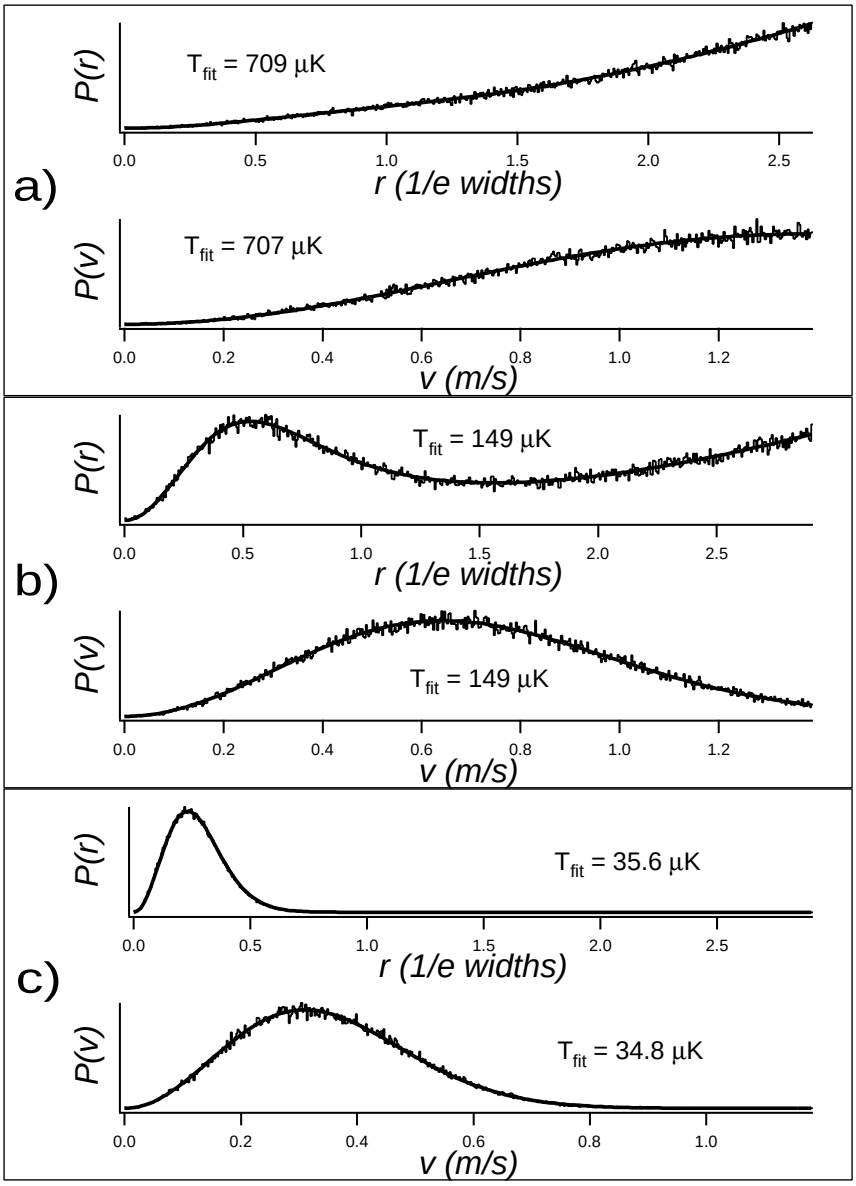

Figure 4.1: Validation of the random number generation algorithms. Each case shows the actual distribution of the radii and speeds (jagged histogram) and an analytical fit with the temperature and an overall scaling as the only free parameters (smooth curve). Each graph gives the temperature extracted by the fit. In all cases the agreement is excellent. The random numbers were generated at temperatures of a) 700 μK, b) 150 μK, and c) 35 μK.

converted into 500-bin histograms as in the previous section.

Figure 4.2 shows that the speed- and radii-distributions do not, in general, follow the probability distributions we used to generate the random numbers. In the figure, the smooth curves are the fits from Figure 4.1, normalized to have the same area as the histograms in Figure 4.2. Clearly, only the lowest-temperature case does not modify the probability distributions. The physical rationale for this is actually quite easy to understand. The probability distributions (4.3) and (4.4), especially for high temperatures, can produce atoms with too much energy to be bound in the well. Since we are only dealing with bound atoms, the rejection of unbound pairs modifies the probability distributions for high temperatures. Only in the case of extremely high well-depth-to-temperature ratios is the probability of an unbound pair negligible. In this case the resulting probability distribution is unmodified. The reader should note that this effect is essentially another example of the *acceptance-rejection* method [48] of modifying probability distributions (see Section B.3).

If the distributions are modified, how will we know if we are producing the proper distribution? The probability of an atom having energy E can be written in terms of the density of states, $\mathcal{D}(E)$, and the occupation number $f(E)$ as

$$p(E)) \propto \mathcal{D}(E)\ f(E) = \mathcal{D}(E)\ e^{-E/k_B T}, \tag{4.5}$$

where k_B is the Boltzmann constant. Here the occupation number has been replaced by a Boltzmann factor, as is appropriate for a classical gas.

Previously, our group derived the density of states for a gaussian well of depth U_0 [21],

$$\mathcal{D}_{\text{Gauss}}(E) = g(E)\,\mathcal{D}_{\text{HO}}(E). \tag{4.6}$$

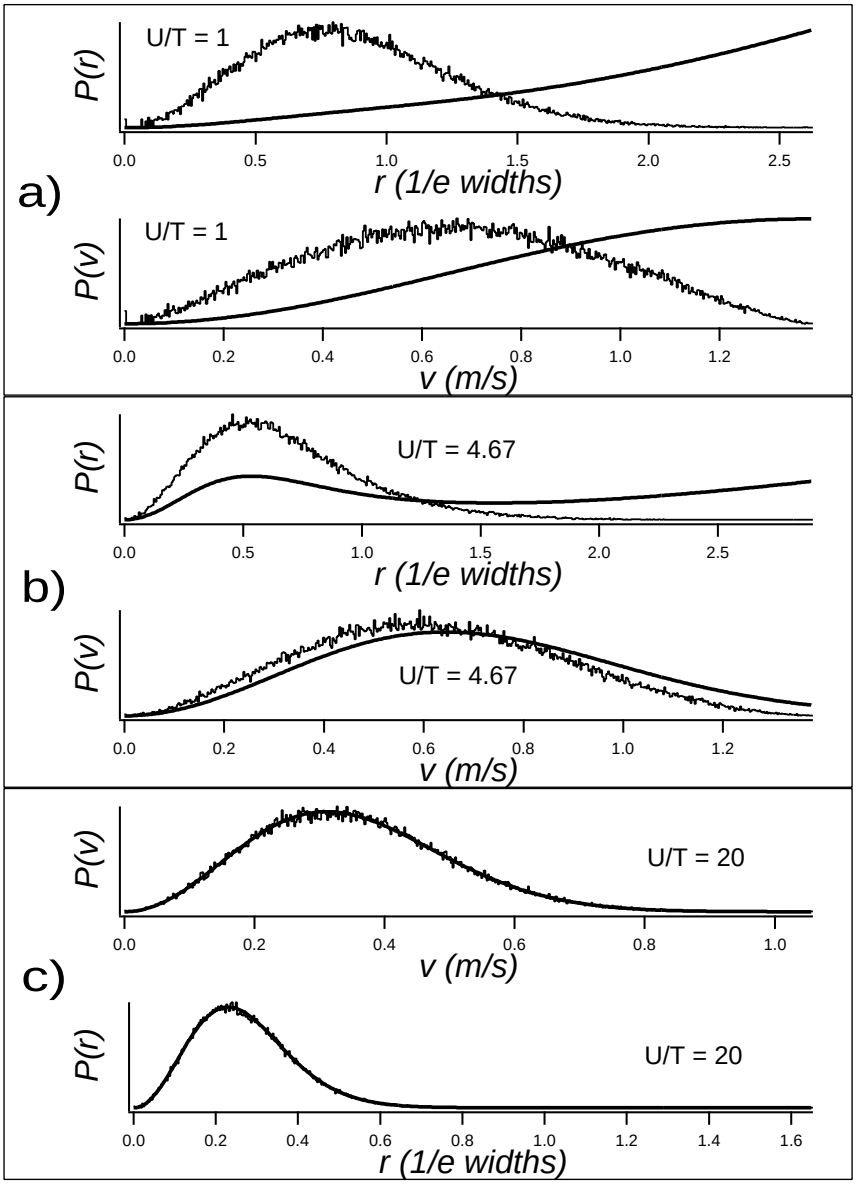

Figure 4.2: Radius and speed distributions of bound atoms. Each case shows the actual distribution of the radii and speeds (jagged histogram) and the analytical fits of Figure 4.1 (smooth curve). The discrepancy in the high-temperature cases is easily understood. In those cases the random number generators produce many radius/speed pairs that are unbound. Ignoring these pairs effectively modifies the distributions. Only in the high well-depth-to-temperature case are unbound atoms unlikely, and hence the distributions agree. The random numbers were generated at temperatures of a) 700 μK, b) 150 μK, and c) 35 μK.

Here, $\mathcal{D}_{\mathrm{HO}}(E)$ is the well known harmonic-oscillator density of states:

$$\mathcal{D}_{\mathrm{HO}}(E) = \frac{E^2}{2\hbar^3\omega_x\omega_y\omega_z}, \tag{4.7}$$

with ω_i the oscillator frequency in the i-direction.

We found $g(E)$ to be given by

$$g(E) = \frac{16}{\pi}\,\frac{\alpha^{3/2}\sqrt{1-\beta}}{\beta^2}\int_0^1 dw w^2\sqrt{e^{\alpha(1-w^2)}-1}, \tag{4.8}$$

with $\beta \equiv E/U_0$ and $\alpha \equiv -\ln(1-\beta)$ defined for simplicity.

This means that the probability of total energy E for an atom bound in a gaussian well can be written as

$$p(E) \propto E^2 e^{-E/k_BT}\frac{\alpha^{3/2}\sqrt{1-\beta}}{\beta^2}\int_0^1 dw w^2\sqrt{e^{\alpha(1-w^2)}-1}. \tag{4.9}$$

The multiplicative constants have been dropped as we will always be normalizing the distribution to match an unnormalized histogram.

We can take the 100,000 randomly generated bound atoms and compute the total (kinetic plus potential) energy for each. Once again, 500-bin histograms are generated for the three cases (700 μK, 150 μK, and 35 μK). In Figure 4.3, these histograms are plotted, along with the corresponding theoretical predictions based on (4.9). The theoretical predictions had no free parameters other than an overall scaling to match the normalization of the histograms. The correspondence between the histogram and the theoretical expectation is excellent in all cases. Thus we may conclude that the Monte-Carlo program produces accurate bound atomic ensembles.

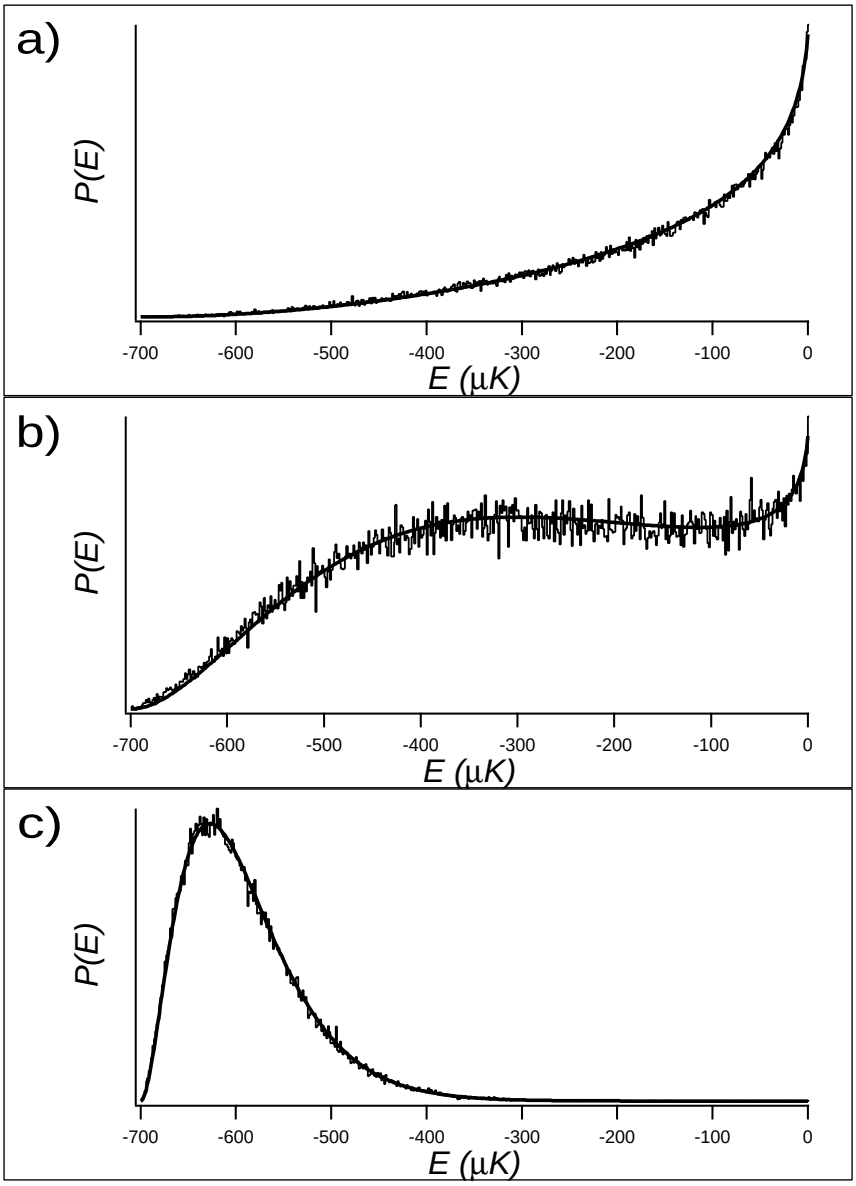

Figure 4.3: Validation of the simulated atomic ensembles. Each case shows the actual distribution of total energy for the bound atoms (jagged histogram) and the expected analytical distribution (smooth curve) from (4.9). The only free parameter in the analytic distribution is the overall normalization. Agreement is excellent in all three cases. The atoms were generated at a temperature of a) 700 μK, b) 150 μK, and c) 35 μK.

4.4.3 Atomic Motion in the Well

We now see that the Monte-Carlo program generates realistic atomic ensembles. The only remaining validation task is to show that the motion of the atoms in the well obeys the proper equations of motion.

For this test, a potential well is designed that has oscillation frequencies of 100, 1000, and 2000 Hz in the three directions for particles with $E \ll U_0$. A low-energy particle of mass, m, in a gaussian well of depth, U_0 has an oscillation frequency in the i-direction of

$$\nu_i = \sqrt{\frac{U_0}{2\pi^2 m a_i^2}}, \tag{4.10}$$

where a_i is the 1/e-dimension of the trapping potential in the i-direction. This arises from representing the potential by the harmonic term in the Taylor expansion of the potential. Correspondingly, to have a trap frequency of ν_i in the i-direction, the trap must have a 1/e dimension in the i-direction of

$$a_i = \sqrt{\frac{U_0}{2\pi^2 m \nu_i^2}}. \tag{4.11}$$

Thus, to generate the desired trap frequencies in a trap of depth 700 μK, we specify 1/e dimensions according to (4.11).

A low-energy atom is placed in the well (thereby avoiding the anharmonicity inherent at higher energies) and its position and velocity are tracked throughout the evolution of its motion. In Figure 4.4, a portion of the position evolution is shown for all three cartesian directions. The amplitude of the oscillation does not decay over many (>1000) oscillations. The full position evolution in each direction is then analyzed with a discrete Fourier transform (DFT) to extract the oscillation frequencies. The second part of Figure 4.4 shows the power spectrum (given by the

square of the DFTs) for each direction. In each direction there is a sharp spike located at precisely the expected oscillation frequency. There are no features anywhere else in the spectra. Thus, we have shown that the motion of the atoms in the well precisely reproduces the expected physical motion.

4.5 Applications

Having satisfied ourselves in the validity of the Monte-Carlo model (at least in the collisionless regime), we utilized it in a number of situations over the past several years. This section discusses these uses of the code and provides representative results.

4.5.1 Parametric Resonance

How can we know the parameters of the CO_2 trap? The focus occurs inside the vacuum chamber where we can not access it. Even if we could, the power density is so high ($> 2\,\mathrm{MW/cm^2}$), that working at the focus would be difficult and dangerous. We *do* know the power of the beam and the static polarizability of ^{6}Li. If we could measure the three trap frequencies, we could determine the trap depth and the three 1/e dimensions of the gaussian well (subject, of course, to the caveat that the CO_2 trap must closely approximate a Gaussian well).

Luckily, this is possible without access to the beam focus through the use of the phenomenon of *parametric resonance* [49]. Parametric resonance is a process where the modulation of the spring constant of an oscillator at twice its natural frequency produces a resonant response. While details of this mechanism are discussed in greater detail in Chapter 5, the underlying physics is readily understood.

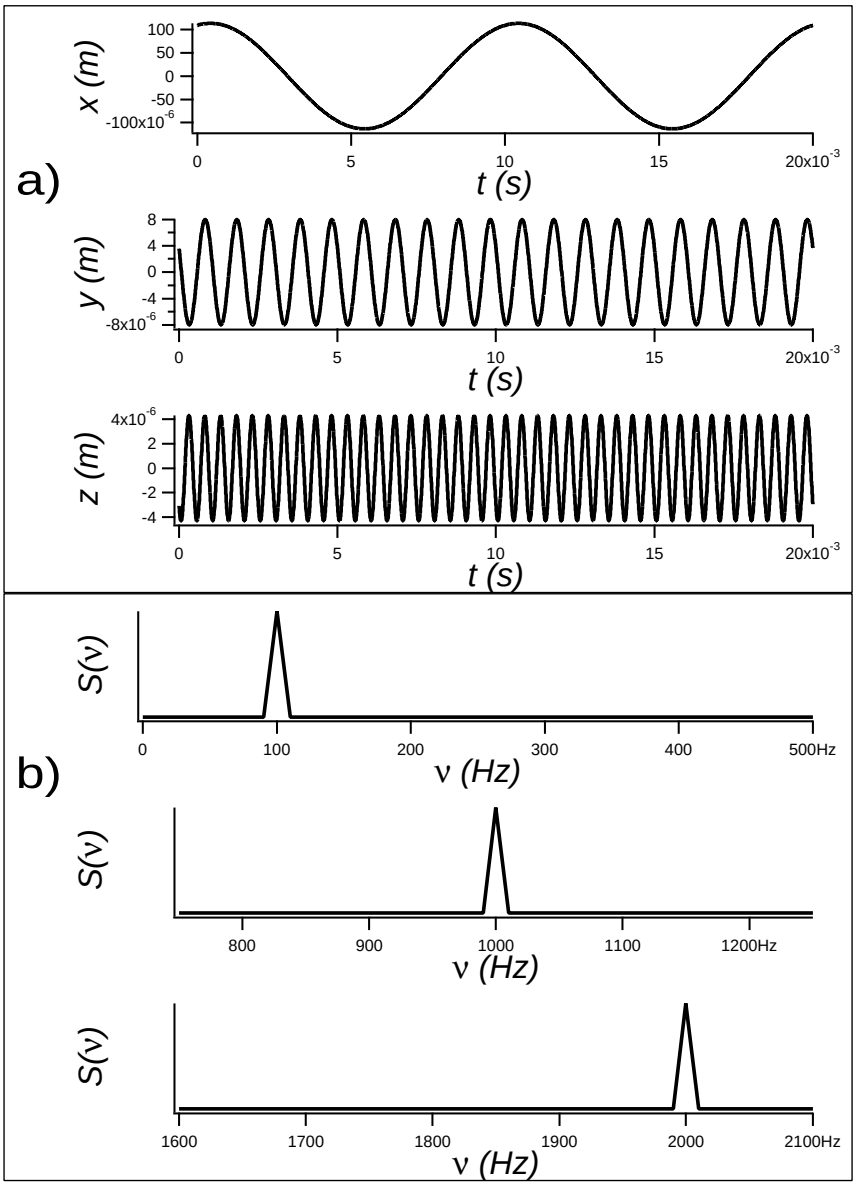

Figure 4.4: Validation of the atomic motion. A low energy atom was placed in a trap with oscillation frequencies of 100, 1000, and 2000 Hz. In a) a portion of the position evolution of the atom in each direction is shown. The amplitude of the oscillation did not decrease during the period of observation. In b) the power spectrum in arbitrary units (given by the square of the DFT) of the atomic motion in each direction is shown. Each spectra has a sharp peak at the expected oscillation frequency as its sole feature.

By modulating at twice the natural frequency, the conversion from velocity (kinetic energy) to displacement (potential energy) occurs at a low spring-constant, while the opposite conversion occurs at a high spring constant. The result is a cycle of ever increasing peak velocities and displacements.

At the time we built our first CO_2 laser trap, the process of using parametric resonance to measure trap parameters was an established technique [50]. However, we had no experience using this technique, and we were faced with a number of uncertainties. How much modulation was required? How broad would the resonance be? Would we be able to accurately determine the trap frequencies from the location of the peaks? Would the anharmonic nature of the gaussian well cause unexpected complications? The situation was further complicated by the fact that, at that time, our experiment did not have a charge-coupled-device (CCD) camera that could directly image the atomic distributions in the trap (or after release in time-of-flight imaging). All our atom measurements were made using fluorescence resonance signals as detected by a photomultiplier tube (PMT). We decided to simulate the proposed experiments with the Monte-Carlo code to hopefully gain some answers to our many questions.

Because we were working with PMT signals, the experimental protocol was planned as follows:

1. Modulate the trap depth at a factor ϵ at a frequency Ω for a duration Δt.

2. Suddenly lower the trap to a fraction f of its full depth. This releases atoms that had total energies above fU_0.

3. Measure the remaining trap population by applying a resonant probe pulse and recording the fluorescence signal detected by the PMT. This signal should

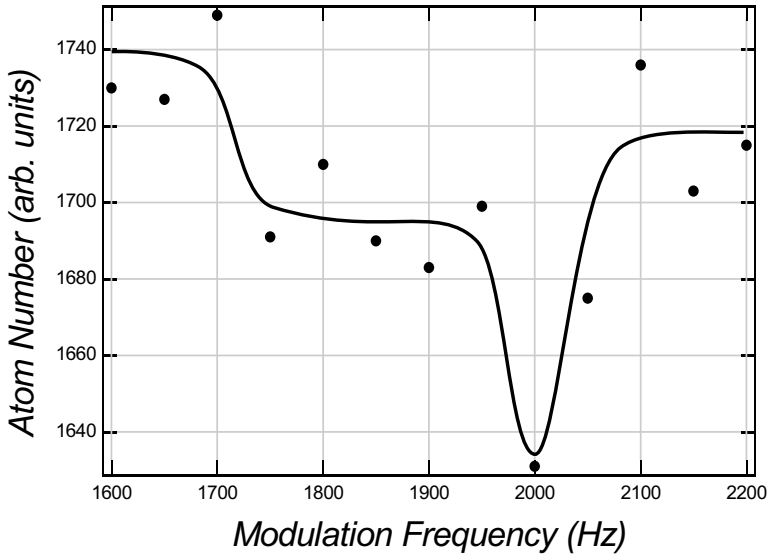

Figure 4.5: Simulated results of a parametric resonance experiment. The circles are the output of the Monte-Carlo code. The solid line has been included to guide the eye. The general shape of the peak appears to be a systemic feature of parametric resonance in a gaussian well.

be lowest when the atoms have been resonantly excited upwards in the trap.

4. Repeat for a range of Ω values. The resonance should be appear as a dip in the signal when Ω is in the vicinity of $2\omega_{\rm trap}$.

In Figure 4.5, we see the output of the Monte-Carlo code for a simulated gaussian beam trap with a natural frequency $\omega_{\rm trap}$ of 1000 Hz. The trap is 700 μK deep and contains atoms initially at 70 μK. The modulation index ϵ is 20% and lasts for a duration Δt of 1.0 s. The well was lowered to 10% of it full value (f=0.1) for the number measurement.

The results show that we should be able to detect the parametric resonance frequency of this hypothetical trap. The shape of the resonance, consisting of a broad shelf at frequencies below the peak, and a sharp drop-off at frequencies above the peak is a general feature of resonance peaks in gaussian wells. At high-energy,

a gaussian well is *soft*—that is, its trap frequencies are energy dependent and are less than or equal to the harmonic frequency of the well bottom. As a result, there are atoms in the well that are resonant with lower frequencies (producing the shelf) but no atoms resonant with higher frequencies (resulting in the rapid drop-off).

As the temperature of the atoms increases further, the number of atoms resonant at lower frequencies increases, eventually "pulling" the peak towards lower frequencies. The shift tends to saturate at approximately 10% of the resonance frequency. The shift appears to be a consistent feature of high-temperature excitation in a gaussian well, and we saw it often in many of our early simulations (we now work with significantly colder atoms, so it does not appear). The effect has recently been seen in analytical treatments of the system [51].

4.5.2 Release and Recapture

As mentioned previously, a PMT was our only method for making measurements of the atoms in our early experiments [21]. To determine the temperature of the atomic cloud in those experiments, we used a technique known as *release-and-recapture* [32]. The concept of release-and-recapture is simple enough. The trapping potential is suddenly turned off and then back on again after a variable delay time. While the potential is off, the atoms expand ballistically (the release). When the trapping potential is restored, some fraction of atoms will have moved to a position where, given their kinetic energy, they are now unbound. The remainder are once again bound in the trap (the recapture). After a short delay to allow the unbound atoms to leave the vicinity of the trap, a resonant probe beam measures the number of atoms that have been recaptured. A plot of how this number varies as a function of the delay time produces a curve which can be used to determine the temperature

of the cloud.

An analytical expression can be developed to describe the number of atoms that remain trapped. However, it contains an integral over six dimensions (three spatial and three momentum) which cannot be evaluated in closed form. The integral must be determined numerically. As we were preparing to write the computer code to calculate the integral, we realized that the Monte-Carlo code could be trivially modified to *simulate* the experiment with clouds of various temperatures.

Measuring the temperature of the cloud then became an exercise in determining which simulated curve best matched the experimental data. The results are shown in Figure 4.6. The data and the analysis are from the experiment of [52]. The circles represent the experimentally measured data (the error bars indicate the standard deviation of the mean for the several measurements at each point). The curves represent the output of the Monte-Carlo code for clouds of differing temperatures. The solid line is the temperature ($25\,\mu$K) that had the best correspondence to the data. The other two curves ($15\,\mu$K and $35\,\mu$K) are shown for comparison. Thus we were able to conclude that the temperature of the atomic cloud was approximately $25\,\mu$K.

4.5.3 Variation of Cloud Size

Eventually, we acquired a CCD camera capable of high-resolution images of the atomic distributions (see Chapter 7 for a discussion of the relevant techniques and the associated physics). Clearly, one of the highest priorities was to develop an imaging-based method of temperature measurement. At that time, the size of the imaging signal was not large enough that we could use time-of-flight imaging, as it reduces the signal even further as the cloud expands ballistically. Therefore, we

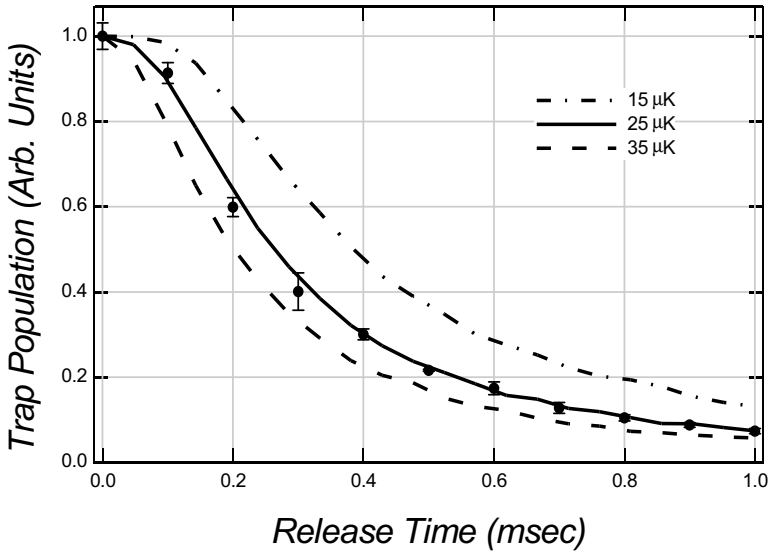

Figure 4.6: Using the Monte-Carlo code to determine temperature. The graph shows the correspondence between the experimentally measured data (circles) and the output of the Monte-Carlo code with a cloud temperature of 25 μK (solid line). The dashed curves are Monte-Carlo output for temperatures of 15 μK and 35 μK. They are presented for comparison.

were limited to *in situ* imaging of the atomic cloud in the trap.

In Chapter 3, we developed expressions for the spatial distribution of an atomic cloud in harmonic and gaussian wells. In a harmonic well, the cloud takes on a gaussian density profile, with the 1/e length scale in the i-th direction given by

$$b_i = a_i \sqrt{T/U}. \tag{4.12}$$

Here, a_i is the 1/e length scale of the trapping potential in the i-th direction, T is the temperature of the cloud, and U is the well depth in Kelvin. Hence, we could determine the temperature of the cloud by measuring the 1/e length scale of the cloud in the axial direction (the radial size is too small for accurate measurement) since we know the a_i and U for our trap.

This technique worked passably well, but is, after all, only an approximation.

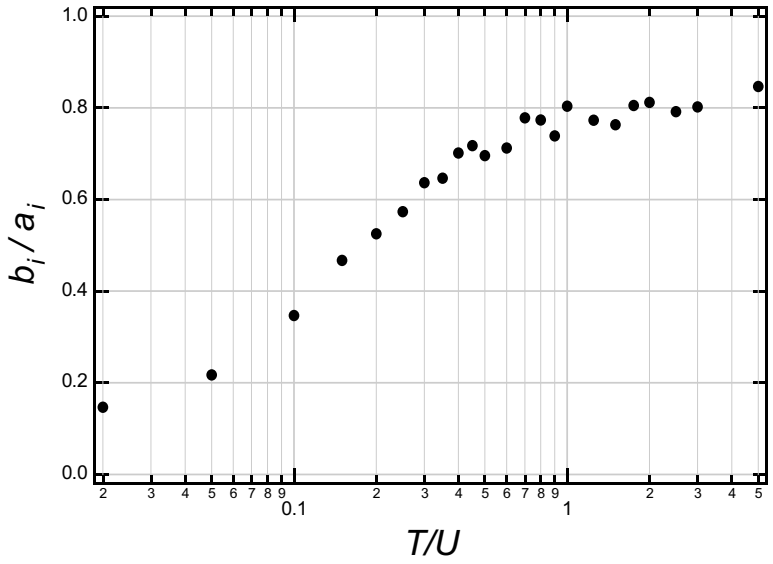

Figure 4.7: Temperature dependance of gaussian 1/e cloud size. The circles indicate the value of b_i/a_i from gaussian fits of the atomic distributions generated by the Monte-Carlo code. The data deviates from the harmonic square-root behavior

The real trap is not harmonic, and its true gaussian nature must have some effect on the characteristic size of the cloud as a function of temperature. We began investigating the size of the effect with the Monte-Carlo code.

The Monte-Carlo code is used to generate atomic distributions at different values of T/U. To mimic the measurement technique we are using in the experiment, the distributions are then fit to a gaussian and the 1/e length scale is extracted. In Figure 4.7, b_i/a_i is plotted as a function of T/U.

If the atoms are held in a harmonic well, (4.12) predicts that there should be a square-root dependance. While the overall shape is approximately square-root in nature, there are significant deviations. To better see the deviation from harmonic behavior, we introduce a scaling factor α, defined through the relation

$$b_i = \alpha \, a_i \sqrt{T/U}, \tag{4.13}$$

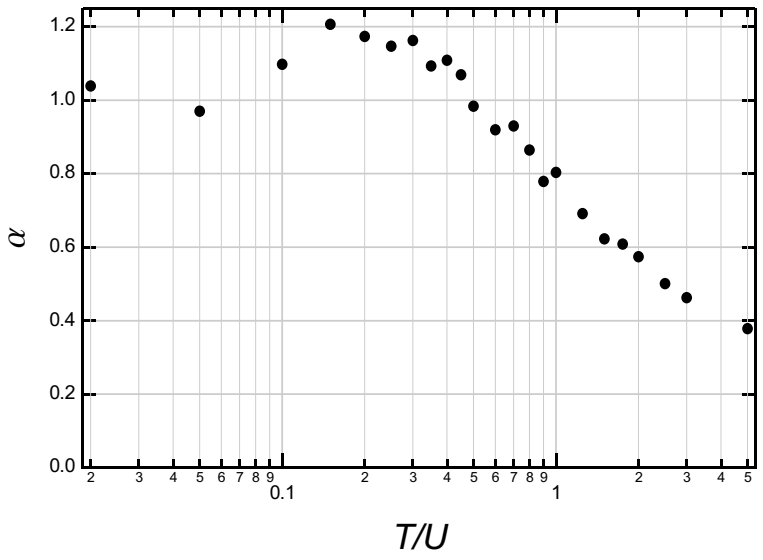

Figure 4.8: Deviation of gaussian 1/e cloud size from the harmonic result. Here the scale factor α is plotted versus temperature for the data of Figure 4.7. Harmonic behavior appears in the low-T/U limit, but the magnitude of the deviation at relatively low ($T/U \simeq 0.1$) temperatures, as well as the fact that at high-temperatures, the cloud gets smaller than a harmonically-confined cloud are quite surprising.

and plot α as a function of T/U as shown in Figure 4.8. We see that we recover the harmonic result $\alpha = 1$ in the extreme low-T/U limit. However, as T/U is increased from zero, the cloud first becomes significantly larger than the harmonic prediction, then dramatically smaller than the harmonic value! This result is actually very surprising, since a gaussian well, as a soft oscillator, is *less* confining than the equivalent harmonic well.

This surprising result made us reconsider the methodology we were using. We had been fitting the distributions to a gaussian—the expected shape of the cloud in a harmonic well. If the cloud shape varied from a gaussian, it was possible that the fit routine itself was responsible for the deviations we were seeing. We then developed an approach that did not rely on curve fits.

For each distribution, we computed the root-mean-square size of the cloud in

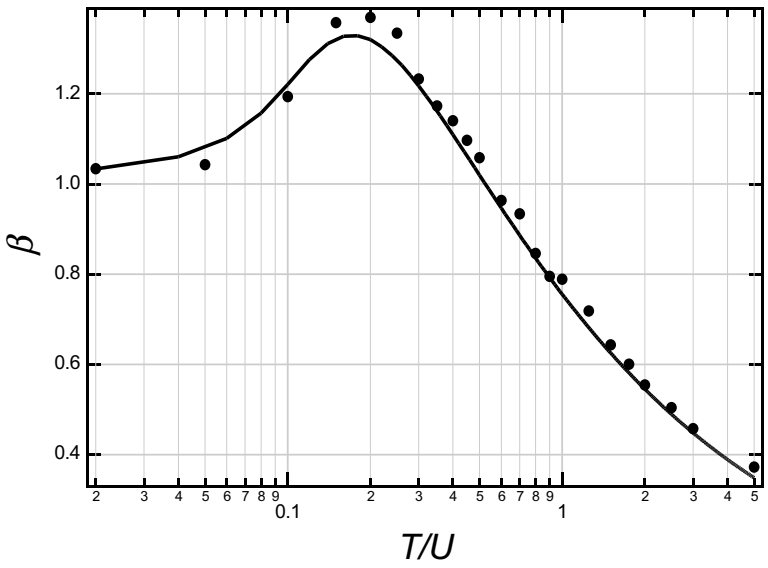

Figure 4.9: Deviation of the RMS cloud size from the harmonic result. Here the scale factor β from (4.14)is plotted versus T/U. Dots indicate calculated values based on the output of the Monte-Carlo Code, while the solid line is a theoretical prediction. Clearly the deviation is not solely an artifact of the curve fitting used to generate Figure 4.8

.

the i-th direction, $c_i \equiv \sqrt{\overline{i^2}}$. For a gaussian distribution, $c_i = b_i/\sqrt{2}$, so we can write

$$c_i = \beta \frac{a_i}{\sqrt{2}} \sqrt{T/U}, \tag{4.14}$$

in analogy with (4.13). In Figure 4.9, we see the results.

Again, we recover the harmonic result in the low-T/U limit. Once again the cloud begins to grow faster than the harmonic result as T/U increases. However, the size of the deviation is even larger than we first believed! Clouds as cold as 10% of the well depth are 40% larger than we would expect based on a harmonic-well estimate. Also, the cloud size again becomes *smaller* than the corresponding harmonically-trapped cloud when T/U approaches 0.5.

Can we believe these counterintuitive results? To double check, we performed

an analysis based on the analytic techniques introduced in Chapter 3. The analysis agrees with the Monte-Carlo model on all accounts (solid line in Figure 4.9). The dramatic effect that the gaussian potential has on the cloud shape discouraged us from continuing to use *in situ* cloud-size measurements as a thermometry technique. Luckily, at about this time, improvements in the trapping apparatus began providing signals large enough for us to switch to time of flight imaging. However, we learned an important lesson from this analysis—the anharmonicity of the gaussian well can dramatically impact the behavior of the atoms, even when they are quite low in the well.

Chapter 5

Dynamics of Noise-Induced Heating

For then our atoms, which in order lay,
are scatter'd from their heap, and puff'd away...

—John Dryden

5.1 Overview

In previous chapters we presented analytical and numerical tools for understanding and exploring trapped atomic clouds. These tools allow us to describe the equilibrium distributions of both classical and Fermi gases, as well as the dynamics of a classical gas. In earlier work, our group identified noise-induced heating of the atoms as a possible cause of the poor trap lifetimes in early optical traps [26]. Our ultimate experimental goals depended on being able to construct or purchase a CO_2 laser with suitably low levels of noise. A major result of [26] was a relationship between the noise-spectra of the laser and the related heating timescales. However, in that work, the timescales were derived for the simplified case of a single particle in an infinite well. An important question, then, is: How are the timescales modified when we consider an atomic ensemble in a finite well? This chapter develops the tools necessary to answer that question and provides the answers that we found

(and which were subsequently published in [27]).

5.2 Fluctuations in the Trapping Potential

We consider two different types of fluctuations in trapping potential. There can be *position noise* in the location of the trap center. Alternatively, there can be *intensity noise* in the trapping laser beam. This translates into a modulation of the trap spring constant. This section addresses each of these mechanisms in the context of a harmonic confining potential, and derives the heating rate for each in terms of the measurable fluctuation spectrum [26, 27].

5.2.1 Position Noise

Position noise in the trap center results in a side-to-side shaking of the trap. Shaking the trap can heat the atoms in much the same way that side-to-side shaking of a bowl which contains a ball can excite the ball. We consider the one-dimensional case and write the Hamiltonian:

$$H = \frac{p^2}{2m} + \frac{1}{2}\, m\, \omega_{\rm trap}^2 \left[x - \epsilon(t)\right]^2, \tag{5.1}$$

where $\epsilon(t)$ is the fluctuation of the trap center in time. The perturbation is written as

$$H'(t) = -m\, \omega^2\, x\, \epsilon(t), \tag{5.2}$$

where we have dropped the $\epsilon^2(t)$-term since we are only going to work to first order and it is spatially constant. Because the perturbation contains only a single power of x, it drives $n-1 \leftrightarrow n$ and $n \leftrightarrow n+1$ transitions between quantum states of

the harmonic oscillator. Using Fermi's Golden Rule, we can derive the average transition rates between these adjacent levels, and hence the average heating rate.

Given this perturbation, the heating rate is given by

$$\left\langle \dot{E} \right\rangle = \frac{\pi}{2} m \, \omega_{\text{trap}}^4 \, S_x(\omega_{\text{trap}}). \tag{5.3}$$

Here, $S_x(\omega_{\text{trap}})$ is the one-sided power spectrum of fluctuations in the trap center, evaluated at the harmonic trap frequency. From Parseval's theorem,

$$\int_0^\infty d\omega S_x(\omega) \equiv \left\langle \epsilon^2(t) \right\rangle \equiv \epsilon_0^2, \tag{5.4}$$

where ϵ_0 is the RMS position fluctuation in the trap center. For brevity in future sections, we make the definition

$$\dot{Q} \equiv \frac{\pi}{2} m \, \omega_{\text{trap}}^4 \, S_x(\omega_{\text{trap}}). \tag{5.5}$$

Thus we can write the average heating rate due to position fluctuations in the trapping potential as

$$\left\langle \dot{E} \right\rangle = \dot{Q}. \tag{5.6}$$

5.2.2 Intensity Noise

Fluctuations in the laser intensity result in modulation of the trap spring-constant. This can heat the atoms through the well known process of *parametric resonance* [49]. In parametric resonance, a parameter of the oscillator (such as the spring constant) is modulated. Resonant excitation occurs when the modulation is at twice the natural frequency of the (undisturbed) oscillator.

We write the Hamiltonian for this case as

$$H = \frac{p^2}{2m} + \frac{1}{2}\, m\, \omega_{\text{trap}}^2\, [1 + \epsilon(t)]\; x^2. \tag{5.7}$$

Here $\epsilon(t)$ is the *fractional* intensity fluctuation of the laser

$$\epsilon(t) = \frac{I(t) - I_0}{I_0}, \tag{5.8}$$

where I_0 is the time-average laser intensity.

We proceed as before. The perturbation Hamiltonian is

$$H'(t) = \frac{1}{2}\, \epsilon(t)\, m\, \omega_{\text{trap}}^2\, x^2. \tag{5.9}$$

Here we see that, unlike the perturbation for position noise, this perturbation depends on x^2. Hence, it drives $n - 2 \leftrightarrow n$ and $n \leftrightarrow n + 2$ transitions between quantum states of the harmonic oscillator. Again using Fermi's Golden Rule, we can determine the average transition rates between these linked levels, and hence the average heating rate. In this case we find

$$\left\langle \dot{E} \right\rangle = \frac{\pi}{2}\, \omega_{\text{trap}}^2\, S_I(2\omega_{\text{trap}}) E. \tag{5.10}$$

Here $S_I(2\omega_{\text{trap}})$ is the one-sided power spectrum of fractional intensity fluctuations, evaluated at *twice* the natural frequency of the undisturbed oscillator. This factor of two confirms that this is a parametric process. Note that the heating rate is energy dependent, and leads to exponential heating.

We define the heating rate constant, Γ

$$\Gamma = \frac{\pi}{2}\,\omega_{\mathrm{trap}}^2\,S_I(2\omega_{\mathrm{trap}}). \tag{5.11}$$

This allows us to write the heating rate as

$$\left\langle \dot{E} \right\rangle = \Gamma\,E. \tag{5.12}$$

5.3 The Fokker-Planck Equation

The previous sections describe how the average energy of the atoms increases as a result of position and intensity fluctuations in the trapping laser. While crude estimates of the trap lifetime can be generated from these results (by dividing the well depth by the total heating rate, for example), such an approach necessarily misses many important details.

We have shown that the fluctuations drive transitions between the discrete states of the harmonic oscillator. While we can derive *average* rates for these transitions, the underlying process is probabilistic. This type of situation is known as a *Markov Chain*. However, to a very good approximation, we can ignore the discrete nature of the states of the harmonic oscillator and treat the states as a continuum. When we do this, we have changed the Markov Chain into a *Markov Process*. A standard technique for describing the time-evolution of statistical distributions subject to a Markov Process is the *Fokker-Planck equation* [53]. The Fokker-Planck equation is a partial-differential diffusion equation for a distribution function. In order to provide a more detailed description of the noise-induced heating process, we developed a Fokker-Planck equation that describes the evolution of $n(E)$ (the number density

of atoms as a function of energy) as a result of position and intensity fluctuations in the trapping laser.

The general form of a one-dimensional Fokker-Planck equation is [54]

$$\frac{\partial W(x,t)}{\partial t} = \mathcal{L}_{\mathrm{FP}}\, W(x,t). \tag{5.13}$$

Here, $W(x,t)$ is the generalized statistical distribution, while x and t are generalized space and time variables, respectively. The symbol $\mathcal{L}_{\mathrm{FP}}$ is the Fokker-Planck operator given by

$$\mathcal{L}_{\mathrm{FP}}(x) = -\frac{\partial}{\partial x} D^{(1)}(x) + \frac{\partial^2}{\partial x^2} D^{(2)}(x). \tag{5.14}$$

In the above, $D^{(1)}$ and $D^{(2)}$ are the *drift* and *diffusion* coefficients, respectively for the random process forcing the evolution. They are expressible as [54]:

$$D^{(1)}(x) = \frac{d}{dt}\,\langle x \rangle\,, \tag{5.15}$$

$$D^{(2)}(x) = \frac{1}{2}\,\frac{d}{dt}\,\left(\langle x^2 \rangle - \langle x \rangle^2\right). \tag{5.16}$$

5.3.1 One Dimensional Fokker-Planck Equation

We can compute the the values of the drift and diffusion coefficients from the average transition rates. In one dimension, we find [27]:

$$D^{(1)}(E_1) = \dot{Q}_1 + \Gamma_1 E_1, \tag{5.17}$$

$$D^{(2)}(E_1) = \dot{Q}_1 E_1 + \frac{\Gamma_1}{2} E_1^2. \tag{5.18}$$

In the above, $\dot{Q}_1$ and Γ_1 are the constants we defined in (5.5) and (5.11). Inserting these values for $D^{(1)}$ and $D^{(2)}$ into the general form for the Fokker-Planck

equation (5.13), and taking the energy E_1 as the generalized spatial dimension and $n(E_1, t)$ as the statistical distribution we wish to evolve, we find

$$\frac{\partial n(E_1,t)}{\partial t} = \frac{\partial^2}{\partial E_1^2}\left[\left(\frac{\Gamma_1}{2}E_1^2 + \dot{Q}_1 E_1\right) n(E_1,t)\right] - \frac{\partial}{\partial E_1}\left[\left(\Gamma_1 E_1 + \dot{Q}_1\right) n(E_1,t)\right]. \tag{5.19}$$

Performing the differentiations and collecting similar terms results in the somewhat simpler form

$$\frac{\partial n(E_1,t)}{\partial t} = \left(\frac{\Gamma_1}{2}E_1^2 + \dot{Q}_1 E_1\right)\frac{\partial^2 n(E_1,t)}{\partial E_1^2} + \left(\Gamma E_1 + \dot{Q}_1\right)\frac{\partial n(E_1,t)}{\partial E_1}. \tag{5.20}$$

5.3.2 Three Dimensional Fokker-Planck Equation

Of course, our trap exists not in one dimension, but in three. We must therefore find a way to extend the treatment above to three dimensions. The drift and diffusion coefficients become the sum of the drift and diffusion coefficients in the **x**, **y**, and **z** directions:

$$D^{(1)}(E) = \sum_{i=x,y,z}\left(\dot{Q}_i + \Gamma_i \left\langle E_i\right\rangle_E\right), \tag{5.21}$$

$$D^{(2)}(E) = \sum_{i=x,y,z}\left(\dot{Q}_i \left\langle E_i\right\rangle_E + \frac{\Gamma_i}{2}\left\langle E_i\right\rangle_E\right). \tag{5.22}$$

Here $\langle\cdots\rangle_E$ indicates an average over all states of fixed total energy $E = E_x + E_y + E_z$. This form of $D^{(1)}$ and $D^{(2)}$ do not appear very tractable. However, we can make the assumption of *sufficient ergodicity* and dramatically simplify the results. For our system, sufficient ergodicity is equivalent to a statement that, for a given value of total energy E, all possible combinations of E_x, E_y, and E_z are equally likely. How valid is this assumption? It appears quite reasonable, as our system rapidly explores

configuration space as a result of inter-particle collisions and trap anharmonicities.

For a sufficiently ergodic system in a harmonic well, it is easy to show that $\langle E_{x,y,z} \rangle_E = E/3$ and $\left\langle E^2_{x,y,z} \right\rangle_E = E^2/6$. Inserting these values into (5.21) and (5.22) we find:

$$D^{(1)}(E) = 3\dot{Q} + \Gamma E, \tag{5.23}$$

$$D^{(2)}(E) = \dot{Q}E + \frac{\Gamma}{4}E^2. \tag{5.24}$$

In the above, we have defined the average heating rate $\dot{Q}$ and heating rate constant Γ as follows:

$$\dot{Q} = \frac{\dot{Q}_x + \dot{Q}_y + \dot{Q}_z}{3}, \tag{5.25}$$

$$\Gamma = \frac{\Gamma_x + \Gamma_y + \Gamma_z}{3}. \tag{5.26}$$

Here $\dot{Q}_i$ and Γ_i represent the appropriate values of $\dot{Q}_1$ and Γ_1 in the i-direction.

Inserting (5.23) and (5.24) into the general form of the Fokker-Planck equation (5.13) and proceeding as before yields the desired result

$$\frac{\partial n(E,t)}{\partial t} = \left(\frac{\Gamma}{4}E^2 + \dot{Q}E\right)\frac{\partial^2 n(E,t)}{\partial E^2} - \dot{Q}\frac{\partial n(E,t)}{\partial E} - \frac{\Gamma}{2}n(E,t). \tag{5.27}$$

Here $E = E_x + E_y + E_z$ is the total energy and $\dot{Q}$ and Γ are the averages defined in (5.25) and (5.26).

5.4 Solving the Fokker-Planck Equation

We can bring several types of analytic and numerical machinery to bear on the problem of solving (5.27). The next few sections describe several approaches and the insights we can gain from each.

5.4.1 Stationary Solution

We can derive the stationary solution to the general Fokker-Planck equation as follows. For a stationary solution, there is no time evolution, hence $\partial n(E,t)/\partial t = 0$. This implies that $\mathcal{L}_{\rm FP}\, W_{\rm stat}(x)$ is zero. Therefore we can make the sequence of steps:

$$\begin{aligned} \frac{\partial}{\partial x} D^{(1)}(x) W_{\rm stat}(x) &= \frac{\partial^2}{\partial x^2} D^{(2)}(x) W_{\rm stat}(x) \\ D^{(1)}(x) W_{\rm stat}(x) &= \frac{\partial}{\partial x} D^{(2)}(x) W_{\rm stat}(x) \\ \frac{D^{(1)}(x)}{D^{(2)}(x)} D^{(2)}(x) W_{\rm stat}(x) &= \frac{\partial}{\partial x} D^{(2)}(x) W_{\rm stat}(x). \end{aligned} \tag{5.28}$$

The solution to the last line is clearly

$$D^{(2)}(x) W_{\rm stat}(x) = C \exp\left[\int \frac{D^{(1)}(x')}{D^{(2)}(x')} dx' \right], \tag{5.29}$$

where C is the constant required to normalize $W_{\rm stat}(x)$. Solving for $W_{\rm stat}(x)$, we can write

$$W_{\rm stat}(x) = C \exp\left[-\ln D^{(2)}(x) + \int \frac{D^{(1)}(x')}{D^{(2)}(x')} dx' \right], \tag{5.30}$$

with C defined as before. Specializing to our notation and inserting the values of $D^{(1)}$ and $D^{(2)}$, we find that the stationary solution is

$$n_{\rm stat}(E) = 4\, C E^2. \tag{5.31}$$

We see the striking result that the stationary solution is proportional to the density of states of the 3-D harmonic oscillator. In fact, this correspondence holds true in arbitrary dimensions. However, for this solution to hold, we must have an infinitely deep potential well and an infinite number of atoms. A physical system, of course, can not supply either, and the introduction of boundary conditions inevitably leads to deviation from the solution in (5.31). Thus, we invariably will see a time dependence to all solutions.

5.4.2 Eigenmode Analysis: General

To address physical solutions, we must address the full, time-dependent equations. If we make the separation *Ansatz*

$$n(E,t) = \phi(E)\, e^{-\lambda t}, \tag{5.32}$$

and insert it into (5.27), we obtain the defining differential equation for the eigenmodes $\phi_\lambda(E)$:

$$\left(\frac{\Gamma}{4}E^2 + \dot{Q}E\right)\frac{\partial^2\phi_\lambda(E)}{\partial E^2} - \dot{Q}\frac{\partial\phi_\lambda(E)}{\partial E} + \left(\lambda - \frac{\Gamma}{2}\right)\phi_\lambda(E) = 0. \tag{5.33}$$

This equation does have an analytical solution in terms of generalized special functions:

$$\begin{aligned}\phi_\lambda(E) =& C_1\ F\left(-\frac{1+A}{2}, -\frac{1-A}{2}; -1; -\frac{\Gamma E}{4\dot{Q}}\right) \\ &+ C_2\left(\frac{\Gamma\dot{Q}E}{4}\right)^2 F\left(\frac{3-A}{2}, \frac{3+A}{2}; 3; -\frac{\Gamma E}{4\dot{Q}}\right),\end{aligned} \tag{5.34}$$

where F is the Gauss hypergeometric function [55], and $A = \sqrt{9 + 16\lambda/\Gamma}$.

Boundary Conditions

Since we cannot experimentally provide a harmonic well of infinite depth, we theoretically treat a truncated harmonic well of depth U_0. We start by remembering that we can write the function $n(E)$ as the product of the occupation number $f(E)$ and the density of states $g(E)$

$$n(E) = f(E)\, g(E), \tag{5.35}$$

where the density of states for a 3-D harmonic oscillator is

$$g(E) = \frac{E^2}{2\hbar^3 \omega_x \omega_y \omega_z}. \tag{5.36}$$

The occupation number $f(E)$ is the probability that a state of energy E is occupied.

For any harmonic oscillator, $g(0) = 0$, since the minimum energy of an oscillator is $\hbar\omega/2$. Further, since we are considering a *truncated* harmonic oscillator, there cannot be any particles at $E = U_0$, so $f(U_0) = 0$. Therefore, from (5.35), we see that the appropriate boundary conditions for our system are

$$n(0) = 0 \tag{5.37}$$

$$n(U_0) = 0. \tag{5.38}$$

In terms of the eigenmodes, ϕ_λ, this becomes

$$\phi_\lambda(0) = 0 \tag{5.39}$$

$$\phi_\lambda(U_0) = 0. \tag{5.40}$$

Applying the constraints (5.39) and (5.40) restricts the possible values of C_1 and C_2 in (5.34), as well as the possible values of λ. We will not perform these calculations for the fully general hypergeometric case. However, we will perform this analysis for the simplified cases of pure position and pure intensity noise in subsequent sections of this chapter.

Initial Condition

We now have an eigenmode solution to the separation *Ansatz* we made in (5.32). To incorporate our desired initial condition, we would proceed as is typical by expanding the initial condition in terms of the eigenmodes

$$n(E, 0) = \sum_\lambda B_\lambda \, \phi_\lambda(E), \tag{5.41}$$

where the weighting coefficients, B_λ are defined by

$$B_\lambda = \int_0^{U_0} dE' \, n(E', 0) \, \phi_\lambda(E'). \tag{5.42}$$

Thus the final solution is

$$n(E, t) = \sum_\lambda B_\lambda \, \phi_\lambda(E) \, e^{-\lambda t}. \tag{5.43}$$

5.4.3 Eigenmode Analysis: Pure Position Noise

While extremely general, the hypergeometric function is not the most convenient of mathematical functions. This section considers the case where $\Gamma = 0$ (pure position noise), while the next section addresses $\dot{Q} = 0$ (pure intensity noise). In these limits, we can not only obtain solutions in terms of less arcane functions, but also extract important information about the long-time behavior of the system.

In the limit that $\Gamma = 0$, the trap experiences pure position noise. In this case the differential equation (5.33) for the eigenmodes $\phi_\lambda(E)$ reduces to

$$E\frac{\partial^2\phi_\lambda(E)}{\partial E^2} - \frac{\partial\phi_\lambda(E)}{\partial E} + \frac{\lambda}{\dot{Q}}\phi_\lambda(E) = 0. \tag{5.44}$$

This equation has the solution

$$\phi_\lambda(E) = C_1\ E\ J_2\left(\sqrt{4\lambda E/\dot{Q}}\right) - C_2\ E\ Y_2\left(\sqrt{4\lambda E/\dot{Q}}\right), \tag{5.45}$$

where J_2 and Y_2 are the Bessel functions of order 2 [55].
From (5.39), we conclude that C_2 is necessarily zero, since the second term of (5.45) diverges at $E = 0$. Further, we find that satisfying (5.40) requires

$$J_2\left(\sqrt{4\lambda U_0/\dot{Q}}\right) = 0. \tag{5.46}$$

Since this is only true for specific values of λ, we have a *discrete eigenvalue spectrum* in the case of pure position noise. We can write the allowed values of λ as

$$\lambda_p = \frac{z_p^2}{4}\frac{\dot{Q}}{U_0}, \tag{5.47}$$

where z_p are the zeros of J_2.

Thus, for the boundary conditions we specified, the full solution is

$$\phi_\lambda = C_1\, E\, J_2\left(\sqrt{4\lambda E/\dot{Q}}\right), \tag{5.48}$$

with λ a value of the form (5.47). The first few values of λ are

$$\lambda = 6.59365\frac{\dot{Q}}{U_0},\ 17.7125\frac{\dot{Q}}{U_0},\ 33.7552\frac{\dot{Q}}{U_0},\ 54.7300\frac{\dot{Q}}{U_0},\ \ldots \tag{5.49}$$

Long-Time Behavior

Remembering that the ϕ_λ decays as $e^{-\lambda t}$, we expect that, in the long time limit, the behavior will be dominated by the lowest mode, and the system will decay as

$$n(E,t) \underset{t\gg 0}{\propto} e^{-6.59\,\frac{\dot{Q}}{U_0}\,t}. \tag{5.50}$$

Further, since an eigenmode has a constant spatial shape, when the lowest eigenmode dominates, the mean energy of the system is a constant. Thus, the system evolves towards a constant mean energy. We can write the mean energy as a function of time

$$\bar{E}(t) \equiv \frac{E_{\rm tot}}{N} = \frac{\int_0^{U_0} dE\ E\ n(E,t)}{\int_0^{U_0} dE\ n(E,t)}. \tag{5.51}$$

In the long time limit, $n(E,t)$ can be replaced by the lowest eigenmode. The result is

$$\bar{E} \underset{t\gg 0}{=} \frac{\int_0^{U_0} dE\ E^2\ J_2\left(5.14\sqrt{E/U_0}\right)}{\int_0^{U_0} dE\ E\ J_2\left(5.14\sqrt{E/U_0}\right)}. \tag{5.52}$$

From this, we find that in the long-time limit, the mean energy of the system approaches $\bar{E} = 0.544\,U_0$.

5.4.4 Eigenmode Analysis: Pure Intensity Noise

In the $\dot{Q} = 0$ limit, the system is driven by pure intensity noise. The differential equation (5.33) for the eigenmodes $\phi_\lambda(E)$ reduces to

$$E^2 \frac{\partial^2 \phi_\lambda(E)}{\partial E^2} + \left(\frac{4\lambda}{\Gamma} - 2 \right) \phi_\lambda(E) = 0. \tag{5.53}$$

The resulting solution is

$$\phi_\lambda(E) = C_1 \sqrt{E}\, e^{\frac{iA}{2} \ln E} + C_2 \sqrt{E}\, e^{\frac{iA}{2} \ln E}, \tag{5.54}$$

where $A = \sqrt{(16\lambda/\Gamma) - 9}$.

This solution automatically satisfies the boundary condition at zero (5.39). Applying the other condition (5.40), we find that

$$C_2 = -C_1\, e^{-iA \ln U_0}. \tag{5.55}$$

Inserting this into (5.54) and redefining the initial constant lets us rewrite the solution as

$$\phi_\lambda(E) = C_3 \sqrt{E}\, \sin\left(\frac{A}{2} \ln\left(\frac{E}{U_0} \right) \right), \tag{5.56}$$

with A defined as before. This solution satisfies both boundary conditions (the divergent nature of the logarithm at $E = 0$ is contained within the bounded sine function), without forcing discrete values of λ. Unlike the case of pure position noise, then, this system has a *continuous eigenvalue spectrum*. The eigenvalue λ can take on any value that satisfies

$$\lambda \geq \frac{9}{16}\Gamma. \tag{5.57}$$

We must also modify our expansion of the initial condition. The sums in (5.41) and (5.43) must be replaced with integrals over λ.

Long-Time Behavior

Once again, we remember that the ϕ_λ decays as $e^{-\lambda t}$. Unlike the previous case, the lack of a discrete eigenvalue spectrum means that the system does not ever cleanly evolve into a single mode, as there are always competing modes arbitrarily close to the lowest mode. Instead, we can make the claim that the decay will have the lowest mode as an asymptotic limit, and thus that the decay rate will always be greater than or equal to the decay rate of the lowest mode

$$n(E,t) \underset{t\gg 0}{\propto} e^{-\beta\,\Gamma\,t} \qquad \beta \to \frac{9}{16}^{+} \text{ as } t \to \infty. \tag{5.58}$$

The calculation of the mean energy at long times is also complicated by the continuous eigenvalue spectrum. Computing the mean energy for an arbitrary value of A, we find

$$\bar{E} = \frac{\int_0^{U_0} dE\; E^{3/2}\; \sin\left(\frac{A}{2}\ln\left(\frac{E}{U_0}\right)\right)}{\int_0^{U_0} dE\; \sqrt{E}\; \sin\left(\frac{A}{2}\ln\left(\frac{E}{U_0}\right)\right)} = \frac{9+A^2}{25+A^2}\,U_0. \tag{5.59}$$

The lowest eigenvalue is $\lambda = 9\,\Gamma/16$, for which $A = 0$. The associated mode has a mean energy $\bar{E} = 9\,U_0/25$. The continuous eigenvalue spectrum makes this the asymptotic limit of the mean energy. Further, at long time the mean energy is always greater than or equal to the mean energy of the lowest mode

$$\bar{E} \underset{t\gg 0}{=} \left(\frac{9}{25}+\delta\right) U_0 \qquad \delta \to 0^{+} \text{ as } t \to \infty. \tag{5.60}$$

5.4.5 Numerical Solution via Finite-Difference Techniques

We can now fully treat the problem analytically. Any desired initial condition can be evolved in the truncated harmonic well with any amount of position and intensity noise. However, for anything but a few eigenmodes, the problem rapidly exceeds our capabilities when treated as a pencil and paper problem. The best approach evolves the Fokker-Planck equation numerically, and turns to the analytical solutions for insight into the results. The next section details the methodology of our numerical solution technique.

Dimensionless Form

We begin our numerical treatment of the problem by rewriting the 3-D Fokker-Planck equation of (5.27) in dimensionless form. While the energy rescaling is obvious

$$E = U_0\,\epsilon, \tag{5.61}$$

we have two possible time rescalings

$$t = \frac{U_0}{\dot{Q}}\,\tau, \tag{5.62}$$

$$t = \frac{1}{\Gamma}\,\tau. \tag{5.63}$$

The former works well unless $\dot{Q} = 0$, while the latter works unless $\Gamma = 0$. Since we are interested in both cases, we must develop two different dimensionless equations. We will refer to the equation arising from (5.62) as the *dimensionless position noise* equation, while the result of (5.63) will be known as the *dimensionless intensity noise* equation. The reader should note that both equations can accommodate a mixture of the two noise sources. It is only in the $\dot{Q} \to 0$ and $\Gamma \to 0$ limits that the

equations become intractable.

Making the scalings above, we find the dimensionless position noise equation is

$$\frac{\partial n(\epsilon,\tau)}{\partial \tau} = \left(\frac{\Gamma U_0}{4\dot{Q}}\,\epsilon^2 + \epsilon\right)\frac{\partial^2 n(\epsilon,\tau)}{\partial \epsilon^2} - \frac{\partial n(\epsilon,\tau)}{\partial \epsilon} - \frac{\Gamma U_0}{2\dot{Q}}\,n(\epsilon,\tau). \tag{5.64}$$

while the dimensionless intensity noise equation is

$$\frac{\partial n(\epsilon,\tau)}{\partial \tau} = \left(\frac{1}{4}\,\epsilon^2 + \frac{\dot{Q}}{\Gamma U_0}\,\epsilon\right)\frac{\partial^2 n(\epsilon,\tau)}{\partial \epsilon^2} - \frac{\dot{Q}}{\Gamma U_0}\,\frac{\partial n(\epsilon,\tau)}{\partial \epsilon} - \frac{1}{2}\,n(\epsilon,\tau), \tag{5.65}$$

We will find it convenient to define a parameter to describe the relative mixture of intensity and position noise. We define

$$\mathcal{X}_Q \equiv \frac{\Gamma U_0}{\dot{Q}}, \tag{5.66}$$

$$\mathcal{X}_\Gamma \equiv \frac{\dot{Q}}{\Gamma U_0}. \tag{5.67}$$

Inserting (5.66) into (5.64), we find the dimensionless position noise equation can be written as

$$\frac{\partial n(\epsilon,\tau)}{\partial \tau} = \left(\frac{\mathcal{X}_Q}{4}\,\epsilon^2 + \epsilon\right)\frac{\partial^2 n(\epsilon,\tau)}{\partial \epsilon^2} - \frac{\partial n(\epsilon,\tau)}{\partial \epsilon} - \frac{\mathcal{X}_Q}{2}\,n(\epsilon,\tau). \tag{5.68}$$

Making the equivalent substitution, we find that the dimensionless intensity noise equation is

$$\frac{\partial n(\epsilon,\tau)}{\partial \tau} = \left(\frac{1}{4}\,\epsilon^2 + \mathcal{X}_\Gamma\,\epsilon\right)\frac{\partial^2 n(\epsilon,\tau)}{\partial \epsilon^2} - \mathcal{X}_\Gamma\,\frac{\partial n(\epsilon,\tau)}{\partial \epsilon} - \frac{1}{2}\,n(\epsilon,\tau). \tag{5.69}$$

Note that in this form, the two equations differ only by the mapping

$$\mathcal{X}_Q \leftrightarrow 1 \qquad 1 \leftrightarrow \mathcal{X}_\Gamma. \tag{5.70}$$

Finite Difference Method

We will employ a finite-difference technique to solve (5.68) and (5.69) numerically. We will discretize the problem and work on a grid in ϵ and take discrete timesteps in τ. The gridpoints are separated by distances of $\Delta\epsilon$ and the timesteps by $\Delta\tau$ (we will discuss the actual values of $\Delta\epsilon$ and $\Delta\tau$ later). We will denote the value of the function $n(\epsilon, \tau)$ at the j-th gridpoint and the m-th timestep as n_j^m.

There are many ways of converting derivatives into functions on gridpoints. The technique we will use is known as the *centered-space, forward-time* (CSFT) [55] method for reasons which will become immediately clear. We represent a spatial derivative at the j-th gridpoint as

$$n'^m_j = \frac{n^m_{j+1} - n^m_{j-1}}{2\Delta\epsilon}. \tag{5.71}$$

We represent a second spatial derivative as

$$n''^m_j = \frac{n^m_{j-1} - 2n^m_j + n^m_{j+1}}{\Delta\epsilon^2}. \tag{5.72}$$

Both approximations are correct to second-order in $\Delta\epsilon$. A time derivative is expressed as

$$\dot{n}^m_j = \frac{n^{m+1}_j - n^m_j}{\Delta\tau}. \tag{5.73}$$

This is a first-order approximation in $\Delta\tau$.

Inserting these derivative representations into (5.68) and collecting similar terms,

we find the update procedure for the dimensionless position noise equation in our finite difference method

$$\begin{aligned} n_j^{m+1} = & \left[\left(\frac{\mathcal{X}_Q}{4}\,\epsilon_j^2 + \epsilon_j\right)\left(\frac{\Delta\tau}{\Delta\epsilon^2}\right) - \left(\frac{1}{2}\right)\left(\frac{\Delta\tau}{\Delta\epsilon}\right)\right] n_{j+1}^m \\ & + \left[\left(\frac{\mathcal{X}_Q}{4}\,\epsilon_j^2 + \epsilon_j\right)\left(\frac{\Delta\tau}{\Delta\epsilon^2}\right) + \left(\frac{1}{2}\right)\left(\frac{\Delta\tau}{\Delta\epsilon}\right)\right] n_{j-1}^m \\ & + \left[-2\left(\frac{\mathcal{X}_Q}{4}\,\epsilon_j^2 + \epsilon_j\right)\left(\frac{\Delta\tau}{\Delta\epsilon^2}\right) - \left(\frac{\mathcal{X}_Q}{2}\right)(\Delta\tau) + 1\right] n_j^m. \end{aligned} \tag{5.74}$$

Here ϵ_j is the ϵ-value at the j-th gridpoint. For the case of the dimensionless intensity noise equation, we insert the derivative representations into (5.69) to get the update procedure

$$\begin{aligned} n_j^{m+1} = & \left[\left(\frac{1}{4}\,\epsilon_j^2 + \mathcal{X}_\Gamma\,\epsilon_j\right)\left(\frac{\Delta\tau}{\Delta\epsilon^2}\right) - \left(\frac{\mathcal{X}_\Gamma}{2}\right)\left(\frac{\Delta\tau}{\Delta\epsilon}\right)\right] n_{j+1}^m \\ & + \left[\left(\frac{1}{4}\,\epsilon_j^2 + \mathcal{X}_\Gamma\,\epsilon_j\right)\left(\frac{\Delta\tau}{\Delta\epsilon^2}\right) + \left(\frac{\mathcal{X}_\Gamma}{2}\right)\left(\frac{\Delta\tau}{\Delta\epsilon}\right)\right] n_{j-1}^m \\ & + \left[-2\left(\frac{1}{4}\,\epsilon_j^2 + \mathcal{X}_\Gamma\,\epsilon_j\right)\left(\frac{\Delta\tau}{\Delta\epsilon^2}\right) - \left(\frac{1}{2}\right)(\Delta\tau) + 1\right] n_j^m. \end{aligned} \tag{5.75}$$

These equation show how to calculate the value of a gridpoint at timestep $m+1$, based only on values of gridpoints at timestep m. It is customary to graphically represent the nature of the update procedure with a *computational cluster*. This is done in Figure 5.1. This figure demonstrates the relationship between gridpoints at consecutive timesteps.

Once we have an initial condition (n_j^0 for all j from 0 to $j_{\max}$), and boundary conditions (n_0^m and $n_{j_{\max}}^m$), we simply apply the update procedure for all non-boundary condition gridpoints ($j = 1$ to $j = (j_{\max} - 1)$) in each timestep before repeating the procedure at the next timestep.

The specific initial condition can be any function we desire, sampled at the

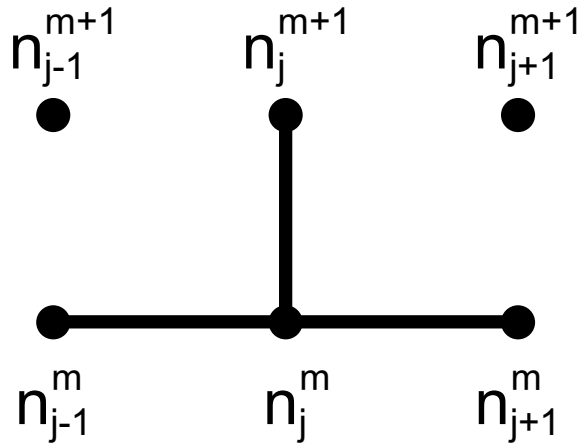

Figure 5.1: Computational cluster for the finite-difference method. This figure shows how a gridpoint in the numerical calculation is related to gridpoints at an earlier timestep. This is the cluster for the CSFT method.

gridpoints we use in the model. The boundary conditions we use are the same ones we derived in the analytical treatment of the problem (5.37), namely

$$n_0^m = 0 \tag{5.76}$$

$$n_{j_{\max}}^m = 0. \tag{5.77}$$

The remaining issue which we must address is the overall stability of the numerical approach and the constraints that stability places on $\Delta\epsilon$, $\Delta\tau$, and $j_{\max}$.

Von Neumann Stability Analysis

We can analyze the stability of the algorithm by making the *Ansatz* [53]

$$n_j^m = A^m e^{ikj\epsilon}. \tag{5.78}$$

The numerical approximation is stable (that is errors do not grow without bound) if $|A| \leq 1$ for all values of k. Inserting the *Ansatz* into the update procedures (5.74)

and (5.75) and dividing through by A^m and $e^{ikj\epsilon}$ yields

$$A = [B - C]e^{ik\epsilon} + [B + C]e^{-ik\epsilon} - [2B + D], \tag{5.79}$$

where B, C, and D are defined as

$$B = \left(\frac{\mathcal{X}_Q}{4} + 1\right)\left(\frac{\Delta\tau}{\Delta\epsilon^2}\right) \tag{5.80}$$

$$C = \left(\frac{1}{2}\right)\left(\frac{\Delta\tau}{\Delta\epsilon}\right) \tag{5.81}$$

$$D = \frac{\mathcal{X}_Q}{2}\Delta\tau - 1, \tag{5.82}$$

for the dimensionless position noise equation and

$$B = \left(\frac{1}{4} + \mathcal{X}_\Gamma\right)\left(\frac{\Delta\tau}{\Delta\epsilon^2}\right) \tag{5.83}$$

$$C = \left(\frac{\mathcal{X}_\Gamma}{2}\right)\left(\frac{\Delta\tau}{\Delta\epsilon}\right) \tag{5.84}$$

$$D = \frac{1}{2}\Delta\tau - 1, \tag{5.85}$$

for the dimensionless intensity noise equation. Note also that we have evaluated the update procedure at $\epsilon = 1$ for our definition of B. This is the maximum value of B over the entire range of ϵ.

We can rewrite (5.79) as

$$A = 2B\left(\cos(k\epsilon) - 1\right) - i\,2C\sin(k\epsilon) - D. \tag{5.86}$$

The equation describes an ellipse in the complex plane as $k\epsilon$ varies. The center of the ellipse is offset $2B + D$ to the left of the origin. The semi-major axis of the

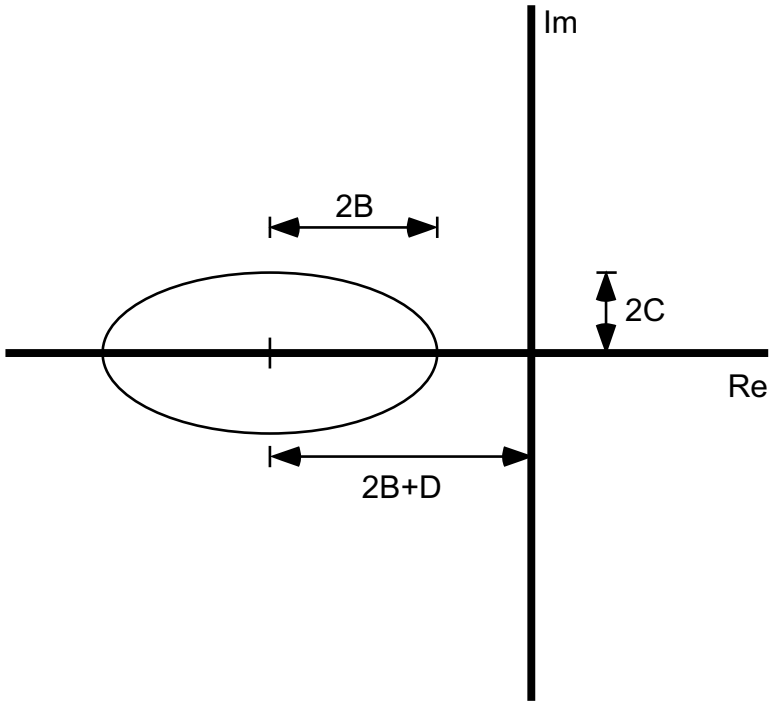

Figure 5.2: Trajectory of the stability function. This graph shows the trajectory traced out by the tip of the vector defined by the complex number A. To ensure that the numerical technique is stable, the magnitude of the vector must always be ≤ 1.

ellipse is $2B$, and the semi-minor axis is $2C$. See Figure 5.2 for a schematic.

In the case of the dimensionless position noise equation, we know this is the proper orientation because if we write B in terms of C as

$$B = \left(\frac{\mathcal{X}_Q}{4}\right)\left(\frac{\Delta\tau}{\Delta\epsilon^2}\right) + \left(\frac{2C}{\Delta\epsilon}\right), \tag{5.87}$$

we immediately see that the second term alone is greater than C, since $\Delta\epsilon$ is necessarily less than 1. Hence, $B - C > 0$ and we can confidently say $B > C$. A similar argument holds for the dimensionless intensity noise equation.

The value of $|A|$ is given by the length of the vector from the origin to points on the ellipse shown in Figure 5.2. Clearly, the largest magnitude occurs at the leftmost

point of the ellipse. At that point, the magnitude is $|A| = 4B + D$. Expanding this expression based on the definitions of B and D, we find for the dimesnionless position noise equation that the numerical approach is stable if

$$(\mathcal{X}_Q + 4)\left(\frac{\Delta\tau}{\Delta\epsilon^2}\right) + \left(\frac{\mathcal{X}_Q}{2}\right)(\Delta\tau) - 1 \leq 1. \tag{5.88}$$

We move the constant to the other side of the inequality:

$$(\mathcal{X}_Q + 4)\left(\frac{\Delta\tau}{\Delta\epsilon^2}\right) + \left(\frac{\mathcal{X}_Q}{2}\right)(\Delta\tau) \leq 2. \tag{5.89}$$

We note that since $\Delta\epsilon \ll 1$, we can essentially ignore the second term to find

$$(\mathcal{X}_Q + 4)\left(\frac{\Delta\tau}{\Delta\epsilon^2}\right) \lesssim 2. \tag{5.90}$$

From this we get the final stability criterion for the dimensionless position noise equation

$$\frac{\Delta\tau}{\Delta\epsilon^2} \lesssim \frac{2}{\mathcal{X}_Q + 4}. \tag{5.91}$$

A similar analysis can be made for the case of the dimensionless intensity noise equation. In that case, we find the stability criterion is

$$\frac{\Delta\tau}{\Delta\epsilon^2} \lesssim \frac{2}{1 + 4\mathcal{X}_Q}. \tag{5.92}$$

5.4.6 Characteristic Results

A computer code which numerically solves the Fokker-Planck equation for arbitrary initial condition, and subject to the boundary conditions and stability criterion of the preceding sections was developed by this group. In the past, we used it to

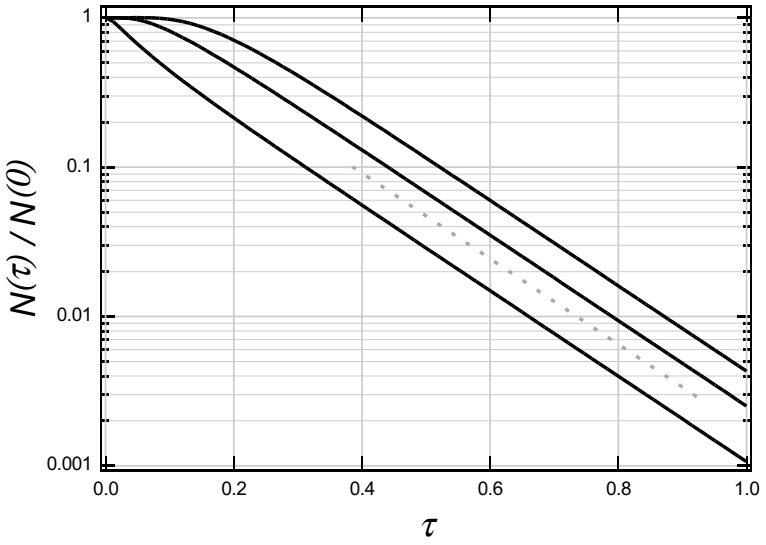

Figure 5.3: Position noise-induced atom loss as a function of time. The curves show how the number of trapped atoms decreases with (dimensionless) time as a result of position noise-induced heating. The top solid curve is an initial condition that starts low in the well, the middle solid curve is an initial condition that starts moderately high in the well, while the lower solid curve is an initial condition that starts high in the well. The dashed line shows the slope of the decay rate of the lowest eigenmode. Note that the different cases quickly reach a point where they decay at the rate of the lowest eigenmode.

investigate the noise-induced atom loss rate, and to show that the loss rate can be significantly faster than simple estimates would suggest [27]. The computer code used to perform the simulation is shown in Section C.5. This section provides an overview of some of our earlier results.

Pure Position Noise

We began by considering the case of pure position noise. We generated various initial conditions with different mean energies (the details of the initial condition are unimportant to the qualitative results we present). The evolution of the number of trapped atoms as a function of (dimensionless) time is shown in Figure 5.3.

The most important feature to note in this figure is that all the curves decay at

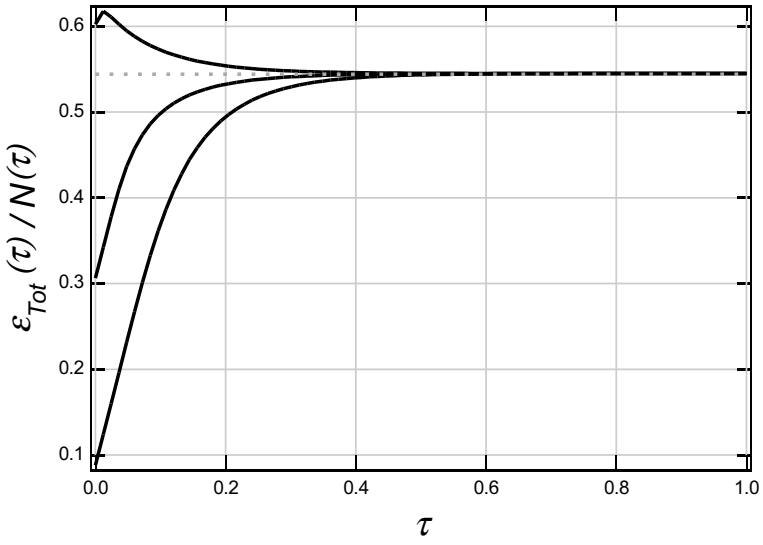

Figure 5.4: Position noise-induced energy evolution. The curves show how the mean energy of the trapped atoms evolves as a function of (dimensionless) time as a result of position noise-induced heating. The top solid curve is an initial condition that starts high in the well, the middle solid curve is an initial condition that starts moderately high in the well, while the lower solid curve is an initial condition that starts low in the well. The dashed curve shows the mean energy of the lowest eigenmode. Note that the different initial conditions quickly evolve to this value.

the same rate in the long-time limit despite their different initial conditions.

Working with the same initial conditions, we can investigate how the mean energy of the trapped atoms evolves as a function of time. The results of this investigation are shown in Figure 5.4. Note how the individual curves converge on a constant value regardless of their initial energies.

We can explain both the constant decay rate at long time and the constant mean energy at long time in terms of the eigenmode expansions we developed when treating the Fokker-Planck equation analytically. Remember that the solution is a sum of eigenmodes, each decaying according to their associated eigenvalue:

$$n(E,t) = \sum_{\lambda} B_\lambda \, \phi_\lambda(E) \, e^{-\lambda\tau}. \tag{5.93}$$

In the case of pure position noise, we showed that the lowest eigenmode decayed as $\exp(-6.6\,\dot{Q}\,t/U_0) \Rightarrow \exp(-6.6\,\tau)$. Further, we showed that the mean energy of this eigenmode is $\bar{E} = 0.544\,U_0 \Rightarrow \bar{\epsilon} = 0.544$. These results exactly match the long-time behavior shown in Figure 5.3 and Figure 5.4.

Pure Intensity Noise

Similarly to the case of pure position noise, we can investigate the effects of pure intensity noise by using the Fokker-Planck equation to evolve initial conditions with differing mean energies. The number and mean energy evolution for these different initial conditions are shown in Figure 5.5 and Figure 5.6, respectively.

Unlike the case of pure position noise, we note that while the decay curves are becoming more similar, and while the mean energies are converging, the process seems quite slow. In our analytical treatment of pure intensity noise, we predicted just such behavior as a result of the continuous eigenvalue spectrum. We expect the long-time decay to be *faster* than $\exp(-9\,\Gamma t/16) \Rightarrow \exp(-9\,\tau/16)$. Also, we expect the long-time value of the mean energy to be $\bar{E} \geq 0.36\,U_0 \Rightarrow \bar{\epsilon} \geq 0.36$. The numerical results seem to bear this out.

Mixed Noise

When we consider a combination of position and intensity noise, we find that the atom number decreases more rapidly than we expect. We can explain this effect in terms of the types of heating produced by each type of fluctuation. Position noise produces a constant heating rate, regardless of the energy of the atom, while intensity noise has an exponential heating rate that heats atoms high in the well much faster than those low in the well. The combination of the two is able to

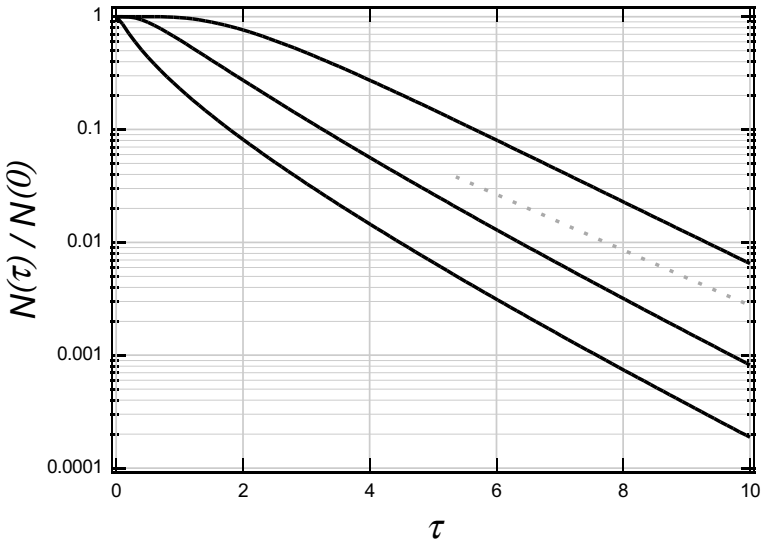

Figure 5.5: Position noise-induced atom loss as a function of time. The curves show how the number of trapped atoms decreases with (dimensionless) time as a result of intensity noise-induced heating. The top solid curve is an initial condition that starts low in the well, the middle solid curve is an initial condition that starts moderately high in the well, while the lower solid curve is an initial condition that starts high in the well. The dashed curve shows the decay rate associated with the lowest eigenmode. Note that while the three solid curves are becoming more parallel, they are not responding as fast as the decay curves for pure position noise heating. We would expect this slow, asymptotic approach to the limit based on the continuous eigenvalue spectrum.

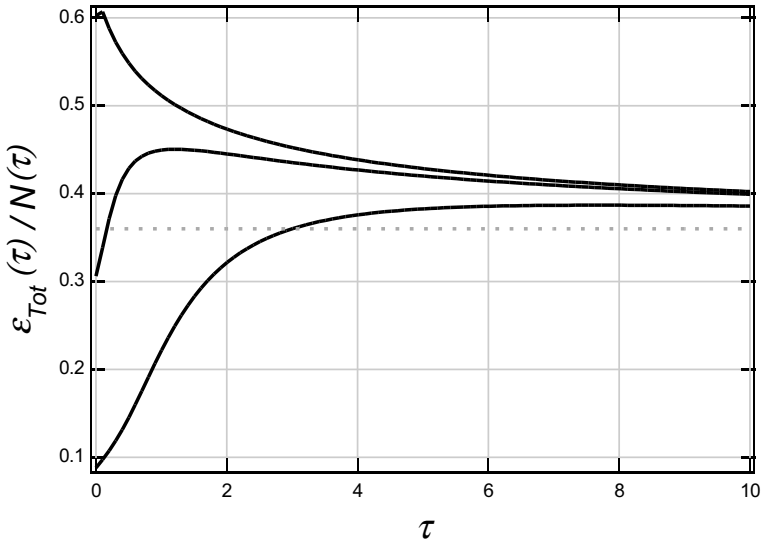

Figure 5.6: Intensity noise-induced energy evolution. The curves show how the mean energy of the trapped atoms evolves as a function of (dimensionless) time as a result of position noise-induced heating. The top solid curve is an initial condition that starts high in the well, the middle solid curve is an initial condition that starts moderately high in the well, while the lower solid curve is an initial condition that starts low in the well. The dashed curve shows the mean energy of the lowest eigenmode. Note that while the three solid curves are converging on one another and the limit, they show only an asymptotic behavior. This behavior is expected as a result of the continuous eigenvalue spectrum.

work synergistically. The position noise efficiently heats atoms low in the well, thereby moving them from a region where the exponential heating of intensity noise is ineffective into a region where the exponential heating is significantly faster than the constant heating provided by position noise. Thus, the combination of the two heating mechanisms avoids the drawbacks of both, and the atom loss rate is significantly enhanced. A plot of the number evolution for a variety of mixtures of position and intensity noise is shown in Figure 5.7. We present results for $\mathcal{X}_Q = 0.5$, 2.0, and 5.0.

Analysis of Results

In this section we have discovered a number of qualitative results about noise-induced evolution of trapped atoms in a harmonic well. First, we have shown that the loss rates can be significantly faster than the simple estimates we developed prior to a Fokker-Planck model. Second, we have shown that the loss rate for a process with position and intensity noise is greater than the sum of the two loss rates individually. Finally, we have discovered that the system evolves into the lowest eigenmode where the long-time behavior of the system combines continual atom loss with a non-varying mean energy (or temperature). *This is exactly the confusing behavior which was observed in early optical trapping experiments* [28]. Thus, our results lend credence to the argument that it was indeed noise-induced heating which limited the lifetime of optical traps.

5.5 Gaussian Confining Potential

The treatment in this chapter has been entirely within the context of a harmonic confining potential. In general, the potential in our experiment is much more closely

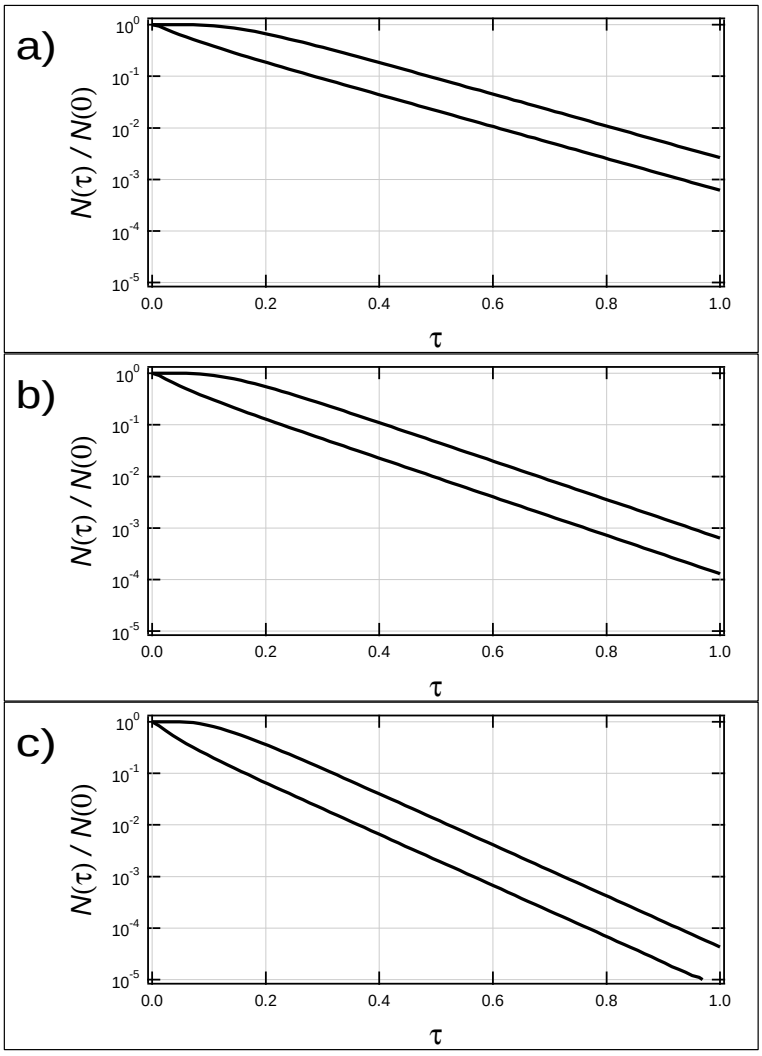

Figure 5.7: Position and intensity noise-induced atom loss. In each graph the top solid curve is an initial condition that starts low in the well while the lower solid curve is an initial condition that starts high in the well. Each graph shows the number loss for different mixtures of position and intensity noise, $\mathcal{X}_Q$. a) $\mathcal{X}_Q = 0.5$, b) $\mathcal{X}_Q = 2.0$, c) $\mathcal{X}_Q = 5.0$. The loss rates are significantly enhanced over position or intensity noise alone.

approximated as a Gaussian. We have developed a Fokker-Planck equation similar to the one presented here, but which describes noise-induced heating in a Gaussian well. However, as part of the derivation, we are forced to make the assumption that the fluctuation spectra are *white noise*, that is, constant:

$$S_x(\nu) = \alpha \tag{5.94}$$

$$S_I(\nu) = \beta. \tag{5.95}$$

Based on our measurements of several different lasers, we believe that the real fluctuation spectra are not approximately constant, and hence that the Gaussian model does not currently describe real-world systems.

In the future, we suspect it may be possible to derive a Gaussian well Fokker-Planck equation based on the assumption of *brown noise*, that is:

$$S_x(\nu) = \frac{\alpha}{\nu^2} \tag{5.96}$$

$$S_I(\nu) = \frac{\beta}{\nu^2}. \tag{5.97}$$

Such spectra are known to arise naturally in systems with multiple relaxation mechanisms. Further, our measurements show that the fluctuation spectra of several lasers does closely approximate brown noise. This is promising area for future theoretical work.

Finally, our experiments now produce temperatures so low that the potential well is, to a good approximation, harmonic. Thus we can use the models derived in this chapter with reasonable results.

Chapter 6

Experimental Setup and Procedure

. . . no one believes an hypothesis except its originator, but everyone believes an experiment except the experimenter.

—W.I.B. Beveridge

6.1 Overview

The key experimental result of this thesis is the successful preparation of a degenerate Fermi gas of ^{6}Li via all-optical means [20]. To provide the reader with a context for the remainder of the chapter, the first section provides a top-level overview of the experimental procedure. Since this effort has spanned several theses, we next summarize the major apparatus changes introduced for *this* thesis, before beginning the detailed discussions of the experimental subsystems and procedure that make up the remainder of this chapter.

6.2 Overview of the Experimental Procedure

While the experiment as a whole is quite complicated, the broad outlines of the procedure are quite simple. We initially prepare ^{6}Li atoms in a MOT at a temperature of approximately 140 μK (see Section 2.2). A small fraction ($\simeq$ 1-3%) of the

atoms in the MOT are transferred to a FORT created by a focused CO_2 laser beam (see Section 2.3). The transferred atoms exist in a roughly 50-50 mixture of the two lowest hyperfine ground states (see Section A.4). Although collisions between spin-polarized atoms are highly suppressed at low temperatures as a result of the Pauli exclusion principle, the presence of two distinct hyperfine states ensures that collisions are allowed (see Section A.7.3). For the two states we work with, the elastic scattering cross-section is zero at zero field (see Section A.7.3). A DC magnetic field is applied to the sample to "turn-on" elastic collisions between the two states. This initiates the evaporative cooling process (see Section 2.4).

After a short time, the gas has cooled to the point where collisional ejection of atoms from the trap is extremely unlikely. At this point, evaporative cooling stagnates (see Section 2.4). To proceed further, we adiabatically lower the intensity of the trap laser, reducing the trap depth and increasing the probability of collisional ejections. By lowering the trap in a controlled manner, we can maintain efficient evaporative cooling into the degenerate regime. Once we have finished the evaporative cooling process, we switch off the DC magnetic field and adiabatically raise the trap depth. This maintains the degeneracy parameter we achieved in the lowered well, and places the sample in a confining potential that is well characterized and invariant between experimental trials. To characterize the degenerate gas, we suddenly turn off the trapping potential. As the cloud expands, we illuminate it with a near-resonant probe beam, and record the absorption profile with a CCD camera (we will address this topic in Chapter 7). From this profile, we can extract all the important experimental information about the degenerate sample (we will address this topic in Chapter 8).

6.3 Major Apparatus Changes in this Thesis

The effort to produce a degenerate sample of ^{6}Li stretches back approximately five years and portions of the trapping apparatus are over seven years old. As such, significant portions of the apparatus and experimental methodology date from prior theses [21,29,30]. While a detailed description of the remainder of the experimental apparatus is provided later in the chapter, this section describes the major additions and changes to the apparatus during the progress of this thesis.

6.3.1 Commercial CO_2 Laser

In prior experiments in our group [21], the FORT was produced by a home-built, CO_2 laser with a maximum power of approximately 70 W. For this thesis, we installed a Coherent-DEOS LC-100NV commercial CO_2 laser with a maximum power of approximately 140 W. This RF-discharge laser is powered by an ultrastable Agilent 6573A DC power supply.

The original decision to construct a CO_2 laser was based on the necessity of having a trapping laser with very low intensity noise fluctuations. As discussed in Chapter 5, intensity fluctuations can lead to heating of the trapped atoms [26,27], and were most likely responsible for the short confinement times exhibited in early FORTs [28]. The Coherent-DEOS laser was originally developed for the *laser radar* (LIDAR) industry and exhibits extremely good intensity stability. We characterized the effect of intensity noise on a trap by the exponential heating rate, Γ which is a function of the trap fluctuations (5.11). In Figure 6.1, we plot $1/\Gamma$ as a function of trap frequency for the measured fluctuation spectrum of the DEOS laser. In Figure 6.2, we provide a high-resolution view of low frequencies. Note that for trap frequencies as high as 7 kHz, $1/\Gamma \gtrsim 10^4$ s. These values are large enough that

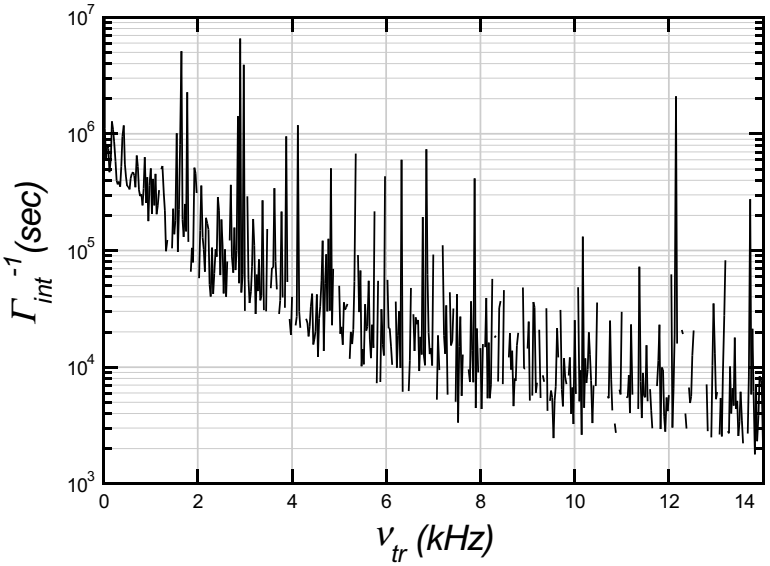

Figure 6.1: Noise-heating lifetime as a function of trap frequency (low-resolution).

we expect negligible noise-induced heating during the experiment.

The nearly twofold increase in laser power not only increases the number of atoms loaded into the FORT, but the deeper well makes the initial evaporative cooling more efficient as well (the increased difference between the well depth and the initial cloud temperature means that each ejected atom carries away proportionally more energy). This greater efficiency results in a larger number of atoms at the end of the evaporative cooling process, and hence an improved signal-to-noise ratio during imaging.

As an additional benefit, the commercial laser is substantially safer than the home-built laser for a number of reasons. First, the plasma in the commercial laser is produced by an RF-excitation of a sealed gas sample. This requires only a stable, 35 V DC power supply, and contact with the plasma is impossible. The home-built laser excited a flowing gas sample with an electric discharge. The discharge was energized by a 13 kV DC power supply. Further, the exhaust of the system

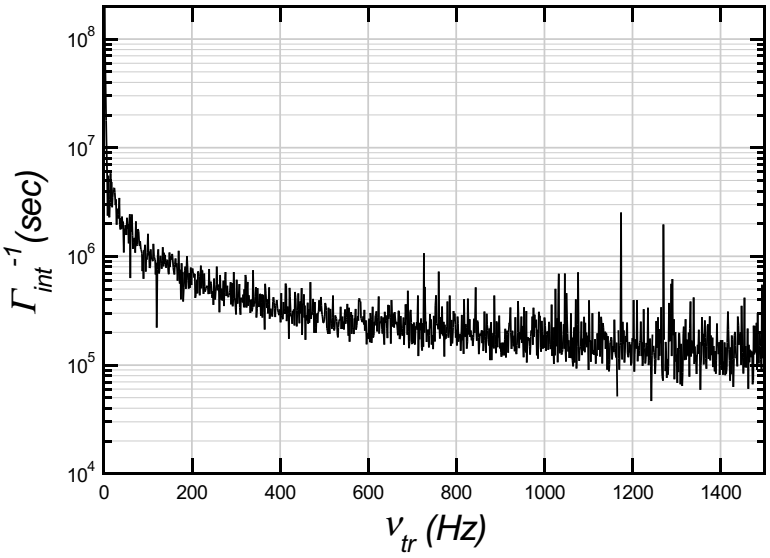

Figure 6.2: Noise-heating lifetime as a function of trap frequency (high-resolution).

required a connection to ground to avoid static build-up of dangerous voltages on the fittings. Second, the fact that the new laser is excited by RF means that the laser intensity can be pulse-modulated. The control panel for the laser has a knob that adjusts the duty-cycle of the pulse-modulation from 0% to 100%. Consequently, the *average* laser power can be varied anywhere from 1-140 W. Thus, during alignment procedures, we can work with low-power beams. This is in contrast to the home-built laser, which always produced 70 W.

Although the size, ellipticity, and curvature of the new beam are different, we simultaneously modified the beam-conditioning optics so that the size and location of the focus remain roughly the same as in our previous experiments. The net result is a potential well that is significantly deeper than our previous implementations.

6.3.2 CO_2 Laser Intensity Lowering System

As discussed in Chapter 2, we provide forced evaporative cooling by continuously lowering the intensity of the laser beam (see Section 2.4.2). While this, in itself, is not new, previous experiments by this group [52] used a simple exponential lowering curve as opposed to one of the shape (2.48)—which should provide superior evaporation. Unlike the exponential lowering curve, this new shape is not easily generated by analog electronics. To provide a means for lowering the laser intensity according to this curve, we developed a new method for controlling the output of the AO-modulator. The new system bypasses a large portion of the control electronics in the RF-supply portion of the IntraAction GE-4050 AO-driver. An external RF source (Agilent E4423B) is amplitude modulated by the desired lowering curve. This curve is produced by an Agilent 33250A digital arbitrary waveform generator. The amplitude modulated RF signal is injected into the input of the RF-amplifier in the AO, which then produces a laser intensity proportional to the lowering curve.

The switch to digital generation of the lowering curve gives us the ability to easily generate arbitrary intensity modulations. This has three important benefits. First, the same system can be used for parametric-resonance measurements of the trap oscillation frequencies (see Section 4.5.1). We merely replace the traditional lowering curve with a sinusoidal amplitude modulation. Second, we can rapidly switch between different lowering curves in a controlled fashion. This allows us to respond to variations in trap loading by adjusting the constants in the lowering curve. Finally, we can easily correct nonlinearities in the AO. By measuring the laser output as we modulate with a known function (*e.g.* a ramp), we can determine how the output of the AO varies from what we command. We can then generate a "correction function," which we digitally apply to a desired modulation function

before sending it to the waveform generator. This corrects for the nonlinearities in the AO.

6.3.3 Retroreflected Loader

Based on the analysis in [56], we expect dramatic enhancement of the number of atoms loaded into the FORT as the well depth is increased. While the new CO_2 laser provides a significant increase over the well depth we achieved with the home-built laser, we realized that a simple technique could further increase our well depth during FORT loading.

By retroreflecting the CO_2 laser during the loading phase, we can increase the intensity at the focus of the trap by a factor of approximately 1.5 over the single beam alone. By using a "rooftop"-mirror to reflect the beam, we can rotate the polarization by $\pi/2$. This has two important benefits. First, it avoids the formation of a standing wave in the trapping region (it does create a polarization-gradient [57], but the detuning of the FORT is so great that the interaction is purely scalar, so this has no effect on the atoms). Thus, we retain the simple potential well of a single-beam trap, despite doubling our well depth. Second, by giving the retroreflected beam an orthogonal polarization to the original beam, we can use a polarization analyzer near the output of the laser to reject the retro-reflected beam into a beam-dump, and thereby avoid feeding it back into the laser resonator where it might cause noise.

The beam from the CO_2 laser is focused into the trapping region by a lens just outside the vacuum system. After coming to a focus in the trapping region, the beam begins to diverge. In order to retroreflect the beam, we must first recollimate it. We do this with a lens just outside the exit window. The recollimated beam then

strikes the rooftop mirror, has its polarization rotated by $\pi/2$ and is retroreflected. It then strikes the recollimating lens, which now acts to focus the beam back into the trapping region. The input lens now acts as a recollimating lens, as the beam heads back towards the AO (see Figure 6.3 A).

However, we do not always wish to have the retroreflected beam present. One of the primary features of our system is the extreme stability of the trapping potential. Slight relative motions of the two beams can lead to significant modulation of the trapping potential—and consequently, heating of the atoms. Thus, we want the retroreflected beam to only be present during the loading phase of the experiment. We realized that the the beam shape just after the rooftop mirror is Fourier-transform-related [38] to the beam shape at the trap. Hence, the trap shape is primarily dominated by the *low-frequency spatial components* of the beam at the rooftop mirror. This property allows us to insert a deflecting mirror into the beam at the rooftop mirror without significantly disturbing the trapping potential (the only effect is a gradual reduction in well-depth to the single-beam value). To accomplish this, we developed a piece of equipment we call the "chopper", in honor of its guillotine-like motion.

A deflecting mirror is mounted to ball-bearing races which travel a vertical track. A pneumatic cylinder lifts the mirror during the loading phase, exposing the rooftop mirror to the laser and producing a retroreflected beam. After we initiate evaporative cooling in the trap, but before we begin lowering the laser intensity, the pneumatic supply is turned off, and the cylinder now acts as a dashpot as gravity pulls the deflecting mirror down. After several seconds, the mirror has traversed the entire beam, thoroughly blocking the rooftop mirror, deflecting the laser into a beam-dump, and extinguishing the retroreflected beam (see Figure 6.3 B). Because

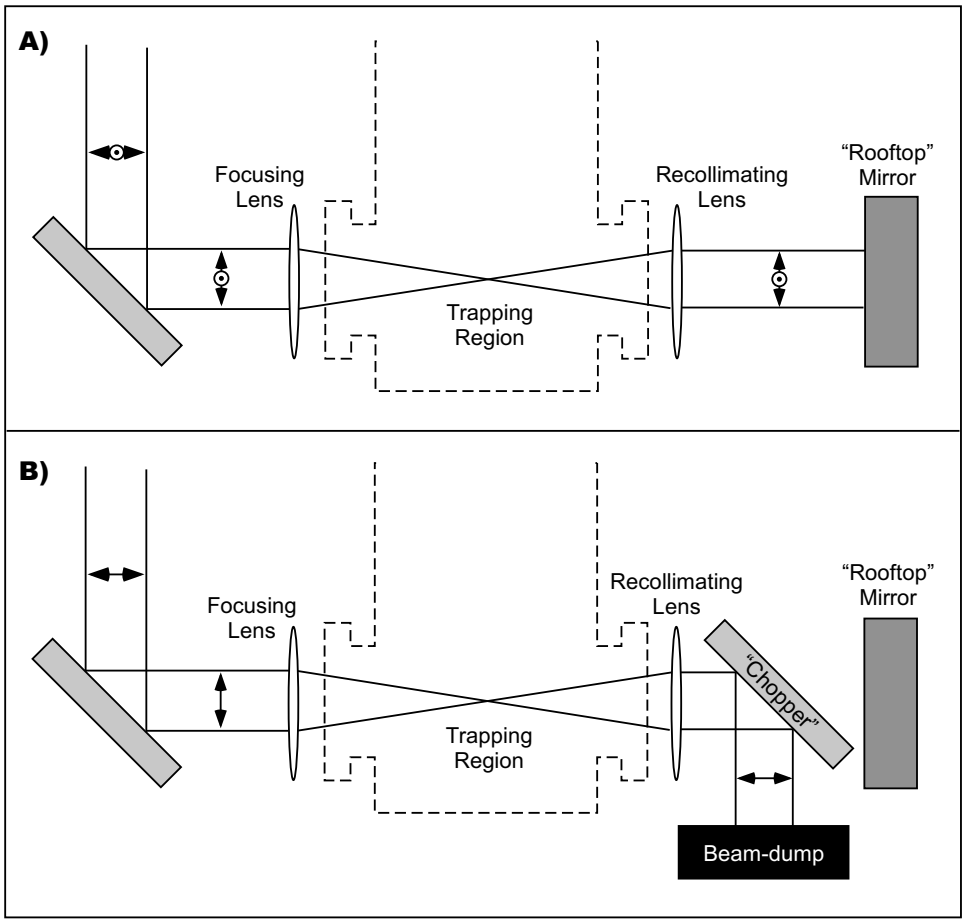

Figure 6.3: Operation of the retroreflected loader. In A), we see the system when the chopper is raised and the retroreflected beam is present. Note that all beams contain both horizontal (original) and vertical (retroreflected) polarization. In B) the chopper has been lowered into the beam path and deflects the beam to a beam dump.

evaporation is present, the atomic cloud simply cools as the well depth is slowly reduced by the chopper, finally stagnating in the single beam potential, and ready for the initiation of forced evaporation.

6.3.4 CCD Imaging System

In previous theses, we gathered information about the atomic clouds solely through resonance fluorescence [58]. A resonant (or near-resonant) beam excited the atoms and a *photomultiplier tube* (PMT) recorded the resulting fluorescence. This technique is works quite well at determining the *number* of trapped atoms, but any measurement of atomic spatial distributions requires complicated arrangements of resonant beams and reliance on multiple assumptions about the initial shape of the cloud. Since many of the effects we wished to study had direct connections to the shape of the cloud, we decided to implement an imaging system using a *charge-coupled device* (CCD). The imaging techniques uses a near-resonant beam to illuminate the atomic cloud. The atoms cast a shadow on the beam, and the result strikes the imaging sensor in the CCD camera. The physics of imaging are discussed in Chapter 7.

We use an Andor Technology slow-scan DV434-BV CCD camera. The camera has a 1024×1024 pixel sensor with a pixel size of 13 μm. The camera contains a *thermo-electric cooler* (TEC) that allows us to maintain the sensor at -40 °C. At this temperature, the *dark-current* (charge-buildup that is uncorrelated to the actual light striking the sensor) is reduced to well less than $1\,e^-/\text{pixel}\cdot\text{image}$. The read-out electronics operate slowly (approximately 1 s per image) to minimize electronic noise—yielding an RMS electron noise per pixel of less than 2. The sensor has a quantum efficiency of approximately 95%. The exposure time is effectively set by

the duration of the illuminating pulse. The imaging optics provide an approximate magnification of $M \simeq 4$.

The camera observes the cloud at an angle of 35 ° from the long axis of the cloud. This produces an apparent foreshortening of the cloud which must be accounted for in any analysis of the images.

6.3.5 Timing System

Previous experiments in our lab used daisy-chained Stanford Research Systems DG535 Digital Pulse Generators to provide the TTL control pulses to the various pieces of experimental equipment. Unfortunately, a single DG535 can produce a sequence containing at most 8 TTL edges. Worse, a single channel could be fired only *once* in the experimental sequence. Given the large number of edges we required and the high cost of DG535s, we were forced to use single pulse outputs to control multiple pieces of equipment. The consequence of this coupling was that changing the control sequence was a highly non-trivial exercise. Simply shifting the turn-on point of a single piece of equipment could take one or more days of work.

To avoid this problem in the future, we switched to an entirely computer-controlled timing system. A detailed discussion of this timing system is presented in the concurrent thesis by Stephen Granade [20]. The new system uses a National Instruments DIO6533 Digital Pattern Generator card to produce the desired TTL edges. This card has 32 independent TTL outputs which can be switched an arbitrary number of times in the experimental sequence. We developed a standard format for a *timing file*—a textual description of how we wished the 32 channels to be controlled. A software program (written by Stephen Granade) reads in this description, parses it into a gigantic matrix which describes the on/off state of each

channel at every time step in the experiment (The size of the timestep is user defined. We typically use $100\,\mu$s—meaning that for an experiment lasting 60 s, the matrix is $32\times(6\times10^5)$), and stores it in computer memory. The National Instruments card is then triggered, and it outputs the desired pulse sequence directly from memory.

The large number of channels, along with the ability to output arbitrary TTL signals on a single channel makes it possible to *independently* control every piece of experimental equipment. This makes creating new timing files simple—we need only describe exactly what we want the individual components to do. Further, storing the description of the timing in *software* (the timing file) rather than in *hardware* (the interconnections between DG535 pulse generators) means that changing experiments is now a matter of simply loading a new file. A timing file, once created, exists forever, waiting for the next time it is needed. Thus, in mere seconds, we can switch from one type of experiment to another.

6.4 Experimental Setup

This section provides a description of the remainder of the experimental setup. For additional descriptions of these components the reader is directed to the earlier thesis by Ken O'Hara [21] and a concurrent thesis by Stephen Granade [20].

6.4.1 Main Vacuum Chamber

The heart of any atomic cooling and trapping experiment is the vacuum chamber. In our experiment, the primary science chamber is a stainless-steel chamber custom build by MDC Vacuum Products. A drawing of the vacuum chamber is shown

in Figure 6.4. The chamber is roughly in the shape of an inverted "T." The primary observation cluster (and hence, the trapping region) is located at one end of the horizontal portion of the chamber. All of the ports are standard *ConFlat* (CF) knife-edge fittings with a copper gasket.

The chamber is maintained at *ultra-high vacuum* (UHV) levels ($P \leq 1\times10^{-11}$ Torr). The pumping is provided at ports V1 and V2. Port V1 is attached to a 300 liter/s ion-pump. An ion-pump creates a region of high electric field between a cathode and anode. Any atom that wanders into the high-field region is ionized and the resulting electron and positively charged ion are electrostatically drawn to the appropriate titanium electrodes, where their (substantial) speed embeds them in the material, effectively removing them from the chamber.

To achieve an even better vacuum than can be provided by the ion-pump, we have a *titanium-sublimation* (Ti-sub) pump attached to port V2. A Ti-sub pump consists of one or more large filaments of titanium. Driving a high-current (47 A) through the filament causes the a sputtering action that deposits a monolayer of titanium on all surfaces in direct line-of-sight with the filament. The current is then turned off after 7 minutes. Titanium is a *getter*—a highly-reactive element that bonds strongly to all but the most inert atomic species. Thus, with application of a titanium monolayer, we turn the interior walls of the vacuum chamber into a very effective "pump" with a pumping speed of many thousands of liters per second. Eventually the monolayer becomes saturated, requiring the reapplication of current to the filament and deposition of a new monolayer. Additionally, as noted above, titanium does not work well on inert atoms like the noble gases (most notably helium). Thus, a Ti-sub pump should always be used in conjunction with a species-independent pumping mechanism (such as an ion-pump).

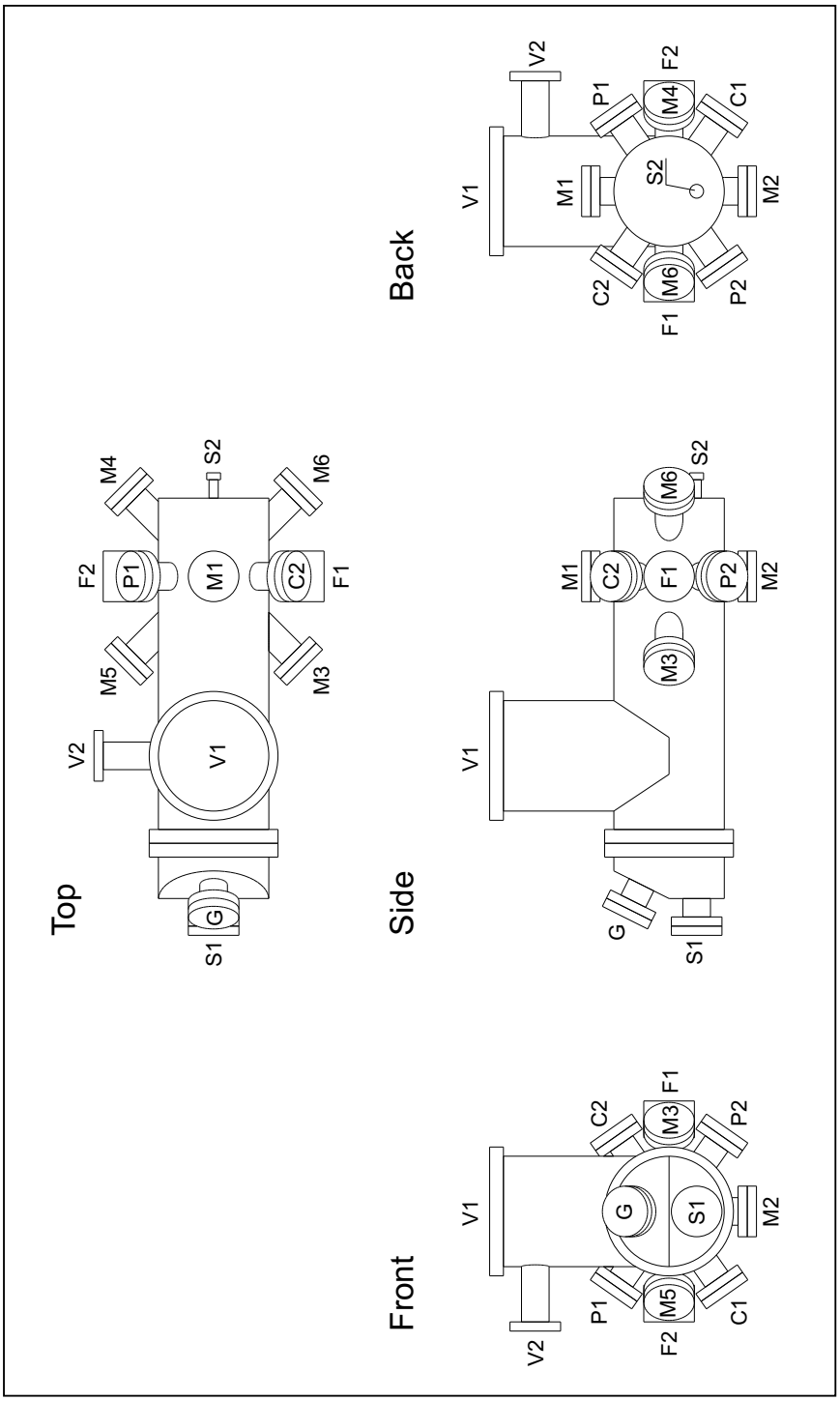

Figure 6.4: Main experimental vacuum chamber (not to scale). The port labels will be used throughout the text to describe the experimental setup.

There are two more ports that are not used for optical access to the trapping region. Port G contains an ionization vacuum gauge which we use to monitor the vacuum in the main chamber. Port S2 provides a physical connection to the atomic slower and the atomic source region beyond (described in Section 6.4.2 and Section 6.4.3, respectively).

Ports S1, M1–M6, C1, C2, P1, and P2 are capped with standard 2.75 in. CF windows that have been AR-coated for 671 nm light. They provide optical access to the trapping region for the slower beam, MOT beam, and the imaging and resonance-fluorescence probe beams. Ports F1 and F2 are used to inject the CO_2 laser into the trapping region and are capped with custom-built windows from Insulator Seal Corporation. These windows contain crystalline Zinc-Selenide (ZnSe) windows. Unlike glass, ZnSe transmits light at CO_2-laser wavelengths. A seal between the ZnSe and the metal is made on each side of the crystal, and the space between the two seals is pumped to approximately 1×10^{-9} Torr by a 10 liter/s ion pump. This is necessary because the technology for making a ZnSe-metal seal is not yet capable of maintaining the 1×10^{-11} Torr pressure differential required for our chamber. With two seals on each window, the required pressure differential can be maintained.

6.4.2 Atomic Slower

As stated previously, the main vacuum chamber is connected to the atomic slower via the small CF port S2. The atomic slower consists of a thin tubular vacuum chamber running down the axis of 10 independently-controllable magnetic coils. A near-resonant laser beam is injected into the main vacuum system at port S1. This beam leaves the chamber and enters the atomic slower at port S1. The beam slows the atoms coming from the atomic source with a physical process identical to that

used in optical molasses (see Section 2.2.2). Initially, the atoms have velocities consistent with the liquid-metal temperatures present in the atomic source ($\simeq$2 km/s). However, the interaction with the slowing beam produces accelerations on the order of 2×10^5 g's, rapidly slowing the atoms.

If we did nothing, the Doppler shift would quickly tune the atoms out of resonance with the slowing beam. The magnetic coils of the atomic slower provide a precisely tailored magnetic field that Zeeman tunes the atomic levels of the atoms, keeping them in resonance with the laser light as they are slowed. After traversing the length of the slower, the atoms have a velocity on the order of 30 m/s, which is within the capture velocity of the MOT. A detailed description of the physics and construction of the atomic slower can be found in [29].

The atomic slower provides an additional benefit beyond compressing the velocity distribution of the atoms. The slowing region acts as a *differential-pumping region* between the main vacuum chamber and the lower vacuum present in the atomic source. A pressure differential can only be maintained between two regions if the connection between them has a *conductance* that is low enough (analogous to how two regions in an electric circuit can be at different voltages only if their connection has a low enough conductivity). The long, narrow tube of the atomic slower has a very low conductance. This allows us to have a relatively high pressure in the atomic source region, without affecting the quality of the vacuum in the main experimental chamber.

6.4.3 Atomic Source Region

The atomic source region of the experiment is a stainless-steel vacuum chamber approximately in the form of a vertical tube (see Figure 6.5). Port S provides a

connection to the atomic slower (Section 6.4.2). The interior of the chamber is maintained at approximately 1×10^{-9} Torr by the presence of a 300 liter/s ion pump at port V1 and a Ti-sub pump at port V2. Port V3 is normally sealed with a CF blank. However, if the system has been up to atmosphere, a turbopump can be attached to port V3 and used to pump both the atomic source region and the main vacuum chamber down to a pressure where the ion pumps can be started. Once this has been accomplished, the gate valve can be closed, the turbopump removed, and the CF blank attached. The pressure in the atomic source region is monitored by an ionization pressure gauge attached at port G.

Also at the top of the chamber are connections to the ^{6}Li oven, an observation window (port O) and a solenoid-activated shutter for blocking the atomic beam.

The oven consists of a home-built stainless steel reservoir and collimating tube. The inside of the oven and collimating tube are lined with a fine stainless-steel mesh. As the oven is used, ^{6}Li atoms that do not successfully transverse the collimating tube are deposited on the mesh. When a suitable number have accumulated, the liquid ^{6}Li is wicked by the mesh back to the reservoir. In this way, the oven *recirculates* the unused ^{6}Li, dramatically lengthening the lifetime of the oven.

The oven and collimating tube are wrapped with 5 independent heating coils. The exit-velocity of the atoms is determined by the temperature of the oven at the point where the reservoir joins with the collimating tube (this point acts as a nozzle). This point is maintained at approximately 700 K (see Section A.2 for a discussion of the temperature dependence of the vapor pressure).

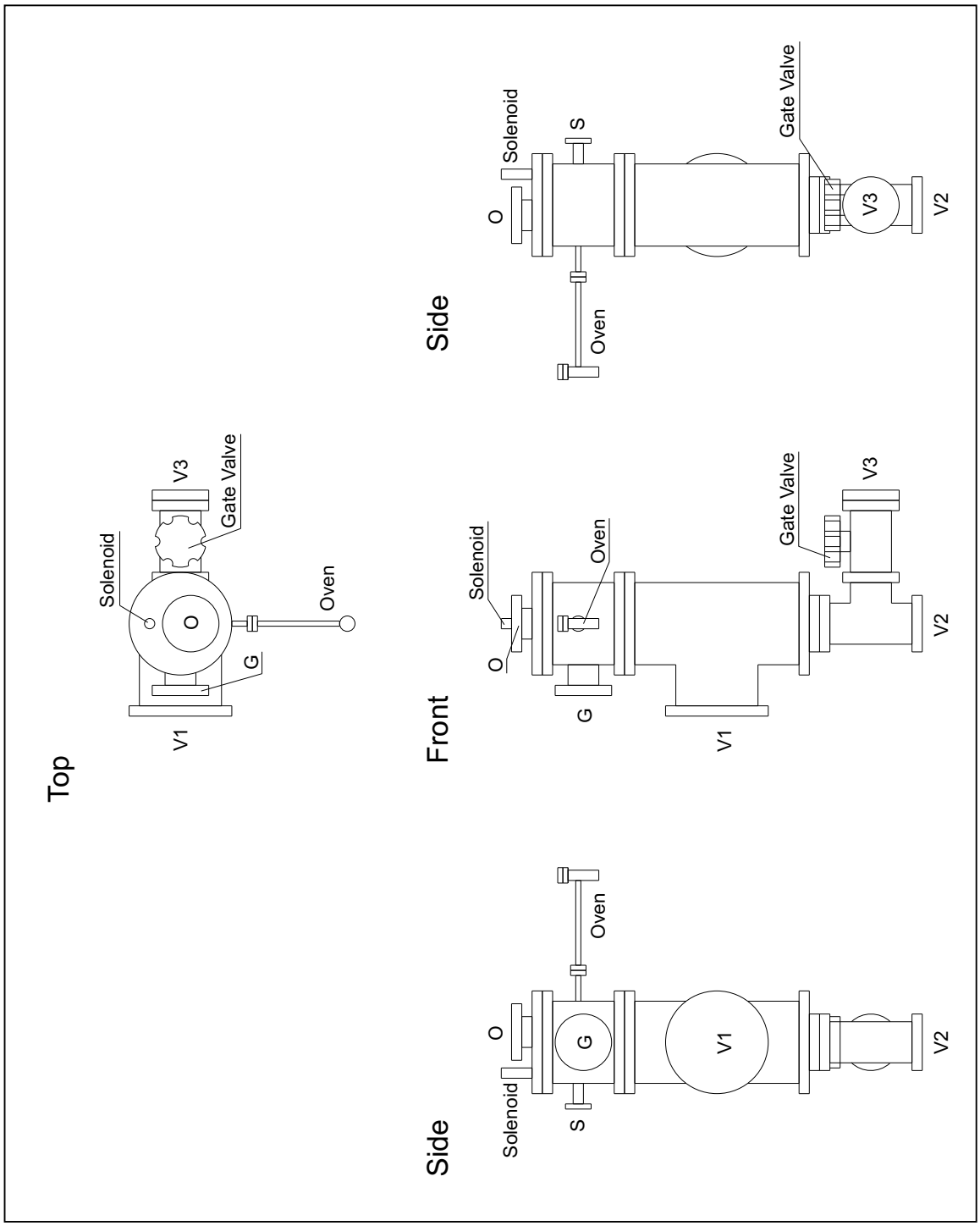

Figure 6.5: Atomic source region (not to scale). The port labels will be used throughout the text to describe the experimental setup.

6.4.4 Ring Dye Laser

The experiment relies on a large number of optical beams of approximately 671 nm wavelength. In our experiment, this light is generated by a Coherent 699-21 ring dye laser. The dye laser uses LD-688 dye in a 2-Phenoxyethanol solvent. The dye laser is pumped by a Coherent Innova 300 Argon-Ion laser (see Section 6.4.5). With fresh dye, the laser is capable of producing approximately 900 mW of 671 nm light in a TEM_{00} mode. The laser is locked to an internal reference cavity, which is in turn locked to a ^{6}Li fluorescence signal (see Section 6.4.6). The frequency stability of the dye laser has been measured to be approximately 2 MHz peak-to-peak.

6.4.5 Argon-Ion Laser

The pump laser in our experiment is a Coherent Innova 300 Argon-Ion laser. The Innova is capable of producing up to 12 W of power, but we typically pump the dye laser with 6-7 W (we start with 6 W on fresh dye and increase the pump power as the dye ages).

6.4.6 Locking System

The dye laser is locked to its internal reference cavity. However, to further stabilize the laser, we lock the reference cavity to an external fluorescence signal derived from the ^{6}Li D_2 line. A small portion of the laser output is deflected to the locking system. The locking beam is double-passed through an AO before being expanded and routed into a vacuum chamber containing a supersonic beam of ^{6}Li. The AO provides a DC upshift to the light frequency of approximately 200 MHz. In addition, there is a small modulation of the frequency about this point at a frequency of 11 kHz.

The locking beam strikes a supersonic atomic beam perpendicularly to minimize

any Doppler effect. The fluorescence of the atoms is collected by a fiber optic bundle and routed to a PMT. The PMT signal is then monitored by a Stanford Research Systems SR510 Lock-In Amplifier. The lock-in looks for fluctuations in the fluorescence occurring at the frequency of and in phase with the modulation introduced by the AO. The output of the lock-in is a linear error signal which is used as the feedback in a home-built servo system that drives the overall laser frequency. The result is that the laser constantly adjusts itself to maintain a fluorescence maximum in the locking region. Because of the +200 MHz DC shift applied by the AO, this means that the laser produces light approximately 200 MHz *below* the atomic resonance.

6.4.7 Beam Routing

The dye laser does not produce enough power to provide all of the optical beams needed by the experiment at all times. Since there is never an occasion where we simultaneously need the MOT beams and the probe/camera beams (the MOT fluorescence dominates), this provides a natural dividing point. When the MOT arm AO is energized, the system produces the MOT beams. However, when the MOT beams are not needed, the MOT AO is de-energized and the zeroth-order beam of the AO is caught by a small pick-off mirror and directed to the probe and camera section of the experiment. This is shown in Figure 6.6.

The details of this figure will be discussed in sections corresponding to the various portions of the apparatus.

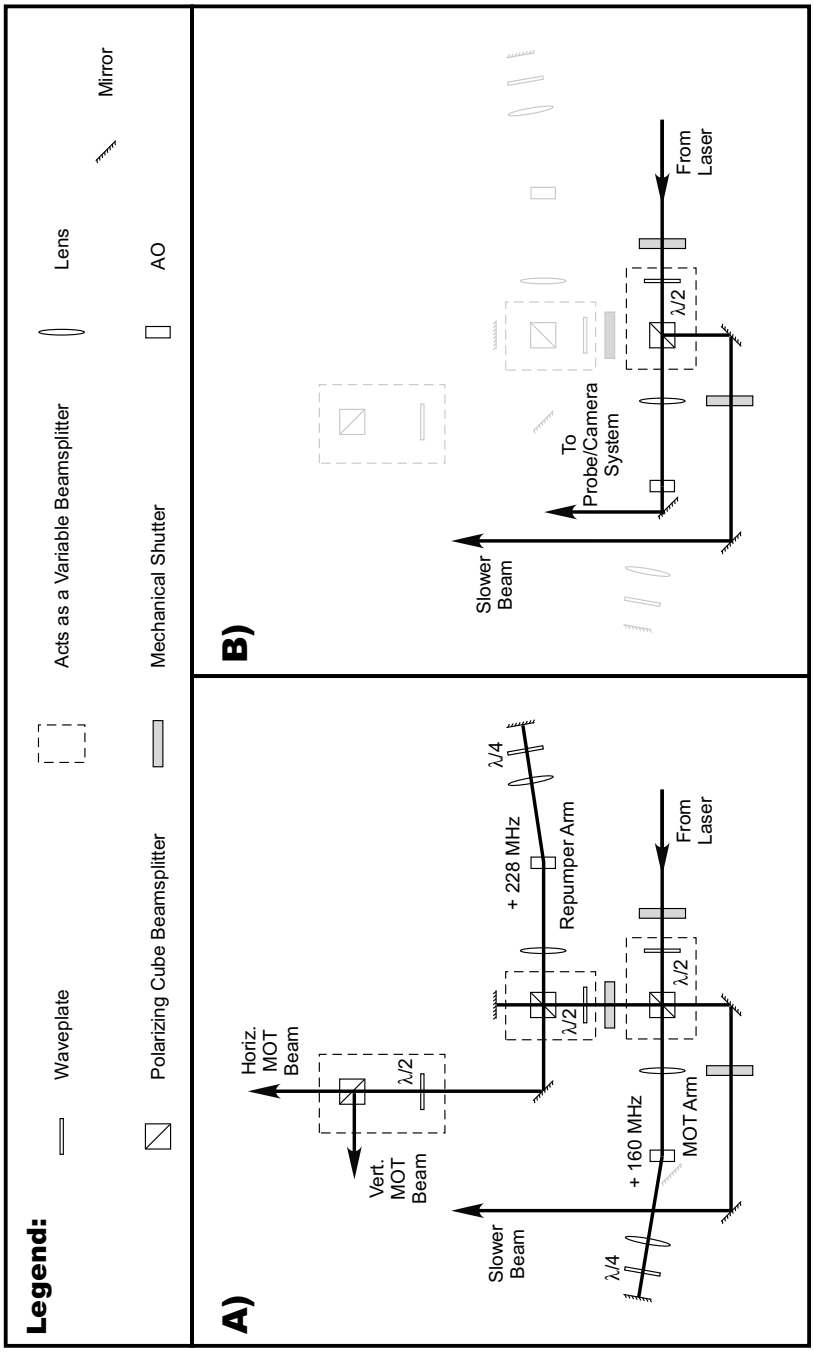

Figure 6.6: Beam routing between MOT beams and probe/camera beams. In A) the MOT AO is energized and the system is producing MOT beams. In B) the MOT AO is de-energized and the system sending power to the probe/camera system. In both cases, unused components are greyed out. In both, the frequency shifts given are those achieved after a double-pass of the AO.

6.4.8 Slower Beam

As shown in Figure 6.6, a portion of the laser power is deflected by a variable waveplate/beamsplitter combination to act as the slower beam. After leaving the portion of the system depicted in Figure 6.6, the slower passes through two lenses and a quarter-waveplate before entering the main experiment chamber through port S1 (see Figure 6.4). The beam exits the chamber through port S2, passes through the slower, and enters the atomic source region through port S (see Figure 6.5), before terminating at the back wall of the oven.

The two lenses mentioned above are set to provide a gently-focusing beam with a beam waist at the back of the oven. The quarter-wave plate converts the linearly-polarized beam into the required circular polarization (see Section 2.2.2). The power of the slower beam prior to entering the main chamber is approximately 100 mW.

6.4.9 MOT Beams

When the MOT beams are needed, the laser power that is not directed into the slower beam is used to create the bichromatic MOT beams (see Section 2.2.2). The light is first directed into the MOT *arm* (see Figure 6.6), where the light is double-passed through an AO to upshift the frequency by approximately 106 MHz. This produces a frequency that is roughly 6 linewidths to the red of the D_2 transition from the upper hyperfine groundstate (see Section A.4). A portion of the output of the MOT arm is then deflected by a variable waveplate/beamsplitter combination into the *repumper arm*. In the repumper arm, the light double-passed through another AO to upshift the frequency by another 228 MHz. This frequency component is then approximately 6 linewidths to the red of the D_2 transition from the lower hyperfine groundstate.

The two beams are combined on the same beamsplitter used to send power into the repumper arm. The now bichromatic beam is then split by another variable waveplate/beamsplitter combination to create the horizontal and vertical MOT beams (see Figure 6.6). Both beams then pass through beam expanders before being directed into the main experimental chamber. The vertical beam enters the chamber through port M1 and exits through port M2 (see Figure 6.4). The beam then encounters a quarter waveplate before striking a retroreflecting mirror. The horizontal beam enters the chamber through port M3, exits through port M4, re-enters through port M5, and exits again at port M6. It then passes through a quarter waveplate and strikes a retroreflecting mirror.

Creating both horizontal beam pairs from a single beam in this manner allows us to provide 50% of the total MOT power in each beam rather than the 33% which we would have available if each beam pair were independent. This increase in power results in a higher capture velocity for the MOT and a correspondingly larger number of atoms in the MOT. One drawback to the approach is that the long beampath for the horizontal beam results in significant attenuation of the beam power along the beam and a resulting imbalance between the forward and backward beams. If uncorrected, this imbalance produces a non-negligible shift in the location of the MOT center. To counteract this effect, the expanding telescope for the horizontal beam is adjusted to make the beam slowly focus. The decrease in size counteracts the decrease in power and serves to keep the intensity of the beam constant along its length.

6.4.10 Probe Beam / Camera Beam

The probe/camera beam section of the experiment also involves power sharing between the probe and camera beams. In this case, switching between the two setups requires manual intervention, and hence no experiment can use both the probe and camera beam as currently designed. The layout of this portion of the system is shown in Figure 6.7. The initial portion of the setup is identical regardless of the probe/camera choice.

The beam from the MOT arm passes into a double-passed AO arrangement that upshifts the frequency by approximately 200 MHz. This makes the frequency resonant with the D_2 transition from the $F = 3/2$ upper hyperfine groundstate (for this reason, we refer to this AO as the "3/2 arm"). A portion of the power is then deflected by a variable waveplate/beamsplitter combination into the "1/2 arm", where a further upshift of 228 MHz occurs. This generates a frequency that is resonant with the D_2 transition from the $F = 1/2$ hyperfine groundstate. The two beams are combined on another beamsplitter and coupled into a polarization-preserving optical fiber. This produces perfect overlap of the two beams.

At the exit of the fiber is a small, flip-up mirror which determines if the system produces a probe beam or a camera beam. The mirror is designed such that it can be flipped in and out of the beam without affecting its alignment. When the mirror is up, the beam coming out of the fiber strikes the mirror and is deflected. This beam, which is a probe beam, is then expanded and inserted into the main experimental chamber through port P1 (see Figure 6.4). The beam strikes the atomic cloud in the center of the trapping region, exits the vacuum chamber through port P2, where it is retroreflected back into the chamber. The retroreflection balances the light pressure on the atoms and allows for longer interrogation times than are possible

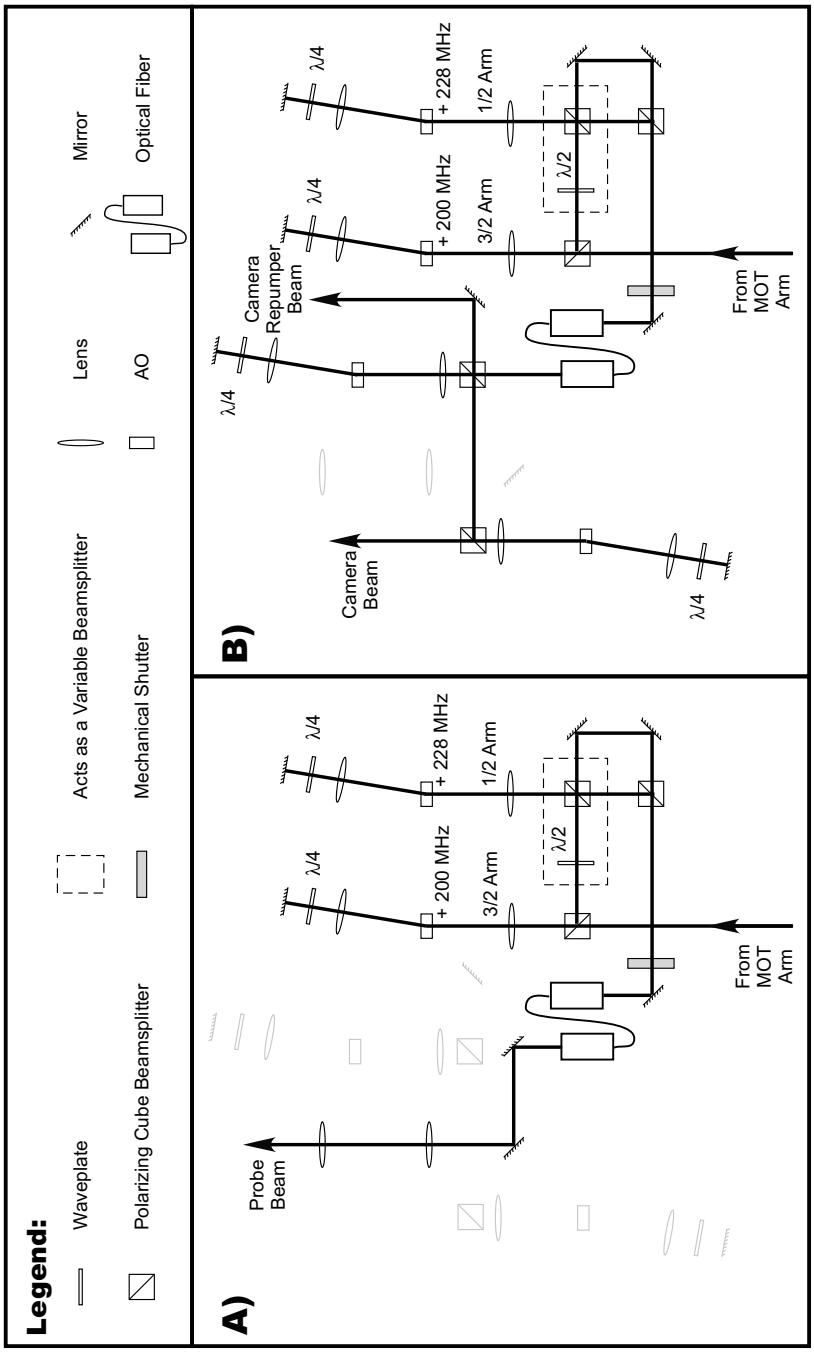

Figure 6.7: Beam routing between probe beam and camera beam. In A) the flip-up mirror after the fiber is up and the system is producing a probe beam. In B) the flip-up mirror after the fiber is down and the system is producing a camera beam. In both cases, unused components are greyed out.

with a single beam.

If the flip-up mirror is down, the beam strikes a polarizing beam splitter that extracts the frequency that is resonant with the D_2 transition of the $F = 3/2$ groundstate to create the camera repumper beam that is injected into the main vacuum chamber along the path used by the probe beam. The remaining polarization enters another double-pass AO which upshifts the light frequency. After exiting this AO arm, the beam enters another double-passed AO where the frequency is downshifted. The upshift and downshift applied to the beam are chosen so that their difference produces the desired detuning of the camera beam. This two-AO setup allows for easy detuning of the frequency above *or* below resonance—a feat which is impossible with a singe-AO setup. After exiting this AO arm the camera beam is expanded and inserted into the main chamber through port C1 (see Figure 6.4). The beam passes through the atomic cloud in the center of the trapping region and exits the system through port C2.

Another manual change is required in the detection apparatus depending on whether the system is configured for a probe beam or a camera beam. If we are using the probe beam, the fluorescence is collected by a lens placed just outside port C2. The fluorescence then strikes a small, removable mirror that directs the light into a fiber optic bundle which routes the light to a PMT. If we are using the camera beam, the small mirror is removed, and the lens on port C2 is part of the imaging system for the camera. The camera beam then propagates through the remainder of the imaging system and into the CCD camera. A schematic of these two situations is shown in Figure 6.8.

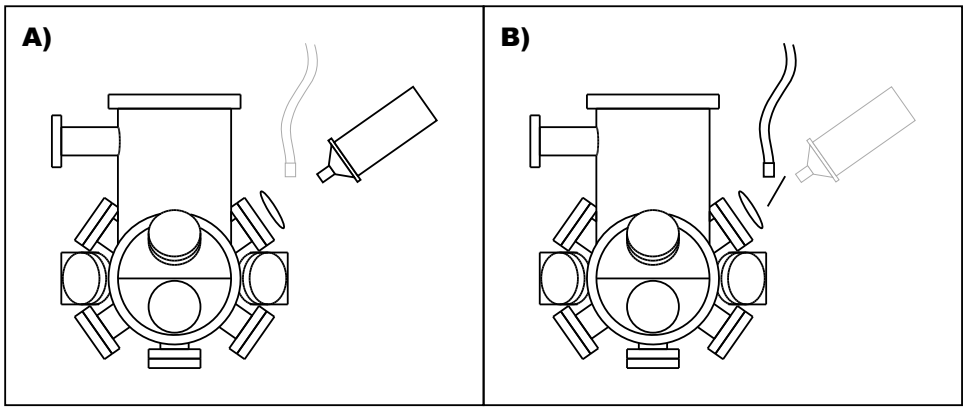

Figure 6.8: Detection of probe signal or camera image. In A) the removable mirror is out and the system passes the camera beam to the CCD camera. In B) the removable mirror is in place and the system directs the fluorescence signal into a fiber bundle for routing to a PMT. In both cases, unused components are greyed out.

6.4.11 MOT Gradient Coils

The magnetic field gradient required for the MOT is produced by a pair of home-built coils mounted around ports M1 and M2 of the main experimental chamber (see Figure 6.4). The coils are in an anti-Helmholtz configuration and are energized with a current of approximately 28 A. This current produces a magnetic field gradient of 30 G/cm at the center of the trapping region. The coilforms are water-cooled to dissipate the heat. Additionally, a radial slit has been cut in the coilforms prior to winding. This helps reduce the production of eddy currents when the coils are shut off and allows for a more rapid turn-off of the magnetic field.

6.4.12 Multiplexer

At certain times during the experiment, we will need to change the tuning or intensity of some of the optical beams. This can be accomplished by adjusting DC voltage levels applied to the input ports of the AOs. However, our timing system

produces TTL edges, not arbitrary DC voltages. To allow the timing system to control these devices, we constructed an electronic device we call the "multiplexer." The multiplexer consists of a number of analog switches and voltage supplies. The analog switches either have 2 or 4 inputs. The 2-input version has a single TTL-logic input and a single analog output. By setting two of the voltage sources to the desired levels and connecting them to the two analog inputs, we can switch between the two voltages on the output by switching the logic input between TTL-low and TTL-high. The 4-input version takes two TTL logic inputs, but otherwise works in a similar fashion. Thus, switching between multiple states of the optical system is simply a matter of having the timing system apply the appropriate TTL logic to the logic inputs of the multiplexer.

6.4.13 Chiller

Both the Coherent/DEOS CO_2 laser and the IntraAction AO require water cooling. We have installed a NesLab Merlin M75 chiller. The chiller operates a closed-loop cooling system that provides 15 °C coolant to both the laser and the AO. The coolant is primarily distilled water, with a slight amount of DowFrost additive to prevent freezing (should we run the chiller at below 0 °C) and to suppress algae growth.

6.4.14 CO_2 Beam Conditioning

The beam that emerges from the CO_2 laser interacts with a number of optics on the way to the main experimental chamber. A schematic is shown in Figure 6.9.

The beam leaves the CO_2 laser and enters an IntraAction Corp AGM-4010BG1 AO driven by a modified IntraAction GE-4050 driver. Even when the AO is fully

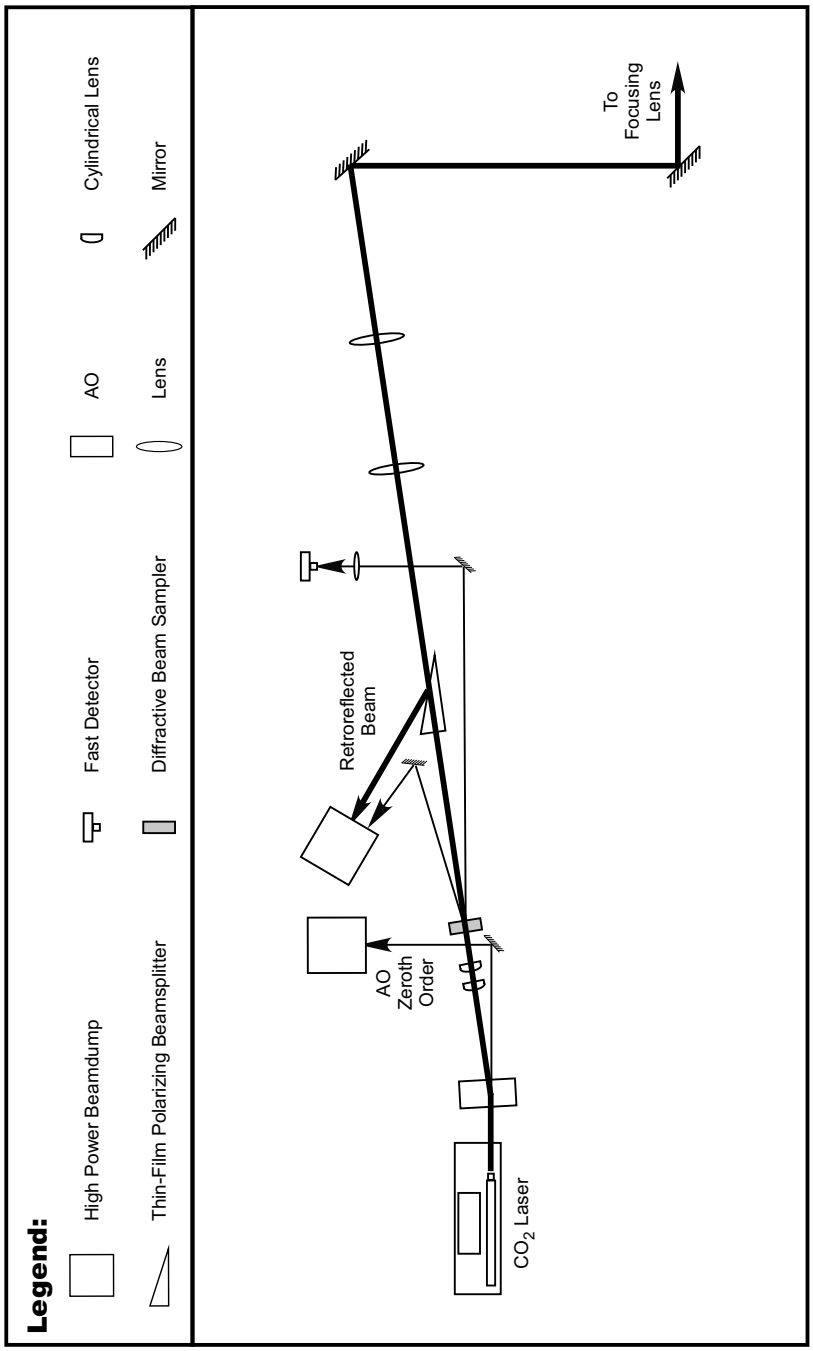

Figure 6.9: CO_2 laser beam conditioning optics.

energized, the zeroth-order beam contains significant power. When we lower the trap depth by lowering the laser power with the AO, the zeroth-order beam reaches power levels in excess of 100 W. For this reason, we are careful to deflect the zeroth-order beam into a water-cooled beam dump.

As the CO_2 laser beam passes through the germanium crystal in the AO, it deposits a non-negligible amount of power. The interaction between this heat source and the water cooling of the crystal creates a temperature gradient in the germanium. This thermal gradient produces a gradient in the index of refraction, making the germanium act as a lens, through a process known as *thermal lensing*. Because the gradient exists primarily in the vertical direction (the cooling for the crystal occurs at the top and bottom surfaces), the beam emerges from the AO with different wavefront radii-of-curvature in the horizontal and vertical directions. If we were to allow the beam to propagate in this condition to the vacuum chamber, the result would be that the final focusing lens would create horizontal and vertical foci that do not overlap. The result would be a non-harmonic potential in the axial direction, and a relative loosening of the atomic confinement. To counteract this effect, the beam strikes a telescope made from cylindrical lenses acting in the vertical direction immediately after the AO. We adjust the telescope so that the horizontal and vertical wavefront radii-of-curvatures are equal.

The CO_2 laser beam next strikes a diffractive beam sampler. This optic has a microscopic pattern etched on it that creates two beams that diffract away from the main beam and each contain approximately 1% of the total beam power. We deflect one of these into a water-cooled beam dump, and route the other to a Boston Electronics diode-detector. We use the detector to make quantitative measurements of the relative CO_2 laser power being provided to the trapping region.

The main CO_2 laser beam then passes through a thin-film polarizer (oriented to pass the beam in its current polarization). When the retroreflected loader is in use (see Section 6.3.3, the retroreflected beam returns with a polarization that has been rotated by 90°. This beam is reflected off of the thin-film polarizer and into a water-cooled beam dump.

After the thin-film polarizer, the beam enters the expanding telescope. This telescope consists of two ZnSe aspherical lenses with focal lengths of 1.25 in. and 11.5 in., respectively. The beam is expanded by a factor of $11.5/1.25 = 9.2$. We perform this expansion because the focal size created by the final focusing lens is inversely proportional to the size of the beam entering the focusing lens [38]. By expanding the beam to this size, we can achieve beam sizes in the trapping region on the order of 50 μm ($1/e^2$ intensity radius).

After being expanded by the telescope, the beam is routed by two mirrors (included to give us control over the beam position and orientation) to the final focusing lens for insertion into the main experimental chamber.

6.4.15 CO_2 Focusing Optics

Both the final focusing lens and the recollimating/refocusing lens for the retroreflected loader (see Section 6.3.3) are ZnSe aspheres with 19 cm focal lengths. The input lens is mounted on two translation stages that have been combined to create an xy-stage. The stages are controlled by standard micrometers (since the goal is simply to hit the center of the MOT). The recollimating/refocusing lens is mounted on an ultra-high resolution xyz-stage with micron resolution (here we have to place the retroreflected focus on top of the first focus—an object approximately 50 μm across). The xyz-stage is mounted on an axially-oriented conventional translation

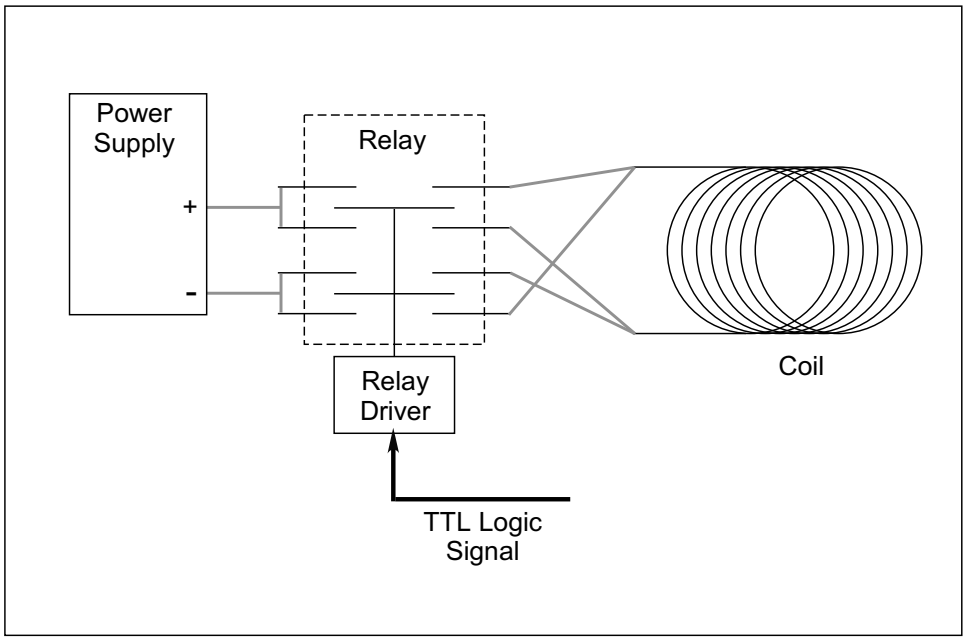

Figure 6.10: Electromechanical relay for flipping coil orientation.

stage since the axial-length scale of the trap exceeds the full travel of the xyz-stage.

6.4.16 Uniform Magnetic Field

The uniform magnetic field needed for evaporative cooling is provided by the same coils that produce the MOT magnetic field gradient (see Section 6.4.11). We placed an electromechanical relay in the current path for the top coil. A TTL logic signal from the timing system can switch the relay, changing the electrical orientation of the coil, and hence whether the coils are in the anti-Helmholtz or Helmholtz configuration. A schematic of this is shown in Figure 6.10.

During evaporation, 23 A are supplied to each coil, producing a field strength at the trap of approximately 130 G. This results in an s-wave scattering length (see Section A.7.3) of approximately -100 a_0.

6.5 Experimental Procedure

This section provides a detailed description of the experimental procedure first outlined in Section 6.2. The subsections below address the individual phases of the experiment.

6.5.1 MOT Loading

The MOT loading phase lasts 10 s and is initiated by turning on the MOT beams (tuned approximately six linewidths below the D_2 resonance), the slower beam (tuned approximately 200 MHz below the D_2 resonance), and the MOT gradient magnets. After approximately 5 s, the MOT population saturates at $\simeq 1 - 3 \times 10^8$ atoms.

6.5.2 FORT Loading and Optical Pumping

The FORT potential is essentially conservative (see Section 2.3.2). As a result, it is capable of capturing only those atoms that lie in its (relatively small) capture volume in phase space. By taking advantage of the dissipative effect of optical molasses (see Section 2.2.2), we can modify the atomic phase-space trajectories so that a significant number of atoms overlap the FORT capture volume. This is the purpose of the FORT loading phase.

The detunings used in the MOT loading phase are chosen to optimize the MOT capture volume, and hence to maximize the number of atoms in the MOT. The dissipative effect of Doppler cooling, however, is not maximized at our chosen detunings. From Figure 2.1, we see that the greatest dissipation occurs at detunings of one half-linewidth below resonance.

Immediately after the 10 s of MOT loading, we signal the multiplexer to suddenly switch the detuning of the MOT and repumper frequencies from six linewidths below resonance to one half-linewidth below resonance. Simultaneously, the intensity of the beams is lowered. This creates a highly dissipative optical molasses and transfers many atoms into the FORT potential. This phase lasts 20 ms.

At this point, the atoms in the FORT are in a mixture of the upper and lower hyperfine groundstates. For the remainder of the experiment, we wish to work solely with the lower hyperfine groundstates. We use an *optical pumping* phase to convert the upper hyperfine groundstate atoms to the lower hyperfine groundstates. For 100 μs, the MOT frequency is placed precisely on resonance, and its intensity lowered even further. Meanwhile the repumper frequency is extinguished completely (remember, its purpose was to keep the lower hyperfine groundstates empty). Any atoms that decay from the excited state to the lower hyperfine groundstates are no longer effected by the light, while those that return to the upper hyperfine groundstates are continually cycled until they *do* decay to the lower hyperfine groundstates.

At this point the FORT contains ^{6}Li atoms in the lower hyperfine groundstates at a temperature of approximately 140 μK. Since all further work will involve the CO_2 laser, we extinguish all optical beams and turn off the MOT gradient magnets.

6.5.3 Free Evaporation and Elimination of the Retroreflected Beam

We next reverse the electrical orientation of the top MOT gradient magnet using the relay described in Section 6.4.16. Energizing the coils with 23 A produces a -100 a_0 scattering length, which begins the evaporation process (see Section 2.4.2).

The phase we call "free evaporation" lasts 6 s. For the first 4 s, we allow the

atoms to evaporate from the doubled well (the retroreflected beam is present). After this time, we send a TTL signal to the chopper (see Section 6.3.3), turning off the pneumatic supply and causing the deflecting mirror to begin occluding the retroreflector. The transition from a doubled well to the single well take approximately one second, during which time the well depth is smoothly lowered, maintaining the evaporation process. After the mechanical motion is complete, there is approximately one second of further free evaporation to fully stagnate the system in the single well.

6.5.4 Forced Evaporation

After free evaporation, the atoms are at approximately $50\,\mu$K, or $\simeq 1/14$ of the well depth. Evaporation is highly suppressed. We then initiate the lowering of the CO_2 laser intensity using the lowering system described in Section 6.3.2 and the lowering curve derived in Section 2.4.2:

$$U(t) = U_0 \left(\frac{1}{1 + t/3} \right)^{1.446} . \tag{6.1}$$

Here we use a time constant $\tau = 3\,$s that is larger than the time constant $\tau = 0.9\,$s that we would calculate based on the ideas of Section 2.4.2. We chose to slow the lowering slightly because we observe a variation in the beam profile as we lower the CO_2 laser intensity (this problem has been resolved in experiments performed after the experiment described in this thesis). Because the change in profile was likely to lower the collision rate, we felt it judicious to be conservative with the lowering curve.

Since we wish to understand how the evaporation process drives the system

towards degeneracy, we repeat the experiment many times using values for t in (6.1) in the range $t = 0 - 60\,\mathrm{s}$.

6.5.5 Adiabatic Recompression

Once the forced evaporation has been performed, we turn off the uniform magnetic field and adiabatically recompress the trap by raising the CO_2 laser intensity. We use a raising profile where the intensity grows exponentially to full value over 5 s.

6.5.6 Ballistic Expansion and Imaging

At this point in the procedure, we have produced the sample we wish to study. We suddenly extinguish the CO_2 laser and allow that atoms to ballistically expand for $400\,\mu$s. After this expansion time, we illuminate the cloud with a $10\,\mu$s pulse from the camera beam. The absorption profile of the cloud is captured by the CCD (the concepts and physics of imaging the atoms are discussed in Chapter 7). This absorption profile is the data that results from a single run of the experiment. In Chapter 8, we will discuss the analysis of these images to determine the number, temperature, and degeneracy state of the atomic cloud.

6.5.7 Apparatus Reset

The timing system then automatically begins another trial. The CO_2 laser, MOT, repumper, and slower beams are all turned back on in their "MOT loading" states; the orientation of the top coil is flipped and the MOT gradient magnets are energized; and the chopper is raised to reveal the rooftop mirror.

Chapter 7

Imaging of Trapped Atomic Clouds

. . . for behold whenever
The sun's light and the rays, let in, pour down
Across dark halls of houses: thou wilt see
The many mites in many a manner mixed
Amid a void in the very light of the rays,
And battling on, as in eternal strife,
And in battalions contending without halt,
In meetings, partings, harried up and down.
From this thou mayest conjecture of what sort
The ceaseless tossing of primordial seeds
Amid the mightier void. . . .

—Lucretius (c. 50 BCE)

7.1 Overview

In atomic cooling and trapping experiments, creating and manipulating the sample is only part of the required effort. Some means must be used to extract information from the cloud. In many experiments it has become commonplace to use a form of optical imaging.

In an imaging approach, a laser field (resonant or off-resonant) is passed through the cloud and the incident beam and the scattered radiation field are combined on an ultra-sensitive charge-coupled-device (CCD) [46]. The CCD converts the photon

distribution into an electron distribution which is read out by computer-controlled electronics. The resulting computer file can then be processed to yield information about the atomic cloud.

The physics involved in imaging separates quite naturally into two topics: first, the effect that the atomic cloud has on the incident beam (spatially-dependent attenuation and phase-shift of the incident electric field); and second, the propagation of the post-cloud electric field through the imaging system to the CCD where the intensity of the laser field is measured. This chapter address these two topics in detail.

Additionally, once we have expressions for the intensity at the CCD for the different techniques, we can apply a simple signal-to-noise-ratio analysis to determine the situations where the use of a particular technique is advantageous.

7.2 Introduction to the Imaging Techniques

There are three main imaging techniques in use today [46]: *absorption* imaging, *dark-spot* (or dark-ground) imaging, and *phase-contrast* imaging. All three are variations on the general theme outlined above.

In absorption imaging, the probe beam strikes the cloud and the incident beam and the scattered field propagate through the imaging system to the CCD. A schematic of this process is shown in Figure 7.1. A phase-shift between the scattered and incident fields leads to destructive interference at the CCD, where the cloud appears as a dim spot in an otherwise bright background.

In dark-spot imaging, the scattered field propagates to the CCD as in absorption imaging. The incident field however, is intercepted by a small absorber placed in the Fourier plane of the imaging lens. Since the incident field is spatially broad

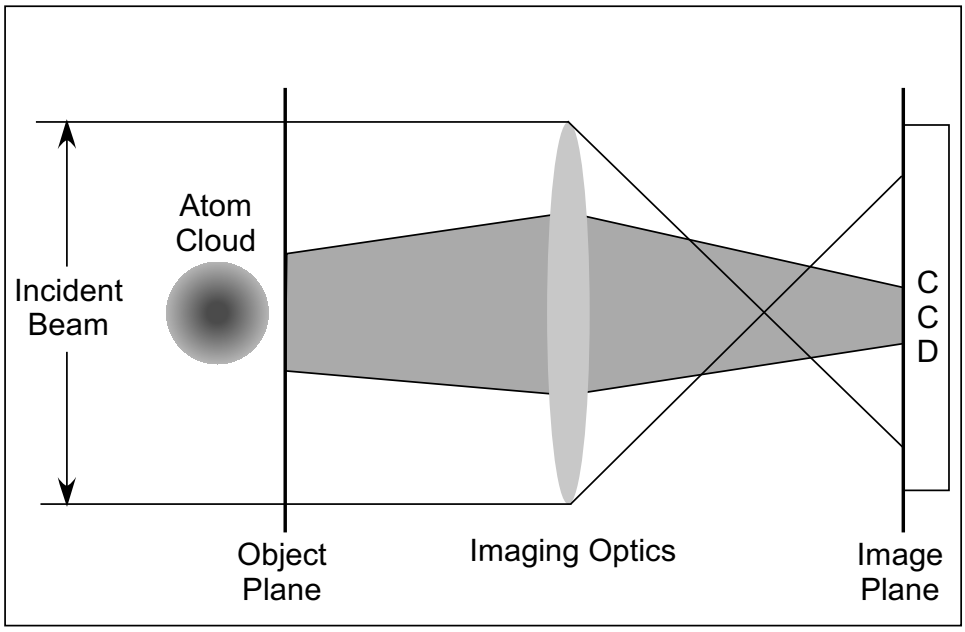

Figure 7.1: Experimental setup for absorption imaging. The beam in white represents the non-scattered field, while the grey beam represents the scattered field.

and collimated, it focuses tightly in the Fourier plane. The scattered field, being uncollimated, is large in the Fourier plane, and is not materially affected by the absorber. A schematic of this technique is shown in Figure 7.2. As a result, only the scattered field reaches the CCD, where the cloud appears as a bright spot on an otherwise zero background.

Phase-contrast imaging has much in common with dark-spot imaging. In place of the small absorber in the Fourier plane, phase-contrast imaging uses a small phase-plate which advances or retards the incident field by $\lambda/4$. A schematic of phase-contrast imaging is shown in Figure 7.3. The result is either constructive or destructive interference (depending on whether the plate advances or retards the phase) between the incident and scattered fields. At the CCD, the cloud appears as either a bright or dim spot on an overall bright background.

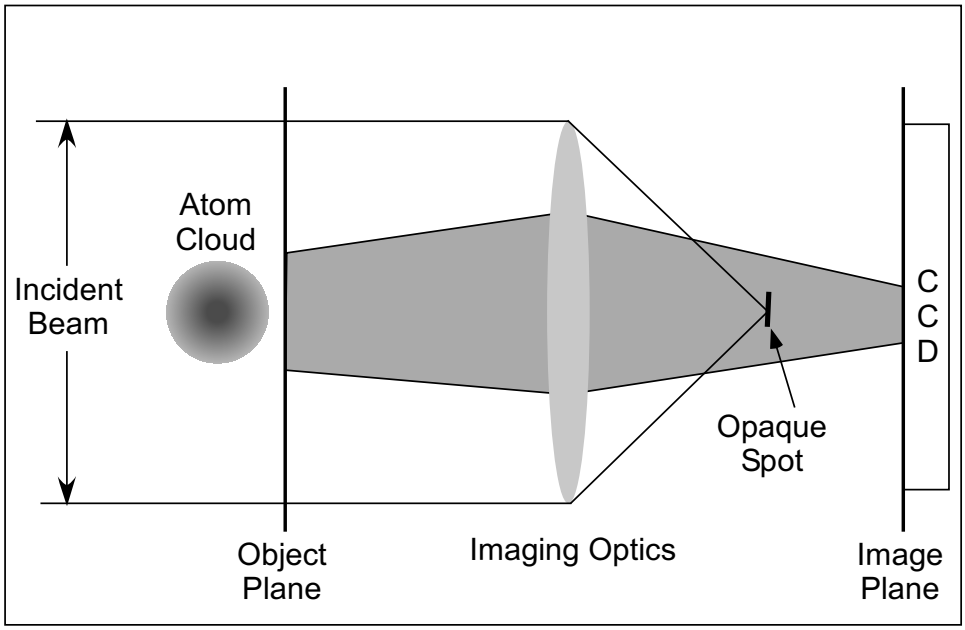

Figure 7.2: Experimental setup for dark-spot imaging. The beam in white represents the non-scattered field, while the grey beam represents the scattered field.

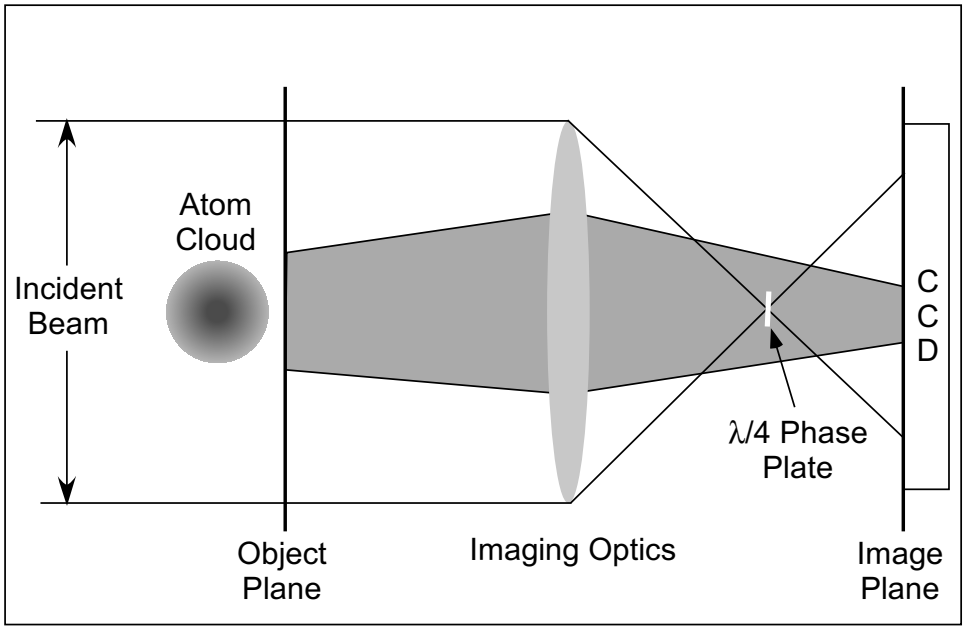

Figure 7.3: Experimental setup for phase-contrast imaging. The beam in white represents the non-scattered field, while the grey beam represents the scattered field.

7.3 Effect of the Cloud on the Electric Field

As the incident probe beam passes through the atomic cloud, the electric field is modified by the atoms, imprinting information about the cloud on the field. In order to extract this information later, we must understand this process.

Let the incident field-strength be given by $\mathcal{E}_{\text{incident}}(x, y)$. We wish to compute the electric field in the object plane of the imaging system, $\mathcal{E}_{\text{object}}(x, y)$. This plane is located immediately past the atomic cloud, at a distance negligible compared to the distance to the imaging lens.

For a field passing through a medium with susceptibility $\mathcal{X}$, we can write the following differential equation [59]:

$$\frac{\partial \mathcal{E}(x, y, z)}{\partial z} = 2\pi i k \, \mathcal{X}(x, y, z, \delta) \, \mathcal{E}(x, y, z). \tag{7.1}$$

In the above, k is the propagation wavenumber, z is the direction of propagation, and δ is the detuning of the probe field from the atomic transition frequency, given in units of half-linewidths.

The susceptibility can be expressed as:

$$\mathcal{X}(x, y, z, \delta) = \left(\frac{i \, \mu^2 \, n(x, y, z)}{\hbar(\Gamma/2)} \right) \left(\frac{1 + i\delta}{1 + \delta^2} \right), \tag{7.2}$$

where μ is the transition matrix element for the atomic transition we are exciting, n is the atomic number density, and Γ is the linewidth (FWHM) of the atomic transition. We can substitute this result into (7.1) to obtain

$$\frac{\partial \mathcal{E}(x, y, z)}{\partial z} = -2\pi k \, \left(\frac{i \, \mu^2 \, n(x, y, z)}{\hbar(\Gamma/2)} \right) \left(\frac{1 + i\delta}{1 + \delta^2} \right) \, \mathcal{E}(x, y, z). \tag{7.3}$$

We also make use of the expression for an optical cross-section [60]:

$$\sigma = \frac{4\pi k \mu^2}{\hbar(\Gamma/2)}. \tag{7.4}$$

Inserting (7.4) into (7.3) yields the simplified differential equation

$$\frac{\partial \mathcal{E}(x,y,z)}{\partial z} = -\left(\frac{n(x,y,z)\,\sigma}{2}\right)\left(\frac{1+i\delta}{1+\delta^2}\right)\,\mathcal{E}(x,y,z). \tag{7.5}$$

The solution to (7.5) is

$$\mathcal{E}(x,y,z) = \mathcal{E}(x,y,z=0)\,\exp\left[-\left(\frac{\sigma}{2}\right)\left(\frac{1+i\delta}{1+\delta^2}\right)\int_{-\infty}^{z} dz_1\, n(x,y,z_1)\right]. \tag{7.6}$$

The integral in (7.6) is so important it has a name, the *column density* [46]. We define a new symbol for the column density

$$\tilde{n}(x,y) = \int_{-\infty}^{\infty} dz_1\, n(x,y,z_1), \tag{7.7}$$

where we have formally extended the upper limit to ∞ by considering only values of z that lie outside the cloud. In this manner we maintain the value of the integral despite the change in limit. Using this symbol in (7.6) and taking the initial electric field to be $\mathcal{E}_{\text{incident}}$ and the resulting field to be $\mathcal{E}_{\text{object}}$ gives the final result

$$\mathcal{E}_{\text{object}}(x,y) = \mathcal{E}_{\text{incident}}(x,y)\,\exp\left[\left(\frac{-\tilde{n}(x,y)\sigma}{2}\right)\left(\frac{1+i\delta}{1+\delta^2}\right)\right]. \tag{7.8}$$

Note that the column density is the only cloud-specific parameter in our final result. This is what we will eventually extract after processing the CCD images. Not surprisingly, as a result of the projective nature of our measurement technique,

we lose all z-information about the cloud.

7.4 Computing the Intensity at the CCD

We now know the electric field strength in the object plane immediately after the atomic cloud. This section describes how this field is propagated through an imaging system of unity magnification to the image plane at the CCD. For this analysis we will use scalar diffraction theory as described by paraxial Fourier optics.

In performing this analysis, it will be useful to independently treat the scattered field and the incident field. Two of the techniques (dark-spot and phase-contrast) place small optical elements in the Fourier plane of the imaging lens, as described above. Because the incident light is highly collimated, it focuses tightly in the Fourier plane and can be intercepted by an extremely small optical element. The scattered field, however, is highly uncollimated, and as such has a very large spatial extent where the incident beam has a focus. As a result, the scattered field is not appreciably affected by the small optical element. Treating the two fields separately allows us to include the effect of the optical element on the incident field, while neglecting it for the scattered field. Further, a general description of this element can be used during the analysis, and then specialized to absorption, dark-spot, or phase-contrast imaging in the final answer.

Previously, (7.8) we had an expression for the electric field strength in the object plane of the imaging system. We can define a new field, $\mathcal{E}_{\text{scattered}}$, such that $\mathcal{E}_{\text{object}} = \mathcal{E}_{\text{scattered}} + \mathcal{E}_{\text{incident}}$,

$$\mathcal{E}_{\text{scattered}}(x,y) = \mathcal{E}_{\text{incident}}(x,y)\left(\exp\left[\left(\frac{-\tilde{n}(x,y)\sigma}{2}\right)\left(\frac{1+i\delta}{1+\delta^2}\right)\right]-1\right) \tag{7.9}$$

7.4.1 Propagating the Scattered Field

We begin with the paraxial propagator in scalar diffraction theory [61],

$$g(x,x';y,y';d) = \left(\frac{-ik}{2\pi d}\right)\ \exp\left[\left(\frac{ik}{2d}\right)\left((x-x')^2+(y-y')^2\right)\right]. \tag{7.10}$$

The above equation propagates an electric field distribution in one plane to another plane a distance d away. The parameter k is the propagation wavenumber. The propagator is used as follows:

$$\mathcal{E}(x,y,z=\Delta z) = \iint\limits_{P'} dP'\ g(x,x';y,y';\Delta z)\ \mathcal{E}(x',y',z=0), \tag{7.11}$$

where P' is the $x'y'$-plane, and $dP' \equiv dx'dy'$.

Additionally, we treat lenses as thin, and as such they add a quadratic phase profile to the electric field distribution [61]:

$$\mathcal{E}_{\text{after lens}}(x,y) = \mathcal{E}_{\text{before lens}}(x,y)\ \exp\left[\left(\frac{-ik}{2f}\right)(x^2+y^2)\right], \tag{7.12}$$

where f is the focal length of the lens.

A schematic of the system we are trying to analyze is shown in Figure 7.4. In the figure, the plane at the left is the object plane of the system, where the electric field distribution is designated $\mathcal{E}_0$. A distance, $2f$ away a plane containing the electric field distribution $\mathcal{E}_{L_1}$ is just in front of the lens. On the other side of the lens we have the distribution $\mathcal{E}_{L_2}$. These two planes are separated by zero distance, since we are making the thin lens approximation. Finally, a distance $2f$ further, we have the image plane, where we label the distribution $\mathcal{E}_i$.

We then simply propagate $\mathcal{E}_0$ a distance $2f$ to the lens, add the effect of the lens,

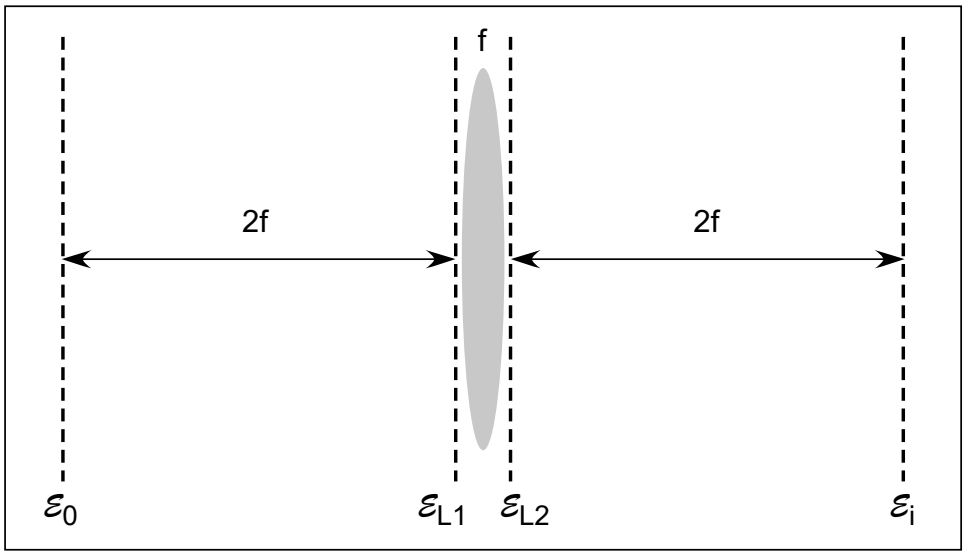

Figure 7.4: Propagating the scattered field.

then propagate a distance $2f$ to get the result we seek, $\mathcal{E}_i$. The equations describing these three steps are:

$$\mathcal{E}_{L_1}(x_2', y_2') = \iint_{P_1'} dP_1' \; g(x_2', x_1'; y_2', y_1'; 2f) \; \mathcal{E}_0(x_1', y_1'), \tag{7.13}$$

$$\mathcal{E}_{L_2}(x_2', y_2') = \mathcal{E}_{L_1}(x_2', y_2') \; \exp\left[\frac{-iq}{2f}\left(x_2'^2 + y_2'^2\right)\right], \tag{7.14}$$

and

$$\mathcal{E}_i(x, y) = \iint_{P_2'} dP_2' \; g(x, x_2'; y, y_2'; 2f) \; \mathcal{E}_{L_2}(x_2', y_2'). \tag{7.15}$$

We can combine these equations to get a single equation for $\mathcal{E}_i$:

$$\begin{aligned}\mathcal{E}_i(x, y) = \iiiint_{P_1', P_2'} dP_1' \, dP_2' \; g(x, x_2'; y, y_2'; 2f) \; \exp\left[\frac{-iq}{2f}\left(x_2'^2 + y_2'^2\right)\right] \; \times \\ g(x_2', x_1'; y_2', y_1'; 2f) \; \mathcal{E}_0(x_1', y_1').\end{aligned} \tag{7.16}$$

If we expand the propagators, we can collect terms so that the exponentials containing the x_2'- and y_2'-dependence are a simple as possible. When this is done, we get

$$\mathcal{E}_i(x,y) = -\left(\frac{q}{4\pi f}\right)^2 \iiiint\limits_{P_1',P_2'} dP_1'\, dP_2'\, \mathcal{E}_0(x_1',y_1')\, \exp\left[\frac{iq}{4f}\left(x^2+y^2+x_1'^2+y_1'^2\right)\right] \times \exp\left[\frac{-iq}{2f}(x_2'(x+x_1'))\right]\, \exp\left[\frac{-iq}{2f}(y_2'(y+y_1'))\right]. \tag{7.17}$$

The simplified exponentials, however, are of the exact form to produce Dirac delta functions when the P_2' integrals are done,

$$\mathcal{E}_i(x,y) = -\iint\limits_{P_1'} dP_1'\, \mathcal{E}_0(x_1',y_1')\, \exp\left[\frac{iq}{4f}(x^2+y^2+x_1'^2+y_1'^2)\right] \times \delta(x+x_1')\delta(y+y_1'). \tag{7.18}$$

The presence of the delta functions collapses the final integrals, giving us our final result

$$\mathcal{E}_i(x,y) = -\mathcal{E}_0(-x,-y)\, \exp\left[\frac{iq}{2f}\left(x^2+y^2\right)\right]. \tag{7.19}$$

From the final result in (7.19), we see that the effects of the propagation of the scattered field through the imaging system are an overall phase-shift of π, an inversion of the coordinate axes (which is expected in a single-lens imaging system), and an overall quadratic wavefront curvature.

7.4.2 Propagating the Incident Field

We take a similar approach to propagating the incident field. However, the potential presence of an optical element in the back focal plane of the imaging lens requires

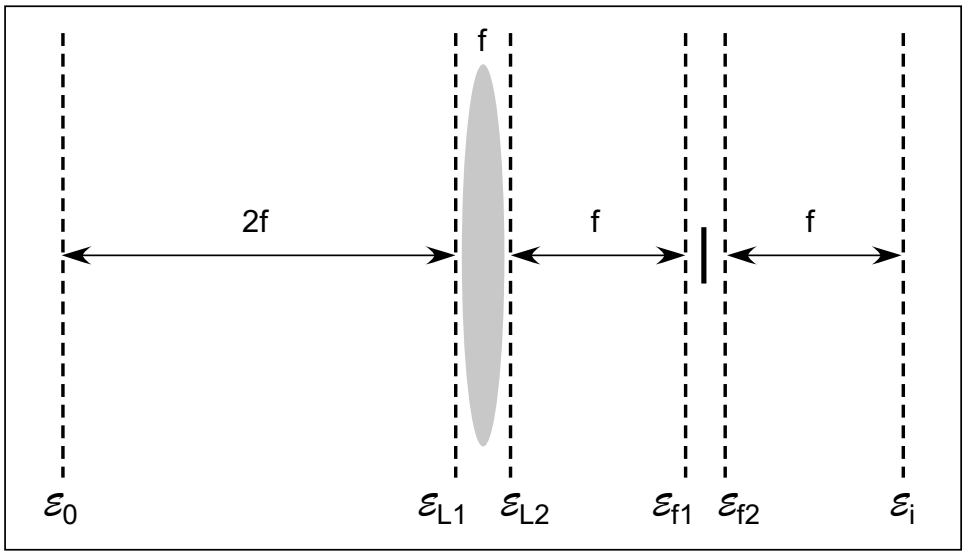

Figure 7.5: Propagating the incident field.

a slightly different approach. A schematic of the system is shown in Figure 7.5. In the second half of the system, we now propagate a distance f, then allow for the effect of the optical element, and then propagate another f to the image plane. We define the electric field distributions in the planes just before and after the optical element as $\mathcal{E}_{f_1}$ and $\mathcal{E}_{f_2}$, respectively.

Following the treatment in [46], we can treat the optical element in a completely general way. If we define τ^2 as the fraction of the light transmitted by the element, and ϕ as the phase-shift induced by the element, then we can define all three imaging techniques by the following parameters:

$$(\tau, \phi) = \begin{cases} (1, 0) & : \quad \text{absorption} \\ (0, \text{N/A}) & : \quad \text{dark-spot} \\ (1, \pm\pi/2) & : \quad \text{phase-contrast} \end{cases} \tag{7.20}$$

The effect of the generalized optical element is then

$$\mathcal{E}_{\text{after element}} = \mathcal{E}_{\text{before element}}\, \tau\, e^{i\phi} \tag{7.21}$$

The relationships between the electric field distributions in the various planes are given by:

$$\mathcal{E}_{L_1}(x_2', y_2') = \iint_{P_1'} dP_1^{'}\; g(x_2', x_1'; y_2', y_1'; 2f)\; \mathcal{E}_0(x_1', y_1'), \tag{7.22}$$

$$\mathcal{E}_{L_2}(x_2', y_2') = \mathcal{E}_{L_1}(x_2', y_2')\; \exp\left[\frac{-iq}{2f}\left(x_2'^2 + y_2'^2\right)\right], \tag{7.23}$$

$$\mathcal{E}_{f_1}(x_3', y_3') = \iint_{P_2'} dP_2^{'}\; g(x_3', x_2'; y_3', y_2'; f)\; \mathcal{E}_{L_2}(x_2', y_2'), \tag{7.24}$$

$$\mathcal{E}_{f_2}(x_3', y_3') = \mathcal{E}_{f_1}(x_3', y_3')\; \tau\; e^{i\phi}, \tag{7.25}$$

and

$$\mathcal{E}_i(x, y) = \iint_{P_3'} dP_3^{'}\; g(x, x_3'; y, y_3'; f)\; \mathcal{E}_{f_2}(x_3', y_3'). \tag{7.26}$$

Combining, we get the somewhat unwieldy expression

$$\begin{aligned}\mathcal{E}_i(x, y) = \int_{P_1', P_2', P_3'} \cdots \int dP_1^{'}\, dP_2^{'}\, dP_3^{'}\; g(x, x_3'; y, y_3'; 2f)\; \tau\; e^{i\phi}\; g(x_3', x_2'; y_3', y_2'; f)\; \times \\ \exp\left[\left(\frac{-ik}{2f}\right)(x_2'^2 + y_2'^2)\right]\; g(x_2', x_1'; y_2', y_1'; f)\; \mathcal{E}_0(x_1', y_1').\end{aligned} \tag{7.27}$$

Doing the $P_3^{'}$ integrals combines two of the propagators,

$$\mathcal{E}_i(x,y) = \tau\, e^{i\phi} \iiiint\limits_{P_1^{'},P_2^{'}} dP_1^{'}\, dP_2^{'}\; g(x,x_2';y,y_2';2f)\; \exp\left[\left(\frac{-ik}{2f}\right)(x_2'^2+y_2'^2)\right] \times \\ g(x_2',x_1';y_2',y_1';f)\; \mathcal{E}_0(x_1',y_1'). \tag{7.28}$$

But the integrals are now just the case considered previously in (7.16). We can use that result, without loss of generality, to write

$$\mathcal{E}_i(x,y) = -\tau\, e^{i\phi}\; \mathcal{E}_0(-x,-y)\; \exp\left[\frac{iq}{2f}\left(x^2+y^2\right)\right]. \tag{7.29}$$

7.4.3 Determining the Intensity

Having calculated how the scattered and incident fields propagate, we now add the two fields to find the total field in the image plane,

$$\begin{aligned}\mathcal{E}_{\text{total}}(x,y) &= -\mathcal{E}_{\text{scattered}}(-x,-y) - \tau\, e^{i\phi}\; \mathcal{E}_{\text{incident}}(-x,-y) \\ &= -\mathcal{E}_{\text{incident}}(-x,-y) \times \\ &\quad \left(\exp\left[\left(\frac{-\tilde{n}(-x,-y)\,\sigma}{2}\right)\left(\frac{1+i\delta}{1+\delta^2}\right)\right] - 1 + \tau\, e^{i\phi}\right)\end{aligned} \tag{7.30}$$

The intensity, $I(x,y)$, is proportional to the square of the electric field,

$$I(x,y) = k\; |\mathcal{E}_{\text{total}}(x,y)|^2. \tag{7.31}$$

Here, k depends on our choice of units (cgs, mks, etc.). If we then define the baseline intensity, $I_0(x,y)$ as

$$I_0(x,y) = k\; |\mathcal{E}_{\text{incident}}(x,y)|^2, \tag{7.32}$$

and insert the appropriate values of τ and ϕ to find the intensity at the CCD for the three techniques we find,

$$I(x,y) = \begin{cases} I_0(-x,-y)\; e^{-\beta} & : \quad \text{absorption} \\ I_0(-x,-y)\; \left[1 + e^{-\beta} - 2e^{-\beta/2}\cos\left(-\delta\beta/2\right)\right] & : \quad \text{dark-spot} \\ I_0(-x,-y)\; \left[2 + e^{-\beta} - 2\sqrt{2}\cos\left(-\delta\beta/2 \pm \pi/4\right)\right] & : \quad \text{phase-contrast} \end{cases} \tag{7.33}$$

where the symbol

$$\beta = \frac{\tilde{n}(-x,-y)\;\sigma}{1+\delta^2} \tag{7.34}$$

has been used for brevity.

7.5 Treating Several Important Cases

The relationship between the intensity profile at the CCD and the column density of the cloud is now completely fixed. The only parameter that we have not discussed in detail is the optical cross-section, σ, and how to calculate it for various situations. This section addresses this issue. I will consider two cases. The first case, that of imaging in the absence of a magnetic field, is quite general, and is the style of imaging used throughout this thesis. The second case, imaging using the photon-burst transition in the presence of a large magnetic field, complicates matters significantly. This technique, however, has much to offer and is currently an important technique in use by our research group.

7.5.1 Zero Magnetic Field

We will use the techniques of Appendix A to compute the optical cross-section, σ, when the atoms are in a region of zero-magnetic field. The atom cloud begins in an equal mixture of all the magnetic sublevels of the initial F-level. We excite the atoms with light that is resonant (or near-resonant) to the D_2-transition. The excited state F-levels are degenerate to within the linewidth of the transition, so we consider all possible values of F. We further consider the incoming light to be an arbitrary mixture of all three polarizations:

$$\hat{\mathbf{e}} = \sum_q a(q)\ \hat{\mathbf{e}}_q. \tag{7.35}$$

Where

$$\sum_q |a(q)|^2 = 1. \tag{7.36}$$

We will see that the final result *does not depend on the specific polarization mixture*. Since we potentially have multiple polarization components, we also consider all possible excited state magnetic sublevels. With all these considerations, the expression for the square of the electric-dipole ($\boldsymbol{\mu} \cdot \hat{\mathbf{e}}$) transition matrix element (see Section A.6.1) becomes:

$$\mu^2 = \frac{1}{2F_1+1} \sum_q |a(q)|^2 \sum_{F_2, m_{F_2}, m_{F_1}} |\, \langle (J_2 I) F_2 m_{F_2} | \hat{\mu}(1,q) | (J_1 I) F_1 m_{F_1} \rangle \,|^2. \tag{7.37}$$

In the case of the D_2-transition in ^{6}Li, $F_1 = 1/2$, $J_1 = 1/2$, and $J_2 = 3/2$. The possible values of F_2 are $1/2$, $3/2$, and $5/2$ (see Figure A.3).

Using the Wigner-Eckart Theorem (see Section A.6.1), we can rewrite the above

equation as:

$$\mu^2 = \frac{1}{2F_1+1}\sum_q |a(q)|^2 \sum_{F_2}\sum_{m_{F_2},m_{F_1}} (-1)^{2(F_2-m_{F_2})} \times \begin{pmatrix} F_2 & 1 & F_1 \\ -m_{F_2} & q & m_{F_1} \end{pmatrix}^2 |\langle (J_2 I)F_2||\hat{\mu}(1)||(J_1 I)F_1\rangle|^2. \tag{7.38}$$

Then, using the closure relation for 3-J symbols [62], this becomes

$$\mu^2 = \frac{1}{3(2F_1+1)}\sum_{F_2} |\langle (J_2, I)F_2||\hat{\mu}(1)||(J_1 I)F_1\rangle|^2. \tag{7.39}$$

In terms of the sum rules we defined in Section A.6.2, this is

$$\mu^2 = \frac{1}{3}\sum_{F_2} S_{F_1,F_2}. \tag{7.40}$$

Which, by equation (A.28), is expressible as

$$\mu^2 = \frac{1}{3(2J_1+1)}|\langle (L_2 S)J_2||\hat{\mu}(1)||(L_1 S)J_1\rangle|^2. \tag{7.41}$$

Remembering that $J_1 = 1/2$, $J_2 = 3/2$, and consulting Table A.9, we find that the effective value of the square of the transition matrix element is:

$$\mu^2 = \frac{2\mu_0^2}{3}, \tag{7.42}$$

where μ_0 is the transition matrix element of the cycling transition. Hence the corresponding optical cross-section is

$$\sigma = \frac{2}{3}\,\sigma_0, \tag{7.43}$$

where $\sigma_0 = 3\,\lambda^2/(2\,\pi)$ is the optical cross-section of the cycling transition [58].

7.5.2 Large B-Field

The presence of a strong magnetic field complicates our previous analysis. We are now forced to use the magnetic field direction as the quantization axis of the problem. As a result, in general, the probe beam does not propagate along the quantization axis. This means we must consider issues such as the orientation of the polarization of the probe light with respect to the atomic quantization axis, and the dipole pattern of the atomic polarization as viewed from the CCD. This also requires us to treat the full vector nature of the slowly-varying field amplitude, $\boldsymbol{\mathcal{E}}$, rather than its magnitude, $\mathcal{E}$, as we did in Section 7.3.

The specific case we are interested in involves imaging a cloud of ^{6}Li atoms in a strong z-oriented magnetic field. We will probe the cloud with an x-polarized beam of light, propagating in the yz-plane at an angle of α with respect to the z-axis. This is shown in Figure 7.6. We introduce another coordinate system that is rotated about the lab x-axis by an angle α so that the $z^{'}$-axis lies along the probe beam propagation axis.

The large field removes the degeneracy of the excited state and makes individual transitions resolvable. The probe frequency is tuned to be near resonant with the $|(L=0, S=1/2)\,J=1/2\,,\, m_J=-1/2\rangle$ to $|(L=1, S=1/2)\,J=3/2,\, m_J=-3/2\rangle$ transition. This transition is chosen because it tunes the least over the range of magnetic field strengths (0 G-1200 G), and hence requires the smallest change in the probe frequency. This transition is a $\hat{\boldsymbol{\sigma}}_-$-transition with respect to the quantization axis.

We will be working in the primed coordinate system for the calculation, so we

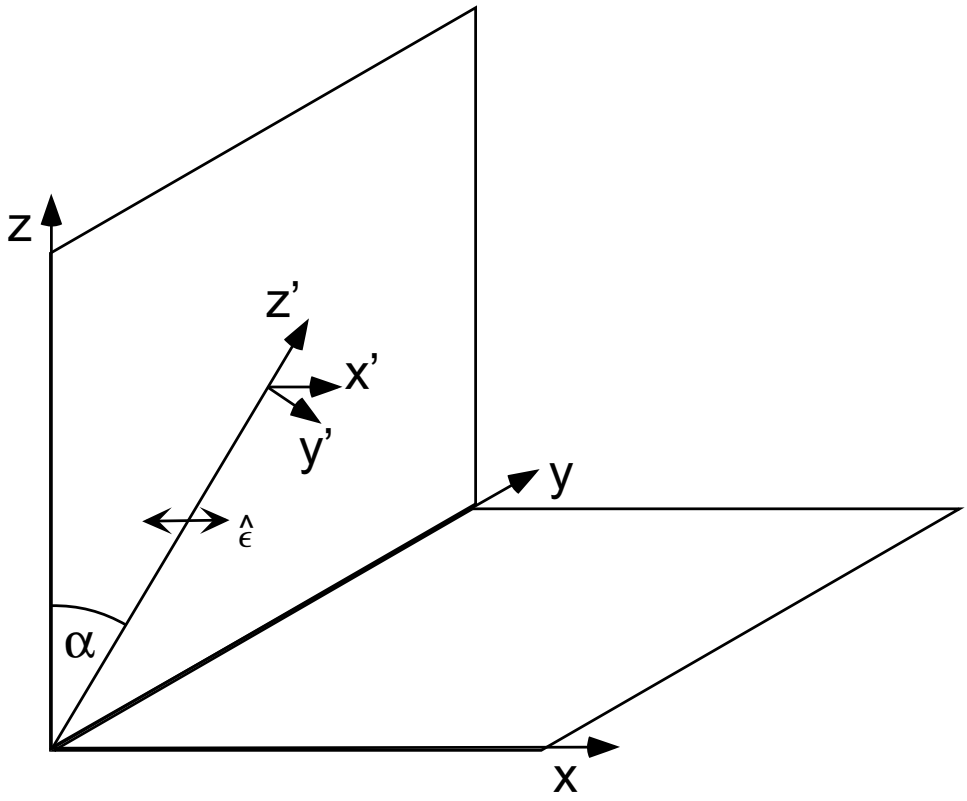

Figure 7.6: The coordinate systems used in the high-field case. The magnetic field is applied along the lab z-axis, making that the quantization axis. The probe propagates in the lab yz-plane and an angle α to the lab y. The incident polarization, $\hat{\boldsymbol{\epsilon}}$ lies in the lab x-direction. A second coordinate system is defined with respect to the propagating light. The direction of propagation is the $z^{'}$-axis. The two transverse directions are labelled $x^{'}$ and $y^{'}$ respectively. The $x^{'}$-axis is parallel to the lab x-axis and the $y^{'}$-axis lies in the lab yz-plane.

must first convert several vectors from the lab system into the primed system. In the lab frame, the polarization of the atomic transition is $\hat{\boldsymbol{\sigma}}_{-} = {}^{1}/\sqrt{2}\ (\hat{\mathbf{x}} - i\hat{\mathbf{y}})$. In the primed system, this is $\hat{\boldsymbol{\sigma}}_{-} = {}^{1}/\sqrt{2}\ (\hat{\mathbf{x}}^{'} - i\cos(\alpha)\,\hat{\mathbf{y}}^{'} - i\sin(\alpha)\,\hat{\mathbf{z}}^{'})$. The incident polarization is $\hat{\boldsymbol{\epsilon}}_{inc} = \hat{\mathbf{x}}$ in the lab frame. In the primed system this is simply $\hat{\boldsymbol{\epsilon}}_{inc} = \hat{\mathbf{x}}^{'}$.

We begin by modifying (7.5). We write:

$$\frac{\partial \boldsymbol{\mathcal{E}}(x^{'}, y^{'}, z^{'})}{\partial z^{'}} = -\left(\frac{n(x^{'}, y^{'}, z^{'})\,\sigma}{2(1+\delta^2)}\right)(1+i\delta)(\mathbb{I} - \hat{\mathbf{z}}^{'}\hat{\mathbf{z}}^{'}) \cdot \hat{\boldsymbol{\sigma}}_{-}\hat{\boldsymbol{\sigma}}^{*}_{-} \cdot \boldsymbol{\mathcal{E}}(x^{'}, y^{'}, z^{'}) \quad (7.44)$$

Here, $\mathbb{I}$ is the identity matrix, and $\hat{\boldsymbol{\sigma}}_{-}$ is the is the left-circular unit vector. The physical implications of this equation are relatively straightforward. The incoming field can excite the atom, but only the projection of the field onto the excitation vector contributes to the excitation ($\hat{\boldsymbol{\sigma}}^{*}_{-} \cdot \boldsymbol{\mathcal{E}}$). This excitation can result in electromagnetic radiation of polarization $\hat{\boldsymbol{\sigma}}_{-}$, but the dipole pattern must be taken into account. Only the portion of the excitation that is transverse to the direction of propagation can appear as a radiation field ($(\mathbb{I} - \hat{\mathbf{z}}^{'}\hat{\mathbf{z}}^{'}) \cdot \hat{\boldsymbol{\sigma}}_{-}$).

There are eigenvector solutions to (7.44) for which the incident polarization is preserved. We begin by making the *Ansatz*

$$\boldsymbol{\mathcal{E}}(x^{'}, y^{'}, z^{'}) = \mathcal{E}_0 \exp\left[\left(\frac{-\tilde{n}\,\xi\,\sigma}{2(1+\delta^2)}\right)(1+i\delta)\right]\ \hat{\boldsymbol{\epsilon}}. \quad (7.45)$$

Here $\tilde{n}$ is defined in analogy to (7.7) with the integration performed in the $\hat{\mathbf{z}}^{'}$-direction. The term in the exponential has been modified to include an arbitrary (for now) factor, ξ, that describes how the optical cross-section deviates from the maximum cross-section of the $\hat{\boldsymbol{\sigma}}_{-}$ transition. $\hat{\boldsymbol{\epsilon}}$ is the polarization unit-vector for the field.

Inserting this *Ansatz* into (7.44) yields an eigenvalue equation for the parameter ξ and the polarization direction $\hat{\boldsymbol{\epsilon}}$.

$$\xi\hat{\boldsymbol{\epsilon}} = (\mathbb{I} - \hat{\mathbf{z}}'\hat{\mathbf{z}}') \cdot \hat{\boldsymbol{\sigma}}_{-}\hat{\boldsymbol{\sigma}}_{-}^{*} \cdot \hat{\boldsymbol{\epsilon}}. \tag{7.46}$$

One solution can be extracted rapidly by noting that on the right hand side of (7.46), we clearly have a vector ($(\mathbb{I} - \hat{\mathbf{z}}'\hat{\mathbf{z}}') \cdot \hat{\boldsymbol{\sigma}}_{-}$), and a scalar ($\hat{\boldsymbol{\sigma}}_{-}^{*} \cdot \hat{\boldsymbol{\epsilon}}$).

One polarization eigensolution must therefore be of the form:

$$\hat{\boldsymbol{\epsilon}}_1 = \gamma(\mathbb{I} - \hat{\mathbf{z}}'\hat{\mathbf{z}}') \cdot \hat{\boldsymbol{\sigma}}_{-} \qquad \xi_1 = \left(\frac{1}{\gamma}\right) \hat{\boldsymbol{\sigma}}_{-}^{*} \cdot \hat{\boldsymbol{\epsilon}}_1. \tag{7.47}$$

The value of γ is set by the normalization of $\hat{\boldsymbol{\epsilon}}_1$. When normalized, the solution is

$$\hat{\boldsymbol{\epsilon}}_1 = \left(\frac{1}{\sqrt{1+\cos^2\alpha}}\right)(\hat{\mathbf{x}}' - i\cos\alpha\,\hat{\mathbf{y}}') \qquad \xi_1 = \frac{1+\cos^2\alpha}{2}. \tag{7.48}$$

The second polarization eigensolution can then be derived by realizing that it must be perpendicular to both the direction of propagation ($\hat{\mathbf{z}}' \cdot \hat{\boldsymbol{\epsilon}}_2 = 0$) and the known eigensolution ($\hat{\boldsymbol{\epsilon}}_2^{*} \cdot \hat{\boldsymbol{\epsilon}}_1 = 0$). The easiest way to generate the solution is to compute the cross-product $\hat{\boldsymbol{\epsilon}}_2^{*} = \hat{\mathbf{z}}' \times \hat{\boldsymbol{\epsilon}}_1$, which is a unit vector that meets these orthogonality requirements by construction.

We then need only compute the eigenvalue to have the second solution

$$\hat{\boldsymbol{\epsilon}}_2 = \left(\frac{1}{\sqrt{1+\cos^2\alpha}}\right)(-i\cos\alpha\,\hat{\mathbf{x}}' + \hat{\mathbf{y}}') \qquad \xi_2 = 0. \tag{7.49}$$

From the eigenvalues, we see that any incident polarization can be decomposed into two eigenpolarizations, one of which interacts with the atoms ($\hat{\boldsymbol{\epsilon}}_1$), and one which does not ($\hat{\boldsymbol{\epsilon}}_2$). The orthogonal nature of the two eigenvectors is obvious.

If the incident field is taken to be

$$\boldsymbol{\mathcal{E}}_{inc} = \mathcal{E}_0 \, \hat{\boldsymbol{\epsilon}}_{inc}, \tag{7.50}$$

we can expand it in terms of the two eigenpolarizations and apply our *Ansatz* to each term to get the field in the object plane of the imaging system

$$\boldsymbol{\mathcal{E}}_{obj} = \mathcal{E}_0(\hat{\boldsymbol{\epsilon}}_{inc} \cdot \hat{\boldsymbol{\epsilon}}_1^*) \exp\left[\left(\frac{-\tilde{n}\,\xi_1\,\sigma}{2(1+\delta^2)}\right)(1+i\delta)\right] \hat{\boldsymbol{\epsilon}}_1 + \mathcal{E}_0(\hat{\boldsymbol{\epsilon}}_{inc} \cdot \hat{\boldsymbol{\epsilon}}_2^*)\, \hat{\boldsymbol{\epsilon}}_2. \tag{7.51}$$

For our case, we wish to specialize to an incident x-polarization, $\hat{\boldsymbol{\epsilon}}_{inc} = \hat{\mathbf{x}} = \hat{\mathbf{x}}'$. With this choice, we find

$$\boldsymbol{\mathcal{E}}_{obj} = \frac{\mathcal{E}_0}{\sqrt{1+\cos^2\alpha}} \exp\left[\left(\frac{-\tilde{n}(1+\cos^2\alpha)\,\sigma}{4(1+\delta^2)}\right)(1+i\delta)\right] \hat{\boldsymbol{\epsilon}}_1 + \frac{i\mathcal{E}_0 \cos\alpha}{\sqrt{1+\cos^2\alpha}}\, \hat{\boldsymbol{\epsilon}}_2. \tag{7.52}$$

We now subtract off the incident field, in analogy with the earlier scalar derivation, to find the scattered field.

$$\boldsymbol{\mathcal{E}}_{scat} = \frac{\mathcal{E}_0}{\sqrt{1+\cos^2\alpha}} \left(\exp\left[\left(\frac{-\tilde{n}(1+\cos^2\alpha)\,\sigma}{4(1+\delta^2)}\right)(1+i\delta)\right] - 1\right) \hat{\boldsymbol{\epsilon}}_1. \tag{7.53}$$

We can now directly apply the results of the Fourier optics calculations of Section 7.4.1 and Section 7.4.2. In the image plane, the scattered field is

$$\begin{aligned}\boldsymbol{\mathcal{E}}_{scat}(x', y') = &\frac{-\mathcal{E}_0}{\sqrt{1+\cos^2\alpha}} \left(\exp\left[\left(\frac{-\tilde{n}(-x', -y')(1+\cos^2\alpha)\,\sigma}{4(1+\delta^2)}\right)(1+i\delta)\right] - 1\right) \times \\ &\exp\left[\frac{iq}{2f}\left(x'^2 + y'^2\right)\right] \hat{\boldsymbol{\epsilon}}_1,\end{aligned} \tag{7.54}$$

while the incident field is

$$\boldsymbol{\mathcal{E}}_{inc}(x',y') = -\tau e^{i\phi}\mathcal{E}_0 \ \exp\left[\frac{iq}{2f}\left(x'^2+y'^2\right)\right]\hat{\boldsymbol{\epsilon}}_{inc}, \tag{7.55}$$

In this, τ and ϕ are the generalized imaging parameters as before. Their values for the three imaging techniques are given in (7.20).

Writing the total field ($\boldsymbol{\mathcal{E}}_{tot} = \boldsymbol{\mathcal{E}}_{inc} + \boldsymbol{\mathcal{E}}_{scat}$) in terms of x'-, y'-, and z'-coordinates we find:

$$\begin{aligned}\boldsymbol{\mathcal{E}}_{tot} = &-\mathcal{E}_0\left(\frac{1}{2\xi}\left(\exp\left[\frac{-\beta\xi}{2}(1+i\delta)\right]-1\right)+\tau e^{i\phi}\right)\exp\left[\frac{iq}{2f}(x'^2+y'^2)\right]\hat{\mathbf{x}}' \\ &-\mathcal{E}_0\left(\frac{i\cos\alpha}{2\xi}\left(\exp\left[\frac{-\beta\xi}{2}(1+i\delta)\right]-1\right)\right)\exp\left[\frac{iq}{2f}(x'^2+y'^2)\right]\hat{\mathbf{y}}'\end{aligned} \tag{7.56}$$

where β is defined as in (7.34) and $\xi = \xi_1 = (1+\cos^2\alpha)/2$. We again define I and I_0 as in (7.31) and (7.32) and find:

$$I = I_0\left[\frac{1}{2\xi}\left(e^{-\beta\xi}+1+2e^{-\beta\xi/2}\left[\tau\cos(\beta\xi\delta/2-\phi)-\cos(\beta\xi\delta/2)\right]-2\tau\cos\phi\right)+\tau^2\right]. \tag{7.57}$$

We can specialize to the three imaging techniques to find:

$$I = \begin{cases} I_0\left[\frac{1}{2\xi}\left(e^{-\beta\xi}-1\right)\right)+1\right] & : \quad \text{absorption} \\ I_0\left[\frac{1}{2\xi}\left(e^{-\beta\xi}-2e^{-\beta\xi/2}\cos\left(\beta\xi\delta/2\right)+1\right)\right] & : \quad \text{dark-spot} \\ I_0\left[\frac{1}{2\xi}\left(e^{-\beta\xi}-2e^{-\beta\xi/2}\left(\cos\left(\beta\xi\delta/2\right)\mp\sin\left(\beta\xi\delta/2\right)\right)+1\right)+1\right] & : \quad \text{phase-contrast.} \end{cases} \tag{7.58}$$

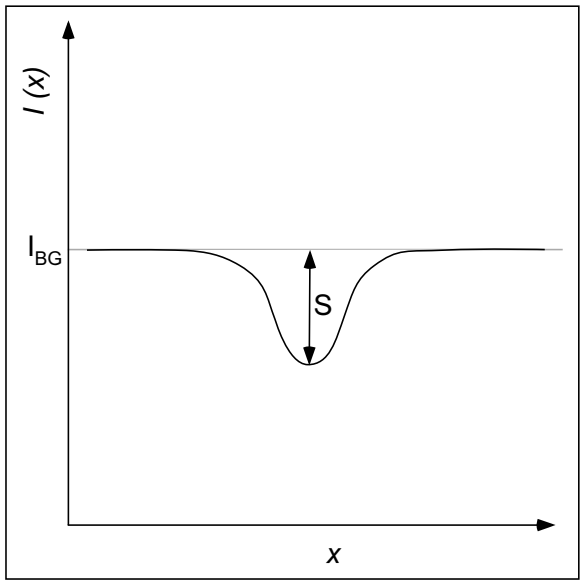

Figure 7.7: Representative intensity profile at the CCD.

7.6 Signal to Noise Analysis

It is not difficult to develop a simple model of CCD imaging that incorporates signal-to-noise ratio, fluence, number of scattered photons per atom per image, detuning of the probe field, and several CCD parameters. In this section, we derive the results for imaging in zero magnetic field. The results for high-field imaging can be derived in a similar manner.

In Figure 7.7 we see a representation of a one-dimensional slice through the intensity profile at the CCD. There is an overall background level, I_{BG} (which may be zero), and a signal that deviates from the background, S (which may deviate either upwards or downwards, depending on the imaging technique used).

We can get expressions for the background intensity in the three techniques by

evaluating their intensity distributions (7.33) with $\tilde{n} = 0$. We find

$$I_{BG} = \begin{cases} I_0 & : \quad \text{absorption} \\ 0 & : \quad \text{dark-spot} \\ I_0 & : \quad \text{phase-contrast.} \end{cases} \tag{7.59}$$

The signal is then the overall intensity profile (7.33) minus the background (7.59) (for the remainder of this analysis, we will work solely with peak values and suppress the spatial-dependence).

$$S = \begin{cases} I_0 \left[e^{-\beta} - 1\right] & : \quad \text{absorption} \\ I_0 \left[1 + e^{-\beta} - 2e^{-\beta/2} \cos\left(-\delta\beta/2\right)\right] & : \quad \text{dark-spot} \\ I_0 \left[1 + e^{-\beta} - 2\sqrt{2} \cos\left(-\delta\beta/2 \pm \pi/4\right)\right] & : \quad \text{phase-contrast.} \end{cases} \tag{7.60}$$

Clearly both the signal and the background are proportional to I_0. It will prove convenient to define these constants of proportionality and continue with a generalized treatment:

$$S = \varepsilon_S \, I_0 \tag{7.61}$$

$$I_{BG} = \varepsilon_{BG} \, I_0. \tag{7.62}$$

In this new notation, the three techniques can be summarized as

$$(\varepsilon_{BG}, \, \varepsilon_S) = \begin{cases} (1, \; e^{-\beta} - 1) & : \quad \text{absorption} \\ (0, \; 1 + e^{-\beta} - 2e^{-\beta/2} \cos\left(-\delta\beta/2\right)) & : \quad \text{dark-spot} \\ (1, \; 1 + e^{-\beta} - 2\sqrt{2} \cos\left(-\delta\beta/2 \pm \pi/4\right)) & : \quad \text{phase-contrast} \end{cases} \tag{7.63}$$

If the CCD is exposed to the background intensity for a duration, t, the number of electrons deposited per pixel is

$$\begin{aligned} N_{BG} &= \frac{I_{BG}t}{h\nu}L^2\eta \\ &= \frac{I_0 t}{h\nu}L^2\eta\,\varepsilon_{BG}. \end{aligned} \tag{7.64}$$

where L is the pixel size and η is the *quantum efficiency*—a measure of how effective the CCD is in turning photons into electrons. Likewise, we can compute the number of electrons represented by the signal:

$$\begin{aligned} N_S &= \frac{St}{h\nu}L^2\eta \\ &= \frac{I_0 t}{h\nu}L^2\eta\,\varepsilon_S. \end{aligned} \tag{7.65}$$

We can then define the signal-to-noise ratio, Λ, as

$$\Lambda = \frac{|N_S|}{\sqrt{N_{BG} + N_S + N_{e^-}^2}}, \tag{7.66}$$

where $\sqrt{N_{BG} + N_S}$ is the total shot-noise of the light and N_{e^-} is the RMS electron noise specification for the CCD (It is a combination of discretization noise, readout noise, and dark-current). The absolute value in the numerator is necessary as the signal can be negative, and we desire a positive value for Λ. Using our definitions in (7.64) and (7.65), we can rewrite the signal-to-noise ratio as

$$\Lambda = \frac{|\varepsilon_S|\left(\frac{I_0 t L^2\eta}{h\nu}\right)}{\sqrt{(\varepsilon_{BG} + \varepsilon_S)\left(\frac{I_0 t L^2\eta}{h\nu}\right) + N_{e^-}^2}}. \tag{7.67}$$

If we then have a desired value of Λ, for a given imaging technique and CCD, we find that we require a fluence of

$$I_0 t = \left(\frac{h\nu}{L^2\eta}\right)\left(\frac{\Lambda^2(\varepsilon_{BG}+\varepsilon_S)+\sqrt{\Lambda^4(\varepsilon_{BG}+\varepsilon_S)^2+4\varepsilon_S^2\Lambda^2N_{e^-}^2}}{2\varepsilon_S^2}\right) \tag{7.68}$$

incident on the CCD (the alternative solution is ignored as it is always negative). This has two important limits: the shot-noise limit ($N_S + N_{BG} \gg N_{e^-}^2$),

$$I_0 t = \left(\frac{h\nu}{L^2\eta}\right)\left(\frac{\Lambda^2(\varepsilon_{BG}+\varepsilon_S)}{\varepsilon_S^2}\right), \tag{7.69}$$

and the large-background limit ($N_{BG} \gg N_S, N_{e^-}^2$),

$$I_0 t = \left(\frac{h\nu}{L^2\eta}\right)\left(\frac{\Lambda^2\varepsilon_{BG}}{\varepsilon_S^2}\right). \tag{7.70}$$

We now turn to calculating the number of photons scattered per atom. This is an important experimental parameter, for in a variety of experiments (*e.g.* collective oscillations of the cloud) it is useful to image a single cloud several times without significantly affecting it. As we saw in Section A.3, scattering a single photon off of an atom in a degenerate or near-degenerate cloud is sufficient to heat it dramatically, perhaps even ejecting it from a shallow trap. An imaging setup that allows the experimenter to take multiple images of the sample is said to be *non-destructive*.

We also now consider the possibility that the imaging system has non-unity magnification. This generalization does not effect any of our earlier results (other than applying a trivial spatial scaling of M, the magnification, in each transverse direction).

In Figure 7.8, we define two new intensities, I_{0_L}, the intensity of light striking

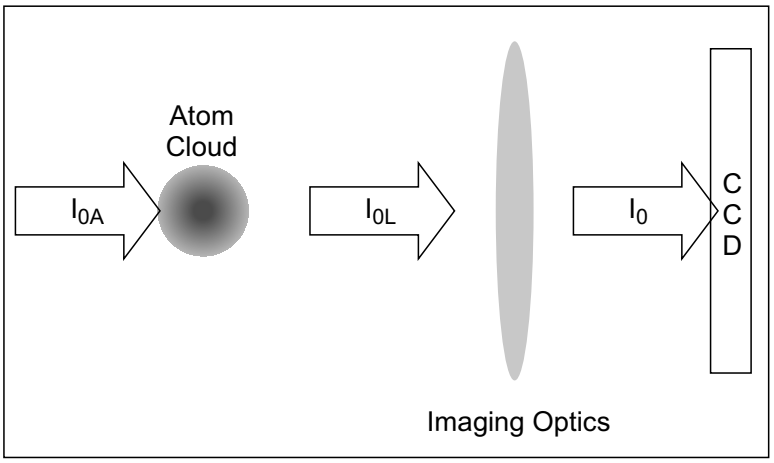

Figure 7.8: Definition of intensities.

the imaging lens, and I_{0_A}, the intensity of light striking the atoms. With an imaging magnification of M, a fluence of $I_0 t$ at the CCD implies a fluence prior to the lens of

$$I_{0L} t = M^2 I_0 t. \tag{7.71}$$

Further, $I_{0_A} = I_{0_L}$, since we are considering the *incident* beam—whose magnitude is not affected by the atoms. So the fluence incident on the atoms is represented by

$$I_{0_A} t = I_{0_L} t = M^2 I_0 t. \tag{7.72}$$

Now, in the low-intensity limit, the number of photons scattered by an atom in fluence $I_{0_A} t$ is

$$N_{phot} = \left(\frac{\sigma}{1 + \delta^2} \right) \left(\frac{I_{0_A} t}{h\nu} \right), \tag{7.73}$$

where σ is the resonant optical cross-section, and δ is the detuning in half-linewidths,

as before. Combining this result with (7.72) and (7.68), we get

$$N_{phot} = \left(\frac{\sigma}{1+\delta^2}\right)\left(\frac{M^2}{L^2\eta}\right)\left(\frac{\Lambda^2(\varepsilon_{BG}+\varepsilon_S)+\sqrt{\Lambda^4(\varepsilon_{BG}+\varepsilon_S^2)+4\varepsilon_S^2\Lambda^2N_{e^-}^2}}{2\varepsilon_S^2}\right). \tag{7.74}$$

This result also has the two limits discussed before, the shot-noise limit,

$$N_{phot} = \left(\frac{\sigma}{1+\delta^2}\right)\left(\frac{M^2}{L^2\eta}\right)\left(\frac{\Lambda^2(\varepsilon_{BG}+\varepsilon_S)}{\varepsilon_S^2}\right), \tag{7.75}$$

and the large-background limit,

$$N_{phot} = \left(\frac{\sigma}{1+\delta^2}\right)\left(\frac{M^2}{L^2\eta}\right)\left(\frac{\Lambda^2\varepsilon_{BG}}{\varepsilon_S^2}\right). \tag{7.76}$$

To specialize these results to absorption and phase-contrast imaging, we only need the appropriate values of ε_{BG} and ε_S from (7.63). The reader is advised to note that the large-background limit is nonsensical for the case of dark-spot imaging.

The results that we have derived are very useful. They were used in the progress of this experiment to evaluate the suitability of a number of commercial CCDs for use in destructive and non-destructive imaging techniques. The next section gives an overview of some of the results.

7.7 Choice of Technique

The formulas derived above were used to calculate the required incident probe intensity (I_{0_A}) to achieve a constant signal-to-noise-ratio as the detuning was varied and the resulting number of photons scattered per atom per image for conditions resembling our experiment and for CCD parameters representative of our scientific

Parameter	Value
Number of Atoms	1×10^5
Temperature to Well-Depth Ratio	$1/10$
Desired Signal-to-Noise Ratio	5
Magnification of Imaging System	4
CCD Pixel Size	$13\,\mu$m
CCD Quantum Efficiency	0.95
CCD RMS Electron Noise	2
Exposure Time	$1\,\mu$s

Table 7.1: Experimental parameters used in the imaging model.

camera. The values of the parameters are given in Table 7.1.

The required intensity for the three techniques is plotted as a function of detuning in Figure 7.9. The general structure is as expected—as the probe field is detuned, absorption imaging quickly becomes prohibitive, while phase-contrast imaging outperforms dark-spot. The resonant structure in the phase-contrast technique occurs where the detuning is such that $\varepsilon_S = 0$. At this point, the technique fails. Because the waveplate adds a retardation of a specific sign, the feature only occurs to one side of zero, making it easy to avoid.

In the figure it is difficult to discern the performance of absorption and dark-spot imaging in the region near the origin. A zoomed view can be seen in Figure 7.10. Here we clearly see that absorption imaging is the most efficient technique for resonant and near resonant-imaging.

But how destructive are the techniques to the atomic sample? In Figure 7.11, the number of photons scattered per atom per image is plotted as a function of detuning. Again, the general behavior is as expected. Off-resonance, absorption imaging is a completely destructive technique, while phase-contrast and dark-spot

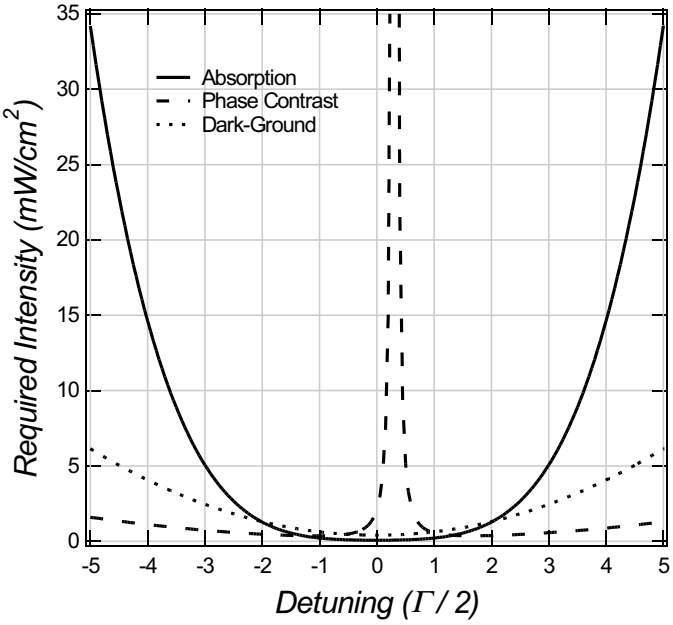

Figure 7.9: Required intensity as a function of detuning for the experimental parameters given in Table 7.1.

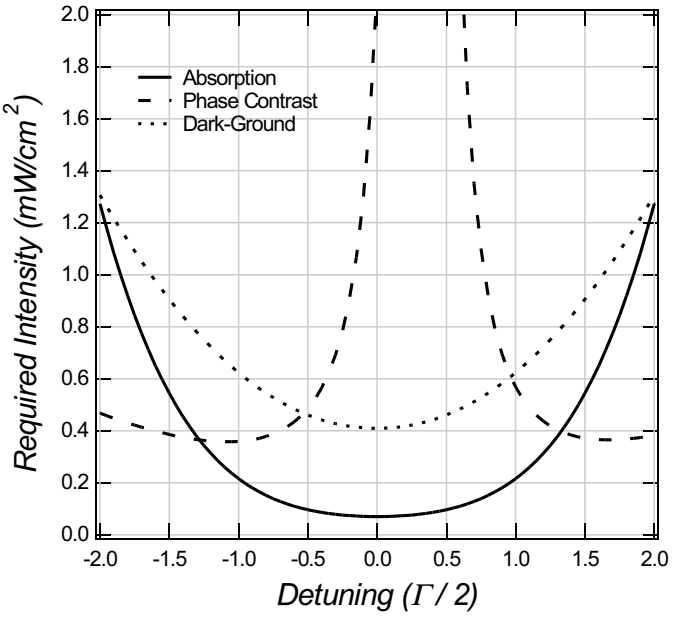

Figure 7.10: Required intensity as a function of detuning for the experimental parameters given in Table 7.1.

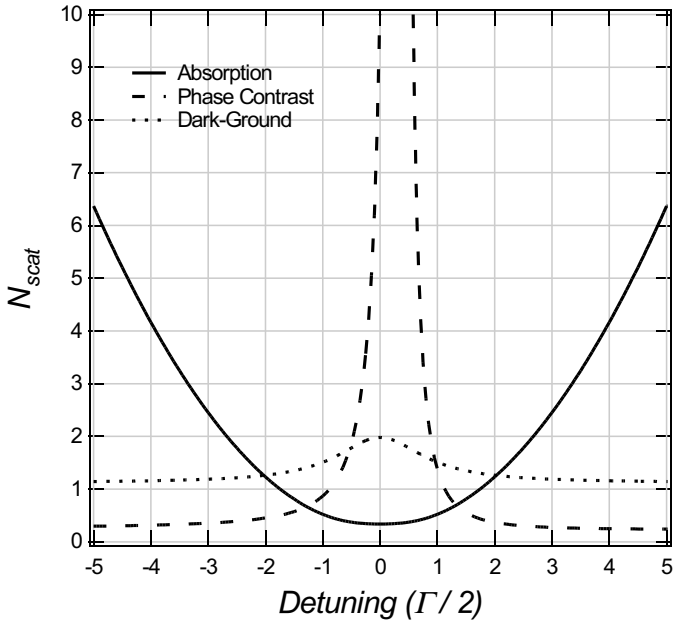

Figure 7.11: Number of photons scattered per atom per image as a function of detuning for the experimental parameters given in Table 7.1.

imaging are relatively benign at large detuning and dense samples (for a sample at $T/U = 1/100$, a $\Lambda = 5$ signal-to-noise-ratio can be achieved in phase contrast imaging with fewer than 0.01 photons scattered per atom for detunings $\delta \gtrapprox 6.5$!).

In order to determine the number of photons scattered near resonance, an enlargement of this region is shown in Figure 7.12. In this figure we see that although the number of photons scattered in absorption imaging near resonance is small ($\simeq 0.35$), this is still too large to allow for non-destructive imaging (roughly a third of the sample is destroyed with every shot).

Based on the overall strengths and weaknesses discussed earlier, and on the specific results addressed immediately above, our group has settled on resonant or near-resonant absorption imaging for all experiments that do not require non-destructive techniques. This covers all experiments performed in this thesis, but most likely excludes future experiments on collective oscillations. For experiments

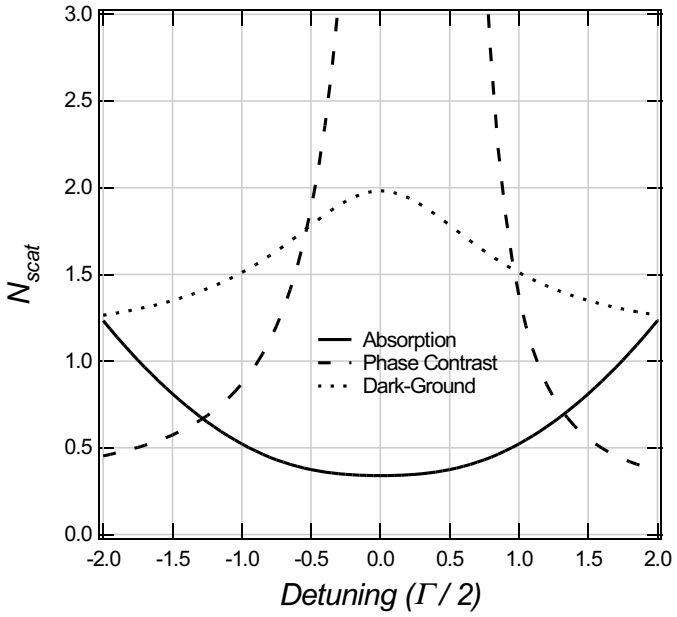

Figure 7.12: Number of photons scattered per atom per image as a function of detuning for the experimental parameters given in Table 7.1.

requiring non-destructive techniques, we will use phase-contrast imaging, and have the required waveplate on hand.

Chapter 8

Detection of Degeneracy

I often say that when you can measure what you are speaking about, and express it in numbers, you know something about it; but when you cannot express it in numbers, your knowledge is of a meagre and unsatisfactory kind.

—William Thomson (Lord Kelvin)

8.1 Overview

The experimental procedure of Chapter 6 ends with the generation of CCD images of the expanding atomic cloud generated via the low-field absorption imaging technique of Chapter 7. Earlier in the thesis, in Chapter 3, we derived expressions for an expanding cloud of atomic fermions in both the classical and quantum degenerate regimes. These expressions gave the density of the cloud as a function of the atom number, the temperature, the trap frequencies, and the expansion time.

Analysis of the experimental data is then a matter of fitting the the observed data to the expected profiles to extract the unknown parameters (the atom number and the temperature). This chapter begins by discussing the processing of the CCD images to convert the absorption images into density profiles which can be fit to the expected functional forms. A subsequent section shows how the theoretical functions of Chapter 3 need to be modified to include imaging parameters like pixel-

size and magnification. This section also addresses small procedures we performed to measure the exact values of the parameters where they were not known. The final portion of the chapter presents the analysis of the experimental data, showing conclusively that we succeeded in producing a degenerate gas of ^{6}Li using purely optical means.

A more detailed discussion of the analysis techniques discussed in this chapter can be found in a concurrent thesis by Stephen Granade [20], where the characterization of degeneracy is the central topic of the thesis.

8.2 Processing the CCD Images

As noted in the Chapter 6, the absorption images saved by the CCD camera and the computer have already undergone rudimentary processing. At the start of an experimental run, we take a *background* [46] or *dark-field* image. This is a camera image, taken without the illuminating laser or the presence of atoms. The result measures the typical electronic noise of the camera readout system. All subsequent images have this background image subtracted from them.

Further, although the illuminating laser is stable, it still drifts in power over the course of the experiment. As part of each experimental run, we take a *reference* [46] or *light-field* image with the illuminating laser on but without atoms. This reference image is taken immediately after each experimental shot.

If we represent the experimental signal as $S(i, j)$, the background as $B(i, j)$, and the reference as $R(i, j)$, the absorption signal $A(i, j)$ which we save for each shot is given by [46]

$$A(i,j) = 1 - \frac{S(i,j) - B(i,j)}{R(i,j) - B(i,j)}, \tag{8.1}$$

where i and j are pixel indices corresponding to the spatial directions x and y respectively.

The absorption image $A(i, j)$, then, is the starting point for processing described in this chapter. All further processing is done by manipulating the image with the software package IGOR-PRO (hereafter IGOR). IGOR is a data analysis program available for the Windows and Macintosh computer platforms.

8.2.1 Eliminating Residual Background

Despite our best efforts, there remains a residual (small) background on the image. This background is primarily the result of fluctuations in the imaging laser power and shape that occur in the finite time between taking the signal and reference images. To eliminate this background, we use a built-in feature of IGOR.

On each image, we designate a *region-of-interest* (ROI). The ROI is chosen to fully encompass the atomic cloud. The pixels *outside* the ROI are then least squares fit to a plane and that plane is then subtracted from the entire image (including the ROI). This removes any residual background from the image.

8.2.2 Converting to Column Density

As previously discussed in Chapter 7, the absorption images captured by the CCD have pixel values that reflect how much the incident beam was absorbed by the atomic cloud at the spatial location corresponding to that pixel. In (7.33), we gave the relationship between the intensity striking the atomic cloud and the intensity reaching the CCD. By dividing by the incident intensity, I_0, we can put (7.33) in

terms of the fraction of light transmitted by the atoms:

$$T(i,j) = e^{-\beta} = \exp\left[\frac{-\tilde{n}(i,j)\sigma}{1+\delta^2}\right]. \tag{8.2}$$

Here, β is the *optical density*. As before $\tilde{n}$ is the column density, σ is the effective cross section, and δ is the optical detuning in half-linewidths. The spatial coordinates x and y have been replaced with pixel locations i and j (we will make similar adjustments to the theoretical distributions of Chapter 3 later).

As stated above, the camera images are in terms of the fraction of light *absorbed* by the atoms. Since the absorption and the transmission necessarily sum to 1 ($A + T = 1$), we can write the absorption profile as

$$A(i,j) = 1 - T(i,j) = 1 - \exp\left[\frac{-\tilde{n}(i,j)\sigma}{1+\delta^2}\right]. \tag{8.3}$$

We must then invert this equation to get an expression for the column density $\tilde{n}(i,j)$ as a function of the measured absorption profile $A(i,j)$.

$$\tilde{n}(i,j) = -\left(\frac{1+\delta^2}{\sigma}\right)\ln\left[1 - A(i,j)\right]. \tag{8.4}$$

We showed previously in Section 7.5.1, that for the imaging technique used in this thesis, the effective cross section, σ is

$$\sigma = \frac{2}{3}\sigma_0 = \frac{\lambda^2}{\pi}. \tag{8.5}$$

Inserting this in (8.4), we find the final expression for the column density, $\tilde{n}(i,j)$, in terms of the measured absorption profile, the wavelength of the probe laser λ, and

the detuning δ of the laser from the atomic transition

$$\tilde{n}(i,j) = -\left(\frac{\pi(1+\delta^2)}{\lambda^2}\right)\ln\left[1 - A(i,j)\right]. \tag{8.6}$$

Note that the value of $\tilde{n}(i,j)$ is *local*. That is, it relies only on the value of A at the pixel location (i,j). Hence, we can process the absorption image $A(i,j)$ on a pixel-by-pixel basis to determine the column density $\tilde{n}(i,j)$.

8.2.3 Creating the 1-D Integrated Density Profile

While we now have a representation of the column density $\tilde{n}(i,j)$ that we *could* fit to the theoretical expressions (3.49) and (3.52) (with suitable modifications to convert from x, y coordinates to i, j pixel values), we have found that fitting the two-dimensional distributions is exceedingly slow and insensitive, in addition to being overly complicated. We instead numerically integrate the column density $\tilde{n}(i,j)$ to get the one-dimensional density $\check{n}(i)$. This is then compared to the one-dimensional theoretical expectations (3.50) and (3.53) (again, after modification to pixel coordinates). Note that numerical integration is not just a sum. It requires an overall multiplication by the effective bin size. The bin size is given by the effective pixel size in the y-direction—that is, the camera's physical pixel size in the y-direction divided by the imaging magnification M.

The numerical integration is performed along the axial direction of the optical trap. To avoid introducing unnecessary noise, the integration is performed over a limited range of pixels that excludes rows that are clearly outside the cloud.

In addition to simplifying the fitting process, this integration also eliminates any effects arising from the fact that the CCD observes the cloud from an angle. The

numerical integration we perform here, coupled with the integration that takes place physically along the direction of observation eliminate the two dimensions that are coupled as a result of the oblique observation angle. The resulting one-dimensional distribution $\check{n}(i)$ is completely free of any associated complications.

A schematic of the image processing procedure is shown in Figure 8.1

8.3 Pixel-Based Theoretical Distributions

The theoretical distributions derived in Chapter 3 were expressed in terms of spatial coordinates x, y, and z. In order to fit the expressions to the pixel-based images produced by the CCD, we must convert the distributions to use pixel values instead of spatial coordinates. We will specifically address only the expressions for the one-dimensional density $\check{n}$, but a similar approach can be used to convert the column density $\tilde{n}$ as well.

The conversion to pixels from spatial coordinates is primarily a scale transformation to dimensionless variables. All length scales in the expression we wish to convert must be divided by the effective pixel size. For the one-dimensional density $\check{n}$, the relevant mappings are

$$i \leftrightarrow \frac{x}{\Delta x_{\text{eff}}}\,, \qquad c_i \leftrightarrow \frac{c_x}{\Delta x_{\text{eff}}}\,. \tag{8.7}$$

Here Δx_{eff} is the effective pixel size in the imaging plane and c_x is the length scale defined in Chapter 3

$$c_x = a_x \sqrt{\left(\frac{k_B T}{U_0}\right)(1+\omega_x^2\tau^2)}. \tag{8.8}$$

In the above a_x is the $1/e$ size of the trapping potential in the x direction, T is

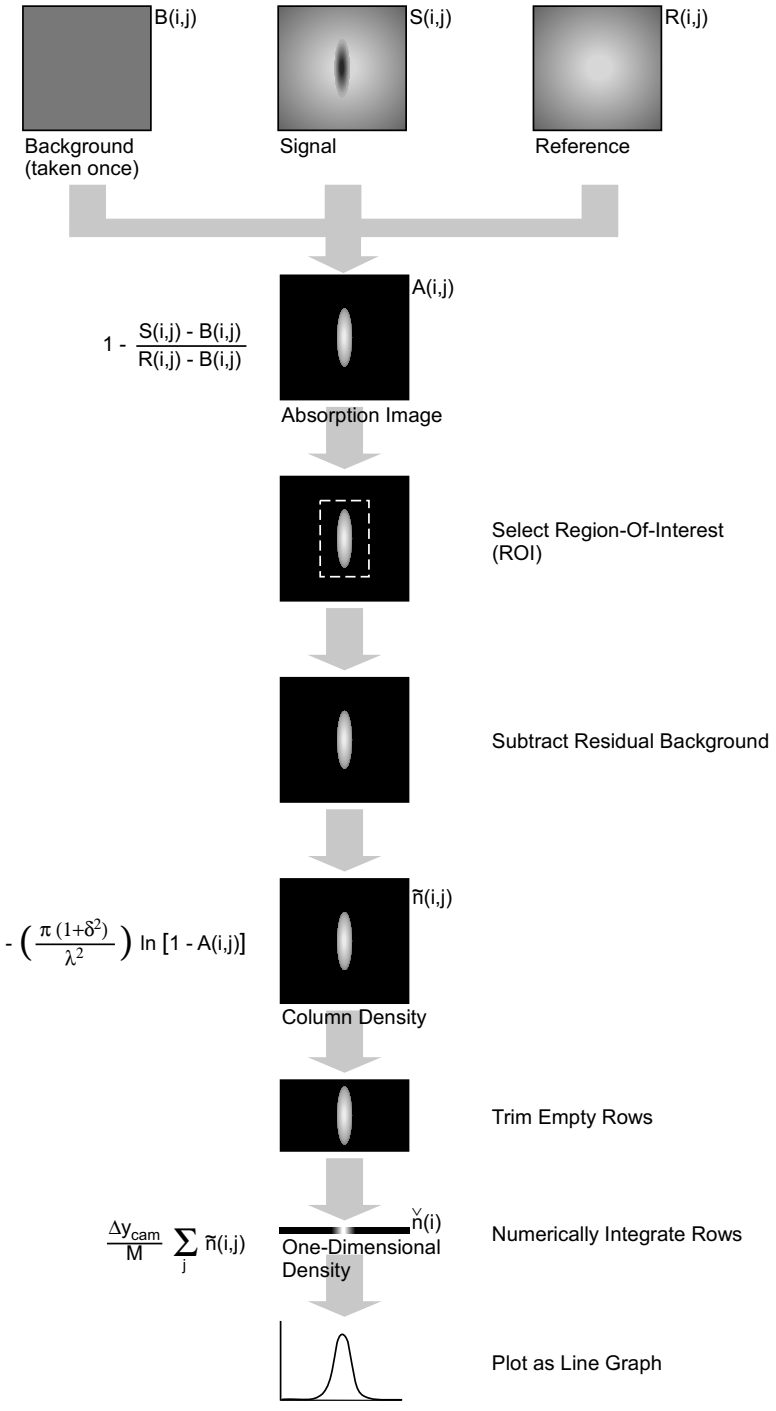

Figure 8.1: Image processing procedure.

the temperature of the gas, U_0 is the depth of the potential well, ω_x is the trap oscillation frequency in the x-direction, and τ is the duration of ballistic expansion.

There is one more conversion we must make. The effective pixel size Δx_{eff} is not directly measureable. However, it can be expressed in terms of the actual pixel size of the camera Δx_{cam} and the magnification of the imaging system M

$$\Delta x_{\text{eff}} = \Delta x_{\text{cam}}/M. \tag{8.9}$$

Inserting this relation into (8.7) yields the final mapping to pixel values

$$i \leftrightarrow \frac{Mx}{\Delta x_{\text{cam}}}\,, \qquad c_i \leftrightarrow \frac{Mc_x}{\Delta x_{\text{cam}}}\,. \tag{8.10}$$

Applying this mapping to the theoretical expectation for a Maxwell-Boltzmann gas (3.50) provides the theoretical distribution in pixel units

$$\check{n}_{\text{class}}(i,\tau) = \frac{NM}{c_i\,\Delta x_{\text{cam}}\,\sqrt{\pi}}\; e^{-\frac{i^2}{c_i^2}}. \tag{8.11}$$

8.4 Determining the System Parameters

From the result of (8.11), we see that to analyze the experimental data, we must know the magnification M of the imaging system as well as the trap well depth U_0 and the trap oscillation frequencies ω_x, ω_y, and ω_z (contained in the definition of c_i). The following sections detail the methods we used to measure these system parameters.

8.4.1 Trap Parameters

The trap depth and oscillation frequencies are interrelated according to the expressions given in (2.21) (the cylindrical symmetry of the trap allows us to take $\omega_x = \omega_y = \omega_r$), while the trap depth is related to the peak laser intensity via (2.17). We can use a combination of methods to determine these parameters.

Beam Properties

Using a pinhole, we can measure the size of the focal spot created by the final focusing lens. We find that the laser produces a $1/e^2$-intensity radius of $r_{\text{focus}} = 47\,\mu\text{m}$. A measurement of the laser power just before the final focusing lens, combined with an estimate of the transmission characteristics of the focusing lens and the vacuum window allow us to estimate the power at the trap as $P_{\text{focus}} = 65\,\text{W}$.

The peak intensity is then given by [38]

$$I_0 = \frac{2P_{\text{focus}}}{\pi r_{\text{focus}}^2}. \tag{8.12}$$

Inserting the result in (2.17), we find a trap depth of $U_0 = 690\,\mu\text{K}$.

From r_{focus} we can compute the expected Rayleigh range [38]

$$z_0 = \frac{\pi r_{\text{focus}}^2}{\lambda} \simeq 650\,\mu\text{m}. \tag{8.13}$$

With r_{focus}, z_0, and U_0, we can use (2.21) to predict the trap frequencies. We find

$$\omega_z \simeq 2100\,\text{s}^{-1} \rightarrow \nu_z \simeq 340\,\text{Hz} \tag{8.14}$$

$$\omega_r \simeq 41500\,\text{s}^{-1} \rightarrow \nu_r \simeq 6600\,\text{Hz}. \tag{8.15}$$

Transverse Shaking of the Trap

Of course we would like to confirm these predicted trap frequencies via direct measurement. One method we use is to shake the trap transversely by applying a frequency modulation (FM) perturbation to the AO driving frequency. This modulates the direction of the laser beam coming out of the AO. The final focusing lens then turns this angular modulation into a transverse modulation of the trap. As we previously discussed in Section 5.2.1, fluctuations of this type in the trapping potential can heat the atoms when the modulation occurs at the radial trap frequency. (Note: recently we have come to realize that this procedure is also likely to excite the "scissors mode"—a shape-preserving oscillation that is nonetheless degenerate in frequency with the transverse oscillation we had been assuming).

The experimental procedure is as follows. We begin by preparing a cold atom sample in the trap by evaporatively cooling the atoms and recompressing the well to full well depth. We then switch the Agilent RF generator from providing a steady 40 MHz frequency to the AO to a sinusoidal FM signal with a center frequency of 40 MHz, a deviation of ± 6 kHz, and a duration of 1 s:

$$\nu = 40\,\mathrm{MHz} + 6\,\mathrm{kHz}\ \sin(2\pi\nu_{\mathrm{mod}}). \tag{8.16}$$

The modulation frequency ν_{mod} is linearly swept downward across a 10 Hz bandwidth during the 1 s excitation (this is done so that anharmonicity in the well does not tune the atoms out of resonance as they heat). After the modulation is complete, the trapping laser is extinguished for 500 μs, and then reinstated. The number of atoms recaptured in the trap is then probed via resonance fluorescence.

If the atoms were heated by the excitation, we would expect a significant fraction

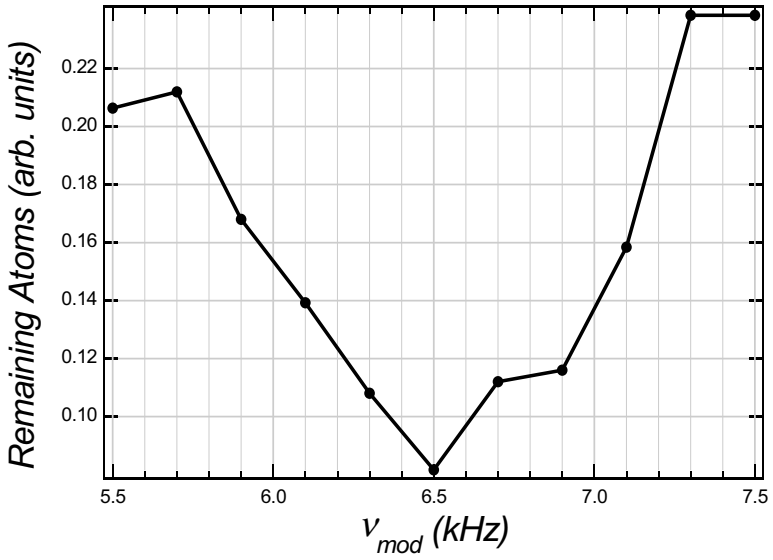

Figure 8.2: Atom loss as a function of shaking frequency. The plot clearly shows that there is a trap frequency in the vicinity of 6.5 kHz.

to gain sufficient energy that they are not recaptured when the trapping laser is reapplied. A plot of the fluorescence as a function of $\nu_{\rm mod}$ is shown in Figure 8.2.

From the graph we see that there is indeed a radial trap frequency near 6.6 kHz, as predicted. The slight hint of two resonance peaks is likely an indication of a slight ellipticity in the beam, breaking the symmetry between ν_x and ν_y. Studies of this type of excitation with the Monte-Carlo code of Chapter 4 show that the real resonance lies slightly above the peak frequency indicated in the experiment and in good agreement with the predicted value of 6.6 kHz.

Parametric Resonance

Shaking the trap is highly effective for measuring the radial oscillation frequency, but the nature of an optical trap makes it difficult to provide a modulation in the axial direction at the necessary frequencies. To measure the axial frequency we use the other heating mechanism of Chapter 5: intensity fluctuations. Here we apply

an amplitude modulation (AM) to the AO to modulate the depth of the trap and hence the trapping frequencies. As we showed earlier, modulation at twice a trap frequency heats the atoms via parametric resonance.

Experimentally, we again produce a cold atomic sample via evaporative cooling and then recompress the well. However, rather than recompressing to full well depth, we recompress to $U_{\rm new} = 0.85U_0$. We work at this offset so that even when the modulation is applied, the commanded well depth is never greater than U_0 (and cannot be supplied by the system). AM corresponding to $\pm 0.05U_0$ is applied for 1 s at a modulation frequency $\nu_{\rm mod}$ which is linearly swept downward across a bandwidth (again this keeps atoms from tuning out of resonance as they heat).

The large difference between the axial and radial frequencies further complicates detection. A release and recapture method, as used in the transverse shaking experiment will not work. The low axial frequency ensures that the atoms move many radial length scales before they have moved appreciably in the axial direction. Thus loss from the trap during release and recapture is dominated by normal radial motion, regardless of any axial heating.

To determine if we have heated the atoms, we instead suddenly truncate the well depth to $0.1U_0$, wait for any newly unbound atoms to clear, and then record the trap population with resonance fluorescence. By truncating the well, we become sensitive to atoms that were initially in the bottom of the well (where the trap is approximately harmonic) but were then heated above this threshold. A plot of fluorescence as a function of modulation frequency is shown in Figure 8.3

In the figure, we see that there is a clear peak at $\nu_{\rm mod} = 450\,{\rm Hz}$, meaning that the trap frequency is at $\nu_z = \nu_{\rm mod}/2 = 225\,{\rm Hz}$. However, we must apply a correction of $1/\sqrt{0.85}$ to correct for the fact that we were working at a reduced trap depth. When

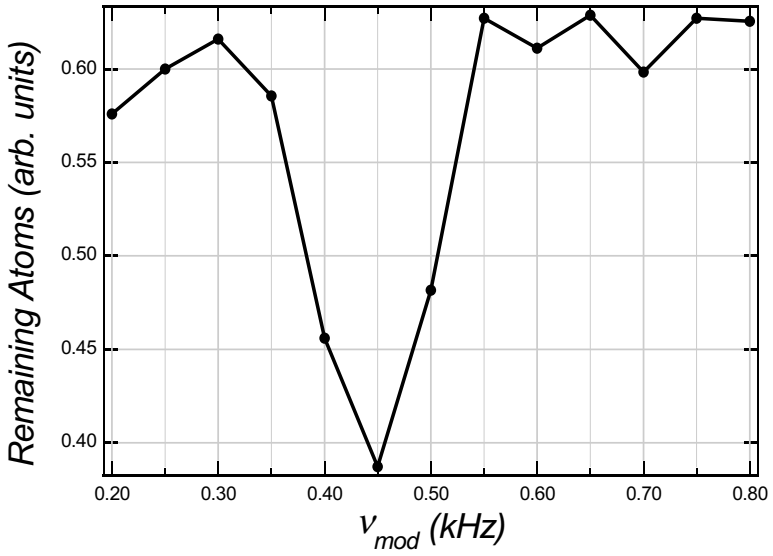

Figure 8.3: Atom loss as a function of parametric modulation frequency. The plot clearly shows a parametric resonance near 450 Hz.

this factor is included, we find $\nu_z = 245\,\mathrm{Hz}$. This value is in significant disagreement with the predicted value of 340 Hz. In Monte-Carlo studies of parametric resonance (Section 4.5.1), we found that the observed frequency was typically reduced by 10% from the true value. An analytical treatment of this system [51], shows a similar shift. After correcting for this shift, our measurement is then $\nu_z \simeq 275\,\mathrm{Hz}$, a value that is still in some disagreement with our prediction.

We believe that the discrepancy likely lies in variations in the beam parameters as we lower the well, making the conversion from 85% well depth to full well depth not as simple as we assumed above. Because the axial frequency will only enter into our analysis in the parameter $\bar{\omega} = (\omega_r^2\omega_z)^{1/3}$, the discrepancy will have little effect on our results. We will use the (corrected) measured value of 275 Hz in the remainder of the analysis.

8.4.2 Measuring the Imaging Magnification

The imaging system of the experiment was designed to provide an overall magnification factor of 4. However, given that the imaging system is constructed of free-space optical elements, slight variations in spacing and alignment can be expected to produce a variation of the magnification from the design specification. To determine the actual magnification of our imaging system, we take advantage of a particular feature of optical traps.

In general, magnifications are measured in atomic trapping experiments by causing a known displacement of the atoms and then comparing that to the observed displacement. In previous experiments with magnetic traps, the only possibility for controlled motion of the atoms was to release the cloud and watch the motion of its center of mass under the influence of gravity. The downside to this approach is that at long times after release, when the displacement is maximized, the cloud has expanded reducing the signal-to-noise ratio and making precise observations more difficult.

In our optical trap, the longitudinal location of the trap occurs a fixed distance from the final focusing lens. By translating that lens (it is mounted on a translation stage), we can translate the longitudinal location of the trap precisely. Meanwhile, the atoms remain confined in the trapping potential, providing images with extremely high signal-to-noise ratios.

Images of the cloud at several positions are shown in Figure 8.4. In each image, the trap has been shifted by 0.025 in compared to the previous image.

To determine the magnification, the images are processed according to the procedure depicted in Figure 8.1, with the exception that since we are interested in the *longitudinal* position of the cloud, we compute the one-dimensional density by sum-

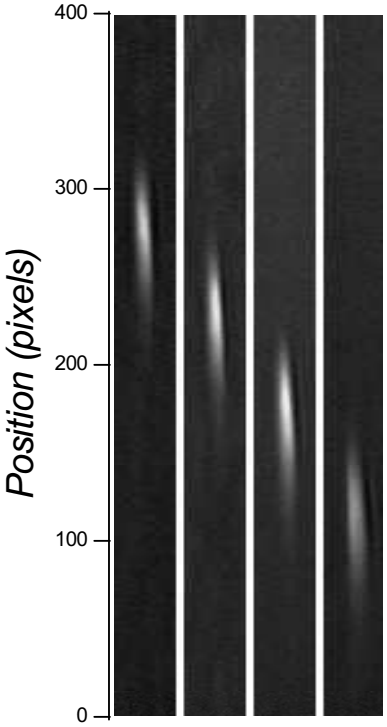

Figure 8.4: Observed shift of the atomic cloud resulting from an applied translation to the final focusing lens. In each image, the cloud has been translated by 0.025 in from the previous one. From this observed shift it is possible to determine the magnification of the imaging system.

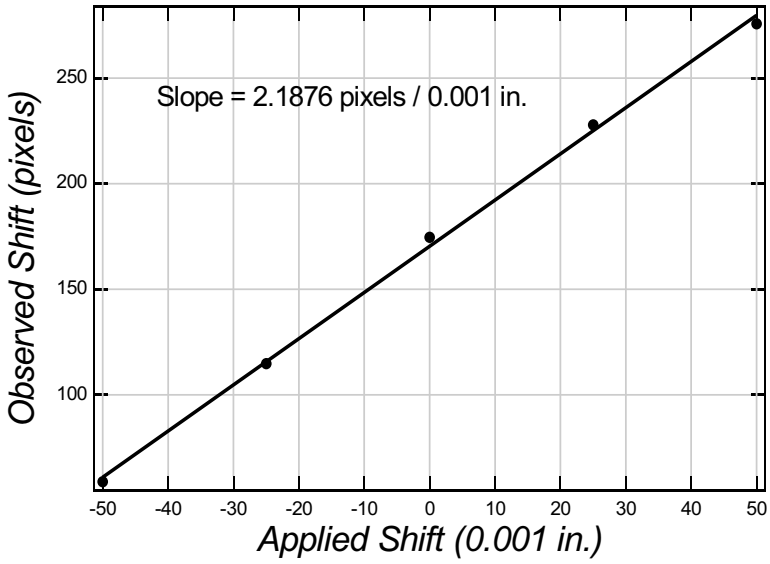

Figure 8.5: Observed shift versus applied translation. The slope of this line is the primary factor in determining the imaging magnification.

ming *columns* of the column-density image rather than rows. The one-dimensional distributions are then fit to simple Gaussian functions to locate their centers. The resulting positions of the cloud centers are then plotted against the known cloud translations and are fit to a linear function to extract the slope of the line. This is shown in Figure 8.5.

To extract the value of M from the slope, we use the following formula

$$M = \frac{bZL}{\gamma}. \tag{8.17}$$

Here, b is the slope of the fit in Figure 8.5, Z is the number of pixels being *binned* by the CCD, γ is the projective cosine resulting from the oblique observation angle (its presence accounts for an observed foreshortening of the translation), and L is the pixel size of the CCD.

For the images used here, $Z = 2$ (the CCD is reporting images made up of 2×2

superpixels. The camera observes at an angle of 35 ° from the long axis of the trap, meaning that $\gamma = \cos(55\,^\circ) = 0.5736$. Finally, the camera pixels are physically $13\,\mu$m in size, making $L = 13/25.4 = 0.5118$ thousandths of an inch. Inserting these numbers into (8.17), we find $M = 3.9$.

8.5 Analysis

Once we have values of the system parameters, we can begin analyzing the absorption images to determine the atom number, temperature, and degeneracy state of the atoms.

8.5.1 Atom Number

From the classical distribution in (8.11), we see that we should be able to fit the one-dimensional density distributions $\check{n}(i,\tau)$, to a one-dimensional Gaussian of amplitude A and width w. From (8.11), we can then relate these fit parameters to physical parameters as follows:

$$A = \frac{NM}{c_i \Delta x_{\mathrm{cam}} \sqrt{\pi}}, \qquad w = c_i. \tag{8.18}$$

Hence, the atom number is given by the expression

$$N = \frac{Aw\Delta x_{\mathrm{cam}} \sqrt{\pi}}{M}. \tag{8.19}$$

Of course, we could have simply taken $\check{n}(i)$ and numerically integrated in the i-direction to get N, but for the signal-to-noise ratios in this experiment, we found that the atom numbers generated by integration were not as consistent as those

generated from the fit. In experiments performed after those reported in this thesis, where improvements to the imaging system and trapping system have dramatically enhanced the signal-to-noise ratios, we find that numerical integration does indeed provide reliable determination of atom number. This is now the preferred approach in our lab.

8.5.2 Temperature

We first compute the temperature of the cloud using the relationships we developed for the classical gas. Surprisingly, the estimates produced by this method remain accurate even when the gas is slightly degenerate. Only when the gas is clearly degenerate do we add quantum statistical corrections to our temperature measurement. The following sections address these two techniques.

Classical Fits

In determining the atom number, we fit the one-dimensional density $\check{n}(i)$ to a Gaussian function and related the width w of the Gaussian to the theoretical parameter c_i. It is through this relationship that we will extract the temperature of the cloud.

When we modified our theoretical distribution to a pixel-based description we wrote

$$c_i \leftrightarrow \frac{M c_x}{\Delta x_{\mathrm{cam}}}\,. \tag{8.20}$$

In Chapter 3, we defined c_x as

$$c_x = b_x\sqrt{1+\omega_x^2\tau^2}, \tag{8.21}$$

and b_x as

$$b_x = a_x \sqrt{\frac{k_B T}{U_0}}, \tag{8.22}$$

while in Chapter 2 we related a_x to the well-depth and trap frequencies by

$$\omega_x = \sqrt{\frac{4\,U_0}{m a_x}}. \tag{8.23}$$

Combining all these expressions, we find that

$$c_i = \frac{2M}{\Delta x_{\rm cam}} \sqrt{\left(\frac{k_B T}{m}\right)\left(\frac{1}{\omega_x^2} + \tau^2\right)}. \tag{8.24}$$

Since we have previously related the fit parameter w with c_i, we get the following expression for the temperature of the gas:

$$T = \frac{m w^2 \Delta x_{\rm cam}^2}{4\,k_B M^2}\ \frac{\omega_x^2}{1 + \omega_x^2 \tau^2}. \tag{8.25}$$

Every quantity on the RHS of (8.25) is a known physical, system, experimental, or fit parameter.

Quantum Statistical Corrections

As stated above, the classical result produce reasonable temperature values for all but clearly-degenerate gases. In the degenerate regime, however, we must make some corrections to our treatment. It is worth noting, however, the *direction* in which the classical results fail. As the gas becomes degenerate and the Pauli exclusion principle forces atoms to occupy higher and higher quantum states, upon release the gas necessarily expands faster than a classical gas at the same temperature (since it consists of more high-momentum atoms than the corresponding

classical gas). Thus an analysis based on classical thought will see this excess energy and attribute it (falsely) to a higher temperature. Hence, analysis based on classical ideas always results in overestimating the temperature of the gas.

Unfortunately, simply fitting to the full Fermi-Dirac distribution (3.53) (suitably adjusted for pixels), is not practical. The "surface" explored by the fitting routines has many local minima, and the result is highly sensitive to the initial values of the parameters. In the months since this experiment we have dramatically lowered the temperature of our gas and have since had some success with a Sommerfeld expansion [43] of the density. Further, we are now able to perform full FD-fits on extremely low temperature clouds. However, in the temperature regimes explored in this thesis, we still have no completely suitable approach.

As a first attempt at applying quantum concepts to our temperature measurement, we begin by computing the chemical potential of the gas based on our measurements using the classical formulas. To calculate the chemical potential [10], we make use of an approximation from [63],

$$\mu(T,N) = k_B T_F \left[1 - \frac{\pi^2}{3}\left(\frac{T}{T_F}\right)^2\right]. \tag{8.26}$$

This approximation is quite good in the degenerate regime (which is the only case where we attempt to apply this approach). In the above we take T as the temperature determined from the classical fit, and compute T_F, the Fermi temperature, from the number using [63]

$$T_F = \frac{\hbar\bar{\omega}}{k_B}(6N)^{1/3}, \tag{8.27}$$

where $\bar{\omega} = (\omega_x\omega_y\omega_z)^{1/3}$. Note that this takes N to be the number of atoms *in a given spin state*, while the N measured by the experiment is the *total* number of

atoms.

Once we have a value of the chemical potential, we refit the data to a form of the Fermi-Dirac distribution (3.53). We use an unnormalized version

$$f(i) = A\frac{\mathrm{Li}_{5/2}\left[-\lambda\, e^{\frac{U_0}{k_BT}} e^{-\frac{i^2}{c_i^2}}\right]}{\mathrm{Li}_{5/2}\left[-\lambda\, e^{\frac{U_0}{k_BT}}\right]}\,. \tag{8.28}$$

Here A is a fit parameter included to allow the fit routine to adjust the overall scale, and the denominator is included so that the overall scale is set by the parameter A. As before, $\lambda = \exp\left[\mu/(k_BT)\right]$. Of course IGOR does not have a built-in polylogarithm function, so we use a series expansion. In Chapter 3 we provided the series expansion for when the argument has magnitude less than one (3.21), but here we must also work outside this region. The appropriate expansion for arguments with magnitude greater than one is [45]

$$\mathrm{Li}_n\left[x\right] = \Gamma(1-n)\left[\ln\left(\frac{1}{x}\right)\right]^{n-1} + \sum_{k=0}^{\infty}\frac{\zeta(n-k)\ln^k(x)}{k!}\,; \qquad |x| > 1, \tag{8.29}$$

where $\Gamma(n)$ is the gamma function and $\zeta(n)$ is the Riemann zeta function. We take 5 terms in each series.

The fitting is performed holding all parameters except c_i and A constant. This new value for c_i is then converted into a temperature using (8.25).

8.5.3 Degeneracy Parameter

An important question now arises: How should we characterize the degeneracy of a gas that obeys Fermi-Dirac statistics? The answer to this question is not so clear cut.

In the case of Bose-Einstein statistics, it makes sense to compute the *semiclassical phase-space density* ρ. For N atoms in a given spin state, the semiclassical phase-space density is given by

$$\rho = N \left(\frac{\hbar \bar{\omega}}{k_B T} \right)^3 . \tag{8.30}$$

This result assumes a classical gas, so it clearly breaks down as we approach degeneracy. However, for Bose-Einstein statistics, a reasonable definition of degeneracy is when $\rho > 1$. This is arguably the start of the macroscopic occupation of the ground state that is the hallmark of BEC. Of course, the situation is clarified by the existence of a phase-transition in a Bose-Einstein system—when the system reaches degeneracy, dramatic changes occur in the gas.

For a Fermi-Dirac system, (8.30) makes sense only until we approach degeneracy. Then, the real quantum occupation asymptotically approaches unity [10], while (8.30) predicts ever increasing occupations. Further, the lack of a phase transition makes it difficult to pick any particular point as the "onset of degeneracy". The groups working in the field have chosen $\rho = 1$ as the dividing line. Because (8.30) has no physical relevance to a Fermi-Dirac system in this regime, we would prefer to work with a different parameter. A more relevant factor is the *degeneracy parameter* T/T_F, the ratio of the temperature to the Fermi temperature. From the expression for the Fermi temperature (8.27), we see that we can write the phase-space density in terms of the Fermi temperature

$$\rho = \frac{1}{6} \left(\frac{T_F}{T} \right)^3 . \tag{8.31}$$

Thus, our definition of degeneracy ($\rho < 1$), becomes $T/T_F < 0.55$, and the determi-

nation of the degeneracy state becomes simply an exercise in computing this ratio from the number and temperature data extracted from the atomic distributions. A schematic of the analysis procedure is shown in Figure 8.6

8.6 Results

As described in Chapter 6, we prepared atomic samples using forced evaporation durations of 10, 15, 20, 40, and 60 s. After forced evaporation, the trap is adiabatically recompressed (maintaining the degeneracy state), and the gas is released and imaged after ballistic expansion. The data were analyzed according to the techniques presented above. The values of N, T, and T/T_F from the analysis are shown in Figure 8.7, Figure 8.8, and Figure 8.9, respectively.

At approximately $\tau \simeq 40\,\mathrm{s}$, $T/T_F = 0.55$, and we have entered the degenerate regime. To provide a more visual representation of this fact, we can convert the one-dimensional density distributions $\check{n}(i)$ from spatial distributions to velocity distributions by dividing by the expansion time τ (This neglects the finite initial size of the cloud. However, given the extremely small transverse dimension of the trapped optical cloud, this is negligible for all but the shortest of expansion times). Similarly, we can convert the Fermi temperature T_F into a Fermi velocity v_F:

$$v_F = \sqrt{\frac{2\,k_B T_F}{m}}. \tag{8.32}$$

We can then plot the velocity distributions and examine the fraction of the distribution that lies above v_F. At zero-temperature, of course, the cloud lies entirely within v_F, while in the classical limit, large portions of the cloud lie above v_F.

These types of plots are presented in Figure 8.10, Figure 8.11, Figure 8.12,

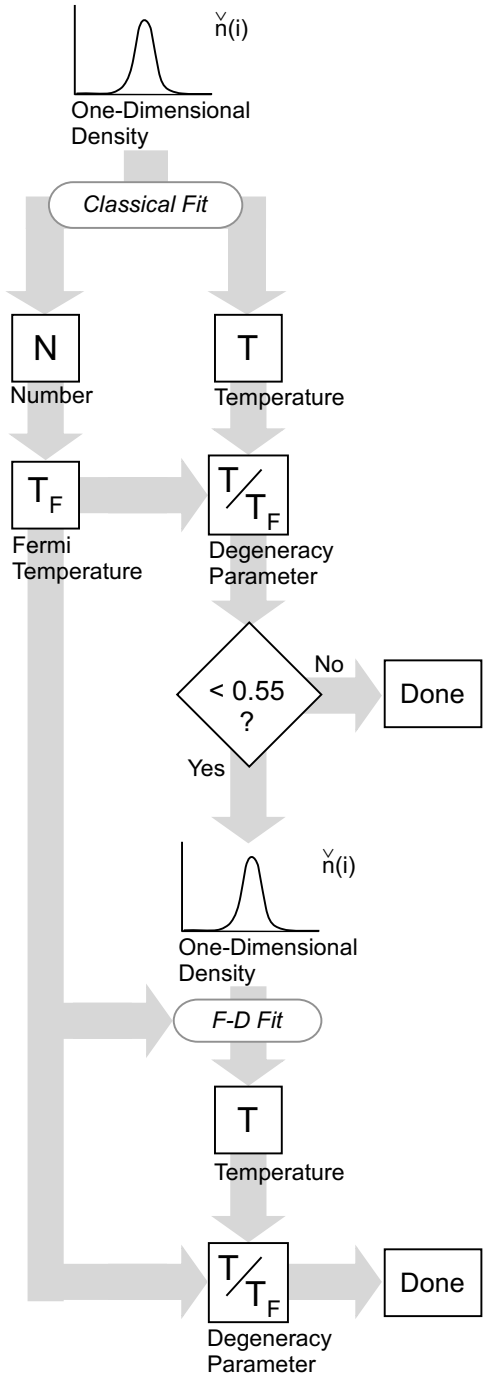

Figure 8.6: Analysis procedure.

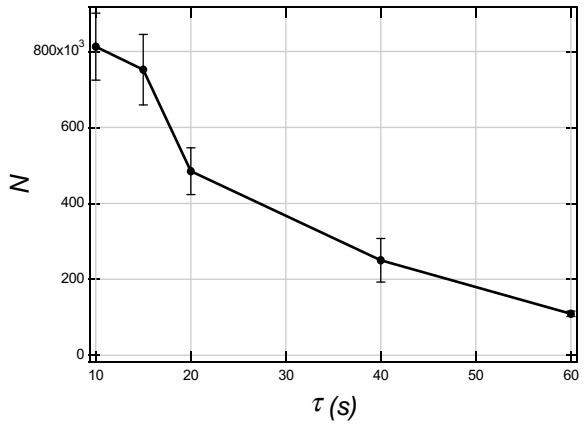

Figure 8.7: Atom number as a function of forced evaporation time.

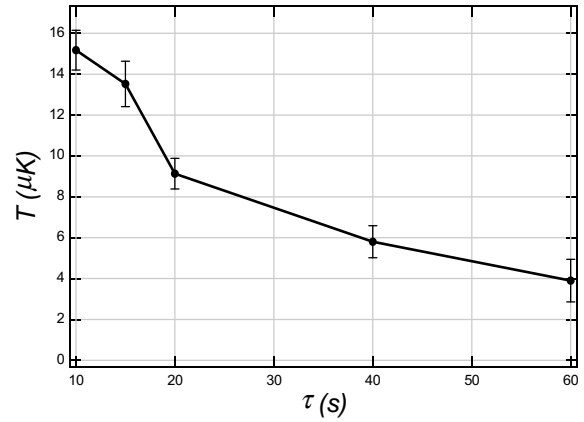

Figure 8.8: Cloud temperature as a function of forced evaporation time.

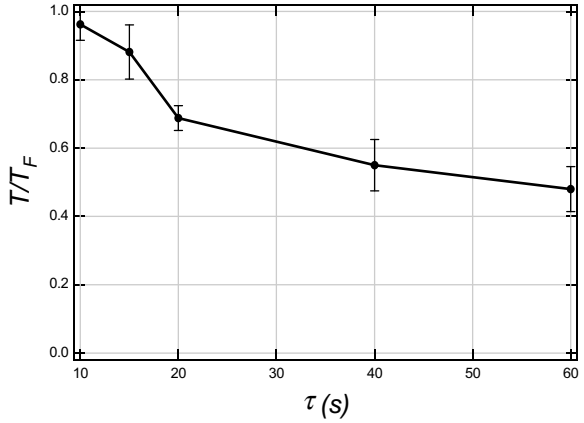

Figure 8.9: Degeneracy state (T/T_F) as a function of forced evaporation time.

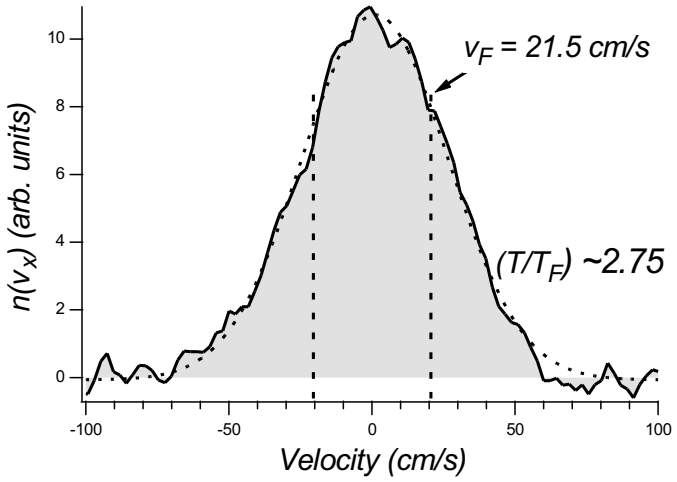

Figure 8.10: Velocity distribution of trapped atoms with 0 s of forced evaporative cooling.

and Figure 8.13 for data taken after 0, 10, 40, and 60 s of forced evaporative cooling. Each plot shows the atomic distribution (filled, solid curve), the fit to the data (thin, dashed curve), and the Fermi velocity v_F (broad, dashed, vertical lines). The cloud with no forced evaporative cooling is quite broad, with a majority of the atoms above the Fermi velocity. As expected, for the data taken after 10 s of forced evaporative cooling, the cloud has shrunk, but still has significant tails above v_F. The data at 40 s, however, has narrowed dramatically. Finally the data from 60 s of forced evaporative cooling has only the slightest wings above v_F.

These data support the claim that we have successfully created a degenerate Fermi gas of ^{6}Li (in actuality, it is two degenerate Fermi gases, as both spin states are degenerate). This represents the fourth experimental realization of a degenerate Fermi gas, and the first time a degenerate Fermi gas was created by all-optical techniques.

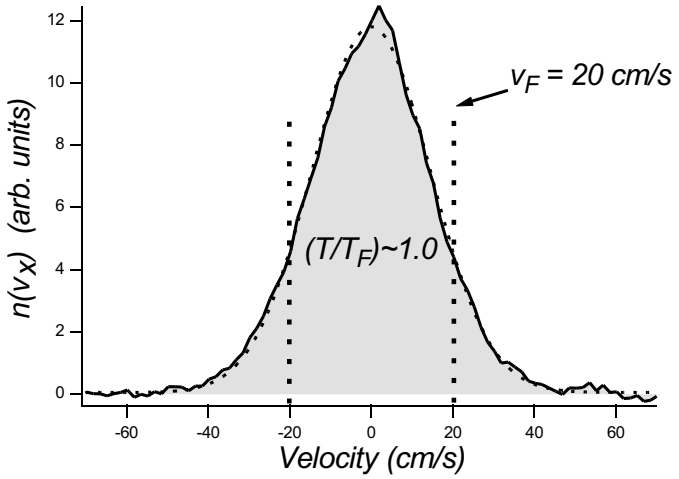

Figure 8.11: Velocity distribution of trapped atoms with 10 s of forced evaporative cooling.

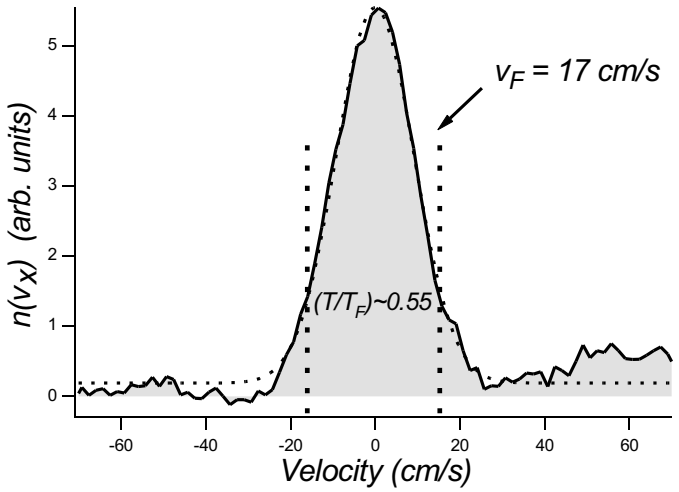

Figure 8.12: Velocity distribution of trapped atoms with 40 s of forced evaporative cooling.

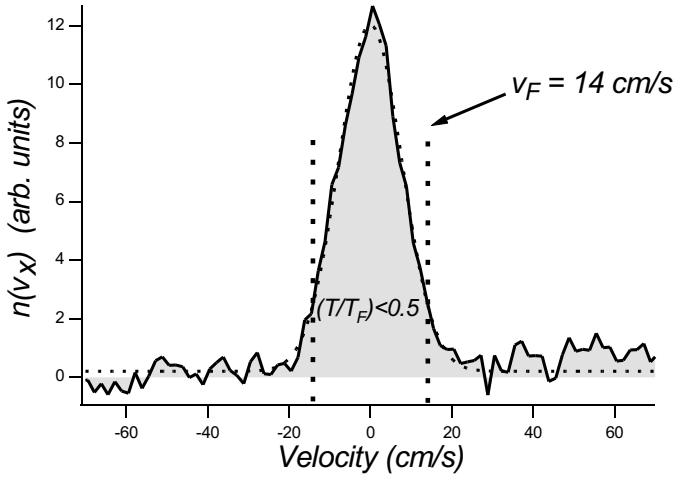

Figure 8.13: Velocity distribution of trapped atoms with 60 s of forced evaporative cooling.

8.6.1 Error Discussion

How certain can we be that the system has indeed prepared a degenerate sample? This section addresses that concern by presenting a discussion of the likely error magnitudes.

Number

The uncertainty in the number is dominated by uncertainty in the physical process of absorption (the system is not truly a simple two-level atom). The analysis we performed at the time we wrote [64], showed that our measured atom number was accurate to 10%.

Temperature

The temperature determination in the experiment derives from the relationship given in (8.25). We rewrite the result, organizing the terms differently to get

$$T = \frac{m}{4k_B}\, w^2 \left(\frac{\Delta x_{\rm cam}}{M}\right)^2 \frac{\omega_x^2}{1+\omega_x^2\tau^2}. \tag{8.33}$$

We now consider each of these terms to determine which require an uncertainty estimate. The first term, $m/(4k_B)$, contains only the mass of ^{6}Li and the Boltzmann constant, both of which have been determined to levels of precision far beyond this experiment. Uncertainty in this term can be neglected. The second term, w, is the measurement that we make in the experiment. For the purposes of this analysis, it also has no uncertainty contribution. The third term, $(\Delta x_{\rm cam}/M)^2$ contains the physical size of the camera pixels and the overall magnification of our imaging system. Current semiconductor lithographic techniques are capable of producing features many orders of magnitude smaller than the 13 μm size of the camera pixels. The uncertainty in $\Delta x_{\rm cam}$, is therefore also negligible. M, the camera magnification, was determined by an experiment reported earlier in this chapter, and does contribute in a significant way to the overall uncertainty in the temperature. The final term, $\omega_x^2/(1+\omega_x^2\tau^2)$ can be simplified somewhat. For the parameters used in our experiment, $\omega_x^2\tau^2 \simeq 300$. Therefore, the 1 in the denominator can be safely neglected, and the final term is very closely approximated by $1/\tau^2$. The expansion time is controlled in our experiment by a pulse generator with 50 ps error, which is completely negligible on the timescales used in this experiment. However, there *is* some timing uncertainty because of the finite imaging pulse duration.

We must now attempt to estimate the magnitude of the uncertainty in the error-

contributing term $1/(M^2\tau^2)$. From Section 8.4.2, we see that the uncertainty in the magnification arises from uncertainty in the slope of the line relating the several measurements made in that section. From the analysis done at that time, the uncertainty in the magnification is approximately 2%, implying that the uncertainty in M^2 is 4%. The uncertainty in τ arises, as mentioned previously, through the fact that the imaging pulse has a finite duration. The imaging pulse used in the experiment is $10\,\mu$s, compared to an expansion time of $400\,\mu$s, for an uncertainty of 2.5%. Thus, the uncertainty in τ^2 is 5%. Adding these values quadratically, we get an overall uncertainty in the temperature of 6.4%.

Degeneracy Parameter, T/T_F

From (8.27), we see that the uncertainty in the Fermi temperature T_F arises from uncertainty in $(\omega N)^{1/3}$. The uncertainty in our trap frequencies is, at worst, 5%, while our number measurement is accurate to 10%, as mentioned above. Combining these results quadratically and accounting for the cube-root dependence, we see that the uncertainty in T_F is 4%. We then combine this with the 6.4% uncertainty in the temperature to find the overall uncertainty in our determination of T/T_F to be 7.5%. Thus, we can indeed claim to have produced degenerate samples of ^{6}Li.

Chapter 9

Conclusions

9.1 Overview

The primary experimental result of this thesis is the experimental production of a degenerate Fermi gas of ^{6}Li [20]. This represents the fourth degenerate Fermi gas of neutral atoms, and the first ever produced via all-optical means. In addition, the thesis focuses on the conceptual models, theoretical treatments, and experimental procedures we had to develop over the years as we first learned how to trap neutral atoms, then how to manipulate and measure them, and finally how to cool them to degeneracy. The next section of this chapter provides a detailed summary of the individual chapters. Subsequent sections discuss possible improvements to the experiment and the future outlook for this type of research.

9.2 Chapter Summaries

The Introduction describes how research on degenerate Fermi gases arose as a natural offshoot of the earlier work on Bose-Einstein condensates and discusses how the current thinking on degnerate Fermi gases has evolved greatly from those early days. It presents the broad outlines of this thesis and illuminates the connections to

prior theses by this group (most notably [21] by Ken O'Hara) and to a concurrent thesis on the same experiment ([20] by Stephen Granade).

Chapter 2, "Basic Cooling and Trapping Techniques," describes the underlying techniques used in the experiment presented in this thesis. It presents the basic physics of the MOT, the FORT, and evaporative cooling. Real world complications to the techniques are discussed, particularly in the context of ^{6}Li. The chapter concludes with a discussion of the scaling laws exhibited in evaporative cooling and the derivation of the appropriate lowering curve for the CO_2 laser intensity [40].

Chapter 3, "Trapped Atomic Clouds: Equilibrium Distributions and Ballistic Expansion," derives expressions for the spatial and momentum distributions of trapped Maxwell-Boltzmann and Fermi-Dirac gases. In addition, the chapter treats the case where the trapped gases are allowed to expand ballistically and derives the appropriate time-dependent spatial distributions. These results play a large role in the analysis of the experimental data in Chapter 8.

Chapter 4, "The Monte-Carlo Model," presents the first entirely new result of this thesis. Monte-Carlo techniques are applied to the problem of numerically simulating a trapped Maxwell-Boltzmann gas in a Gaussian potential well. The relevant probability distributions for generating a random atomic ensemble under these conditions are derived and the output of a computer program using these distributions is validated. The remainder of the chapter addresses applications of the model, ranging from early temperature measurement techniques to discoveries of deviations from harmonic behavior for even atoms quite low in the Gaussian well.

Chapter 5, "Dynamics of Noise-Induced Heating," addresses the problem of heating in atom traps as a result of fluctuations in the trapping potential. The chapter presents the basic physics of the phenomenon as well as a Fokker-Planck treatment

of the evolution of an atomic distribution subject to these heating mechanisms (as previously published in [26] and [27]). The chapter goes far beyond these results, however, and develops a full, analytic eigenmode analysis of the Fokker-Planck equation, as well as a complete stability analysis of the corresponding difference equations. An important observation of the chapter is that the predicted long-time evolution is consistent with the observed behavior of early optical traps [28]. This lends credence to the argument that it was noise-induced heating that was the fundamental obstacle to the creation of a working optical trap (an argument that gains further credence by our success in creating a working trap with an ultrastable optical source [39]).

Chapter 6, "Experimental Setup and Procedure," is a detailed discussion of the experiment to produce a degenerate Fermi gas of ^{6}Li via all-optical means. It provides a description of all the major portions of the experimental apparatus as well as a step-by-step presentation of the procedure.

Chapter 7, "Imaging of Trapped Atomic Clouds," presents the physics of the basic imaging techniques used in atomic cooling and trapping experiments. For each technique, the intensity distribution of the imaging beam is given as a function of the column density of the atomic cloud that the beam passes through. An important parameter in these expressions is the optical scattering cross-section. The value of the optical cross-section is derived for the specific case used in this experiment, and for a more general case that may become useful in the future. The chapter concludes with an development of a simple model relating the signal-to-noise ratio of images to the physical parameters of the imaging system. The model is useful in analyzing prospective imaging systems to see if they will produce data of sufficient quality.

Chapter 8, "Detection of Degeneracy," discusses the analysis of the images that were the end result of the experiment described in Chapter 6. The chapter builds upon the theoretical distributions derived in Chapter 3 and the basics of imaging presented in Chapter 7 to develop an analysis procedure for the experimental data. The chapter further discusses experimental techniques for determining system parameters needed for the analysis. The analysis procedure clearly shows that the experiment succeeded in generating a degenerate Fermi gas of ^{6}Li.

This chapter, "Conclusions," provides a short overview of the broad accomplishments of this thesis. In addition, it includes detailed chapter summaries, a discussion of future improvements to the apparatus, and a discussion of the future outlook for research on degenerate Fermi gases.

Appendix A, "Properties of ^{6}Li," is a detailed look at the fundamental physical and optical properties of atomic ^{6}Li. The atomic structure of the groundstate and first excited state are presented, along with a discussion of how the atomic levels tune in the presence of applied magnetic and electric fields. Complete tables of transition matrix elements are provided for the D_1 and D_2 lines. The appendix concludes with a simple presentation of basic scattering theory for ultracold gases, and the specific details for a mixture of the two lowest hyperfine groundstates of ^{6}Li—the particular mixture we use in our experiments.

Appendix B, "Techniques for Generating Nonuniform Probability Density Functions," discusses the general approaches for producing random numbers distributed according to nonuniform probability distributions. Such techniques are applied in the Monte-Carlo code of Chapter 4 to generate the proper atomic ensembles. An important part of the techniques is the use of a probability distribution that approximates the desired distribution while always equalling or exceeding it in magnitude.

The final portion of the appendix describes the specific approximations used in the Monte-Carlo code.

Appendix C, "Computer Code Listings," presents computer codes used in throughout the thesis. The Mathematica codes that generated the ^{6}Li transition matrix elements, as well as the Zeeman and Stark effect tunings presented in Appendix A are included. The C-programs for the Monte-Carlo code of Chapter 4 and the numerical solution to the Fokker-Planck equation of Chapter 5 are included as well.

9.3 Improvements to the Experiment

There are a number of obvious improvements that can be made to the apparatus described in this thesis. Many of these have been implemented by Ken O'Hara and Staci Hemmer during the time it took to write this thesis. The next section describes the improvements that have already been made to the apparatus, while the subsequent section describes further improvements that can be made.

9.3.1 Implemented Improvements

High-Field Magnets

The apparatus presented in this experiment was capable of providing a uniform magnetic field for evaporative cooling of approximately 100 G, which translated to an s-wave scattering length on the order of -100 a_0. While this was sufficient for producing a degenerate gas, the evaporation rate this produced required experimental durations of many tens of seconds. Additionally, this field magnitude is far from the fields that are necessary to reach the broad Feshbach resonance in this system (see Section A.7.3). Producing the large scattering lengths possible in a Feshbach

resonance [15] is central to many of the most exciting possibilities in this system.

Even while the experiment of this thesis were underway, work was in progress to design a new set of magnetic coils. The decision was to build a pair of coils where the windings of each were encased inside a waterproof coilform. By placing the winding directly in contact with the coolant, it is possible to greatly increase the current driven through the coils. At full current, each coil receives 240 A and dissipates approximately 5 kW of power. When fully energized, the coils are capable of producing fields in excess of 1100 G and scattering lengths in excess of 1×10^4 a_0. In addition to allowing us to explore the new physical effects that appear at large scattering length, these fields also greatly enhance the efficiency and rate of evaporative cooling. We can now produce degenerate samples superior to those produced in this thesis in a fraction of a second [19] rather than the 40-60 s necessary in the experiment described here.

AO Thermal Stabilization

A major problem with the apparatus in this thesis was the deformation of the CO_2 laser beam profile as the laser intensity was lowered. We eventually discovered that this was the result of thermal effects in the germanium crystal of the AO. As discussed in Section 6.4.14, thermal lensing effects in the crystal cause a variation in the beam curvature that we correct with cylindrical lenses. As we lower the CO_2 intensity by lowering the power of the injected RF, the crystal cools somewhat, changing its lensing properties. As a result, the cylindrical lenses no longer properly correct the beam profile. The result is a change in the parameters of the trapping potential.

To combat this problem, we have added a method of thermal stabilization.

Rather than injecting the AO with only 40 MHz RF, we add a 35 MHz component as well. The power in the 35 MHz component is raised in counterpoint to the lowering of the 40 MHz RF component. In this way, the RF power to the crystal is constant. This maintains the temperature of the crystal and keeps the thermal lensing constant over the duration of the experiment. The presence of two frequency components in the AO generates two first-order beams. We use a pick-off mirror to deflect the beam corresponding to the 35 MHz component into a water-cooled beam dump.

RF Equalization of State Populations

In the experiment of this thesis, we optically-pump the atoms from the upper hyperfine groundstates into the lower hyperfine groundstates as part of the FORT loading process. We took no particular precautions to ensure that the populations of the two lower hyperfine groundstates were exactly equal at the end of this process. The symmetry of the system ensures that the two populations will be close to equal, but as the system is cooled, mismatches between the Fermi surfaces (the only place the two species interact) can cause slowing of the evaporative cooling process.

To ensure that the populations of the two states are equal, we installed an RF coil inside the vacuum chamber. We now apply a magnetic field of 8 G and simultaneously use the RF coil to generate a broadband RF field centered at 7.4 MHz [19]. This frequency matches the splitting of the two hyperfine states at the applied magnetic field and quickly mixes the populations, producing a very precise balance between the two states.

9.3.2 Possible Further Improvements

Increased Software Abstraction

Of all the improvements that were clearly necessary at the time of this experiment, only one remains undone—increasing the level of software abstraction in the timing system. The new timing system was a great improvement over the previous system largely because in introduced *abstraction* into the timing design. The details of the wiring were no longer important to the user. Creating a timing file is merely a matter of describing how you want the individual channels to behave.

However, there remain several places where increased abstraction could provide great benefit. The current form of a timing file is quite sufficient for describing the states of the individual channels. However, the channels in the file are essentially identified by their order. Swap the positions of two lines in the file, even if they remain labelled with the proper channel name, and the system sends the channel commands to the wrong pieces of equipment. We should insert an additional layer of abstraction that relates channel names with physical channel numbers. There is no reason the creator of a timing file should have to know that the "camera shutter" is line 28, but merely that they wish to control the camera shutter. Implementing such a layer would be quite trivial, but would eliminate a number of hard-to-troubleshoot errors.

Further, the current timing structure allows for the sending of *General Purpose Instrument Bus* (GPIB) commands to those pieces of equipment that accept them. However, the current formulation allows these commands to be sent only *once*. In the case where we wish to run the same general *form* of the experiment, but with varying parameters (such as when we step through modulation frequencies looking for a parametric resonance peak), the user must design a single-use LabView

program that repeatedly sends the new GPIB commands and runs the same timing file at each new setting. We should design a higher-level abstraction to the timing file—the *experiment file*. This file should describe what timing files to run, in what sequence, and what GPIB commands to send throughout the sequence. This would greatly speed the creation of new large-scale experimental procedures and allow a single, general-purpose LabView program to serve our many needs.

9.4 Future Outlook

The outlook for continued research in degenerate Fermi gases is quite good. In the time since we completed the experiment in this thesis, our group has used the new high-field magnets to observe the zero-crossing in the s-wave scattering length near 530 G [65]. Similar measurements and experiments have been performed by other groups [66, 67]. These measurements provide important constraints on the molecular potentials that determine the precise location of the Feshbach resonance.

Our group has gone further and performed the first experiment on a *strongly-interacting* degenerate Fermi gas [19]. This experiment provided the first measurement of a universal fermion parameter [11, 12] as well as strong evidence for the formation of a resonance superfluid [16–18]. We currently have experiments underway to directly observe superfluid properties and pairing interactions in the degenerate gas. Other groups no doubt have similar efforts in progress. It seems quite likely that the next year will see success on these fronts and the first experiments on collective oscillations and vortices in a fermionic superfluid.

Appendix A

Properties of ^{6}Li

. . . in order to understand the nature of things, we must begin by asking, not whether a thing is good or bad, . . . but of what kind it is? And how much is there of it?

—James Clerk Maxwell

A.1 Overview

This chapter attempts to provide many of the important physical properties of bulk and atomic ^{6}Li that are relevant to atomic cooling and trapping experiments. Parameters that result from experimental measurement are referenced to their source (either primary or secondary), while the calculations behind derived quantities are explained and references to detailed treatments are provided where possible. The content and presentation style of the beginning portions of this chapter are heavily inspired by Steck's excellent unpublished resources on ^{133}Cs and ^{23}Na [68,69], while the later half draws on the exposition of scattering presented in a previous thesis by O'Hara [21].

The reader will notice this chapter is written at an elementary level, and includes atomic properties not directly related to the work in the remainder of this thesis. This approach is intentional, and is taken in the hope that, in the future, this chapter can be excerpted for use as a reference to ^{6}Li within our research group.

Property	Symbol	Value	Ref.
Density (300 K)	ρ	$0.534\,\mathrm{g}\cdot\mathrm{cm}^{-3}$	[70]
Melting Point	T_M	453.69 K	[70]
Heat of Fusion	Q_F	$2.99\,\mathrm{kJ}\cdot\mathrm{mol}^{-1}$	[70]
Boiling Point	T_B	1615 K	[70]
Heat of Vaporization	Q_V	$134.7\,\mathrm{kJ}\cdot\mathrm{mol}^{-1}$	[70]

Table A.1: Fundamental physical properties of bulk lithium.

A.2 Fundamental Physical Properties

Lithium, in solid form, is the lightest of the metals and presents a silvery-grey appearance. Like all alkalis, it reacts with water, but not as violently as sodium [70]. The fundamental physical properties of bulk lithium are listed in Table A.1. The concentration on thermodynamic properties is indicative of the fact that in atomic cooling and trapping experiments, the bulk element is only used as a consumable for the atomic source. In addition to the numerical data in the table, there is one more important bulk property—vapor pressure. The atomic number density is directly related to the vapor pressure and is the primary adjustable parameter for a given atomic-beam or vapor-cell atom source. The vapor pressure of lithium in the solid and liquid phases is given by [71]

$$\begin{aligned}
\log_{10} P_{V_{sol}} &= -54.87864 - \frac{6450.944}{T} - 0.01487480\,T + 24.82251\,\log_{10} T\,, \\
\log_{10} P_{V_{liq}} &= 10.34540 - \frac{8345.574}{T} - 0.00008840\,T - 0.68106\,\log_{10} T\,.
\end{aligned}$$

Above, pressure is in Torr (mm Hg) and temperature is in Kelvin. A plot of the vapor pressure over temperature ranges relevant to our experiment is shown in Figure A.1.

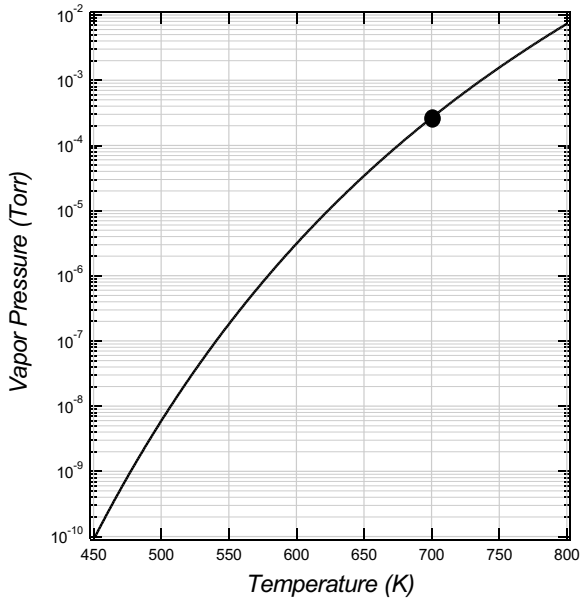

Figure A.1: Vapor pressure of ^{6}Li. The melting point of ^{6}Li occurs at the left axis. The circle marks the approximate operating point of our atomic source.

Lithium appears naturally in two stable isotopes. ^{7}Li with four neutrons, and ^{6}Li with three. Since the two isotopes differ by a single spin-$1/2$ particle, they exhibit different quantum statistics. ^{7}Li is a composite boson, while ^{6}Li is a composite fermion. This thesis is solely concerned with the fermionic isotope. The fundamental physical properties of ^{6}Li in its atomic form are shown in Table A.2

A.3 Optical Properties

Like all alkalis, the optical spectrum of lithium contains a prominent spectroscopic feature, called the *D*-line for historical reasons. It is fairly easy to discern that this line consists of two narrowly separated features, logically named the D_1 (redmost) and D_2 lines. The physical principles underlying the two components and their, as yet unmentioned, internal structure will be briefly discussed in the next section. Some basic properties of the D_1 and D_2 transitions in ^{6}Li are listed in Table A.3

Property	Symbol	Value	Ref.
Atomic Number	Z	3	
Nucleons	$Z+N$	6	
Natural Abundance	η	7.6%	[70]
Nuclear Lifetime	τ_n	stable	[70]
Atomic Mass	m	$6.015\,121\,4\,\mathrm{u}$ $9.988\,341\,4\times10^{-27}\,\mathrm{kg}$	[72]
Total Electronic Spin	S	$1/2$	
Total Nuclear Spin	I	1	

Table A.2: Fundamental physical properties of atomic ^{6}Li.

and Table A.4, respectively.

The wavenumber, k, wavelength, λ, and the frequency, ν, in the tables are related by the expressions

$$k = \frac{2\pi}{\lambda} \qquad \text{and} \qquad \lambda\nu = c, \tag{A.1}$$

with c the speed of light in vacuum. It is interesting to note that the excited-state lifetimes for both the D_1 and D_2 lines are identical. This is not typical in the alkalis, however, for ^{6}Li the difference in the two lifetimes is within the uncertainty of the most precise measurement to date [73]. The natural linewidth of the the optical transitions is inversely related to the excited state lifetime,

$$\Gamma = \frac{1}{\tau}. \tag{A.2}$$

The recoil velocity is the velocity associated with the momentum of a single resonant

Property	Symbol	Value	Ref.
Wavelength (vacuum)	λ	670.992 421 nm	
Wavenumber (vacuum)	$k/2\pi$	14 903.298 cm^{-1}	[74]
Frequency	ν	446.789 634 THz	
Lifetime	τ	27.102 ns	[73]
Natural Linewidth	Γ	$36.898 \times 10^6\ \mathrm{s}^{-1}$ 5.872 4 MHz	
Atomic Recoil Velocity	v_{rec}	9.886 554 cm $\cdot$ sec^{-1}	
Recoil Temperature	T_{rec}	3.535 652 56 μK	

Table A.3: Optical properties of the D_1 line of ^{6}Li.

photon absorption or emission. It is easily calculated from

$$mv_{rec} = p_{rec} = \hbar k. \tag{A.3}$$

For atomic cooling and trapping experiments, it is customary to convert many parameters to temperature *units* (noting that the resulting values, since they do not represent equilibrium energy distributions, are not, strictly speaking, temperatures). The recoil velocity is converted to a recoil temperature by relating the kinetic and thermal energies:

$$\frac{1}{2}\, m\, v_{rec}^2 = k_b\, T_{rec}. \tag{A.4}$$

This shows that, were it possible for a ^{6}Li atom to be perfectly at rest, the absorption or emission of a single resonant photon will give the atom a speed comparable to atomic speeds in a gas of ^{6}Li at $\simeq 3.5\,\mu$K. Clearly, for an ultracold gas of ^{6}Li at $T_{\mathrm{gas}} \leq 1\,\mu$k (not unusual for a degenerate or near-degenerate sample), heating of this magnitude is to be avoided!

Property	Symbol	Value	Ref.
Wavelength (vacuum)	λ	670.977 338 nm	
Wavenumber (vacuum)	$k/2\pi$	14 903.633 cm^{-1}	[74]
Frequency	ν	446.799 677 THz	
Lifetime	τ	27.102 ns	[73]
Natural Linewidth	Γ	$36.898 \times 10^6\ \mathrm{s}^{-1}$ 5.872 4 MHz	
Atomic Recoil Velocity	v_{rec}	9.886 776 cm $\cdot$ sec^{-1}	
Recoil Temperature	T_{rec}	3.535 811 52 μK	

Table A.4: Optical properties of the D_2 line of ^{6}Li.

A.4 Fine and Hyperfine Structure

^{6}Li has a single, unparied valence electron. The ground state configuration is $1s^2\,2s^1$; while the excited state configuration is $1s^2\,2p^1$. The simplest view of the energy levels of ^{6}Li, the *central-field approximation*, takes only this fact into account, and computes the energy of the atom assuming that the valence electron is independent, and that the nucleus and closed electron shell produce a spherically-symmetric electric field. The resulting ground and excited states are schematically indicated in the leftmost column of Figure A.2. The transition between these two states is responsible for the broad structure of the spectroscopic D-line. The ground and excited levels are given the spectroscopic notation $2\,^2S$ and $2\,^2P$, respectively.

The two sub-features of the D-line, the D_1- and D_2-lines, result from the interaction between the intrinsic angular momentum (spin) of the valence electron and the angular momentum of its orbit. This interaction is known, naturally enough, as the *spin-orbit* coupling, and the splitting of the D-line into the D_1- and D_2-lines is the *fine structure*. Physically, the fact that there is an energy contribution from the interaction of the two angular momenta can be understood by considering the

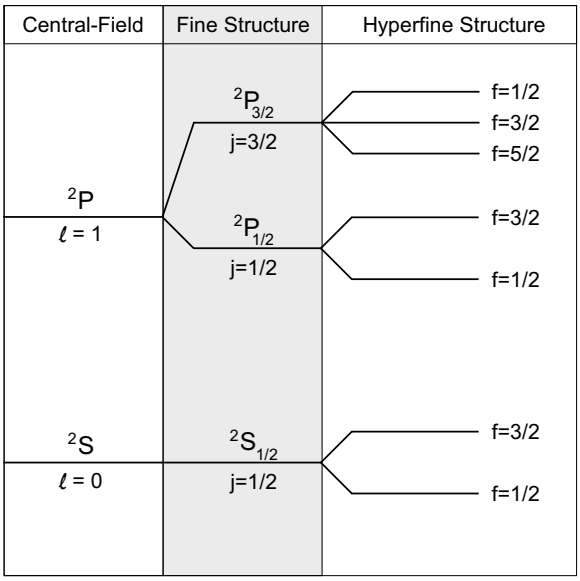

Figure A.2: Ground (lower) and first excited (upper) states of ^{6}Li in the L, J, and F bases. The states are also labelled with spectroscopic notation where appropriate. Energy splittings are not to scale.

gyromagnetic ratios (*g-factors*). The g-factors describe the fact that a charged particle with angular momentum naturally gives rise to a magnetic dipole moment—the g-factor is the constant of proportionality between the the two quantities. So the orbital angular momentum produces a magnetic dipole moment, as does the electron spin. There is an interaction energy between two dipole moments, however, and hence a contribution to the Hamiltonian. The interaction can be written as [75]:

$$\hat{H}'_{SO} = \frac{e}{2m^2c^2\hbar^2}\left[\frac{1}{r}\frac{d\Phi}{dr}\right]\hat{\mathbf{L}}\cdot\hat{\mathbf{S}} \equiv f(r)\,\hat{\mathbf{L}}\cdot\hat{\mathbf{S}}, \tag{A.5}$$

where $\hat{\mathbf{L}}$ and $\hat{\mathbf{S}}$ are the orbital angular momentum and spin operators, respectively. ϕ is the electric potential produced by the nucleus and the inner electrons, and r is the radial coordinate. In computing the value of this perturbation Hamiltonian, it is convenient to work in the total electronic angular momentum, $\hat{\mathbf{J}}$, basis. We

define a new operator

$$\hat{\mathbf{J}} = \hat{\mathbf{L}} + \hat{\mathbf{S}}. \tag{A.6}$$

The quantum-number J can then take on values in integral steps in the range

$$|L - S| \leq J \leq (L + S). \tag{A.7}$$

We can then make use of the identity

$$\hat{J}^2 = \hat{L}^2 + \hat{S}^2 + 2\,\hat{\mathbf{L}} \cdot \hat{\mathbf{S}}, \tag{A.8}$$

to write the interaction in (A.5) in terms of the operators $\hat{J}^2$, $\hat{L}^2$, and $\hat{S}^2$ which, along with $\hat{J}_z$ form a complete set of commuting operators.

Let us now apply this knowledge to the ground and excited states of ^{6}Li. The ground state has $S = 1/2$ and $L = 0$. This implies a single value for J, namely $J = 1/2$. The excited state, however, has $S = 1/2$ and $L = 1$. There are two possible values for J, $J = 1/2, 3/2$. Thus, the spin-orbit interaction splits the excited state into two. The state with $J = 1/2$ is given the spectroscopic name $2\,^2P_{1/2}$ and the state with $J = 3/2$ is named $2\,^2P_{3/2}$. The effect of the spin-orbit interaction is schematically indicated in the middle column of Figure A.2. We see now that the D_1-line is the spectroscopic feature that results from $2\,^2S_{1/2} \leftrightarrow 2\,^2P_{1/2}$ transitions and the D_2-line results from $2\,^2S_{1/2} \leftrightarrow 2\,^2P_{3/2}$ transitions. The g-factors for electron spin and $L = 1$ electron orbit, along with an experimental measurement of the fine-structure splitting, is given in Table A.5.

In the previous section, allusions were made to substructure within the D_1- and D_2-lines. This is known as the *hyperfine structure*, and results from the fact that the atomic nucleus is not truly spherically symmetric as we have assumed up to

Property	Symbol	Value	Ref.
Electron Spin g-factor	g_S	2.002 319 304 373 7	[76]
Electron $L = 1$ Orbital g-factor	g_L	0.999 995 87	
$2P$ Fine Structure Splitting	ΔE_{FS}	10.053 044 GHz	[77]

Table A.5: Electron g-factors and fine-structure splitting for ^{6}Li.

this point. Rather than consider the interaction energy of the valence electron in an asymmetric field from the nucleus, we consider the equivalent interaction energy of an asymmetric nucleus in the field of the valence electron. In such a framework, the interaction Hamiltonian is given by [78]:

$$\hat{H}'_{HF} = -\hat{\boldsymbol{\mu}} \cdot \hat{\mathbf{B}}(0) + \frac{1}{6}\, e \sum_{\alpha\beta} \hat{Q}_{\alpha\beta} \frac{\partial^2 \phi(0)}{\partial x_\alpha \partial x_\beta}, \tag{A.9}$$

where $\hat{\boldsymbol{\mu}}$ and $\hat{Q}$ are the nuclear magnetic dipole moment and nuclear electric quadrupole moment operators respectively. $\hat{\mathbf{B}}$ is the magnetic field operator at the location of the nucleus, and ϕ is the electric potential at the nucleus. The first term is a magnetic dipole interaction, and as such, is analogous to the spin-orbit interaction discussed previously. The second term is an electric quadrupole interaction and only contributes when the valence electron is in a state that has a non-spherically-symmetric electric field. Of the states we have considered, the $2\,^2S_{1/2}$ state arises from an orbital state with $L = 0$. As such, its angular wavefunction is given by a spherical harmonic Y_0^0, which is spherically symmetric. Additionally, the $2\,^2P_{1/2}$ state transitions to the ground state with only zero or one unit of transferred angular momentum, and as such can not support a quadrupole interaction with two units of angular momentum. Only the $2\,^2P_{3/2}$ can support such a interaction, and as a result, only it has a non-zero electric quadrupole contribution.

Property	Symbol	Value	Ref.
$2\,^2S_{1/2}$ Magnetic Dipole Constant	$A_{2\,^2S_{1/2}}$	152.136 840 7 MHz	[79]
$2\,^2P_{1/2}$ Magnetic Dipole Constant	$A_{2\,^2P_{1/2}}$	17.386 MHz	[77]
$2\,^2P_{3/2}$ Magnetic Dipole Constant	$A_{2\,^2P_{3/2}}$	-1.155 MHz	[79]
$2\,^2P_{3/2}$ Electric Quadrupole Constant	$B_{2\,^2P_{3/2}}$	-0.10 MHz	[79]

Table A.6: Hyperfine constants for the $2S$ and $2P$ levels of lithium.

To incorporate this interaction, it becomes convenient to work in the total atomic angular momentum, $\hat{\mathbf{F}}$, basis. We define

$$\hat{\mathbf{F}} = \hat{\mathbf{J}} + \hat{\mathbf{I}}, \tag{A.10}$$

where $\hat{\mathbf{I}}$ is the total nuclear angular momentum operator, analogous to $\hat{\mathbf{J}}$ for electrons. The quantum number F can take on values in integral steps in the range

$$|J - I| \leq F \leq (J + I). \tag{A.11}$$

We can then make use of an identity analogous to (A.8) to express the interaction in terms of $\hat{F}^2$, $\hat{J}^2$, and $\hat{I}^2$, which, along with $\hat{F}_z$, again form a complete set of commuting operators. In this new basis, the interaction is given by [78]

$$\Delta E_{HF} = \frac{1}{2}\, A\, C + \frac{3}{8}\, B\, \frac{C(C+1)}{I\,(2I-1)\,J\,(2J-1)}, \tag{A.12}$$

where $C = F(F+1) - J(J+1) - I(I+1)$, and A and B are the *magnetic dipole hyperfine constant* and *electric quadrupole hyperfine constant*, respectively for the F state of interest. Experimental measurements of the hyperfine constants of ^{6}Li are listed in Table A.6.

Applying these concepts to the fine-structure levels, we see that the $2\,^2S_{1/2}$ level with $J = 1/2$ and $I = 1$ (see Table A.2) has two possible values of F: $F = 1/2\,, 3/2$. The $2\,^2P_{1/2}$ state also has possible F-values of $F = 1/2\,, 3/2$. The $2\,^2P_{3/2}$ state, however, has the possible values $F = 1/2\,, 3/2, 5/2$. This splitting is indicated schematically in the rightmost column of Figure A.2.

At this point, we have essentially described the structure of the ground and $2P$ excited states of ^{6}Li in a region free of external fields. The results are summarized in a level diagram in Figure A.3. In the next section, we address the application of external fields.

A.5 Interaction With DC Fields

A.5.1 Magnetic Fields

The tuning of atomic levels in static magnetic field is known as the *Zeeman* effect. As we have previously noted, a charged particle with angular momentum is a magnetic dipole. Any such dipole will have an interaction energy in an applied magnetic field. The interaction Hamiltonian is quite simple, and is given by

$$\hat{H}_B = -\frac{\mu_B}{\hbar} \sum_x g_x \, \hat{\mathbf{X}}_z \cdot \hat{\mathbf{B}} \tag{A.13}$$

where the sum is over *good angular momentum quantum numbers*, and g_x and $\hat{X}_z$ are the g-factor and angular momentum projection operator corresponding to those numbers.

As the B-field increases from zero, the Zeeman interaction is initially small compared to the hyperfine interaction. Thus, we may treat it as a perturbation to

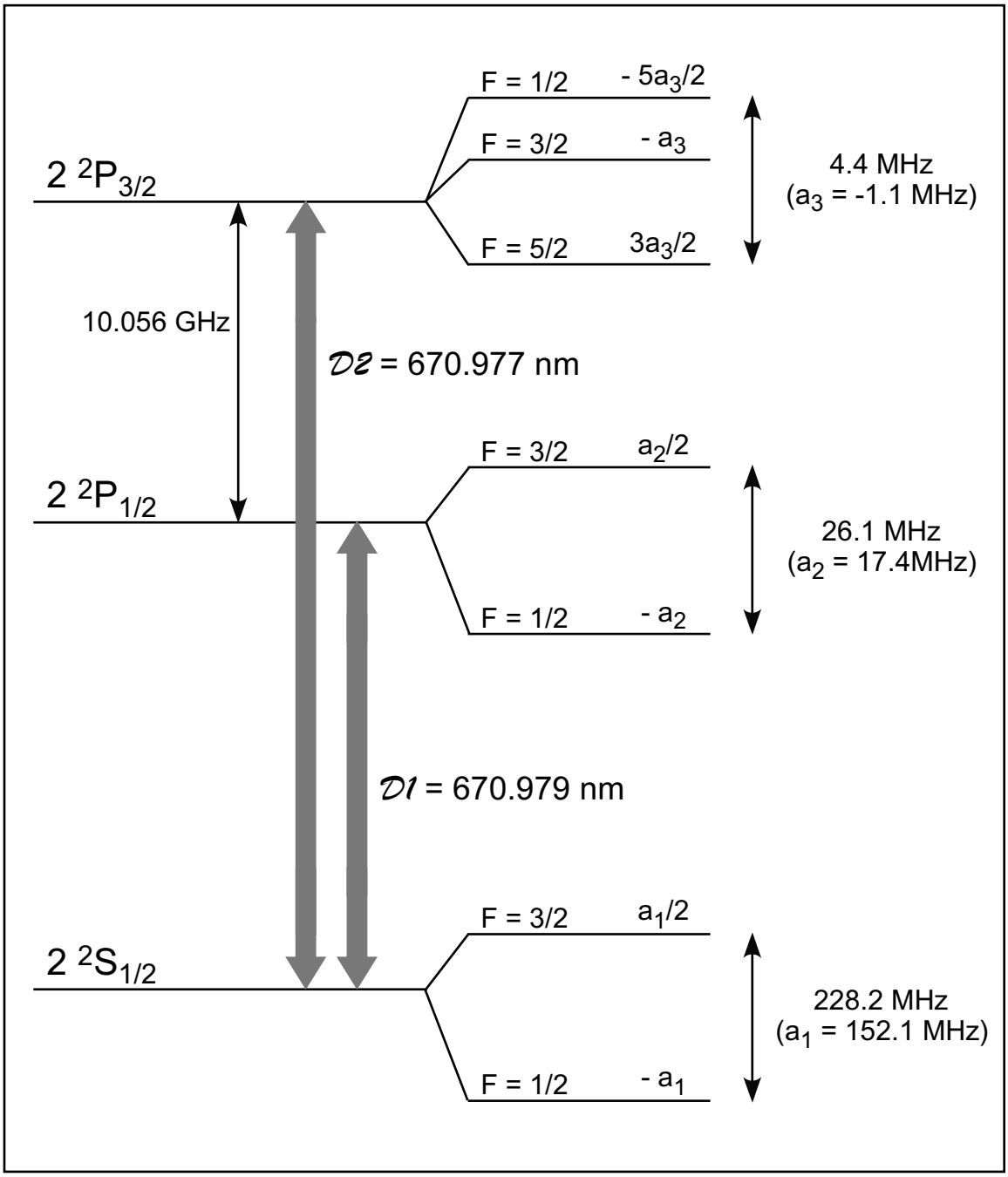

Figure A.3: Level diagram of the ground and 2P excited states of ^{6}Li. Energy splittings are not to scale.

Property	Symbol	Value	Ref.
Total Nuclear g-factor	g_I	-0.000 447 654 0	[79]
Total Electronic g-factor	$g_J\,(2\,^2S_{1/2})$	2.002 301 0	[79]
	$g_J\,(2\,^2P_{1/2})$	0.666 8	[79]
	$g_J\,(2\,^2P_{3/2})$	1.335	[79]

Table A.7: Total nuclear and total electronic g-factors for ^{6}Li.

the hyperfine levels we derived earlier. In this case, **F** precesses around **B**, hence F is still a good quantum number, and (A.13) reduces to

$$\Delta E_z = \frac{\mu_B}{\hbar} g_F m_F B. \tag{A.14}$$

The g-factor, g_F, is given by a *Landé g-factor* expression that combines g_J and g_I

$$g_F = g_J \frac{F(F+1) - I(I+1) + J(J+1)}{2F(F+1)} + g_I \frac{F(F+1) + I(I+1) - J(J+1)}{2F(F+1)}. \tag{A.15}$$

Values of g_J and g_I are given in Table A.7. In this regime, the energies tune linearly with B. In alkalis, this region is known as the *anomalous Zeeman effect*. "Anomalous" because the spectral lines split into doublets, quadruplets, and sextuplets, rather than triplets as predicted by a semiclassical theory of Lorenz (his theory was developed prior to knowledge of spin—as such, only atoms with total spin $S = 0$ exhibit the *normal Zeeman effect* at low field).

Eventually, the magnetic energy becomes significant compared to the hyperfine energy. When this happens, the Zeeman effect can no longer be treated as a perturbation. At this point, **F** ceases to be a good description of the system, and F is no longer a good quantum number. We are now forced to find eigenstates of the

combined interaction Hamiltonian

$$\hat{H}_{int} = \hat{H}_B + \hat{H}_{HF} = \frac{\mu_B}{\hbar} \sum_x g_x \, \hat{\mathbf{X}} \cdot \hat{\mathbf{B}} - \hat{\boldsymbol{\mu}} \cdot \hat{\mathbf{B}}(0) + \frac{1}{6} \, e \sum_{\alpha\beta} \hat{Q}_{\alpha\beta} \frac{\partial^2 \phi(0)}{\partial x_\alpha \partial x_\beta}. \quad \text{(A.16)}$$

This region occurs at very low fields for ^{6}Li. The ground and excited states have extremely small hyperfine splittings compared to other alkalis. As a result, the combined interaction Hamiltonian must be used for fields as small as a few Gauss. Finding the eigenstates is, of course, a matter of diagonalizing the Hamiltonian. While this is generally done numerically, it has been done analytically for the hyperfine ground states of ^{6}Li [42]. Expressed in the $|m_S \; m_I\rangle$ basis, the authors find the eigenstates to be

$$\begin{aligned}
|1\rangle &= \sin\theta_+ \, |1/2 \;\; 0\rangle - \cos\theta_+ \, |-1/2 \;\; 1\rangle \quad \text{(A.17)} \\
|2\rangle &= \sin\theta_- \, |1/2 \;\; -1\rangle - \cos\theta_- \, |-1/2 \;\; 0\rangle \\
|3\rangle &= |-1/2 \;\; -1\rangle \\
|4\rangle &= \cos\theta_- \, |1/2 \;\; -1\rangle + \sin\theta_- \, |-1/2 \;\; 0\rangle \\
|5\rangle &= \cos\theta_+ \, |1/2 \;\; 0\rangle + \sin\theta_+ \, |-1/2 \;\; 1\rangle \\
|6\rangle &= |1/2 \;\; 1\rangle
\end{aligned}$$

where the states are numbered in order of increasing energy. In the above, $\sin\theta_\pm = 1/\sqrt{1 + (Z^\pm + R^\pm)^2/2}$, $\cos\theta_\pm = \sqrt{1 - \sin\theta_\pm}$, $Z^\pm = (\mu_n + 2\mu_e)B/A_{2\,^2S_{1/2}} \pm 1/2$, and $R^\pm = \sqrt{(Z^\pm)^2 + 2}$. Also note that m_J has been replaced with m_S since $L = 0$ for the ground state.

Numerical results for the $2\,^2S_{1/2}$, $2\,^2P_{1/2}$, and $2\,^2P_{3/2}$ states are shown in Figures A.4, A.5 and A.6, respectively. The numerical results for the $2\,^2S_{1/2}$ state are

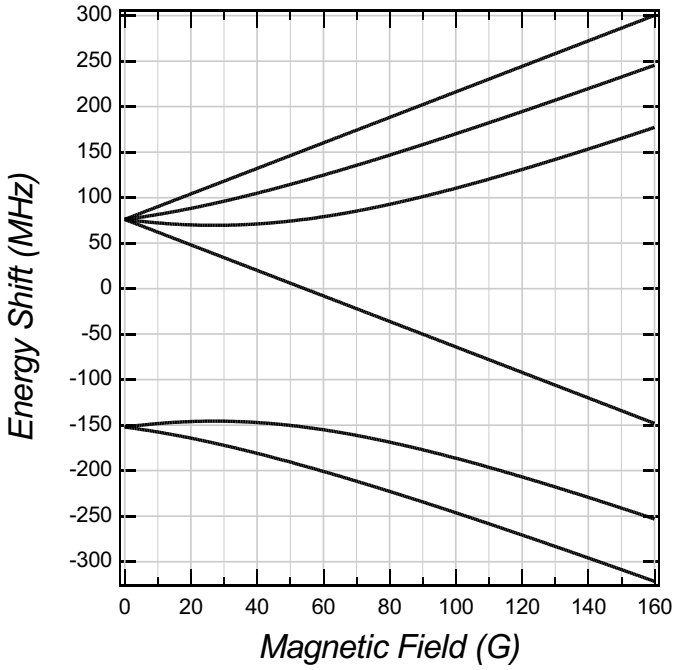

Figure A.4: Magnetic-field dependence of the $2\,^2S_{1/2}$ ground state of ^{6}Li.

identical to those obtained from the analytical results above. The computer code that generated these results is given in Section C.2.

As the field strength continues to grow, eventually the hyperfine energy can be neglected and the eigenstates are those of the Zeeman Hamiltonian. At this point, we can treat the atoms in a pure product state basis $|Jm_J\rangle\,|Im_I\rangle$. Each ket is treated independently with respect to the Zeeman effect—in other words (A.13) becomes:

$$\Delta E_z = \frac{\mu_B}{\hbar}(g_J m_J + g_I m_I)B. \tag{A.18}$$

At this point, the states are arranged into spectroscopic triplets (the normal Zeeman effect). Further, since $g_J \gg g_I$, for sufficiently large fields, the nuclear contribution

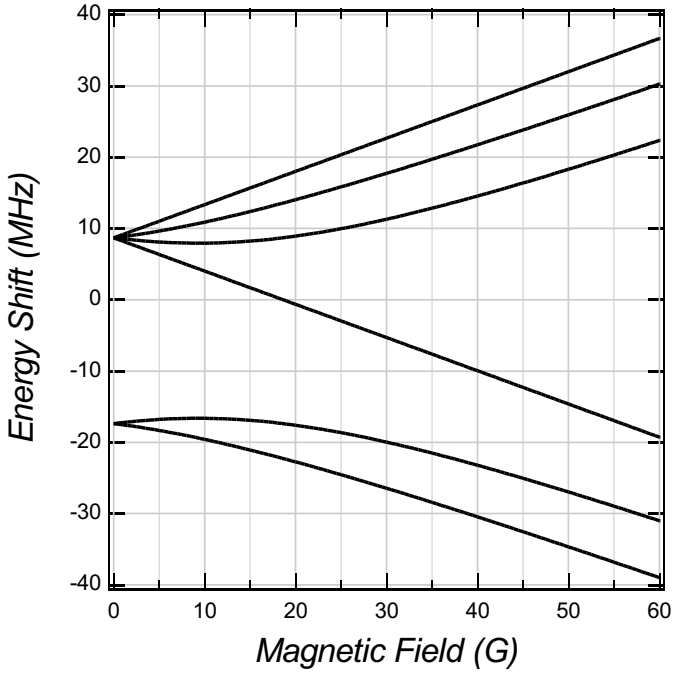

Figure A.5: Magnetic-field dependence of the $2\,^2P_{1/2}$ excited state of ^{6}Li.

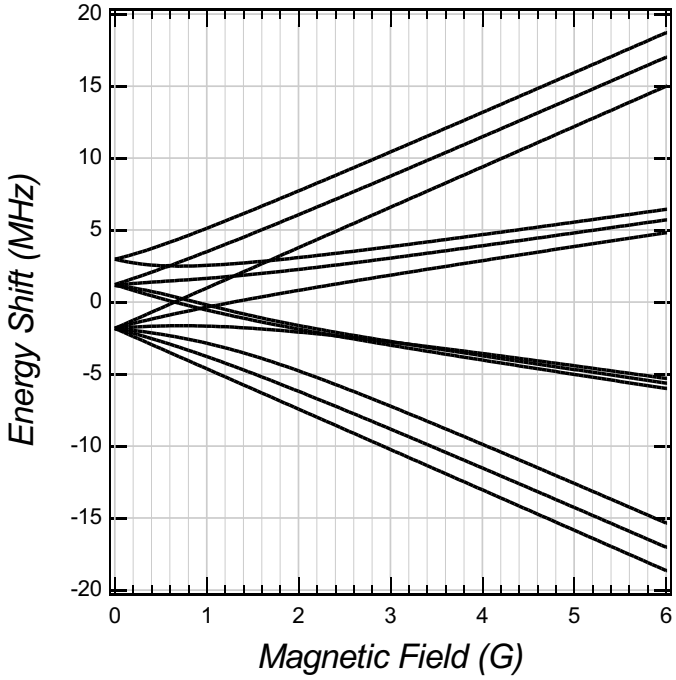

Figure A.6: Magnetic-field dependence of the $2\,^2P_{3/2}$ excited state of ^{6}Li.

can be neglected, and the energies are well approximated by

$$\Delta E_z \simeq \frac{\mu_B}{\hbar} g_J m_J B. \tag{A.19}$$

Of course, the numerical treatment of the complete Hamiltonian captures this behavior as well—note the organization of the levels into triplets in the high-field regions of Figures A.4, A.5 and A.6.

Eventually, the magnetic interaction will become significant with respect to the spin-orbit interaction. The two energies become comparable at fields on the order of 1 T=10 000 G. As a result, precision calculations must cease using the J-basis for field-strengths in excess of about 500-1000 G. Future experiments in our laboratory will place the atoms in field-strengths as large as 1200 G. To treat this problem, the atoms are described in the $|S\ m_S\rangle\,|L\ m_L\rangle\,|I\ m_I\rangle$ product basis, and the combined spin-orbit and Zeeman Hamiltonian is diagonalized (the excited state hyperfine interaction is neglected because of its relatively small contribution). The results of this calculation for the L=1 excited state are shown in Figure A.7.

A.5.2 Electric Fields

The interaction between an atom and a DC electric field is known as the *Stark effect* and is substantially simpler than the Zeeman effect. The interaction is described in the $\hat{\mathbf{J}}$-basis, and the interaction energy is given by [80]:

$$\Delta E_m = -1/2\ \alpha(m)\,\mathcal{E}^2 \tag{A.20}$$

where $\alpha(m)$ is the static polarizability of the atom in a magnetic sublevel m, and $\mathcal{E}$ is the electric field strength. By using irreducible tensor operators, it can be shown

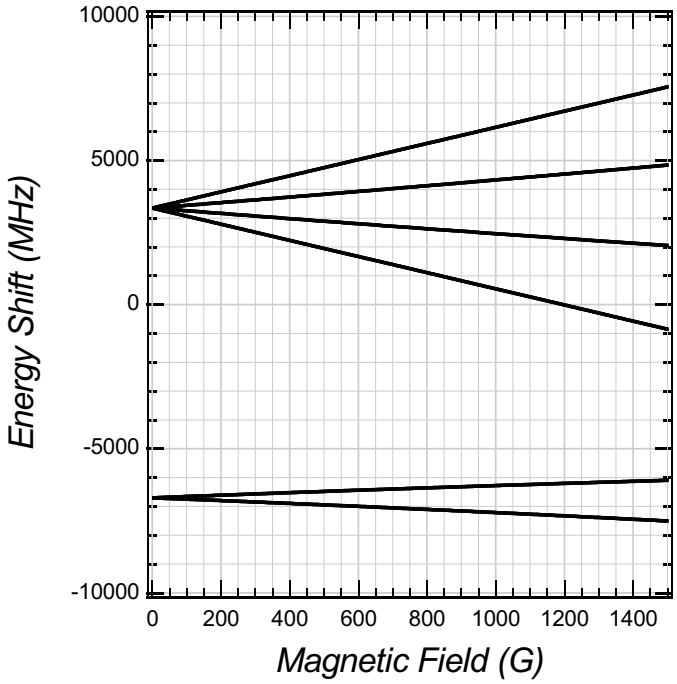

Figure A.7: High-field Zeeman splitting of the D_1 and D_2 excited states of ^{6}Li. The hyperfine contribution has been neglected in this calculation. The size of the nuclear contribution is negligible on this scale; as a result, each line is three-fold degenerate.

Property	Symbol	Value	Ref.
$2\,^2S_{1/2}$ Scalar Polarizability	$\alpha_0\,(2\,^2S_{1/2})$	$0.040\,8\,\mathrm{Hz/(V/cm)^2}$	[82]
$2\,^2P_{1/2}$ Scalar Polarizability	$\alpha_0\,(2\,^2P_{1/2})$	$0.031\,56\,\mathrm{Hz/(V/cm)^2}$	[83]
$2\,^2P_{3/2}$ Scalar Polarizability	$\alpha_0\,(2\,^2P_{3/2})$	$0.031\,63\,\mathrm{Hz/(V/cm)^2}$	[83]
$2\,^2P_{3/2}$ Tensor Polarizability	$\alpha_2\,(2\,^2P_{3/2})$	$0.000\,406\,\mathrm{Hz/(V/cm)^2}$	[83]

Table A.8: D-line polarizabilities of ^{6}Li.

that the static polarizability can always be written in terms of a scalar polarizability α_0 and a tensor polarizability α_2 [81]:

$$\alpha(m) = \alpha_0 + \alpha_2 \frac{3m^2 - J\,(J+1)}{J\,(2J-1)} \quad . \tag{A.21}$$

Table A.8 list the static and tensor polarizabilities for the $2\,^2S_{1/2}$, $2\,^2P_{1/2}$, and $2\,^2P_{3/2}$ levels of ^{6}Li. The tensor polarizability is rank 2, and as we saw before, only the $2\,^2P_{3/2}$ level can support such an operator. Hence, only that state has a tensor polarizability.

If we consider the atom in the $\hat{\mathbf{F}}$-basis, for small enough electric fields, the Stark interaction can be treated as a perturbation on the the hyperfine eigenstates. What is small enough? Well, if we consider an effect of $\simeq 5\%$ of the hyperfine energy as where a perturbation stops being small, then we can write the corresponding electric field strength as:

$$\mathcal{E}^2_{max} \;\simeq\; 2\,(0.05)\,\frac{A_J}{\alpha_{0_J}} \tag{A.22}$$

where A_J is the magnetic dipole hyperfine constant for the appropriate fine structure state (found in Table A.6). From this, we see that in the ground state, a perturbation treatment is acceptable up to a field strength of approximately 19.5 kV/cm! For the states in the $2\,^2P_{1/2}$ and $2\,^2P_{3/2}$ manifolds, we get values of 7.4 kV/cm and 1.9 kV/cm,

respectively.

In this regime, the eigenstates remain eigenstates of the $\hat{\mathbf{F}}$-basis, and we shift the energies of the levels according to (A.20) and (A.21). If we are interested in field strengths outside this range, then we must include both the Stark effect (A.20) and the hyperfine interaction (A.12) in our Hamiltonian, and diagonalize the resulting matrix. Eventually, of course, the Stark effect dominates the hyperfine interaction, and we can work solely with the Stark Hamiltonian.

For realistic experiments, we never have to consider a Hamiltonian that contains the Stark effect and the spin-orbit interaction. Using an equation analogous to (A.22) to calculate the range over which the Stark effect is a perturbation on the fine structure, we find that it takes fields greater than 170 kV/cm before this becomes an issue.

It is important to note that the predominant result of the Stark effect is an overall energy shift that is quadratic in the electric field. Only the $2\,^2P_{3/2}$ state, with a nonzero tensor polarizability, has a change in the relative splitting of its hyperfine constituents. A plot of this splitting, with the overall quadratic shift suppressed, is shown in Figure A.8. The computer code that produced these results is listed in Section C.3.

A.6 Interaction With Near-Resonant Light

A.6.1 Optical Transition Matrix Elements

The interaction between the internal states of the atom and an external, near-resonant optical field is quantified through the *electric-dipole transition matrix elements*. These matrix elements describe how the internal states of the atom couple

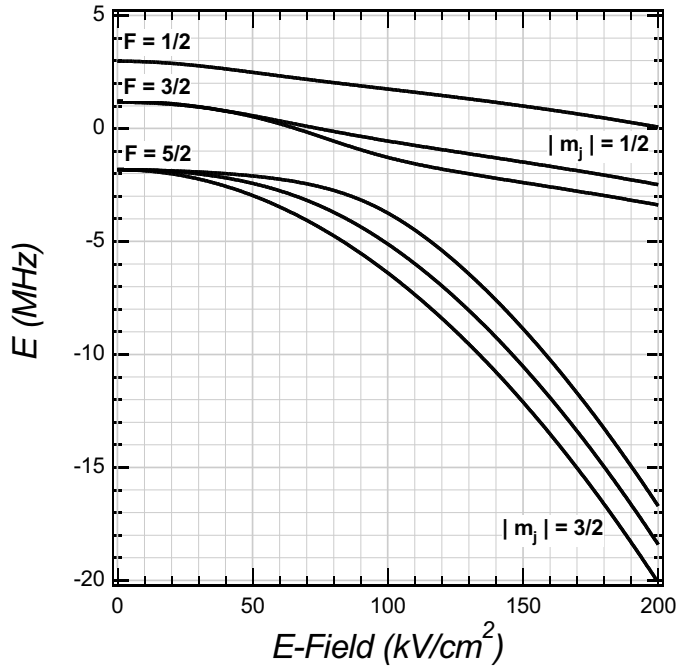

Figure A.8: Stark-effect shifts of the $2\,^2P_{3/2}$ level of ^{6}Li. An overall shift proportional to $\mathcal{E}^2$ has been suppressed.

to one another via an electric-dipole ($-\boldsymbol{\mu}\cdot\mathbf{E}$) interaction with the near-resonant field [58] (magnetic transitions and transitions of higher multipolar order exist, but are substantially weaker than the electric-dipole transition). If we start in a hyperfine state represented by $|(JI)Fm_F\rangle$ and couple to a state $\left|(J'I')F'm_{F'}\right\rangle$, then the matrix element for this transition is given by $\left\langle(J'I')F'm_{F'}\right|\hat{\boldsymbol{\mu}}\left|(JI)Fm_F\right\rangle$, where $\hat{\boldsymbol{\mu}}$ is the electric-dipole operator. We can use the *Wigner-Eckart Theorem* [62] to represent this matrix element in terms of a *reduced* matrix element that is m-independent. Recognizing that we can write the electric-dipole operator, $\hat{\boldsymbol{\mu}}$ as an irreducible spherical tensor operator, $\hat{\mu}(k,q)$, with $k=1$ and $q=-1,0,1$ for electric-dipole radiation with σ^-, π, and σ^+ polarization respectively, we can directly use

the Wigner-Eckart theorem to write [84]:

$$\left\langle (J'I')F'm_{F'}\left|\hat{\mu}(1,q)\right|(JI)Fm_F\right\rangle = (-1)^{F'-m_{F'}}\begin{pmatrix} J' & 1 & J \\ -m_{F'} & q & m_F \end{pmatrix}\times \left\langle (J'I')F'\left|\left|\hat{\mu}(1)\right|\right|(JI)F\right\rangle. \quad (A.23)$$

The reduced matrix element is written with double vertical bars for easy identification. The factor in parenthesis is known as a *Wigner 3-J Symbol* [62], and describes the magnetic-quantum-number-dependence of the matrix element. Most notably, it is identically zero unless $m_{F'} = m_F + q$ and $F' = F \pm 1$. Thus, it automatically enforces the appropriate selection rules.

We can further reduce the expression through the use of *angular momentum recoupling* [62]. Although a transition between two F-states changes F, it does so by changing J and leaving I unchanged. We can rewrite our reduced matrix element in a manner that makes the J-changing nature of the transition more apparent [84]:

$$\left\langle (J'I')F'\left|\left|\hat{\mu}(1)\right|\right|(JI)F\right\rangle = \delta_{I'I}\,(-1)^{J'+I+F+1}\sqrt{(2F'+1)(2F+1)}\times \begin{Bmatrix} J' & I & F' \\ F & 1 & J \end{Bmatrix}\left\langle J'\left|\left|\hat{\mu}(1)\right|\right|J\right\rangle. \quad (A.24)$$

The term in the large braces is a *Wigner 6-J Symbol* [62]. We can combine (A.23) and (A.24) to achieve the final result:

$$\left\langle (J'I')F'm_{F'}\left|\hat{\mu}(1,q)\right|(JI)Fm_F\right\rangle = \delta_{I'I}\,(-1)^{F'+F+J'+I-m_{F'}+1}\sqrt{(2F'+1)(2F+1)}\times \begin{pmatrix} J' & 1 & J \\ -m_{F'} & q & m_F \end{pmatrix}\begin{Bmatrix} J' & I & F' \\ F & 1 & J \end{Bmatrix}\times \left\langle J'\left|\left|\hat{\mu}(1)\right|\right|J\right\rangle. \quad (A.25)$$

It is hard to over-emphasize the importance of (A.25). A moment of reflection will show that for the states we have been considering, there are only two possible values of $\left\langle J' \middle|\middle| \hat{\mu}(1) \middle|\middle| J \right\rangle$—one for the D_1-line and one for the D_2-line! To calculate the transition strength between two F-levels, one merely has to determine whether the transition belongs to the D_1- or D_2-line and multiply the appropriate reduced matrix element by the prefactors of (A.25).

But what are the values of the reduced matrix elements? We can make a step towards answering this question by once again employing angular momentum recoupling. The total electronic angular momentum J is comprised of the orbital angular momentum L and the spin S. The electric dipole transition only changes L, so we can explicitly extract this L-changing nature of the transition. In analogy with (A.24):

$$\begin{aligned} \left\langle (L'S')J' \middle|\middle| \hat{\mu}(1) \middle|\middle| (LS)J \right\rangle &= \delta_{S'S} \, (-1)^{L'+S+J+1} \sqrt{(2J'+1)(2J+1)} \times \\ &\quad \begin{Bmatrix} J' & I & F' \\ F & 1 & J \end{Bmatrix} \left\langle L' \middle|\middle| \hat{\mu}(1) \middle|\middle| L \right\rangle . \end{aligned} \tag{A.26}$$

Now we have a single reduced matrix element that corresponds to the entire D-line. The value of this matrix element and of the D_1 and D_2 matrix elements are given in Table A.9. The prefactors in (A.25) have been tabulated for all all transitions in the D_1- and D_2-lines. The results are shown in Tables A.10, A.11 and A.12. The computer code that generated these values is listed in Section C.1.

A.6.2 Transition Matrix Element Sum Rules

The tables of transition matrix elements exhibit several interesting *sum rules* as a result of the symmetrical nature of the electric dipole operator. These rules can be

Property	Symbol	Value	Ref.
D-Line Reduced Matrix Element	$\langle L' = 1 \Vert \hat{\mu}(1) \Vert L = 0 \rangle$	1.148×10^{-29} C·m 3.443×10^{-18} esu·cm 3.443 Debye $\sqrt{3}\,\mu_0$	
D_1-Line Reduced Matrix Element	$\langle J' = 1/2 \Vert \hat{\mu}(1) \Vert J = 1/2 \rangle$	-2.812×10^{-29} C·m -8.433×10^{-18} esu·cm -8.433 Debye $-\sqrt{2}\,\mu_0$	
D_2-Line Reduced Matrix Element	$\langle J' = 3/2 \Vert \hat{\mu}(1) \Vert J = 1/2 \rangle$	3.977×10^{-29} C·m 11.925×10^{-18} esu·cm 11.925 Debye $2\,\mu_0$	

Table A.9: Reduced matrix elements for ^{6}Li.

simply derived from the mathematical properties of the 3- and 6-J symbols [62].

We begin by considering the sum of the squares of the matrix elements for transitions from a single magnetic sublevel, m_F, in a single level, F, to all magnetic sublevels in a single level, F', via all possible polarizations:

$$\begin{aligned} S_{F,F'} &= \sum_q \left| \left\langle (J'I')F'\,(m_F+q) \middle| \hat{\mu}(1,q) \middle| (JI)F\,m_F \right\rangle \right|^2 \\ &= (2F'+1) \begin{Bmatrix} J' & I & F' \\ F & 1 & J \end{Bmatrix}^2 \left| \left\langle J' \middle\| \hat{\mu}(1) \middle\| J \right\rangle \right|^2 . \end{aligned} \tag{A.27}$$

Note the result does not depend on m_F. Therefore the result is independent of what magnetic sublevel we start in. The values of $S_{F,F'}$ reflect the relative strength of transitions between different F-levels. These values are tabulated in Table A.13.

If we then sum over final F-levels, we derive the rule of primary physical impor-

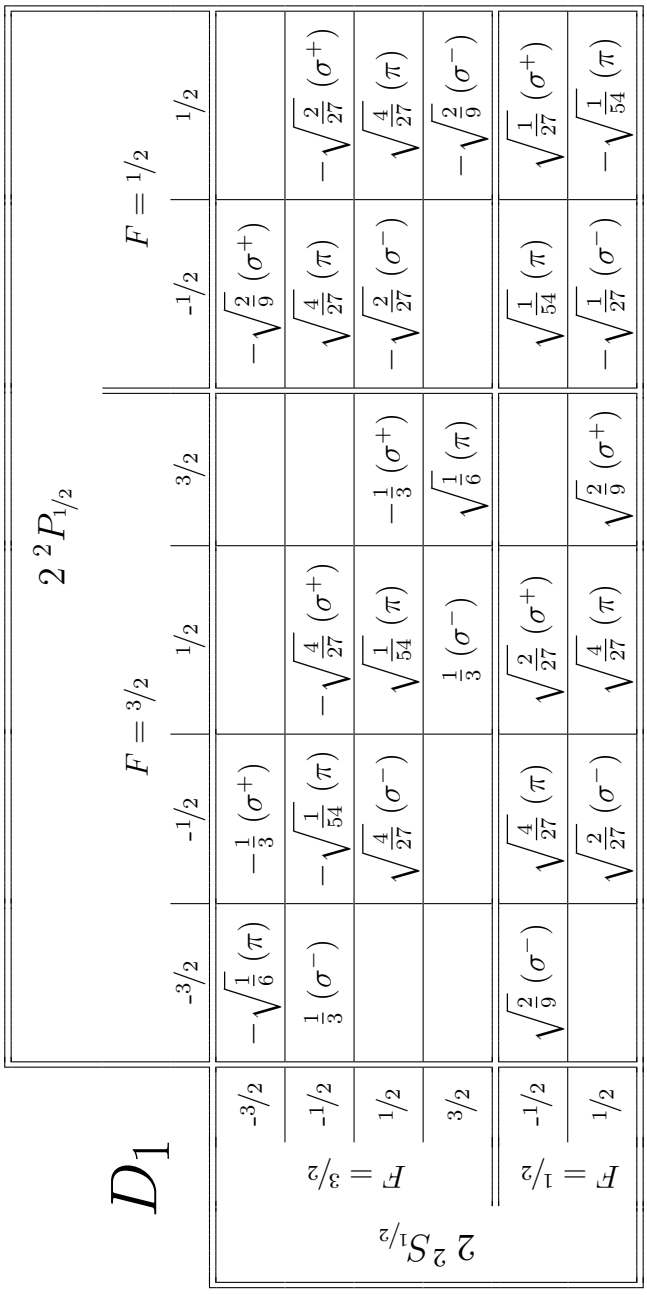

D_1		$2\,^2P_{1/2}$				
		$F = 3/2$			$F = 1/2$	
$2\,^2S_{1/2}$		-3/2	-1/2	1/2	3/2	-1/2	1/2
$F = 3/2$	-3/2	$-\sqrt{\frac{1}{6}}\,(\pi)$	$-\frac{1}{3}\,(\sigma^+)$			$-\sqrt{\frac{2}{9}}\,(\sigma^+)$	
	-1/2	$\frac{1}{3}\,(\sigma^-)$	$-\sqrt{\frac{1}{54}}\,(\pi)$	$-\sqrt{\frac{4}{27}}\,(\sigma^+)$		$\sqrt{\frac{4}{27}}\,(\pi)$	$-\sqrt{\frac{2}{27}}\,(\sigma^+)$
	1/2		$\sqrt{\frac{4}{27}}\,(\sigma^-)$	$\sqrt{\frac{1}{54}}\,(\pi)$	$-\frac{1}{3}\,(\sigma^+)$	$-\sqrt{\frac{2}{27}}\,(\sigma^-)$	$\sqrt{\frac{4}{27}}\,(\pi)$
	3/2			$\frac{1}{3}\,(\sigma^-)$	$\sqrt{\frac{1}{6}}\,(\pi)$		$-\sqrt{\frac{2}{9}}\,(\sigma^-)$
$F = 1/2$	-1/2	$\sqrt{\frac{2}{9}}\,(\sigma^-)$	$\sqrt{\frac{4}{27}}\,(\pi)$	$\sqrt{\frac{2}{27}}\,(\sigma^+)$		$\sqrt{\frac{1}{54}}\,(\pi)$	$\sqrt{\frac{1}{27}}\,(\sigma^+)$
	1/2		$\sqrt{\frac{2}{27}}\,(\sigma^-)$	$\sqrt{\frac{4}{27}}\,(\pi)$	$\sqrt{\frac{2}{9}}\,(\sigma^+)$	$-\sqrt{\frac{1}{27}}\,(\sigma^-)$	$-\sqrt{\frac{1}{54}}\,(\pi)$

Table A.10: D_1-line electric-dipole-transition matrix elements. Results are given in units of $\mu_{D1} = \left\langle J = 1/2 \right|\left|\hat{\mu}(1)\right|\left| J' = 1/2 \right\rangle = -\sqrt{2}\mu_0$. The parenthetical terms indicate the polarization of light required to drive the transition.

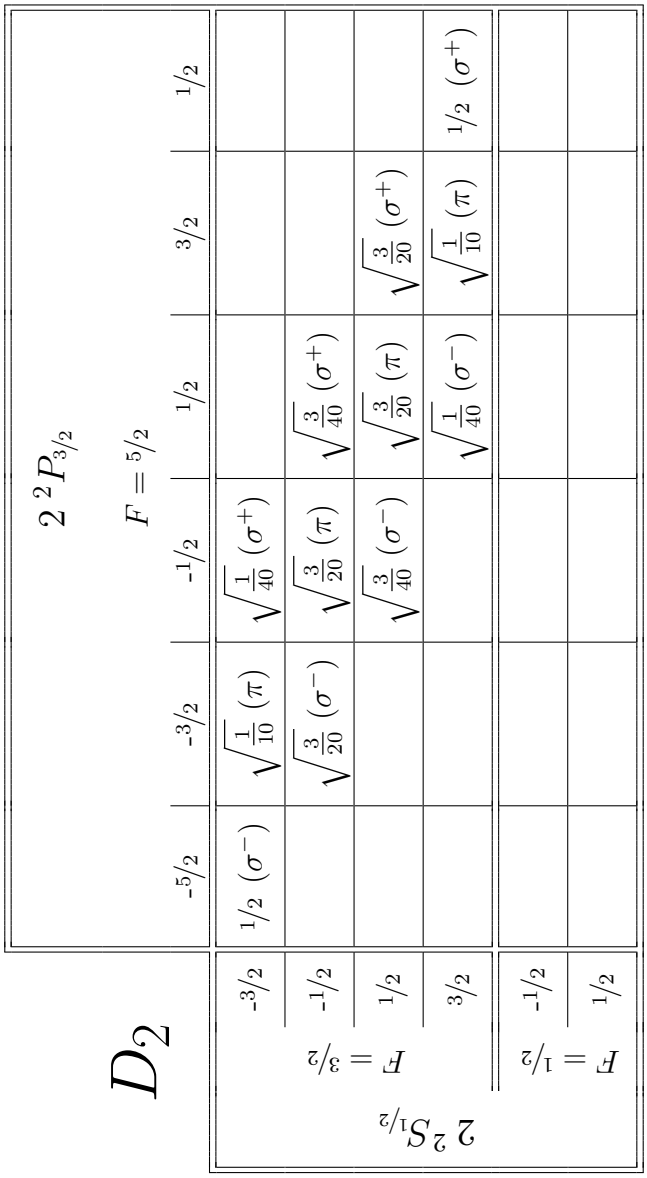

Table A.11: D_2-line electric-dipole-transition matrix elements (part1). Results are given in units of $\mu_{D2} = \left\langle J = 1/2 \left|\left| \hat{\mu}(1) \right|\right| J' = 3/2 \right\rangle = 2\mu_0$. The parenthetical terms indicate the polarization of light required to drive the transition.

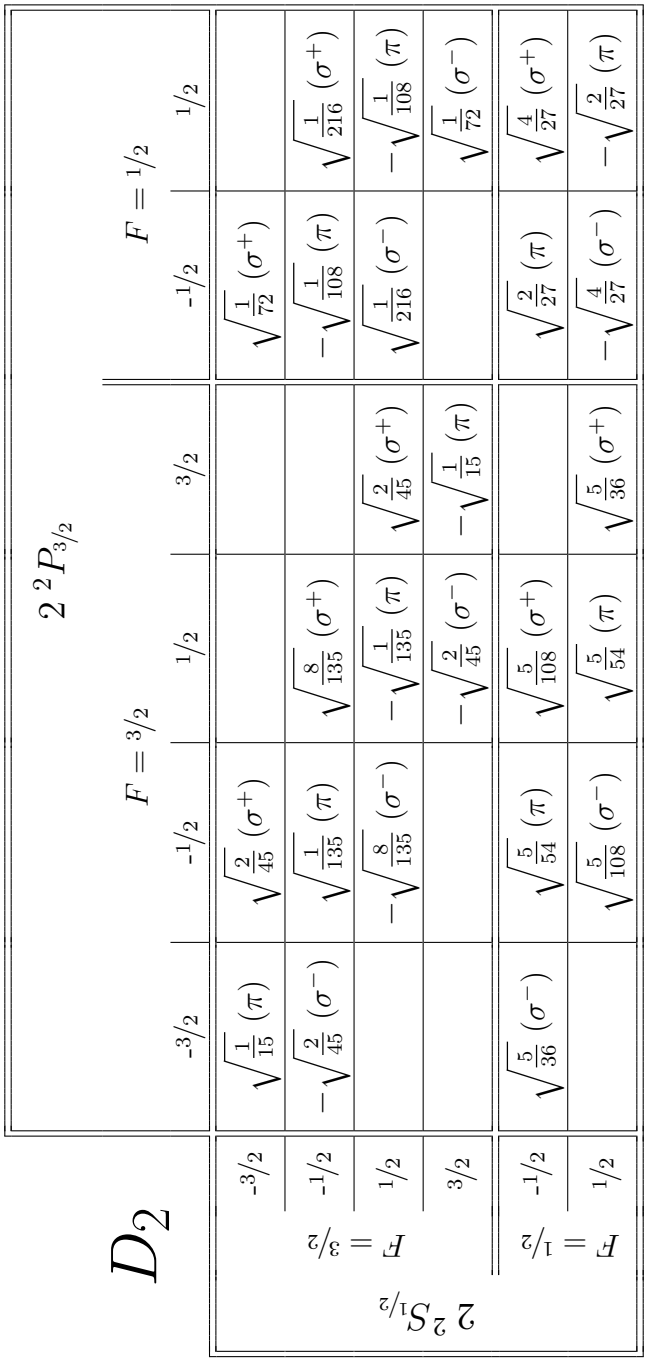

Table A.12: D_2-line electric-dipole-transition matrix elements (part 2). Results are given in units of $\mu_{D2} = \langle J = 1/2 \,||\hat{\mu}(1)||\, J' = 3/2\rangle = 2\mu_0$. The parenthetical terms indicate the polarization of light required to drive the transition.

Transition Type	$S_{F\,F'}$	Value
D_1 Absorption ($2\,^2S_{1/2} \rightarrow 2\,^2P_{1/2}$)	$S_{1/2\,,\,1/2}$	$1/18$
	$S_{1/2\,,\,3/2}$	$4/9$
	$S_{3/2,\,1/2}$	$2/9$
	$S_{3/2,\,3/2}$	$5/18$
D_1 Emission ($2\,^2P_{1/2} \rightarrow 2\,^2S_{1/2}$)	$S_{1/2\,,\,1/2}$	$1/18$
	$S_{1/2\,,\,3/2}$	$4/9$
	$S_{3/2,\,1/2}$	$2/9$
	$S_{3/2,\,3/2}$	$5/18$
D_2 Absorption ($2\,^2S_{1/2} \rightarrow 2\,^2P_{3/2}$)	$S_{1/2\,,\,1/2}$	$2/9$
	$S_{1/2\,,\,3/2}$	$5/18$
	$S_{1/2\,,\,5/2}$	0
	$S_{3/2,\,1/2}$	$1/72$
	$S_{3/2,\,3/2}$	$1/9$
	$S_{3/2,\,5/2}$	$3/8$
D_2 Emission ($2\,^2P_{3/2} \rightarrow 2\,^2S_{1/2}$)	$S_{1/2\,,\,1/2}$	$2/9$
	$S_{1/2\,,\,3/2}$	$1/36$
	$S_{3/2,\,1/2}$	$5/36$
	$S_{3/2,\,3/2}$	$1/9$
	$S_{5/2,\,1/2}$	0
	$S_{5/2,\,3/2}$	$1/4$

Table A.13: Relative Transition Strengths, $S_{F,\,F'}$, for ^{6}Li. Results are given in units of $\left|\left\langle J'\right|\left|\hat{\mu}(1)\right|\left|J\right\rangle\right|^2$.

tance:

$$\begin{aligned}\sum_{F'} S_{F,F'} &= \sum_{F',q} \left|\left\langle F'\,(m_F+q)\right|\hat{\mu}(1,q)\left|F\,m_F\right\rangle\right|^2 \\ &= \frac{1}{2J+1}\left|\left\langle J'\right|\left|\hat{\mu}(1)\right|\left|J\right\rangle\right|^2. \end{aligned} \tag{A.28}$$

While this rule holds for both absorption and emission, the physical implication is most important for emission: *all excited states in a given line (D_1 or D_2) have the same transition strength, and hence decay at the same rate.* In fact, we can relate this result to the decay rate via the *Einstein A-Coefficient* [60]:

$$\begin{aligned}\frac{1}{\tau} &= A_{J,J'} \\ &= \frac{\omega^3}{3\pi\epsilon_0\hbar c^3}\frac{1}{(2J+1)}\left|\left\langle J'\right|\left|\hat{\mu}(1)\right|\left|J\right\rangle\right|^2. \end{aligned} \tag{A.29}$$

In the above, ϵ_0 is the electric permittivity of free space. With this result, we can take experimentally determined decay rates and transition frequencies and compute the fundamental reduced matrix elements. This is how the values in Table A.9 were computed.

A.6.3 The Photon-Burst Transitions

When we examine the transition matrix elements given in Tables A.10, A.11 and A.12, we discover an interesting fact: the excited states $\left|F' = 5/2\; m_{F'} = \pm 5/2\right\rangle$ each couple to a single ground state, namely $|F = 3/2\; m_F = \pm 3/2\rangle$. When driven by light of the proper polarization (σ^+ for the (+)-terms and σ^- for the (−)-terms) the atom must shuttle back and forth between these two states. No other internal states are possible. These transitions are known as the *photon-burst*, *cycling*, or *closed*

transitions [58].

This behavior has a number of important implications. An atom interacting with near-resonant light on a photon-burst transition acts as a perfect two-level system—dramatically simplifying the theoretical treatment of the light-matter interaction. Further, the fact that the atom continually interacts with the light field significantly increases the magnitude of any interaction effect. There are two important instances of this behavior. First, the atomic cooling technique known as *optical molasses* uses repeated absorption-emission cycles to rapidly decelerate (and hence cool) atoms. For this reason, the photon-burst transition is also sometimes known as the *cooling* transition. Second, the photon-burst transition is maximally efficient at converting an incident probe beam into fluorescence—making this transition optimal for optical detection.

Because of the importance of the photon-burst transition, it is sometimes used as the unit of transition strength. To allow easy conversion to this viewpoint, the fundamental reduced matrix elements in Table A.9 are also given in units of μ_0, the transition strength of the photon-burst transition.

A.6.4 Optical Rabi Frequency and Saturation Intensity

For a two-level atom coupled to a near-resonant optical field, we can compute the frequency at which the interaction coherently drives the atom between the two states. This frequency, known as the *optical Rabi frequency*, is given by [58]

$$\begin{aligned} \Omega &= \frac{\langle b \,|\, \hat{\boldsymbol{\mu}} \cdot \boldsymbol{E}| \, a\rangle}{h} \\ &= \frac{\mu_{ba} E_0}{h} \end{aligned} \tag{A.30}$$

where μ_{ba} is the electric-dipole transition matrix element for states a and b, and E_0 is the electric field strength of the incident optical field. We can write this in terms of laboratory units as

$$\Omega = 4.37\ \mu_{ba}\ \sqrt{I} \tag{A.31}$$

with Ω in MHz, μ in Debye, and I, the light intensity, in mW/mm^2.

When the Rabi frequency is less than the spontaneous decay rate Γ, (Tables A.3 and A.4), the atom is likely to spontaneously decay out of the excited state, rather than being driven coherently by the applied field. As the intensity of the applied field (and hence the electric field strength) increases, the Rabi frequency begins to dominate the spontaneous decay rate, and the atom-light interaction becomes stronger and more coherent. In the limit where the $\Omega \gg \Gamma$, the atom is being driven completely coherently, the atomic population is evenly split between the ground and excited levels, and increasing the light intensity ceases to affect the state populations. At this point, the transition is said to be *saturated*.

If we take the intensity of a light field to be $I = (1/2)c\epsilon_0 E^2$, we can define a *saturation intensity*, I_{sat}, given by

$$I_{sat} = \frac{c\epsilon_0 \Gamma^2 \hbar^2}{4\left|\boldsymbol{\mu}\cdot\boldsymbol{e}\right|^2}. \tag{A.32}$$

In the above, $\boldsymbol{e}$ is the unit polarization vector of the light field such that $\boldsymbol{E} = E_0\boldsymbol{e}$. With this definition we find

$$\frac{I}{I_{sat}} = 2\left(\frac{\Omega}{\Gamma}\right)^2. \tag{A.33}$$

Hence, we can say a transition is saturated if $I \gg I_{sat}$. The factor of two is conventional, and being of order unity, does not materially affect whether a transition is saturated or not.

Property	Symbol	Value	Ref.
Representative D_1 Saturation Intensity	I_{sat} (D_1)	$7.59\,\mathrm{mW/cm^2}$	
Representative D_2 Saturation Intensity	I_{sat} (D_2)	$2.54\,\mathrm{mW/cm^2}$	

Table A.14: Representative values of I_{sat} for the D_1 and D_2 lines of ^{6}Li.

Note that the saturation intensity in (A.32) is transition-dependent. In a given line (D_1 or D_2) it is customary to report the smallest saturation intensity as a representative value. These values are tabulated in Table A.14. The value for the D_2 line is particularly relevant, as it corresponds to the photon-burst transition.

A.7 Collisional Properties

The collisional properties of atoms play an important role in many cooling and trapping experiments. Sometimes this role is a negative one—for example, inelastic collisions between atoms change the internal state of the atoms, releasing large amounts of energy and perhaps ejecting one or more atoms from the trap. Other times collisions are harnessed and used by experimenters, such as in evaporative cooling, where elastic collisions eject hot atoms from the trap and rethermalize the remaining gas at a lower temperature.

The following sections are intended to provide an overview of the collisional properties of atoms in general and of ^{6}Li in particular. A much more thorough discussion of atomic collisions in general can be found in a number of standard texts such as [85–87]. A very detailed discussion of the collisional properties of ultracold ^{6}Li in particular can found in an earlier thesis from this research group [21].

A.7.1 The Scattering Problem

In an ultracold atomic gas, each atom is localized to a volume on the order of the cube of the deBroglie wavelength

$$\lambda_{dB} = \sqrt{\frac{2\pi\hbar^2}{mk_bT}}, \tag{A.34}$$

where m is the atomic mass, k_b is the Boltzmann constant, and T is the temperature of the gas. For ^{6}Li at a temperature of $1\,\mu$K we compute a deBroglie wavelength of $0.712\,\mu$m, which yields a localization volume of $3.61\times10^{-1}\,\mu\text{m}^3$.

We can estimate the number of atoms in a given λ^3 volume by computing $N = n\lambda^3$, where n is the atomic number density for the gas. For most cooling and trapping experiments, this ranges from $1\times10^8\,\text{cm}^{-3}$ to $1\times10^{14}\,\text{cm}^{-3}$ at the most. For the localization volume given above, and using a moderate number density ($1\times10^{11}\,\text{cm}^{-3}$) we calculate that, on average, there is only one atom per $\simeq 3000$ localization volumes. This value is not atypical.

For experiments in this regime, clearly an approach based on *binary* collisions (involving only two atoms) is reasonable. In such an approach, we treat the two-atom collision as the scattering of a single particle (of reduced mass, μ) off of an interaction potential. For ^{6}Li-^{6}Li collisions, the interaction potential will be some linear combination of the molecular *singlet* and *triplet* interaction potentials (determining the proper linear combination will be addressed in a future section).

In the singlet potential, the two atoms approach with their unpaired electronic spins antiparallel ($\boldsymbol{S} = \boldsymbol{S}_1 + \boldsymbol{S}_2 = 0$). Considering the symmetry of this state, we see that the spin wavefunction of the electrons is antisymmetric, requiring the spatial wavefunction to be symmetric. In such a case, the electrons are not excluded from

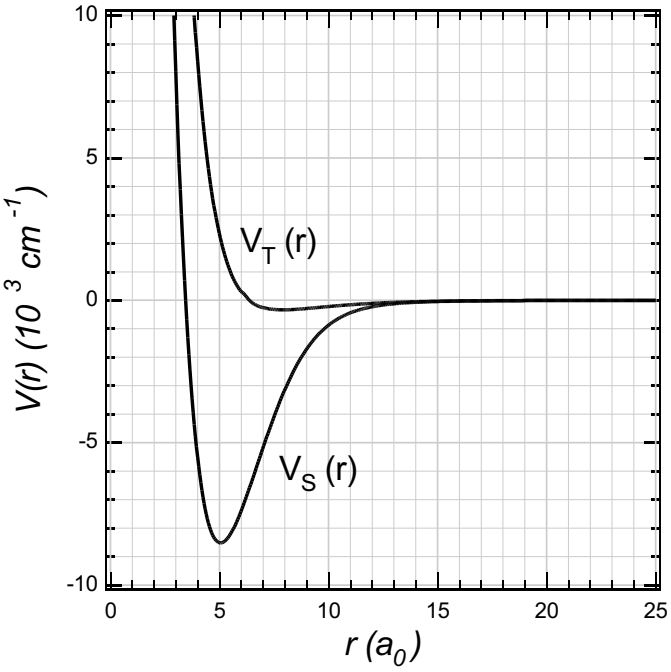

Figure A.9: Singlet and Triplet Molecular Potentials of ^{6}Li.

the region between the nuclei, and the electrostatic attraction between electrons and nuclei leads to a deep potential well. In the triplet case, the two spins approach in the parallel configuration ($\boldsymbol{S} = 1$). Here the spin wavefunction is symmetric, requiring an antisymmetric spatial wavefunction. As a result, the electrons spend very little time in the region between nuclei, and the interaction potential is correspondingly weak.

The singlet and triplet molecular potentials were recreated in [21] from the results of several experiments that measured the potential in different regions. The potentials are plotted in Figure A.9. The vertical axis is in units of cm^{-1}, while the radial coordinate is given in Bohr. Note that the singlet potential is significantly deeper than the triplet, as expected.

While the binary collision approach is a useful starting point, it is of course incomplete. In experiments with degenerate or near degenerate gases, the number

of atoms per localization region necessarily approaches or exceeds one (indeed, this is the very definition of degeneracy). In such cases, and in other extreme situations where the the atomic interactions are resonantly enhanced, three-body collisions do play an increasingly important role—often becoming the a limiting process. Such effects are beyond the scope of this chapter, but the reader is advised to keep their existence in mind.

Strictly speaking, once the interaction potential is known, we have only to solve the full Schrödinger equation

$$(\nabla^2 + k^2)\Psi_{\boldsymbol{k}} = \frac{2\mu}{\hbar^3}\, V\, \Psi_{\boldsymbol{k}} \tag{A.35}$$

for solutions of the form

$$\Psi_{\boldsymbol{k}} = e^{i\boldsymbol{k}\cdot\boldsymbol{r}} + \Psi_{scat}, \tag{A.36}$$

where the first term on the right is a plane wave representing the incoming particle, and the second term represents the outgoing scattered wavefunction. In fact, such an approach, while correct, misses an important simplification that we can make for the case ultracold gases.

A.7.2 Partial Wave Treatment—The Benefit of Ultracold Gases

When the interaction potential is a central potential (as it is in this case), there is no ϕ-dependence in our solution (taking the z-axis of the spherical coordinate system along the direction of propagation of the incoming particle). In this case, we can expand both the incoming and scattered wavefunctions in an angular momentum basis—the coefficients of this expansion are known as the *partial-wave amplitudes*.

Since a central potential cannot change angular momentum, the single Schrödinger equation above becomes an infinite sum of Schródinger equations, *one for each angular momentum component*, which are solved separately. At first glance, this hardly seems an improvement, as we have apparently increased the complexity of the problem enormously. However, it is the case that at low temperatures, only a few of the the partial wave amplitudes are distinguishable from zero. A heuristic explanation of this is provided in [85], as well as almost any other scattering text.

In the case of an *ultracold* atomic gas, we can go even further. In general, only the lowest-order term, the *s-wave* term provides a contribution. This is the power of the partial wave approach as applied to ultracold gases—we again have a single Schrödinger equation, but in that we are working with a single angular momentum component, the analysis is greatly simplified. (At this point, the reader is cautioned that the "only s-wave" approach, much like the "binary collision" approach above, is only an approximation. It appears that in the case of ultracold gases with resonantly enhanced interactions, p-wave and higher interactions may play an important role in the interesting physics that arise.)

The primary physical parameter that we hope to compute with scattering theory is the *total cross section*, σ. The total cross section is dimensionally an area (length^2) and physically represents how large of a "target" the atom presents to other atoms. The rates at which collisions occur in the gas are determined by the atomic number density, n, the gas temperature, T, and the collision cross-sections, σ.

In the partial wave expansion, the total cross section is a sum of partial cross sections, σ_L. For *indistinguishable* particles, the partial wave cross-section for a

symmetric spatial state (even L) is given by

$$\sigma_L = \frac{8\pi}{k^2}(2L+1)\sin^2\delta_L. \tag{A.37}$$

In the above, k is the wavenumber for the incoming particle, and δ_L is the *partial wave phase shift*—the phase imposed on the partial wave by the existence of the potential. Note that since sin is bounded by 0 and 1, σ_L is necessarily positive, and has a maximum value of

$$\sigma_L^{max} = \frac{8\pi}{k^2}(2L+1). \tag{A.38}$$

This limit is known as the *unitarity* limit and occurs when δ_L is an odd multiple of $\pi/2$.

In the case where we have only s-wave scattering, the total cross section is the s-wave partial cross section

$$\sigma = \sigma_{L=0} = \frac{8\pi}{k^2}\sin^2\delta_{L=0}. \tag{A.39}$$

At this point, the problem of finding the total cross section has been reduced to finding the s-wave phase shift. While it is possible to compute the wavefunction both with and without the interaction potential, and compare the two to extract the phase shift, the next section delineates an approach that is both simpler and more elegant.

A.7.3 The S-Wave Scattering Length

In the low-energy limit ($k \to 0$), it is possible to show that for a large class of potentials, we can write $\tan\delta_0 \propto k$, and hence also $\sin\delta_0 \propto k$ [86]. We can then

define the proportionality constant

$$a \equiv -\lim_{k\to 0} \frac{\sin\delta_0(k)}{k}. \tag{A.40}$$

This constant is known as the *s-wave scattering length*. When this result is inserted into (A.39), we get the low energy result

$$\sigma = 8\pi a^2. \tag{A.41}$$

It is important to note that by taking the low-energy limit, the scattering length depends only on the interaction potential and not on the incoming wavenumber (which we treat as zero). Thus we must only compute the scattering lengths for interactions of different pairs of internal ^{6}Li states, and then we have completely characterized the problem.

The scattering length has a simple geometric interpretation. The radial wavefunctions, in the asymptotic limit, have the low energy form $\sin(kr+\delta_0) \simeq \sin(kr) + \delta_0\cos(kr) \to k(r-a)$ as $k \to 0$. This limiting form is a straight line with x-intercept a. The scattering length can thus be computed by calculating the asymptotic wavefunction, and projecting backwards to find the x-intercept. The sign of the scattering length indicates the overall effect of the potential. A negative scattering length indicates a potential which is overall attractive, which a positive scattering length represents an overall repulsive potential. A schematic of the geometrical meaning of the scattering length is shown in Figure A.10.

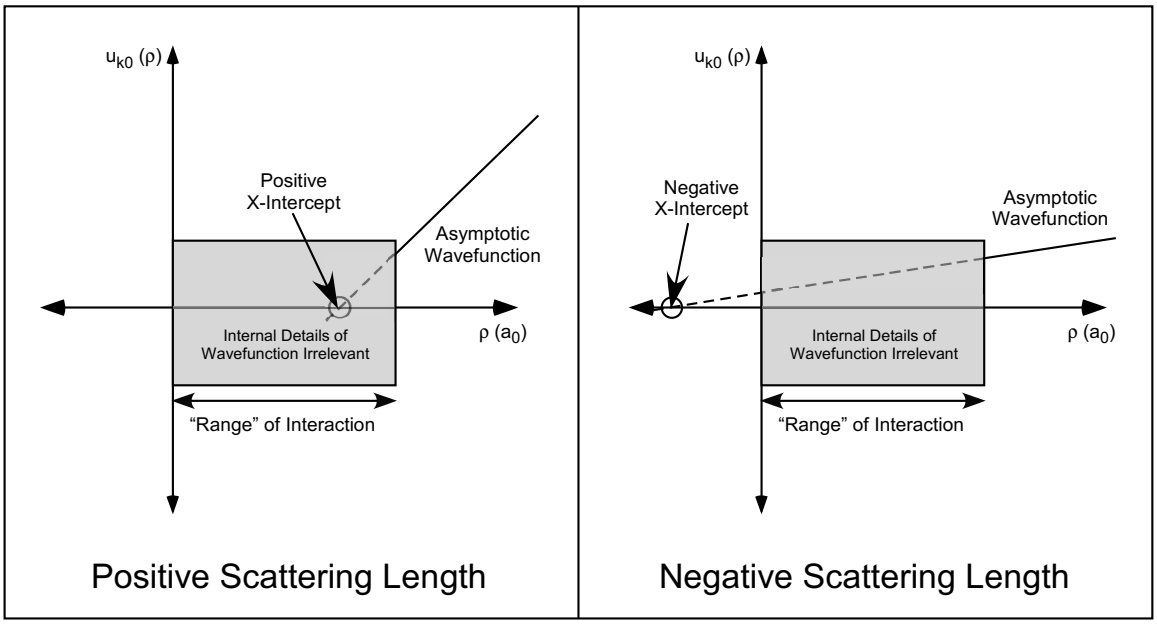

Figure A.10: Determination of Scattering Length.

Singlet and Triplet Scattering Length

In Section A.7.1, it was mentioned that all ^{6}Li-^{6}Li interaction potentials could be described by a linear combination of the molecular singlet and triplet potentials. As we have seen in the preceding sections, for ultracold gases, the effect of an interaction potential can be characterized by a single parameter, the s-wave scattering length, a. The combination of these two facts means all ultracold ^{6}Li-^{6}Li interactions can be characterized by a linear combination of singlet and triplet s-wave scattering lengths. In [21], the values of these scattering lengths are computed from the most recent measurements of the molecular potentials, and the results are in good agreement with experiment [52, 88]. The values of the scattering lengths are given in Table A.15.

It is worth noting the enormously large and negative triplet scattering length. An admixture of states that admits even a small amount of the triplet state will have

Property	Symbol	Value	Ref.
Singlet S-Wave Scattering Length	a_s	38.75 Bohr	[21, 52, 88]
Triplet S-Wave Scattering Length	a_t	-2240 Bohr	[21, 52, 88]

Table A.15: Singlet and triplet s-wave scattering lengths of ^{6}Li.

a scattering length with is both large and negative. As mentioned in Chapter 1, these properties are very desirable for studies of ultracold fermions. This scattering length is the largest in any alkali system, and is why ^{6}Li is so appealing to researchers in the field.

The large triplet scattering length arises from a *zero energy resonance* in the triplet molecular potential. As we have seen, for ultracold gases, the incoming kinetic energy is zero to a good approximation. It turns out that the molecular triplet potential has a quasi-bound state lying just above zero. That is, if the triplet potential were even 0.03% deeper, it would be able to support another bound state. On a heuristic level, this quasi-bound state is able to "capture" an incoming particle for a short period of time prior to allowing it to scatter outward. This dramatically increases the effect of the potential, and hence the size of the scattering length. This state of affairs is depicted in Figure A.11.

Mathematically, we can see how this arises by considering (A.37). It can be shown that when a potential is at a depth such that a state is transferring from bound to unbound, the partial wave phase shift is exactly $\pi/2$. Hence the partial wave cross section in (A.37) becomes

$$\sigma_L = \frac{8\pi}{k^2}, \tag{A.42}$$

which diverges in the low-energy ($k \to 0$) limit.

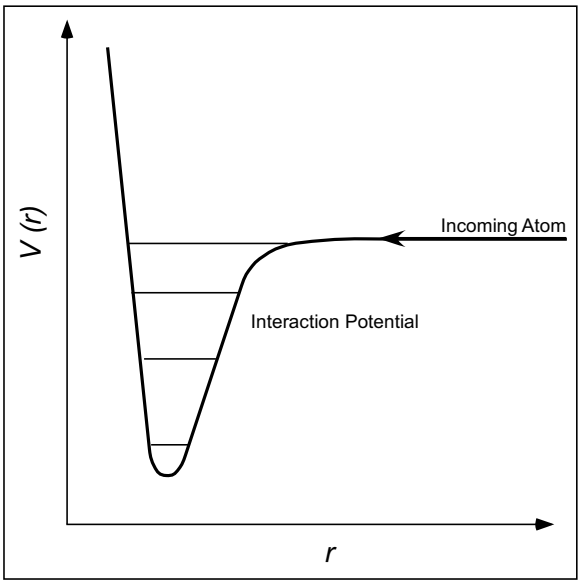

Figure A.11: Phenomenology of a zero-energy resonance.

Wavefunction Symmetry and the $|1\rangle$-$|2\rangle$ Mixture

We begin by considering the symmetry of the wavefunction for an ultracold ^{6}Li-^{6}Li collision. The two-particle wavefunction is a product of three terms: the center-of-mass wavefunction (describing where in the trap the collision takes place), the spatial wavefunction (describing the relative position of the atoms), and the spin wavefunction (describing the intrinsic angular momenta of the atoms). Since ^{6}Li is a composite fermion, the overall wavefunction must be antisymmetric. The center-of-mass wavefunction is clearly symmetric, as switching the two indistinguishable particles has no effect on that term. As a result, the product of the spatial and spin wavefunctions must be antisymmetric.

Now as we have seen before, ultracold collisions are dominated by s-wave interactions. However, s-wave interactions require symmetric spatial wavefunctions. Hence, they also imply antisymmetric spin wavefunctions. This fact underlies one of the most important features of ultracold fermionic gases: *spin-polarized mixtures*

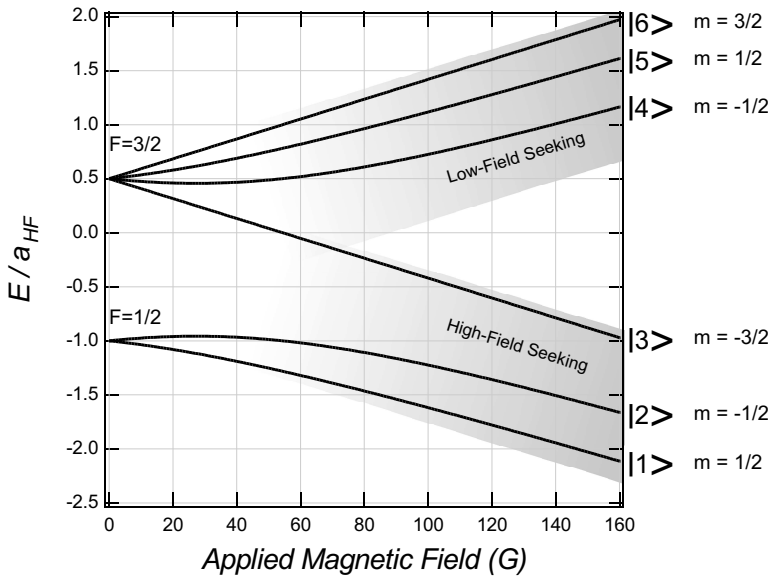

Figure A.12: Ground state hyperfine structure of ^{6}Li. The states are numbered $|1\rangle$-$|6\rangle$ in order of increasing energy in a magnetic field. The vertical axis is plotted in units of the magnetic-dipole hyperfine constant for the ground state.

are non-interacting. A single spin state cannot exist in an antisymmetric spin state. Hence, the spatial wavefunction must be antisymmetric. But antisymmetric spatial wavefunctions can only interact via p-wave (and higher odd) interactions—which are highly suppressed at ultracold temperatures.

Thus, groups wishing to study an interacting fermi gas of ^{6}Li must work with a *mixture* of two or more spin states. But which ones? Consider the states shown in Figure A.12, which shows the magnetic-field dependence of the hyperfine ground states. The states are numbered with what has become standard nomenclature in ^{6}Li; $|1\rangle$-$|6\rangle$, in order of increasing energy in a magnetic field. Further, each state is listed with its z-component of angular momentum. This is useful, as s-wave collisions conserve the total magnetic quantum number.

For the current and future experiments, our group has chosen to work with a mixture of states $|1\rangle$ and $|2\rangle$. This mixture has a number of important properties.

First, it has the lowest internal energy of any interacting mixture (a sample purely in the $|1\rangle$ state would not be interacting for reasons stated above). The low-energy nature of the mixture is important because many higher-energy mixtures have open inelastic collision channels whereby an atom can change internal state and release enough energy to eject one or more atoms from the trap. Mixtures with open inelastic channels tend to destroy themselves. Second, at zero-field, the $|1\rangle$-$|2\rangle$ mixture consists of states that are in some sense mirror images of one another—they differ only in the sign of their magnetic quantum number. This makes the mixture particularly well-suited for future studies of superfluidity. Third, the states in the mixture are *high-field seeking*—that is, when placed in a magnetic gradient, they are drawn to regions of high field. Such states cannot be trapped in a magnetic trap (magnetic traps can produce local minima in the magnetic field strength, but local maxima are forbidden). Since we trap and directly cool in an optical trap, this has no effect on us. Other groups wishing to study this mixture, however, must magnetically trap and cool another ^{6}Li mixture, then transfer that mixture to an optical trap, and then finally convert the atoms to a $|1\rangle$-$|2\rangle$ mixture in some manner. We believe the relative complexity of these steps gives us a competitive advantage. There are two, additional, *serendipitous* features of the $|1\rangle$-$|2\rangle$ mixture that will be discussed below.

Having decided on the $|1\rangle$-$|2\rangle$ mixture, we must determine its collisional properties. In fact, this has been done in [42], via a complete coupled-channel calculation. The result of their calculation, a plot of the s-wave scattering length as a function of applied magnetic field is shown in Figure A.13. There are three items of particular importance in this graph. First, the scattering length appears to be exactly zero at zero applied field. This is not an artifact of the scale of the plot. The authors

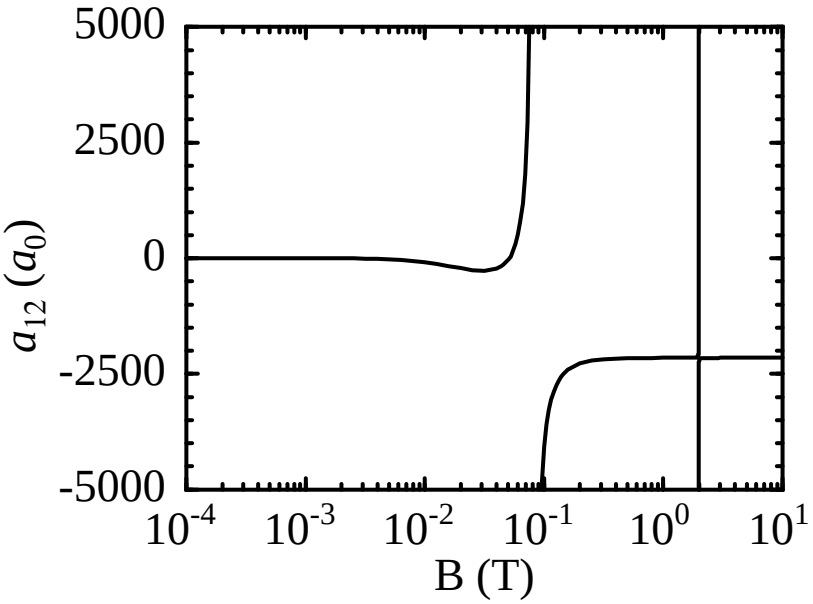

Figure A.13: S-wave scattering length For $|1\rangle$-$|2\rangle$ collisions. The vertical axis is in units of Bohr.

claim the value was always zero to within the precision of their calculation. There is no obvious symmetry argument for why this value should be zero. We, and the authors, believe it to be an accidental feature of the $|1\rangle$-$|2\rangle$ mixture. The other two notable items are the resonances at $\simeq$850 G and $\simeq$1.3 T. These resonances, known as *Feshbach resonances* [15], result when the incoming particle has the same energy as a bound state in an energetically closed collision channel. For example, the $|1\rangle$-$|2\rangle$ mixture, on solely angular momentum grounds, can convert to $|3\rangle$-$|6\rangle$ or $|4\rangle$-$|5\rangle$ (all have total m=0). However, the internal energy of the $|1\rangle$-$|2\rangle$ mixture is such that, for temperatures less than $\simeq$10 mK, these channels are not energetically allowed. But molecular bound states in these channels exist, and for certain magnetic fields, the bound states are resonant with the incoming particles. A schematic of this process is shown in Figure A.14. The practical result is to allow magnetic tuning of the scattering length in both magnitude and sign.

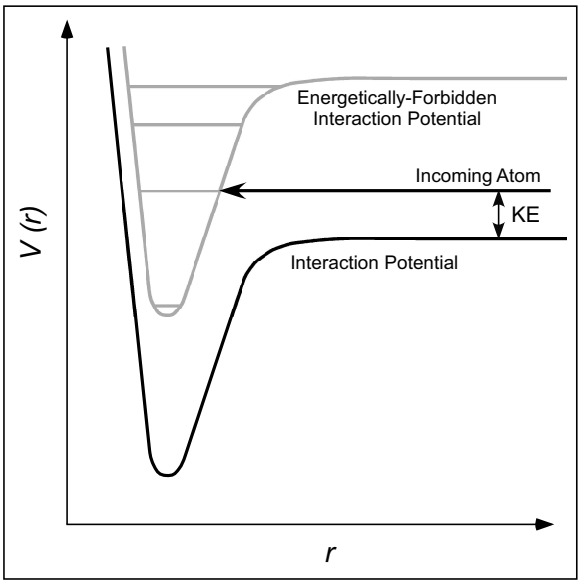

Figure A.14: Phenomenology of a Feshbach Resonance.

These three points of note in the scattering length are the serendipitous features of the $|1\rangle$-$|2\rangle$ mixture mentioned above. The fact that the scattering length is zero at zero applied field means that *the* $|1\rangle$-$|2\rangle$ *mixture can be switched from interacting to noninteracting by simply turning off the applied field.* Further, the existence of a Feshbach resonance means that not only can we explore strongly- and weakly-interacting mixtures (by magnetically-tuning the magnitude of the scattering length), but that we can also change the sign of of the interactions, switching from attractive to repulsive, or vice-versa. Thus we have complete control of not only whether the mixture is interacting or noninteracting, but also over the type and strength of the interaction. Much of the exciting physics of fermionic gases depends on the details of the interatomic interaction—working with this mixture means we have the capability to easily explore all the possible regimes.

Appendix B

Techniques for Generating Nonuniform Probability Density Functions

Anyone who considers arithmetical methods of producing random digits is, of course, in a state of sin.

—John Von Neumann

B.1 Overview

There are a variety of algorithmic techniques for generating *pseudorandom* variates that are uniformly distributed over a given domain. The term "pseudorandom" is used because these techniques, being deterministic, cannot possibly generate truly random numbers. However, within certain constraints, there are a number of approaches that will generate numbers that are "random enough" for a given task.

To generate random numbers according to an *nonuniform* probability density function (PDF), we must turn to an algorithmic approach that takes one or more uniformly distributed variates as inputs. This appendix presents the two simplest approaches towards generating arbitrary distributions, and discusses the specific implementations used in the Monte-Carlo code of Chapter 4.

B.2 Inverse CDF Method

The simplest technique for generating random numbers according to an arbitrary PDF is known as the *inverse cumulative-distribution-function (CDF) method* [48]. This technique is useful for generating random numbers from relatively simple nonuniform distributions. Further, it is an important component in the more complicated technique discussed in the next section.

Given a unit-normalized PDF, $p(X)$, defined on a domain $[a, b]$, from which we wish to generate random variates, X, we begin by considering the CDF, $P(X)$, defined as

$$P(X) = \int_a^X dX' p(X'). \tag{B.1}$$

By construction, $P(X)$ is a monotonically-increasing function where $P(a) = 0$ and $P(b) = 1$. We then find the inverse, $X(P)$. Note that these steps place two constraints on $p(X)$ and $P(X)$:

1. The PDF, $p(X)$, must be piecewise-integrable.

2. The CDF, $P(X)$, must have an inverse, $X(P)$.

If either of these conditions cannot be met, then the inverse CDF method cannot be used.

Once we have $X(P)$, then the actual random number generation is simple. We generate a uniformly distributed random variate, Y, on the interval $[0, 1]$, and take it as the input to our function $X(P)$. That is:

$$X = X(Y). \tag{B.2}$$

The result is a random variate, X, which is distributed according to the PDF,

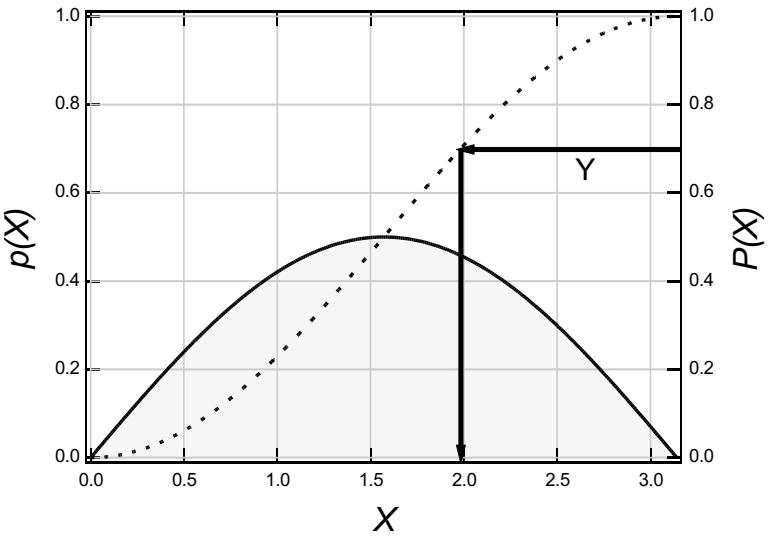

Figure B.1: Example of the inverse CDF method. The desired PDF, $p(X) = \sin(X)/2$, is shown by the solid, filled curve. The corresponding CDF, $P(X) = (1 - \cos(X))/2$, is shown by the dashed curve. The arrows indicate the application of the inverse CDF method. A random variate, Y, (here 0.7) is selected from a uniform distribution on the range $[0, 1]$. The horizontal arrow shows this value being matched to a single point in the CDF. The vertical arrow shows this point being matched with a value on the horizontal axis (here $X(0.7) \simeq 1.98$). This value is the desired random variate. Variates generated in this way will be distributed according to the desired PDF.

$p(X)$. A schematic representation of this process is shown in Figure B.1.

B.3 Acceptance-Rejection Method

If the desired PDF or its associated CDF do not meet the constraints listed above, then the inverse-CDF method cannot be used. Even if the constraints are met, however, it is not always desirable to use the inverse-CDF method. Sometimes implementing the inverse function, $X(Y)$, requires mathematical functions that are not built in to the computer language being used. Alternatively, the computational cost for evaluating $X(Y)$ may be extremely high. In either case, or when the inverse-CDF method fails altogether, the *acceptance-rejection method* [48] is often a good second choice.

In the acceptance-rejection method, we begin by selecting an approximate function, $a(X)$, over the domain $[a, b]$, such that $a(X) \geq p(X)$ over the entire domain. We choose $a(X)$ to have a simple CDF, $A(X)$, and inverse $X(A)$. We then generate a random variate using the inverse-CDF method and our simple inverse $X(A)$. This portion of the procedure is shown in Figure B.2.

Of course, if we stopped here, we would generate random variates distributed according to the function $a(X)$. A further algorithmic step is needed to modify the distribution to the desired $p(X)$. We have seen in Section 4.4.2 that an algorithmic step where random variates are accepted or rejected based on some criterion has the effect of modifying the underlying PDF. There, we generated atoms whose spatial location and speed were appropriate for *all* atoms, *bound and unbound*. By accepting only the atoms whose total energy was small enough to be trapped by the FORT potential, the distributions of position and velocity were modified in such a way that the atomic ensemble had the appropriate distribution for *bound* atoms. The

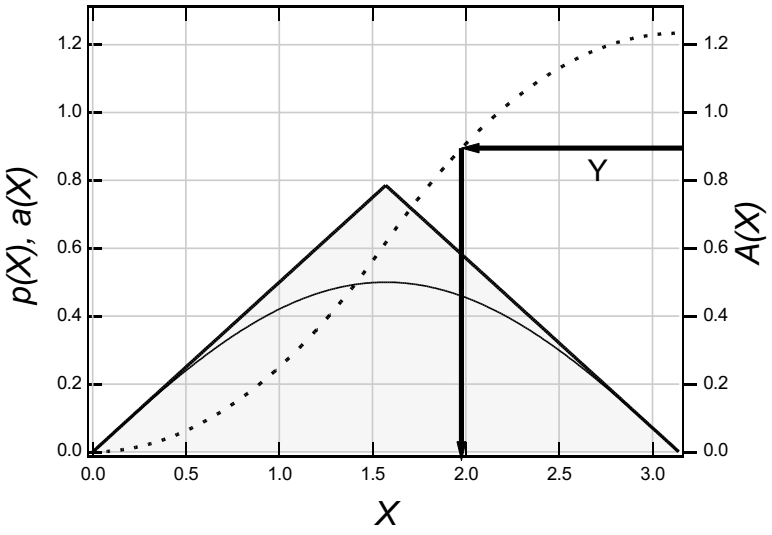

Figure B.2: Step 1 of the acceptance-rejection method. We consider again the PDF shown in Figure B.1, $p(X) = \sin(X)/2$ (shown here by the thin, solid curve). We now consider an approximation to this curve, $a(X)$, which is everywhere greater than the desired pdf (shown here by the thick, solid, filled curve). We then create the CDF of the approximation, $A(X)$ (shown here by the dashed curve). We proceed as in the inverse-CDF method. A uniformly-distributed random variate, Y, is generated over the domain [0,A(b)] (shown $Y = 0.9$). This variate is mapped to a point on the horizontal axis (here $X \simeq 1.99$) through the use of the inverse $X_A(Y)$.

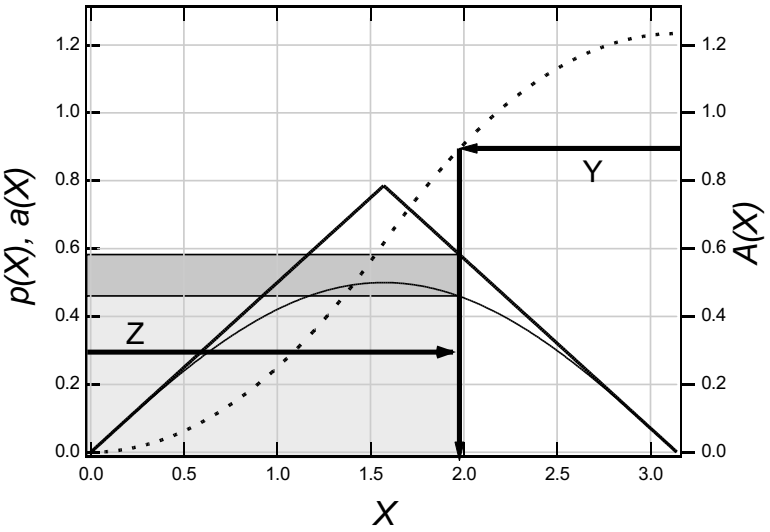

Figure B.3: Step 2 of the acceptance-rejection method. Figure B.2 has been modified to show the second part of the algorithm. Once X_A has been found, a new uniform variate, Z, is generated on the domain $[0, a(X_A)]$. If $Z \leq p(X_A)$ (lightly shaded region), then the X_A is accepted. If $Z \geq p(X_A)$ (darkly shaded region), then X_A is rejected. In this example, $Z = 0.3$ and $Z \leq p(X_A)$, so we accept $X_A \simeq 1.99$ as a random variate.

acceptance-rejection method makes use of this type of effect to filter the random variates generated in accordance with $a(X)$ to produce random variates which are distributed according to $p(X)$.

Adding this step is trivial. Once we have a random variate X_A, we then generate a uniformly distributed random variate, Z on the domain $[0, a(X_A)]$. If $Z > p(X_A)$, then we reject X_A and begin again, by generating a new X_A. If, however, $Z \leq p(X_A)$, then we accept X_A as a random variate. Variates generated in this manner are distributed according to $p(X)$. This portion of the algorithm is shown in Figure B.3.

B.4 Monte-Carlo Implementations

This section will address the specific implementations used in the Monte-Carlo code described in Chapter 4. While the previous section described the basics of the acceptance-rejection method, our usage of this technique in the Monte-Carlo code adds one additional complication. In running the Monte-Carlo code, the user can change the parameters of the problem (*e.g.* the temperature of the trapped atoms). However, it is clear from (4.3) and (4.4), that changing these parameters can significantly modify the distributions we are attempting to reproduce. The approximations to the PDFs that we use in the acceptance-rejection method must therefore also depend on these parameters. In the sections that follow, we will use the convention developed in the Monte-Carlo code and ignore all leading normalization constants.

B.4.1 The Velocity Distribution

The PDF we are attempting to reproduce is

$$p(v) = v^2 \exp\left[-\frac{mv^2}{2k_B T}\right]. \tag{B.3}$$

We must now develop an approximation, $a(v)$ to this distribution that roughly tracks it as parameters in the PDF vary, while always maintaining $a(v) \geq p(v)$.

Since we will eventually reject any unbound atoms, it makes little sense to generate velocities that cannot possibly be bound. The minimum potential energy that an atom can have occurs at the trap center and is given by the negative of the well-depth, $-k_B U$, where k_B is the Boltzmann constant, and U is in temperature

units. We can therefore ignore all velocities such that

$$\frac{1}{2}mv^2 > k_B U. \tag{B.4}$$

Velocities satisfying this inequality cannot be bound. We can define a maximum possible velocity for a bound atom

$$v_{\max} = \sqrt{\frac{2k_b U}{m}}. \tag{B.5}$$

We will not consider velocities greater than $v_{\max}$.

We can make three observations about the shape of $p(v)$ which we can use to construct our approximation, $a(v)$.

1. In the low-v limit, $p(v)$ scales as v^2. As v increases from zero, the exponential in $p(v)$ ensures that $v^2 \geq p(v)$.

2. There will always be a peak in $p(v)$. The peak occurs at

$$v_{\text{peak}} = \sqrt{\frac{2k_B T}{m}}. \tag{B.6}$$

   The value at the peak is

$$p(v_{\text{peak}}) = \frac{2k_B T}{m}\exp(-1). \tag{B.7}$$

3. Past the peak, the distribution decays exponentially to zero.

We can combine these three facts with our previous definition of $v_{\max}$ to determine a reasonable approximation function, $a(v)$. The approximation will consist of,

at most, three distinct pieces. The number of pieces depends on the where $v_{\max}$ lies with respect to the peak of $p(v)$. There are three possible cases:

1. $v_{\max} < \frac{1}{2}\, v_{\text{peak}}$. In this case, we simply use the low-v scaling of $p(v)$,

$$a(v) = v^2 \tag{B.8}$$

2. $\frac{1}{2}\, v_{\text{peak}} \leq v_{\max} \leq \frac{3}{2}\, v_{\text{peak}}$. In this case, we use the low-v scaling for values of v up to one-half of v_{peak}, then switch to a constant value equal to $p(v_{\text{peak}})$,

$$a(v) = \begin{cases} v^2 & : \quad v \in [0, \frac{1}{2}\, v_{\text{peak}}) \\ \frac{2k_B T}{m} \exp(-1) & : \quad v \in [\frac{1}{2}\, v_{\text{peak}}, v_{\max}] \end{cases} \tag{B.9}$$

3. $\frac{3}{2}\, v_{\text{peak}} < v_{\max}$. In this case, we use the constant value for $v \leq \frac{3}{2} v_{\text{peak}}$, then use a straight line between the points $(\frac{3}{2} v_{\text{peak}}, p(v_{\text{peak}}))$ and $(v_{\max}, p(v_{\max}))$.

$$a(v) = \begin{cases} v^2 & : \quad v \in [0, \frac{1}{2}\, v_{\text{peak}}) \\ p(v_{\text{peak}}) & : \quad v \in [\frac{1}{2}\, v_{\text{peak}}, \frac{3}{2}\, v_{\text{peak}}] \\ p(v_{\text{peak}}) + \frac{\left(p(v_{\max}) - p(v_{\text{peak}})\right)}{\left(v_{\max} - \frac{3}{2}\, v_{\text{peak}}\right)} \left(v - \frac{3}{2}\, v_{\text{peak}}\right) & : \quad v \in (\frac{3}{2}\, v_{\text{peak}}, v_{\max}] \end{cases} \tag{B.10}$$

A schematic of case 3 is shown in Figure B.4.

B.4.2 The Radial Distribution

Here we are trying to generate random numbers according to the PDF,

$$p(r) = r^2 \, \exp\left[\frac{U \exp\left[-r^2\right]}{T}\right]. \tag{B.11}$$

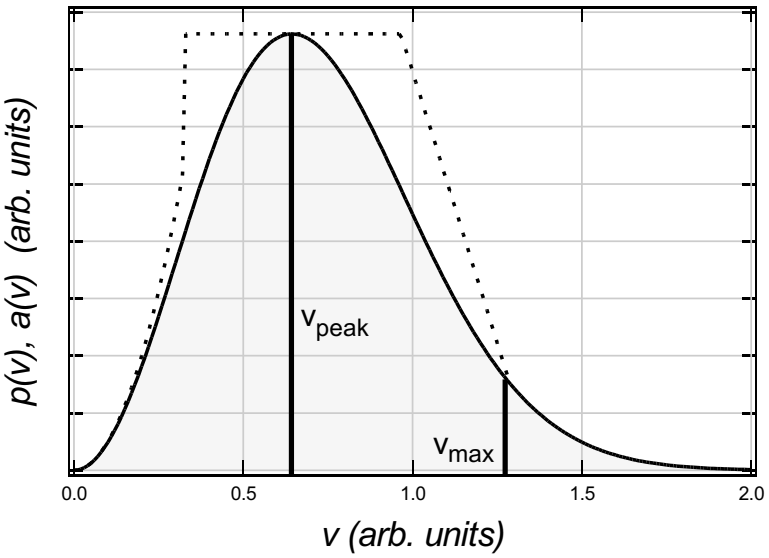

Figure B.4: Approximating the velocity distribution. Shown is a schematic of a case where $v_{\max} > \frac{3}{2} v_{\text{peak}}$. The solid, filled curve is the desired PDF, $p(v)$. The dashed curve shows the approximation, $a(v)$, generated by the technique described in this section. By using the acceptance-rejection technique with this approximation, random numbers distributed according to $p(v)$ are efficiently generated by the Monte-Carlo program of Chapter 4.

As before, we must generate an approximation, $a(r)$, that varies as the parameters in $p(r)$ are varied, while maintaining $a(r) \geq p(r)$.

Unlike the velocity distribution, there is not a maximum radius beyond which the atoms are unbound. However, by examining the form of (B.11), we see that in the large-r limit, $p(r)$ scales as r^2. This is the distribution we would expect if the trap potential were not present. We can then choose a radius, $r_{\max}$ such that $p(r_{\max}) = \kappa r^2$. Here κ is an accuracy parameter that is specified in the algorithm (the Monte-Carlo code uses $\kappa = 1.001$). For κ sufficiently close to 1, we can ignore the distribution beyond $r_{\max}$, as the distribution is indistinguishable from an unbound distribution to within our specified accuracy parameter. By inserting our definition of κ into (B.11), we find

$$r_{\max} = \sqrt{-\ln\left[\frac{T}{U}\ \ln\left[\kappa\right]\right]}. \tag{B.12}$$

Similar to our approach with the velocity distribution, we can make three observations about $p(r)$ which we can use in constructing our approximation, $a(r)$:

1. In the low-r limit, $p(r)$ scales as $r^2 \exp\left[U/T\right]$. As r increases from zero, the exponential in $p(r)$ ensures that $r^2 \exp\left[U/T\right] \geq p(r)$.

2. $p(r)$ does not have a local maximum if $U/T < \exp\left[1\right]$. The location and value of the local maximum that exists when $U/T \geq \exp\left[1\right]$ are not analytically determinable. Experimentation with Mathematica shows that $r_{\text{peak}} \simeq (3/4)\sqrt{T/U}$ is a reasonable approximation.

3. In the large-r limit, $p(r)$ scales as r^2.

We can combine these three observations with our previous definition of $r_{\max}$ (which is based on the third observation, itself), to generate the approximation $a(r)$.

The approximation will consist of at most two pieces. The number of pieces in the approximation depends on the location of $r_{\max}$ with respect to a reference point that is related to the location of the local maximum of $p(r)$.

If there is no local maximum ($U/T < \exp[1]$), then we set the reference point to $r_{\rm ref} = 3/4$. If there is a local maximum, we set the reference point to the approximate location of the maximum, $r_{\rm ref} = (3/4)\sqrt{T/U}$. There are then two possible cases:

1. $r_{\max} \leq r_{\rm ref}$. In this case we use the low-r scaling of $p(r)$.

$$a(r) = r^2 \exp\left[\frac{U}{T}\right]. \tag{B.13}$$

2. $r_{\max} > r_{\rm ref}$. In this case we use the low-r scaling for values of r up to $r_{\rm ref}$, then use a straight line between the points $(r_{\rm ref}, a(r_{\rm ref}))$ and $(r_{\max}, r_{\max}^2)$.

$$a(r) = \begin{cases} r^2 \exp\left[\frac{U}{T}\right] & : \quad r \in [0, v_{\rm ref}] \\ r_{\rm ref}^2 \exp\left[\frac{U}{T}\right] + \frac{\left(r_{\max}^2 - r_{\rm ref}^2 \exp\left[\frac{U}{T}\right]\right)}{(r_{\max} - r_{\rm ref})}(r - r_{\rm ref}) & : \quad r \in (r_{\rm ref}, r_{\max}] \end{cases} \tag{B.14}$$

A schematic of case 2 is shown in Figure B.5.

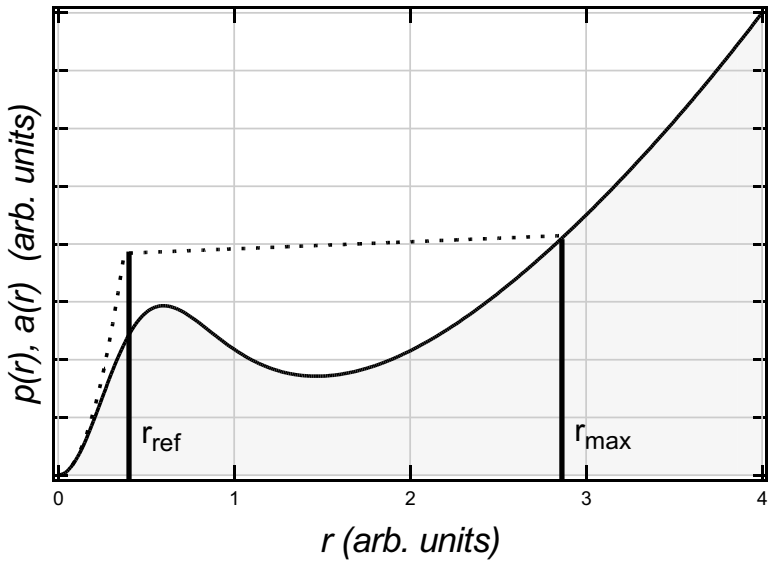

Figure B.5: Approximating the radial distribution. Shown is a schematic of a case where $r_{\max} > r_{\text{ref}}$. The solid, filled curve is the desired PDF, $p(r)$. The dashed curve shows the approximation, $a(r)$, generated by the technique described in this section. By using the acceptance-rejection technique with this approximation, random numbers distributed according to $p(r)$ are efficiently generated by the Monte-Carlo program of Chapter 4.

Appendix C

Computer Code Listings

C.1 Transition Matrix Element Calculator

PROGRAM DESCRIPTION: This program calculates transition matrix elements between atomic hyperfine states.

LANGUAGE: Mathematica 4.1

AUTHOR: Michael E. Gehm

USAGE: There are two modes. `Coeff[A,ma,B,mb]` prints the transition matrix element between state $|A, m_a\rangle$ and state $|B, m_b\rangle$. `MakeTable[A,B]` prints a nicely formatted table of all transition matrix elements between magnetic sublevels of states $|A\rangle$ and $|B\rangle$. All results are given in units of the reduced matrix element $\langle J^{'}||\hat{\boldsymbol{\mu}}(1)||J\rangle$.

```
(* Defines the {S,L,J,I,F} values for the states in the D1 and D2
lines of 6Li. Modify the following lines as appropriate for other
atoms and levels. *)

StateA={1/2,0,1/2,1,1/2};
StateB={1/2,0,1/2,1,3/2};
StateC={1/2,1,1/2,1,1/2};
StateD={1/2,1,1/2,1,3/2};
StateE={1/2,1,3/2,1,1/2};
StateF={1/2,1,3/2,1,3/2};
StateG={1/2,1,3/2,1,5/2};
```

```
(* The remainder of the code requries no modification *)
(* Define functions for extracting quantum numbers from the state
definitions *)

Sval[state_ ]:=state[[1]];
Lval[state_ ]:=state[[2]];
Jval[state_ ]:=state[[3]];
Ival[state_ ]:=state[[4]];
Fval[state_ ]:=state[[5]];

(* Define a function that returns the matrix element. Then define a
function which runs over all magnetic sublevels in both levels to
produce a pretty table. *)

Coeff[A_,ma_,B_,mb_] := (-1)^(Fval[B] - mb)*

                            ThreeJSymbol[
                                         {Fval[B], -mb},
                                         {1, (mb - ma)},
                                         {Fval[A], ma}
                                        ]*

                            (-1)^(Jval[B] + Ival[A] + Fval[A] + 1)*

                            Sqrt[
                                  (2 * Fval[B] + 1)*
                                  (2 * Fval[A] + 1)
                                ]*

                            SixJSymbol[
                                        {Jval[B], Ival[A], Fval[B]},
                                        {Fval[A], 1, Jval[A]}
                                       ];

MakeTable[A_,B_] := Table[
                           Table[
                                  Coeff[A, ma, B, mb],

                                  {mb, -Fval[B], Fval[B], 1}
                                 ],
```

```
    {ma, -Fval[A], Fval[A], 1}
]//TableForm
```

C.2 Zeeman Effect Calculator

PROGRAM DESCRIPTION: This program calculates the hyperfine levels of an arbitrary atom in a magnetic field. The hyperfine interaction and the Zeeman effect are treated as perturbations on the atomic fine structure. The resulting perturbation Hamiltonian is numerically diagonalized to get the eigenvalues for the states. The program outputs a text file containing the eigenvalues as a function of the magnetic field.

LANGUAGE: Mathematica 4.1

AUTHOR: Michael E. Gehm

USAGE: Evaluation of the notebook produces the output file. The beginning of the file is edited to set: a) which states to track, b) what atomic parameters to use, and c) what magnetic field strengths to use

```
(* BEGIN USER MODIFIED PORTION *)
(* Set the j- and i-quantum numbers for the fine-structure state to
track *)

JJ = 1/2;
II = 1;

(* Set the gyromagnetic ratios and the hyperfine constants for the
fine-structure state you are interested in. *)

gj = 2.0023010;
gi = -0.0004476540;
A = 152.1368407;
B = 0;

(* Set the magnetic-field range over which the results should be
calculated, and give the field increment to use. *)

BFieldStart = 0;
BFieldEnd = 160;
BFieldIncr = 0.5;
```

```
(* Give the name for the output filename. *)

filename="2S12 Level Data.dat";

(* END USER MODIFIED PORTION *)
(* Define the Bohr Magneton in MHz/G. *)

MuB = 1.4;

(* Compute the number of states we'll be dealing with and ennumerate
them in the |j mj> |i mi> basis. *)

mj = Table[-JJ + i, {i, 0, 2 * JJ}];
mi = Table[-II + i, {i, 0, 2 * II}];
JStates = Length[mj];
IStates = Length[mi];
NumStates = JStates * IStates;

statelist =
    Flatten[
            Table[
                    {mj, mi},

                    {mi, mi[[1]], mi[[IStates]]},
                    {mj, mj[[1]], mj[[JStates]]}
                ],
            1];

(* For the Clebsch-Gordan work, we'll also need the states listed
in the |f> basis. *)

FVals = Table[i, {i, Abs[JJ-II], (JJ+II)}];
FStates = Length[FVals];
MFList[F_] := Table[i, {i, -F, F}];

ExpandedFVals =
    Module[
            {temp = {}, temp2 = {}},

            For[i = 1, i <= FStates,
                     For[j = 1, j <= (2 * FVals[[i]] + 1),
                             temp2 = Flatten[List[temp, FVals[[i]]]];
```

```
                              temp = temp2;
                              j++
                           ];
                        i++
                ];
                temp
          ];

ExpandedMFVals =
    Module[
            {temp = {},temp2 = {}},

            For[i = 1, i <= FStates,
                    temp2 = Flatten[List[temp, MFList[FVals[[i]]]]];
                    temp=temp2;
                    i++
               ];
               temp
          ];

(* Compute the C-G Coefficients between the two representations. *)

ClebschMatrix =
    Table[
            ClebschGordan[
                           {JJ, statelist[[i]][[1]]},
                           {II, statelist[[i]][[2]]},
                           {ExpandedFVals[[j]], ExpandedMFVals[[j]]}
                         ],

            {i, 1, NumStates},
            {j, 1, NumStates}
         ];

(* Computing the hyperfine contribution is easiest in the coupled
basis. Compute the value of the dot-product of I and J for different
J states. *)

IdotJList=
    Table[
            (ExpandedFVals[[i]] * (ExpandedFVals[[i]] + 1) - JJ *
            (JJ + 1) - II * (II + 1)) / 2,
```

```
           {i, 1, NumStates}
         ];

(* Now use the C-G values computed earlier to get I dot J for an
arbitrary product state. *)

IdotJElement[i_,j_] :=
    Thread[
            Times[
                    ClebschMatrix[[i]],
                    ClebschMatrix[[j]]
                 ]
          ] . IdotJList

(* Now we compute the three interaction matrices: hyperfine, Zeeman,
and total. *)

HFMatrix =
        Table[
                A * IdotJElement[i,j] +
                If[B == 0,

                    0,

                    B * (3 * IdotJElement[i,j] *
                    (IdotJElement[i,j] + 1)) /
                    (2 * II * (2 * II - 1) * 2 * JJ * (2 * JJ - 1))
                   ],

                {i, 1 ,NumStates},
                {j, 1, NumStates}
             ];

ZeemanMatrix =
        Table[
                KroneckerDelta[i,j] *
                (gj * statelist[[i]][[1]] + gi * statelist[[j]][[2]])*
                MuB * BField,

                {i, 1, NumStates},
                {j, 1, NumStates}
```

```
            ];

HamiltonianMatrix = HFMatrix + ZeemanMatrix;

(* Calculate the eigenvalues for a given value of the B-Field. *)

DataPoint[BF_] :=
        Prepend[
                    Eigenvalues[
                                HamiltonianMatrix /. BField -> BF
                               ],
                    BF
                ]

(* And finally, generate a list of datapoints and export them in a
friendly format to the previously specified filename. *)

datalist =
        Table[
                DataPoint[BB],

                {BB, BFieldStart, BFieldEnd, BFieldIncr}
            ];

Export[filename, datalist, "CSV"];
```

C.3 Stark Effect Calculator

PROGRAM DESCRIPTION: This program calculates the hyperfine levels of an arbitrary atom in a electric field. The hyperfine interaction and the Stark effect are treated as perturbations on the atomic fine structure. The resulting perturbation Hamiltonian is numerically diagonalized to get the eigenvalues for the states. The program outputs a text file containing the eigenvalues as a function of the electric field.

LANGUAGE: Mathematica 4.1

AUTHOR: Michael E. Gehm

USAGE: Evaluation of the notebook produces the output file. The beginning of the file is edited to set: a) which states to track, b) what atomic parameters to use, and c) what electric field strengths to use

```
(* BEGIN USER MODIFIED PORTION *)
(* Set the j- and i-quantum numbers for the fine-structure state to
track *)

JJ = 1/2;
II = 1;

(* Set the scalar and tensor polarizabilities and the hyperfine
constants for the fine-structure state you are interested in. *)

alpha0 = 0.03163;
alpha2 = 0.000406;
A = -1.155;
B = -0.10;

(* Set the electric-field range over which the results should be
calculated, and give the field increment to use. *)

EFieldStart = 0;
EFieldEnd = 50;
EFieldIncr = 0.1;
```

```
(* Give the name for the output filename. *)

filename = "2P32 Level Data.dat";

(* END USER MODIFIED PORTION *)
(* Compute the number of states we'll be dealing with and ennumerate
them in the |j mj> |i mi> basis. *)

mj = Table[-JJ + i, {i, 0, 2 * JJ}];
mi = Table[-II + i, {i, 0, 2 * II}];
JStates = Length[mj];
IStates = Length[mi];
NumStates = JStates * IStates;

statelist =
    Flatten[
            Table[
                    {mj, mi},

                    {mi, mi[[1]], mi[[IStates]]},
                    {mj, mj[[1]], mj[[JStates]]}
                ],
            1];

(* For the Clebsch-Gordan work, we'll also need the states listed
in the |f> basis. *)

FVals = Table[i, {i, Abs[JJ - II], (JJ + II)}];
FStates = Length[FVals];
MFList[F_] := Table[i, {i, -F, F}];

ExpandedFVals =
    Module[
            {temp = {}, temp2 = {}},

            For[i = 1, i <= FStates,
                     For[j = 1, j <= (2 * FVals[[i]] + 1),
                             temp2 = Flatten[List[temp, FVals[[i]]]];
                             temp = temp2;
                             j++
                        ];
                     i++
```

```
            ];
            temp
         ];

ExpandedMFVals =
    Module[
            {temp = {},temp2 = {}},

            For[i = 1, i <= FStates,
                    temp2 = Flatten[List[temp, MFList[FVals[[i]]]]];
                    temp=temp2;
                    i++
            ];
            temp
         ];

(* Compute the C-G Coefficients between the two representations. *)

ClebschMatrix =
    Table[
            ClebschGordan[
                            {JJ, statelist[[i]][[1]]},
                            {II, statelist[[i]][[2]]},
                            {ExpandedFVals[[j]], ExpandedMFVals[[j]]}
                        ],

            {i, 1, NumStates},
            {j, 1, NumStates}
        ];

(* Computing the hyperfine contribution is easiest in the coupled
basis. Compute the value of the dot-product of I and J for different
J states. *)

IdotJList=
    Table[
            (ExpandedFVals[[i]] * (ExpandedFVals[[i]] + 1) - JJ *
            (JJ + 1) - II * (II + 1)) / 2,

            {i, 1, NumStates}
        ];
```

```
(* Now use the C-G values computed earlier to get I dot J for an
arbitrary product state. *)

IdotJElement[i_,j_] :=
    Thread[
            Times[
                    ClebschMatrix[[i]],
                    ClebschMatrix[[j]]
                 ]
          ] . IdotJList

(* Now we compute the three interaction matrices: hyperfine, Zeeman,
and total. *)

HFMatrix =
        Table[
                A * IdotJElement[i,j] +
                If[B == 0,

                    0,

                    B * (3 * IdotJElement[i,j] *
                    (IdotJElement[i,j] + 1)) /
                    (2 * II * (2 * II - 1) * 2 * JJ * (2 * JJ - 1))
                   ],

                {i, 1 ,NumStates},
                {j, 1, NumStates}
             ];

StarkMatrix =
        Table[
                KroneckerDelta[
                                statelist[[i]][[2]],
                                statelist[[j]][[2]]
                              ] *
                If[statelist[[i]][[1]] == statelist[[j]][[1]],

                    If[alpha2 == 0,

                         -alpha0 / 2 * EField^2,
```

```
                        (-alpha0 / 2 - (alpha2 / 2) *
                        (3 * statelist[[i]][[1]]^2 - JJ * (JJ + 1)) /
                        (JJ * (2 * JJ - 1))) *
                        EField^2
                      ],

                      0
                    ],

                {i, 1, NumStates},
                {j, 1, NumStates}
            ];

HamiltonianMatrix = HFMatrix + StarkMatrix;

(* Calculate the eigenvalues for a given value of the E-Field. *)

DataPoint[EF_] :=
        Prepend[
                    Eigenvalues[
                                HamiltonianMatrix /. EField -> EF
                               ],
                    EF
              ]

(* And finally, generate a list of datapoints and export them in a
friendly format to the previously specified filename. *)

datalist =
        Table[
                DataPoint[EE],

                {EE, EFieldStart, EFieldEnd, EFieldIncr}
            ];

Export[filename, datalist, "CSV"];
```

C.4 Monte-Carlo Code

PROGRAM DESCRIPTION: This program computes the evolution of a classical gas trapped in a (possibly time-dependent) 3-D Gaussian well. The code presented here is a template on which specific simulations can be constructed by adding small amounts of simulation-specific code. The code creates a random ensemble of atoms and evolves them numerically according to Newton's laws (the general form of the approach is known as "Bird's Method.") This code is the topic of Chapter 4

LANGUAGE: ANSI C

AUTHOR: Michael E. Gehm

USAGE: When run, the code generates a random trapped ensemble according to the parameters in "definitions.h". The program evolves the atoms forward in time. This template contains no reporting features. Simulation-specific code should be added to write to the file "output.txt" according to the specific needs of the simulation.

```
/*********************************************************************
* BEGIN FILE "definitions.h"
*********************************************************************/

/*********************************************************************
* Mathematical and physical constants                                *
*********************************************************************/
#define Pi                  3.14159265359
#define EConst              2.71828182846
#define BoltzmannK          1.381E-23
#define LiMass              1E-26

/*********************************************************************
* Simulation-specific definitions                                    *
*********************************************************************/

#define NumAtoms            10000
#define WellDepth           0.000700
#define StartTemp           0.000015
```

```
#define ax                  0.000221    /*x,y,z size of potential*/
#define ay                  0.000221
#define az                  0.000221

/*************************************************************
* Implementation definitions                                 *
*************************************************************/

#define RadialSigmaLimit    10
#define RFudgeFactor        0.75
#define RAccuracy           1.001

#define Cells_x             2   /*Cell and subcell divisions*/
#define Cells_y             2
#define Cells_z             2

#define Subcells_x          2
#define Subcells_y          2
#define Subcells_z          2

/*************************************************************
* Inline functions for speed                                 *
*************************************************************/

#define min(a,b)    ((a<b)?a:b)
#define max(a,b)    ((a>b)?a:b)
#define sign(a)     ((a<0)?-1:((a>0)?1:0))
#define RandFloat() ((float)rand()/(float)RAND_MAX)
#define RandSign()  ((RandFloat()<0.5)?-1:1)
#define RandTheta() (acos(1-2*RandFloat()))

/*************************************************************
* The main data structure                                    *
*************************************************************/

struct atom{float x,y,z,v_x,v_y,v_z;
    int cell,subcell,inrange;} atomlist[NumAtoms];

/*************************************************************
* Global variable declarations                               *
*************************************************************/
```

```
float Cellscale_x,Cellscale_y,Cellscale_z,Subcellscale_x,
    Subcellscale_y,Subcellscale_z,OscFreq,OscFrac,thetime;
int OscFlag, GravFlag;


/*********************************************************************
* END FILE "definitions.s"
*********************************************************************/




/*********************************************************************
* BEGIN FILE "main.c"
*********************************************************************/


/*********************************************************************
* Monte Carlo code for studying collisional effects in a potential *
*                (Based on the DSMC method of Bird)                 *
*                                                                   *
*                          Mike Gehm                                *
*                           9/18/99                                 *
*                                                                   *
*                          Version 1.0                              *
*                                                                   *
* This code does nothing but evolve a random ensemble forward in   *
* time. It serves as a template on which to construct a specific    *
* simulation. Simulation-specific code should be added to the       *
* function "main". If data reporting during the evolution is        *
* desired, reporting code should be added to the function "evolve,"*
* otherwise, post-evolution reporting code should be added to       *
* "main".                                                           *
*********************************************************************/

#include <stdio.h>
#include <math.h>
#include <stdlib.h>
#include <nr.h>
#include <nrutil.h>
#include "definitions.h"    /*#defs and some global variables*/
```

```
#include "prototypes.h"     /*function prototypes*/


/*****************************************************************
*  This function generates random velocity magnitudes according to *
*  a M-B distribution. U is the well depth and determines the      *
*  maximum possible velocity. The technique is an acceptance/      *
*  rejection method modified to use a piecewise trial function. The*
*  first piece is parabolic and runs from 0 to point1. The second  *
*  runs from point 1 to point 3 and is flat and equal to the max   *
*  value of the M-B (occurs at point 2). The third is a downward   *
*  slope from point 3 to vmax (assuming vmax is past point 3) and  *
*  runs from the constant value in region 2 down to the value of   *
*  the M-B at vmax.                                                *
*****************************************************************/

float RandV(float U, float T) /*U is well depth, T is temp*/
    {
        float kt2m,point1,point2,point3,ktme,vmax,pmax,limit,IRange,
            IRange1,IRange2,IRange3,delv,val,initv,slope,test;
        int goodpoint;

        kt2m=BoltzmannK*T/(2*LiMass);

        point1=sqrt(kt2m);
        point2=2*point1;
        point3=3*point1;

        ktme=2*point1*point1/EConst;

        /*max v that can be trapped*/
        vmax=sqrt(2*BoltzmannK*U/LiMass);
        /*value of M-B at vmax*/
        pmax=vmax*vmax*exp(-LiMass*vmax*vmax/(2*BoltzmannK*T));

        IRange1=4*point1*point1*point1/(3*EConst);
        IRange2=2*ktme*(point3-point1);
        IRange3=(ktme+pmax/2)*(vmax-point3);

        delv=vmax-point3;
        slope=(2*ktme-pmax)/delv;
```

```
/*flag the point for rejection unless it passes a later test*/
goodpoint=0;

while(goodpoint==0)
    {
        if(vmax<=point1) /*is vmax in region 1?*/
            {
                limit=min(vmax,point1);
                IRange=4*limit*limit*limit/(3*EConst);
            }
        else if(vmax<=point3) /*is vmax in region 2?*/
            {
                limit=min(vmax,point3);
                IRange=IRange1+2*ktme*(limit-point1);
            }
        else /*vmax must be in region 3*/
            {
                IRange=IRange1+IRange2+IRange3;
            }

        /*pick from proper sized region*/
        val=IRange*RandFloat();

        if(val<=IRange1) /*is val in region 1?*/
            {
                /*map to v*/
                initv=pow(3*EConst*val/4,0.3333333333);
                /*set scale for test*/
                IRange=4*initv*initv/EConst;
            }
        else if(val<=IRange1+IRange2) /*is val in region 2?*/
            {
                val=val-IRange1;
                /*map to v*/
                initv=point1+(EConst*val/(4*kt2m));
                /*set scale for test*/
                IRange=2*ktme;
            }
        else /*val must be in region 3*/
            {
                val=val-IRange1-IRange2;
                /*map to v*/
```

```
                        initv=point3+(2*ktme/slope-sqrt(4*ktme*
                            ktme/(slope*slope)-2*val/slope));
                        /*set scale for test*/
                        IRange=2*ktme-slope*(initv-point3);
                    }

                /*pick accept/reject value*/
                test=IRange*RandFloat();

                /*less than desired pdf at val?*/
                if(test<=initv*initv*exp(-LiMass*initv*
                    initv/(2*BoltzmannK*T)))
                    {
                        goodpoint=1; /*exit loop*/
                    }
            }

        return initv;
    }

/*****************************************************************
*  This function generates random radial coordinates  according to *
*  a M-B distribution. U is the well depth and T is the temperature*
*  of the atoms.  The technique is an acceptance/rejection method  *
*  modified to use a piecewise trial function. The first piece is  *
*  given by r^2 Exp[U/T] and extends from the origin to point 1.   *
*  The second piece is a line running from the end point of the    *
*  first piece to the value point2^2 at point2. After point2, the  *
*  desired distribution is nearly identical to the distribution of *
*  unbound atoms, so we don't generate any atoms in that range.     *
*****************************************************************/

float RandR(float U, float T,float rmax)
    {
        float a,point1,point2,pmax,pmin,fitmax,fitmin,slope,constant,
            IRange1,IRange,limit,val,initr,test;
        int goodpoint;

        /*precalculate an important factor*
        a=U/T;

        /*If there's no maximum set to fudge factor*/
```

```
if(1/a>=exp(-1))
    {
        point1=RFudgeFactor*1;
    }
else
    {
        /*approximate location of local max*/
        point1=RFudgeFactor*sqrt(1/a);
    }

/*point where dist is approx r^2*/
point2=sqrt(-log((1/a)*log(RAccuracy)));

/*************************************************************
*  don't worry about anything past the point where the     *
*  distribution is approximately equal to the distribution *
*  of unbound atoms.                                        *
*************************************************************/
rmax=min(point2,rmax);

pmax=rmax*rmax*exp(a*exp(-rmax*rmax));
pmin=point1*point1*exp(a*exp(-point1*point1));

fitmax=rmax*rmax;

fitmin=point1*point1*exp(a);

slope=(fitmax-fitmin)/(rmax-point1);
constant=fitmin;

/* compute the integral of the approx. over the first region*/
IRange1=exp(a)*point1*point1*point1/3;

/* flag for rejection unless it passes a later test */
goodpoint=0;

/* keep going until we get a good point */
while(goodpoint==0)
    {
        /* if rmax is in region 1, recompute integral */
        if(rmax<=point1)
            {
```

```
            IRange=exp(a)*rmax*rmax*rmax/3;
        }
    else
        {
            limit=rmax-point1;
            IRange=exp(a)*point1*point1*point1/3 +
                slope*limit*limit/2 + constant*limit;
        }

    /* pick a random point in the range */
    val=IRange*RandFloat();

    /* if the point is in region 1 */
    if(val<=IRange1)
        {
            /* find the point */
            initr=pow(3*val/exp(a),0.3333333333);
            /* set the value for accept/reject */
            IRange=exp(a)*initr*initr;
        }
    else /* we must be outside region 1 */
        {
            val=val-IRange1;
            /* find the point */
            initr=point1+(-constant/slope +
                sqrt(constant*constant/(slope*slope) +
                2*val/slope));

            if(slope<0)
                {
                    initr=point1+(-constant/slope -
                        sqrt(constant*constant/
                        (slope*slope)+2*val/slope));
                }

            /* set the value for accept/reject */
            IRange=constant+slope*(initr-point1);
        }

    /* generate random number for accept/reject */
    test=IRange*RandFloat();
```

```
                /* if it's less than the real distribution, keep it*/
                if(test<=initr*initr*exp(a*exp(-initr*initr)))
                    {
                        goodpoint=1;
                    }
            }

        return initr;
    }

/*****************************************************************
*  This function generates random positions and velocities for the *
*  atoms the cell and subcell numbers of the atoms are also set    *
*  based on the position of the atoms.                             *
*****************************************************************/

void InitAtoms(void)
    {
        int i,goodpoint;
        float en1,en2,pe,ke,totale,r,xp,yp,zp,x,y,z,theta,phi,v,vx,
            vy,vz;

        /* Loop until we have the desired number of atoms */
        for(i=0;i<NumAtoms;i++)
            {
                /* Flag for rejection unless it meets a later test*/
                goodpoint=0;

                while(goodpoint==0)
                    {
                        /* Generate a random r and v pair */
                        r=RandR(WellDepth,StartTemp,RadialSigmaLimit);
                        v=RandV(WellDepth,StartTemp);

                        /* Compute the energy of the atom */
                        pe=-BoltzmannK*WellDepth*exp(-r*r);
                        ke=LiMass*v*v/2;
                        totale=pe+ke;

                        /* If the atom is bound, keep it */
                        if(totale<0)
                            {
```

```
                goodpoint=1;
            }
        }

    /* Generate random angles for the position vector*/
    theta=RandTheta();
    phi=2*Pi*RandFloat();

    /* Convert from spherical to cartesian coords*/
    xp=r*sin(theta)*cos(phi);
    yp=r*sin(theta)*sin(phi);
    zp=r*cos(theta);

    /* Scale out to real coordinates */
    x=xp*ax;
    y=yp*ay;
    z=zp*az;

    /* Generate random angles for the velocity vector*/
    theta=RandTheta();
    phi=2*Pi*RandFloat();

    /* Convert from spherical to cartesian coords*/
    vx=v*sin(theta)*cos(phi);
    vy=v*sin(theta)*sin(phi);
    vz=v*cos(theta);

    /* Place the coordinates into the data structure *
    atomlist[i].x=x;
    atomlist[i].y=y;
    atomlist[i].z=z;
    atomlist[i].v_x=vx;
    atomlist[i].v_y=vy;
    atomlist[i].v_z=vz;

    /************************************************
    * This calls a routine that figures which cell the *
    * atom is in. Since the only use for cells is in   *
    * modelling collisions, and the code doesn't       *
    * currently model collisions, this function call   *
    * is commented out.                                *
    ************************************************/
```

```
                /*UpdateCell(i);*/

                /* Flag the atom as in range */
                atomlist[i].inrange=1;

            }
    }

/*****************************************************************
*  This function computes the cell and subcell number of an atom   *
*  based on its position. The function takes as its argument the   *
*  atom number of the atom to update. This function does not get   *
*  called in the current version, since cells are only useful in   *
*  modelling collisions---which aren't currently implemented.      *
*****************************************************************/

void UpdateCell(int i)
    {
        float shiftx,shifty,shiftz,xrel,yrel,zrel;

        shiftx=atomlist[i].x+RadialSigmaLimit*ax;
        shifty=atomlist[i].y+RadialSigmaLimit*ay;
        shiftz=atomlist[i].z+RadialSigmaLimit*az;

        atomlist[i].cell=(int)(shiftx/Cellscale_x)+(int)(Cells_x*
            (int)(shifty/Cellscale_y))+((int)(Cells_x*Cells_y)*
            (int)(shiftz/Cellscale_z));

        xrel=((shiftx/(float)Cellscale_x)-(int)(shiftx/Cellscale_x))*
            Cellscale_x;
        yrel=((shifty/(float)Cellscale_y)-(int)(shifty/Cellscale_y))*
            Cellscale_y;
        zrel=((shiftz/(float)Cellscale_z)-(int)(shiftz/Cellscale_z))*
            Cellscale_z;

        atomlist[i].subcell=(int)(xrel/Subcellscale_x)+
            (int)(Subcells_x*(int)(yrel/Subcellscale_y))+
            ((int)(Subcells_x*Subcells_y)*(int)(zrel/Subcellscale_z));
    }

/*****************************************************************
*  This function updates the posistion of an atom based on its     *
```

```
*  velocity. The function takes as its argument the atom number of *
*  the atom to update, the time step to propagate through, and     *
*  whether to treat the region as having walls.                    *
*******************************************************************/

void UpdatePosition(int i, float delta_t)
    {
        float x,y,z,vx,vy,vz;

        /*Compute new position assuming constant velocity*/
        x=atomlist[i].x+atomlist[i].v_x*delta_t;
        y=atomlist[i].y+atomlist[i].v_y*delta_t;
        z=atomlist[i].z+atomlist[i].v_z*delta_t;

        /*********************************************************
        *  If the atoms has travelled extremely far, it's likely   *
        *  no longer bound, forget about it.                       *
        *********************************************************/
        if(sqrt(x*x/(ax*ax)+ y*y/(ay*ay)+z*z/(az*az))>
            RadialSigmaLimit)
            {
                /*set in range flag to 0*/
                atomlist[i].inrange=0;
            }
        /*if in range*/
        else
            {
                /*set the new values*/
                atomlist[i].x=x;
                atomlist[i].y=y;
                atomlist[i].z=z;
            }
    }

/*******************************************************************
*  This function updates the velocity of an atom based on the      *
*  acceleration it feels due to the potential at its position. The *
*  function takes as its argument the atom number of the atom to   *
*  update and the time step to propagate through.                  *
*******************************************************************/

void UpdateVelocity(int i,float delta_t)
```

```
    {
        /* Update the velocity assuming constant acceleration */
        atomlist[i].v_x=atomlist[i].v_x+delta_t*ForceX(i)/LiMass;
        atomlist[i].v_y=atomlist[i].v_y+delta_t*ForceY(i)/LiMass;
        atomlist[i].v_z=atomlist[i].v_z+delta_t*ForceZ(i)/LiMass;
    }

/*****************************************************************
*  This function runs the actual DSMC method. It controls the     *
*  loops over particles and over cells. It takes as arguments the *
*  timestep, number of timesteps, and the boundary condition to   *
*  apply when updating particle position.                         *
*****************************************************************/

void Evolve(float inittime, float finaltime, int numtimesteps,FILE *ofp)
    {
        int i,j,n,num,numcells;
        float delta_t,temppe,tempke,tempx,tempen;

        numcells=Cells_x*Cells_y*Cells_z;

        /* Compute the timestep */
        delta_t=(finaltime-inittime)/(numtimesteps);

        /* Loop over timesteps */
        for(n=0;n<numtimesteps;n++)
            {
                thetime=inittime+delta_t*n;

                /* Loop over all atoms */
                for(i=0;i<NumAtoms;i++)
                    {
                        /* If the atom is still in range ...*/
                        if(atomlist[i].inrange==1)
                            {
                                /* Get the new state of the atom */
                                UpdatePosition(i,delta_t);
                                UpdateVelocity(i,delta_t);

                                /*********************************
                                * If it's still in range, compute  *
                                * the new cell number. This        *
```

```
                                * function isn't called because    *
                                * cells aren't currently used.     *
                                ************************************/
                                /*
                                if(atomlist[i].inrange==1)
                                    {
                                        UpdateCell(i);
                                    }
                                */
                            }
                        }
                        /*********************************************
                        * Loop over the cells and call the collision   *
                        * routine for each cell. This function isn't   *
                        * called because collisions aren't implemented *
                        *********************************************/
                        /*
                        for(j=0;j<numcells;j++)
                        {
                            Collide(j,delta_t);
                        }
                        */

                        /*********************************************
                        * Insert appropriate reporting code here       *
                        * depending on the specific purpose of the     *
                        * simulation.                                  *
                        *********************************************/
                }
        }

/*****************************************************************
*  This function calculates the number of atoms that would remain  *
*  trapped if the well were suddenly lowered to 'fraction' of the  *
*  original well depth                                             *
*****************************************************************/

int Measure(float fraction)
    {
        int i,count;

        count=0;
```

```
        /* Loop over atoms */
        for(i=0;i<NumAtoms;i++)
            {
                /* If it's in range ...*/
                if(atomlist[i].inrange==1)
                    {
                        /* Add one to the count for each bound atom*/
                        if(CalcEnergy(fraction,i)<0)
                            {
                                count=count+1;
                            }
                    }
            }

        return count;
    }

/*********************************************************************
*  This function calculates the energy of the atoms if the well    *
*  depth were suddenly lowered to 'fraction' of the original well  *
*  depth                                                           *
*********************************************************************/

float CalcEnergy(float fraction, int i)
    {
        float en;

        en=(fraction*PotEn(i))+KinEn(i);

        return en;
    }

/*********************************************************************
*  This function calculates the potential energy of the atoms at   *
*  time 't'. The time dependence comes from the amplitude          *
*********************************************************************/

float PotEn(int i)
    {
        float pe;
```

```
        pe=-Amplitude(thetime)*BoltzmannK*
            exp(-(atomlist[i].x*atomlist[i].x/(ax*ax)+
            atomlist[i].y*atomlist[i].y/(ay*ay)+
            atomlist[i].z*atomlist[i].z/(az*az)));

        return pe;
    }

/*****************************************************************
*  This function calculates the potential energy the atoms would   *
*  have in the original well. This is useful for heating studies.  *
*****************************************************************/

float NormPotEn(int i)
    {
        float pe;

        pe=-WellDepth*BoltzmannK*
            exp(-(atomlist[i].x*atomlist[i].x/(ax*ax)+
            atomlist[i].y*atomlist[i].y/(ay*ay)+
            atomlist[i].z*atomlist[i].z/(az*az)));

        return pe;
    }


/*****************************************************************
*   This function calculates the kinetic energy of the atoms       *
*****************************************************************/

float KinEn(int i)
    {
        float ke;

        ke=LiMass*(atomlist[i].v_x*atomlist[i].v_x+
            atomlist[i].v_y*atomlist[i].v_y+
            atomlist[i].v_z*atomlist[i].v_z)/2;

        return ke;
    }

/*****************************************************************
```

```
*  These functions calculate the force on the atoms at time 't'.   *
*  The time dependence comes from the amplitude in the potential   *
*  energy function                                                 *
*******************************************************************/

float ForceX(int i)
    {
        float force;

        force=2*(atomlist[i].x/(ax*ax))*PotEn(i);

        return force;
    }

float ForceY(int i)
    {
        float force;

        force=2*(atomlist[i].y/(ay*ay))*PotEn(i);

        return force;
    }

float ForceZ(int i)
    {
        float force;

        force=2*(atomlist[i].z/(az*az))*PotEn(i);

        return force;
    }

/*******************************************************************
*  This function changes the amplitude of the well as a function   *
*  of time. The time dependence can be turned off with a global    *
*  flag                                                            *
*******************************************************************/

float Amplitude(float t)
    {
        float amp;
```

```
        if(OscFlag==1)
            {
                amp=WellDepth*(1+OscFrac*sin(2*Pi*OscFreq*t));
            }
        else
            {
                amp=WellDepth;
            }

        return amp;
    }

/*********************************************************************
* This function is currently not implemented.                        *
*********************************************************************/

void Collide(int j,float delta_t)
    {
    }

/*********************************************************************
*   This is the main routine.                                        *
*********************************************************************/

void main(void)
    {
        FILE *ofp;
        int i,j,f,n,number;
        float init_delta_t,sim_delta_t,DeltaFreq,FreqSteps,InitFreq,
            ifrac,mfrac,temp;

        ofp=fopen("output.dat","w");

        /*************************************************************
        * Insert simulation specific code here. Set global flags,    *
        * oscillation frequencies, etc.                              *
        *************************************************************/

        /*seed the random number generator with the computer clock*/
        srand(clock());

        /*generate random particle positions and velocities*/
```

```
        InitAtoms();

        /* Run the simulation */
        Evolve(0,1.0,1000000,ofp);

        printf("Done.\n");

        fclose(ofp);
    }


/*************************************************************************
* END FILE "main.c"
*************************************************************************/
```

C.5 Fokker-Planck Code

PROGRAM DESCRIPTION: This program computes the evolution of a harmonically-trapped population distribution subject to noise-induced heating. The evolution is based on numerically solving the Fokker-Planck equation derived in Chapter 5

LANGUAGE: ANSI C

AUTHOR: Michael E. Gehm

USAGE: When run, the code reads in the file "input.dat". The required structure of this input file is described in the internal comments of the code below. The output is written to the file "output.dat".

```
/*************************************************************
*   Finite Difference Code For Modelling 3-D Trap Population
*                 as a Function of Time
*
*                       Explicit Method
*
*                         Mike Gehm
*                          06/09/97
*************************************************************/

#include "population.h"

/*************************************************************
*   This function sums the population distribution at a given
*   time step
*************************************************************/

double sum_pop(int elevels, double *the_pop)
    {
        int     l;
        double  num;

        num=0;
```

```
        for(l=0; l<=elevels+1; l++)
            {
                num = num + the_pop[l];
            }

        return(num);
    }

/************************************************************
*   This function sums the energy at a given time step
************************************************************/

double sum_en_pop(int elevels, double *ener, double *the_pop)
    {
        int     l;
        double  en;

        en=0;

        for(l=0; l<=elevels+1; l++)
            {
                en = en + ener[l]*the_pop[l];
            }

        return(en);
    }

/************************************************************
*   This function dynamically allocates 2-D arrays in a
*   non-brain-damaged way
************************************************************/

double **dmatrix(int nrl, int nrh, int ncl, int nch)
    {
        int      i, nrow=nrh-nrl+1, ncol=nch-ncl+1;
        double   **m;

        m=(double **) malloc((size_t)((nrow+1)*sizeof(double*)));
        m += 1;
        m -= nrl;

        m[nrl]=(double *) malloc((size_t)((nrow*ncol+1)*
```

```
            sizeof(double)));
        m[nrl] += 1;
        m[nrl] -= ncl;

        for(i=nrl+1;i<=nrh;i++) m[i]=m[i-1]+ncol;

        return m;
    }

/*************************************************************
*   This is the beginning of the main routine
*************************************************************/

void main(void)
    {

        /*************************************************************
        *   Variable Declaration:
        *
        *   ifp,ofp         input and output file pointers
        *   elevels         number of energy levels to use in
        *                       the mesh
        *   i               iterator
        *   evtime          length of evolution to simulate
        *                       (in units of gamma t)
        *   chi             dimensionless parameter
        *                       (qdot/(gamma E0))
        *   ics             pointer to array of initial conditions
        *************************************************************/

        FILE    *ifp, *ofp;
        int     elevels, i, j, numsteps, numcalcs, approxhours,
                approxminutes,approxseconds,num_reports,report_incr,
                report_style,l,m,limit;
        double  *old_pop_dist,*pop_dist, *eps, tau, en, enzero, num,
                numzero,del_eps, del_tau, evtime, chi,approxtime,
                rho, rho2,a,b,c,d,**distmat;

        /*************************************************************
        *   This section reads in the data file. The file format is
        *   as follows:
        *   0)  Discretization Limit. 0=Pure Gamma Okay,
```

```
*           1=Pure Qdot okay (int)
*   1)  Dimensionless parameter, chi, (qdot/(gamma E0))
*           (in Gamma Limit) (gamma E0)/qdot
*           (in qdot limit)  (float)
*   2)  Dimensionless time to simulate (units of gamma t)
*           (float)
*   3)  Requested report style (0=Fractional Population
*           vs Time,1=Fractional Energy vs Time, 2=Mean
*           Energy vs Time, 3=Combination of 0-2,
*           5=Population distributions)
*   4)  Number of data points (or distributions) to place
*           in the output
*   5)  Number of energy mesh points
*   6 on)   Initial conditions for those energy points,
*           starting with lowest energy level (long doubles)
*************************************************************/

if (( ifp = fopen("input.dat", "r")) == NULL)
    {
        printf("Can't find file.\n");
        exit(1);
    }

fscanf(ifp,"%d",&limit);
fscanf(ifp,"%Lf",&chi);
fscanf(ifp,"%Lf",&evtime);
fscanf(ifp,"%d",&report_style);
fscanf(ifp,"%d",&num_reports);
fscanf(ifp,"%d",&elevels);


pop_dist = (double *)malloc((elevels+2)*sizeof(double));
old_pop_dist = (double *)malloc((elevels+2)*sizeof(double));

for(i=1; i<=elevels; i++)
    {
        fscanf(ifp,"%Lf",&old_pop_dist[i]);
    }

fclose(ifp);

/*************************************************************
```

```
*   A few required initializations
*************************************************************/

old_pop_dist[0]=0.0;
old_pop_dist[elevels+1]=0.0;
pop_dist[0]=0.0;
pop_dist[elevels+1]=0;

/*************************************************************
*   This section calculates the time step necessary for
*   stability and the number of required time steps.
*************************************************************/

del_eps = 1.0 / (elevels + 1);

if(limit==0)
    {
        del_tau = STAB_COEFF * pow(del_eps,2)*(2/(1+4*chi));
    }
else
    {
        del_tau = STAB_COEFF * pow(del_eps,2)*(2/(chi+4));
    }

numsteps = ceil(evtime/del_tau);
numcalcs = numsteps * elevels;

approxtime = numcalcs / MESH_POINTS_PER_SEC;

approxhours = floor(approxtime/3600);
approxtime = approxtime - approxhours*(3600);
approxminutes = floor(approxtime/60);
approxseconds = floor(approxtime - approxminutes*(60));

report_incr = numsteps / (num_reports - 1);

/*************************************************************
*   This section sets up the array for the eps values of
*   the mesh and sets up the variables which will hold the
*   initial time, population, and energy
*************************************************************/
```

```
eps = (double *)malloc((elevels+2)*sizeof(double));

for(i=0; i<=elevels+1; i++)
    {
        eps[i]=0 + i * del_eps;
    }

/*********************************************************
*   This accounts for the fact that the user inputs the
*   initial conditions in terms of occupation number.
*********************************************************/

for(i=0; i<=elevels+1; i++)
    {
        old_pop_dist[i]=old_pop_dist[i] * pow(eps[i],2);
    }

tau = 0.0;

numzero = sum_pop(elevels,old_pop_dist);
enzero = sum_en_pop(elevels,eps,old_pop_dist);
en = enzero;
num = numzero;

/*********************************************************
*   This section calculates certain constants used in the
*   difference method in order to maximize computational
*   speed.
*********************************************************/

rho = del_tau / pow(del_eps,2);
rho2 = del_tau/del_eps;

if(limit==0)
    {
        a = 1.0/4.0;
        b = chi;
        c = chi/2.0;
        d = 1.0/2.0;
    }
else
    {
```

```
        a = chi/4.0;
        b = 1.0;
        c = 1.0/2.0;
        d = chi/2.0;
    }

/*************************************************************
*   This is the main loop for the finite difference method.
*************************************************************/

l = 1;

ofp = fopen("output.dat","w");

/*************************************************************
*   Setup the column headings of the output file.
*************************************************************/

switch (report_style)
    {
        case (0) :
            {
                fprintf(ofp,"Tau\tFracPop\n");
                fprintf(ofp,"%Lf\t%Lf\n",tau,num/numzero);
                break;
            }
        case (1) :
            {
                fprintf(ofp,"Tau\tFracEn\n");
                fprintf(ofp,"%Lf\t%Lf\n",tau,en/enzero);
                break;
            }
        case (2) :
            {
                fprintf(ofp,"Tau\tMeanEn\n");
                fprintf(ofp,"%Lf\t%Lf\n",tau,en/num);
                break;
            }
        case (3) :
            {
                fprintf(ofp,"Tau\tFracPop\tFracEn\tMeanEn\n");
                fprintf(ofp,"%Lf\t%Lf\t%Lf\t%Lf\n",tau,
```

```
                                num/numzero,en/enzero,en/num);
                        break;
                    }
                case (4) :
                    {
                        distmat = dmatrix(0,elevels+1,0,num_reports);
                        fprintf(ofp,"Epsilon\tT0.00000\t");
                        for(j=0; j<=elevels+1; j++)
                            {
                                distmat[j][0]=eps[j];
                                distmat[j][l]=old_pop_dist[j]/
                                    pow(eps[j],2);
                            }
                        l++;
                        break;
                    }
                case (5) :
                    {
                        distmat = dmatrix(0,elevels+1,0,num_reports);
                        fprintf(ofp,"Epsilon\tT0.00000\t");
                        for(j=0; j<=elevels+1; j++)
                            {
                                distmat[j][0]=eps[j];
                                distmat[j][l]=old_pop_dist[j];
                            }
                        l++;
                        break;
                    }
            };

        /*********************************************************
        *   Begin cycling through all the timesteps.
        *********************************************************/

        for(i=1; i<=numsteps; i++)
            {

                /*************************************************
                *   Loop over the energy grid computing the new
                *   values.
                *************************************************/
```

```
for(j=1; j<=elevels; j++)
    {
        pop_dist[j] = ((a*pow(eps[j],2)+b*eps[j])*
            rho-c*rho2)*old_pop_dist[j+1]+
            ((a*pow(eps[j],2)+b*eps[j])*rho+c*rho2)*
            old_pop_dist[j-1]+(-2*(a*pow(eps[j],2)+
            b*eps[j])*rho -d*del_tau + 1)*
            old_pop_dist[j];
    };

tau = tau + del_tau;

for(j=1; j<=elevels; j++)
    {
        old_pop_dist[j]=pop_dist[j];
    }

/*************************************************
*   Write to the output file if it's a reporting
*   increment.
*************************************************/

if(i%report_incr==0)
    {
        switch(report_style)
            {
                case(0) :
                    {
                        num = sum_pop(elevels,
                                pop_dist);
                        fprintf(ofp,"%Lf\t%Lf\n",
                                tau,num/numzero);
                        break;
                    }
                case(1) :
                    {
                        en = sum_en_pop(elevels,eps,
                                pop_dist);
                        fprintf(ofp,"%Lf\t%Lf\n",
                                tau,en/enzero);
                        break;
                    }
```

```
case(2) :
    {
        en = sum_en_pop(elevels,eps,
                pop_dist);
        num = sum_pop(elevels,
                pop_dist);
        fprintf(ofp,"%Lf\t%Lf\n",
                tau,en/num);
        break;
    }
case(3) :
    {
        en = sum_en_pop(elevels,eps,
                pop_dist);
        num = sum_pop(elevels,
                pop_dist);
        fprintf(ofp,"%Lf\t%Lf\t%Lf\t
                %Lf\n",tau,num/
                numzero,en/enzero,
                en/num);
        break;
    }
case(4) :
    {
        if(l==num_reports)
            fprintf(ofp,"T%Lf\n",tau);
        else
            fprintf(ofp,"T%Lf\t",tau);
        for(m=0; m<=elevels+1; m++)
            {
                distmat[m][l]=
                    old_pop_dist[m];
            }
        l++;
        break;
    }
case (5) :
    {
        if(l==num_reports)
            fprintf(ofp,"T%Lf\n",tau);
        else
            fprintf(ofp,"T%Lf\t",tau);
```

```
                                        for(m=0; m<=elevels+1; m++)
                                            {
                                                distmat[m][l]=
                                                    old_pop_dist[m];
                                            }
                                        l++;
                                        break;
                                    }
                            };
                    }
            }

        if(report_style==4||report_style==5)
            {
                for(i=0;i<=elevels+1;i++)
                    {
                        for(j=0;j<=num_reports;j++)
                            {
                                if(j==num_reports)
                                    fprintf(ofp,"%Lf\n",
                                        distmat[i][j]);
                                else
                                    fprintf(ofp,"%Lf\t",distmat[i][j]);
                            }
                    }
            }

        fclose(ofp);

        printf("Program Execution Complete.");
    }
```

Bibliography

[1] A. Einstein. Quantentheorie des einatomigen idealen Gases. Zweite Abhandlung. (Quantum theory of monatomic ideal gases. Second treatment.). *Sitzungberichte, Preussische Akademie der Wissenschaften*, page 3, 1925.

[2] A. Einstein. Quantentheorie des einatomigen idealen Gases. (Quantum theory of monatomic ideal gases.). *Sitzungberichte, Preussische Akademie der Wissenschaften*, page 261, 1924.

[3] M. H. Anderson, J. R. Ensher, M. R. Matthews, C. E. Wieman, and E. A. Cornell. Observation of Bose-Einstein condensation in a dilute atomic vapor. *Science*, 269(0):198, July 1995.

[4] K. B. Davis, M.-O. Mewes, M. R. Andrews, N. J. van Druten, D. S. Durfee, D. M. Kurn, and W. Ketterle. Bose-Einstein condensation in a gas of sodium atoms. *Phys. Rev. Lett.*, 75(22):3969, November 1995.

[5] C. C. Bradley, C. A. Sackett, J. J. Tollett, and R. G. Hulet. Evidence of Bose-Einstein condensation in an atomic gas with attractive interactions. *Phys. Rev. Lett.*, 75(9):1687, August 1995. *ibid.* **79**, 1170 (1997).

[6] S. N. Bose. Plancks gesetz und lichtquantenhypothese (Planck's law and the hypothesis of light quanta). *Z. Phys.*, 26(178), 1924.

[7] E. Fermi. *Z. Phys.*, 36:902, 1926.

[8] P. A. M. Dirac. *Proc. Roy. Soc.*, 112:661, 1926.

[9] W. Pauli. *Z. Phys*, 32:794, 1925.

[10] Charles Kittel and Herbert Kroemer. *Thermal Physics.* W. H. Freeman and Company, New York, 1980.

[11] Henning Heiselberg. Fermi systems with long scattering lengths. *Phys. Rev. A*, 63:043606, 2001.

[12] James V. Steele. Effective field theory power counting at finite density. see nucl-th/0010066, 2000.

[13] J. Bardeen, L. N. Cooper, and J. R. Schrieffer. Theory of superconductivity. *Phys. Rev.*, 108:1175, 1957.

[14] M. Houbiers, R. Ferwerda, H. T. C. Stoof, W. I. McAlexander, C. A. Sackett, and R. G. Hulet. Superfluid state of atomic ^{6}Li in a magnetic trap. *Phys. Rev. A*, 56(6):4864, December 1997.

[15] Herman Feshbach. A unified theory of nuclear reactions. II. *Ann. Phys.*, 19:287, 1962.

[16] M. Holland, S. J. J. M. F. Kokkelmans, M. L. Chiofalo, and R. Walser. Resonance superfluidity in a quantum degenerate Fermi gas. *Phys. Rev. Lett.*, 87:120406, 2001.

[17] E. Timmermans, K. Furuya, P. W. Milonni, and A. K. Kerman. Prospect of creating a composite Fermi/Bose superfluid. *Phys. Lett. A*, 285:228, 2001.

[18] Y. Ohashi and A. Griffin. BCS-BEC crossover in a gas of Fermi atoms with a Feshbach resonance. *Phys. Rev. Lett.*, 89:130402, 2002.

[19] K. M. O'Hara, S. L. Hemmer, M. E. Gehm, S. R. Granade, and J. E. Thomas. Observation of a strongly-interacting degenerate fermi gas of atoms. *Science*, 298(5601):2179, 2002.

[20] S. R. Granade. *Preparation of an Optically-Trapped Degenerate Fermi Gas of ^{6}Li: Characterization of Degeneracy.* PhD thesis, Duke University, 2002.

[21] K. M. O'Hara. *Optical Trapping and Evaporative Cooling of Fermionic Atoms.* PhD thesis, Duke University, 2000.

[22] A. G. Truscott, K. E. Strecker, W. I. McAlexander, G. Partridge, and R. G. Hulet. Observation of Fermi pressure in a gas of trapped atoms. *Science*, 291:2570, 2001.

[23] F. Schreck, L. Khaykovich, K. L. Corwin, G. Ferrari, T. Bourdel, J. Cubizolles, and C. Salomon. Quasipure Bose-Einstein condensate immersed in a Fermi sea. *Phys. Rev. Lett.*, 87:080403, 2001.

[24] Z. Hadzibabic, C. A. Stan, K. Dieckmann, S. Gupta, M. W. Zwierlein, A. G orlitz, , and W. Ketterle. Two-species mixture of quantum degenerate Bose and Fermi gases. *Phys. Rev. Lett.*, 88:160401, 2002.

[25] G. A. Bird. *Molecular gas dynamics and the direct simulation of gas flows.* Clarendon Press, Oxford, 1994.

[26] T. A. Savard, K. M. O'Hara, and J. E. Thomas. Laser-noise-induced heating in far-off resonance optical traps. *Phys. Rev. A*, 56(2):R1095, August 1997.

[27] M. E. Gehm, K. M. O'Hara, T. A. Savard, and J. E. Thomas. Dynamics of noise-induced heating in atom traps. *Phys. Rev. A*, 58(5):3914, November 1998.

[28] H. J. Lee, C. S. Adams, N. Davidson, B. Young, M. Weitz, M. Kasevich, and Steven Chu. Dipole trapping, cooling in traps, and long coherence times. *At. Phys.*, 14(323):258, 1995.

[29] C. A. Baird. Design and characterization of a multi-coil zeeman slower. Master's thesis, Duke University, 1996.

[30] Thomas Alan Savard. *Raman Induced Resonance Imaging of Trapped Atoms*. PhD thesis, Duke University, 1998.

[31] E. L. Raab, M. Prentiss, Alex Cable, Steven Chu, and D. E. Pritchard. Trapping of neutral sodium atoms with radiation pressure. *Phys. Rev. Lett.*, 59(23):2631, December 1987.

[32] Steven Chu, L. Hollberg, J. E. Bjorkholm, Alex Cable, and A. Ashkin. Three-dimensional viscous confinement and cooling of atoms by resonance radiation pressure. *Phys. Rev. Lett.*, 55(1):48, July 1985.

[33] A. Ashkin. Trapping of atoms by resonance radiation pressure. *Phys. Rev. Lett.*, 40(12):729, March 1978.

[34] Steven Chu, J. E. Bjorkholm, A. Ashkin, and A. Cable. Experimental observation of optically trapped atoms. *Phys. Rev. Lett.*, 57(3):314, July 1986.

[35] J. D. Miller, R. A. Cline, and D. J. Heinzen. Far-off-resonance optical trapping of atoms. *Phys. Rev. A*, 47(6):R4567, June 1993.

[36] T. Takekoshi, J. R. Yeh, and R. J. Knize. Quasi-electrostatic trap for neutral atoms. *Opt. Comm.*, 114:421, February 1995.

[37] R. Grimm, M. Weidemüller, and Y. B. Ovchinnikov. Optical dipole traps for neutral atoms. *Adv. At. Mol. Opt. Phys.*, 42:95, 2000.

[38] Amnon Yariv. *Quantum Electronics*. John Wiley and Sons, New York, 2nd edition, 1975.

[39] K. M. O'Hara, S. R. Granade, M. E. Gehm, T. A. Savard, S. Bali, C. Freed, and J. E. Thomas. Ultrastable CO_2 laser trapping of lithium fermions. *Phys. Rev. Lett.*, 82(21):4204, May 1999.

[40] K. M. O'Hara, M. E. Gehm, S. R. Granade, and J. E. Thomas. Scaling laws for evaporative cooling in time-dependent optical traps. *Phys. Rev. A*, 64(051403(R)):051403, October 2001.

[41] K.B. Davis, M.-O. Mewes, and W. Ketterle. An analytical model for evaporative cooling of atoms. *Appl. Phys. B*, 60:155, 1995.

[42] M. Houbiers, H. T. C. Stoof, W. I. McAlexander, and R. G. Hulet. Elastic and inelastic collisions of ^{6}Li atoms in magnetic and optical traps. *Phys. Rev. A*, 57(3):R1497, March 1998.

[43] N. W. Ashcroft and N. D. Mermin. *Solid State Physics*. Holt, Rinehart, and Winston, Philadelphia, 1976.

[44] P. Ring and P. Schuck. *The Nuclear Many-Body Problem*. Springer-Verlag, New York, 1980.

[45] Wolfram Research. Polylogarithm function. see `http://functions.wolfram.com/`.

[46] W. Ketterle, D. S. Durfee, and D. M. Stamper-Kurn. Making, probing and understanding Bose-Einstein condensates. In M. Inguscio, S. Stringari, and C. E. Wieman, editors, *Proceedings of the International School of Physics - Enrico Fermi*, page 67. IOS Press, 1999.

[47] G. M. Bruun and C. W. Clark. Ideal gases in time-dependent traps. *Phys. Rev. A*, 61:061601, 2000.

[48] James E. Gentle. *Random Number Generation and Monte Carlo Methods*. Springer-Verlag, Berlin, 1998.

[49] A. B. Pippard. *The Physics of Vibration*, volume 1. Cambridge University Press, Cambridge, 1978.

[50] S. Friebel, C. D'Andrea, J. Walz, M. Weitz, and T. W. Hänsch. CO_2-laser optical lattice with cold rubidium atoms. *Phys. Rev. A.*, 57(1):R20, January 1998.

[51] R. Jáuregui. Nonperturbative and perturbative treatments of parametric heating in atom traps. *Phys. Rev. A*, 64(053408), 2001.

[52] K. M. O'Hara, M. E. Gehm, S. R. Granade, S. Bali, and J. E. Thomas. Stable, strongly attractive, two-state mixture of lithium fermions in an optical trap. *Phys. Rev. Lett.*, 85(10):2092, September 2000.

[53] Neil Gershenfeld. *The Nature of Mathematical Modeling*. Cambridge University Press, Cambridge, 1999.

[54] F. Reif. *Fundamentals of Statistical and Thermal Physics*. McGraw-Hill, New York, 1965.

[55] D. Zwillinger, editor. *CRC Standard Mathematical Tables and Formulæ*. CRC Press, Boca Raton, 30th edition, 1996.

[56] K.M. O'Hara, S.R. Granade, M.E. Gehm, and J.E. Thomas. Loading dynamics of CO_2 laser traps. *Phys. Rev. A*, 63:043403, July 2001.

[57] Harold Metcalf and Peter van der Straten. Cooling and trapping of neutral atoms. *Phys. Rep.*, 244:203, 1994.

[58] Leslie Allen and Joseph H. Eberly. *Optical Resonance and Two-Level Atoms*. Dover Publications, 1975.

[59] J. E. Thomas. Lecture Notes—Advanced Quantum Optics.
Lecture notes from a course taught at Duke University, 1998.

[60] Rodney Loudon. *The Quantum Theory of Light*. Clarendon Press, Oxford, 1983.

[61] Joseph W. Goodman. *Introduction to Fourier optics*. McGraw-Hill, New York, 1996.

[62] A. R. Edmonds. *Angular Momentum in Quantum Mechanics*. Princeton University Press, 1960.

[63] D. A. Butts and D. S. Rokhsar. Trapped Fermi gases. *Phys. Rev. A*, 55(6):4346, June 1997.

[64] S. R. Granade, M. E. Gehm, K. M O'Hara, and J. E. Thomas. All-optical production of a degenerate Fermi gas. *Phys. Rev. Lett.*, 88:120405, 2002.

[65] K. M. O'Hara, S. L. Hemmer, S. R. Granade, M. E. Gehm, J. E. Thomas, V. Venturi, E. Tiesinga, and C. J. Williams. Measurement of the zero crossing in a Feshbach resonance of fermionic Li. *Phys. Rev. A*, 66:041401(R), 2002.

[66] K. Dieckmann, C. A. Stan, S. Gupta, Z. Hadzibabic, C. H. Schunck, and W. Ketterle. Decay of an ultracold fermionic lithium gas near a Feshbach resonance. *Phys. Rev. Lett.*, 89:203201, 2002.

[67] S. Jochim, M. Bartenstein, G. Hendl, J. Hecker Denschlag, and R. Grimm. Magnetic field control of elastic scattering in a cold gas of fermionic lithium atoms. *Phys. Rev. Lett.*, 89:273202, 2002.

[68] D. A. Steck. Cesium D line data.
see `http://george.ph.utexas.edu/~dsteck/alkalidata`., 2000.

[69] D. A. Steck. Sodium D line data.
see `http://george.ph.utexas.edu/~dsteck/alkalidata`., 2000.

[70] R. C. Weast, M. J. Astle, and W. H. Beyer, editors. *CRC Handbook of Chemistry and Physics*. CRC Press, Boca Raton, 64th edition, 1983.

[71] A. N. Nesmeyanov. *Vapour Pressure of the Elements*. Academic Press, New York, 1963.

[72] I. Mills, T. Cvitas, K. Homann, N. Kallay, and K. Kuchitsu. *Quantities, Units, and Symbols in Physical Chemsitry*. Blackwell Scientific Publishing, Oxford, 1988.

[73] W. I. McAlexander, E. R. I. Abraham, and R. G. Hulet. Radiative lifetime of the $2P$ state of lithium. *Phys. Rev. A*, 54(1):R5, July 1996.

[74] W. Scherf, O. Khait, H. Jäger, and L. Windholz. Re-measurement of the transition frequencies, fine structure splitting and isotope shift of the resonance lnes of lithium, sodium and potassium. *Z. Phys. D*, 36:31, 1996.

[75] R. Liboff. *Introductory Quantum Mechanics*. Addison-Wesley, New York, 2nd edition, 1993.

[76] P. J. Mohr and B. N. Taylor. CODATA recommended values of the fundamental physical constants: 1998. *Rav. Mod. Phys.*, 72, 2000.

[77] J. Walls, R. Ashby, J. Clarke, B. Lu, and W. Wijngaarden. Measurement of isotope shifts, fine and hyperfine structure splittings of the lithium D lines. preprint provided in private communication, 2002.

[78] I. I. Sobel'man. *Introduction to the Theory of Atomic Spectra*. Pergamon Press, Oxford, 1972.

[79] E. Arimondo, M. Inguscio, and P. Violino. Experimental determinations of the hyperfine structure in the alkali atoms. *Rev. Mod. Phys.*, 49(1):31, January 1977.

[80] R. W. Schmieder, A. Lurio, and W. Happer. Quadratic Stark effect in the $^2P_{3/2}$ states of the alkali atoms. *Phys. Rev. A*, 3(4):1209, April 1971.

[81] A Khadjavi, A. Lurio, and W. Happer. Stark effect in excited states of Rb, Cs, Cd, and Hg. *Phys. Rev.*, 167(1):128, March 1968.

[82] R. W. Molof, H. L. Schwartz, T. M. Miller, and B. Bederson. Measurments of electric dipole polarizabilities of the alkali-metal atoms and the metastable noble gas atoms. *Phys. Rev. A*, 10(4):1131, October 1974.

[83] L. Windholz, M. Musso, G Aerza, and H. Jäger. Precise Stark-effect investigations of the lithium D_1 and D_2 lines. *Phys. Rev. A*, 46(9):5812, November 1992.

[84] J. E. Thomas. Lecture Notes—Quantum Mechanics I.
Lecture notes from a course taught at Duke University, 1995.

[85] E. Merzbacher. *Quantum Mechanics*. John Wiley and Sons, New York, 3rd edition, 1998.

[86] C. J. Joachain. *Quantum Collision Theory*. North-Holland Publishing Company, 1983.

[87] N. F. Mott and H. S. W. Massey. *The Theory of Atomic Collisions*. Clarendon Press, Oxford, 1965.

[88] E. R. I. Abraham, W. I. McAlexander, J. M. Gerton, R. G. Hulet, R. Côté, and A. Dalgarno. Triplet s-wave resonance in ^{6}Li collisions and scattering lengths of ^{6}Li and ^{7}Li. *Phys. Rev. A*, 55(5):R3299, May 1997.

Biography

Michael Gehm was born in Würzburg, West Germany on March 14, 1969. As is typical for "army brats," his childhood was spent in a wide variety of locales. Most notable among these was a four-year period spent in Stuttgart, West Germany. In 1987, he graduated from Virgil I. Grissom High School in Huntsville, Alabama. That summer, he travelled to the White House to receive the United States Presidential Scholar Award from President Ronald Reagan. In the fall he matriculated at Washington University in St. Louis, where he had accepted an Army ROTC scholarship to study mechanical engineering. He received his B.S. in 1992, returned to Huntsville, and began work as an engineer. In 1995 he entered the graduate physics program at Duke University. His research at Duke was performed under the supervision of Professor John E. Thomas and focused on the preparation of a degenerate Fermi gas of ^{6}Li atoms. In recognition of this work, he was awarded the 2001 Fritz London Fellowship. His A.M. was awarded in 1998 and his Ph.D. in 2003. His personal life began a new chapter on June 27, 1998, when he married his long-time love, Wendy McDonald.

Publications

M.E. Gehm, S.L. Hemmer, S.R. Granade, K.M. O'Hara, and J.E. Thomas, "Mechanical Stability of a Strongly-Interacting Fermi Gas of Atoms," submitted to *Physical Review Letters*.

K.M. O'Hara, S.L. Hemmer, M.E. Gehm, S.R. Granade, and J.E. Thomas, "Observation of a Strongly Interacting Degernate Fermi Gas of Atoms," *Science*, 13 December, **298**, 2179 (2002).

K.M. O'Hara, S.L. Hemmer, S.R. Granade, M.E. Gehm, J.E. Thomas, V. Venturi, E. Tiesinga, and C.J. Williams, "Measurement of the Zero Crossing in a Feshbach Resonance of Fermionic Li," *Physical Review A*, **66**, 041401(R) (2002).

S.R. Granade, M.E. Gehm, K.M. O'Hara, and J.E. Thomas. "All-Optical Production of a Degenerate Fermi Gas," *Physical Review Letters*, **88**, 120405 (2002).

K.M. O'Hara, M.E. Gehm, S.R. Granade, and J.E. Thomas, "Scaling Laws for Evaporative Cooling in Time-Dependent Optical Traps," *Physical Review A*, **64**, 051403(R)(2001).

K.M. O'Hara, S.R. Granade, M.E. Gehm, and J.E. Thomas, "Loading Dynamics of CO_2 Laser Traps," *Physical Review A* **63**, 043403 (2001).

K.M. O'Hara, M.E. Gehm, S.R. Granade, S. Bali, and J.E. Thomas, "Stable, Strongly Attractive, Two-State Mixture of Lithium Fermions in an Optical Trap," *Physical Review Letters* **85**, 2092 (2000).

T.A. Savard, S.R. Granade, K.M. O'Hara, M.E. Gehm, and J.E. Thomas, "Raman-Induced Magnetic Resonance Imaging of Atoms in a Magneto-Optical Trap," *Physical Review A* **60**, 4788 (1999).

S. Bali, K.M. O'Hara, M.E. Gehm, S.R. Granade, and J.E. Thomas, "Quantum-Diffractive Background Gas Collisions in Atom Trap Heating and Loss," *Physical Review A* **60**, R29 (1999).

K.M. O'Hara, S.R. Granade, M.E. Gehm, T.A. Savard, S. Bali, C. Freed, and J.E. Thomas, "Ultrastable CO_2 Laser Trapping of Lithium Fermions," *Physical Review Letters* **82**, 4204 (1999).

M.E. Gehm, K.M. O'Hara, T.A. Savard, and J.E. Thomas, "Dynamics of Noise-Induced Heating in Atom Traps," *Physical Review A* **58**, 3914 (1998).

Presentations

M.E. Gehm, S.R. Granade, K.M. O'Hara, and J.E. Thomas, "All-Optical Production of a Degenerate Fermi Gas," *Bulletin of the American Physical Society*, DAMOP2002 (2002).

S.R. Granade, M.E. Gehm, K.M. O'Hara, and J.E. Thomas, "Preparation of a Degenerate, Two-Component Fermi Gas by Evaporation in a Single Beam Optical Trap," *OSA Technical Digest Series*, QELS2002 (2002).

J.E. Thomas, K.M. O'Hara, S.R. Granade, M.E. Gehm, and M.-S. Chang, "Optical Trapping of a Two-Component Fermi Gas," *Proceedings of the International Conference on Laser Science*, (2001).

M.E. Gehm, S.R. Granade, M.-S. Chang, K.M. O'Hara, and J.E. Thomas, "Optically Trapped Fermi Gas," *OSA Technical Digest Series*, QELS2001 (2001).

K.M. O'Hara, S.R. Granade, M.E. Gehm, M.-S. Chang, and J.E. Thomas, "Evaporative Cooling of Fermionic Atoms in an Optical Trap," *OSA Technical Digest Series*, QELS2001, (2001).

K.M. O'Hara, M.E. Gehm, S.R. Granade, M.-S. Chang, and J.E. Thomas, "Coherence in an Optically Trapped Fermi Gas," *Proceedings of the Eighth Rochester Conference on Coherence and Quantum Optics*, (2001).

K.M. O'Hara, M.E. Gehm, S.R. Granade, S. Bali, and J.E. Thomas, "Evaporative Cooling of Lithium Fermions in an Ultrastable Optical Trap," *Bulletin of the American Physical Society*, DAMOP2000, (2000).

S.R. Granade, K.M. O'Hara, M.E. Gehm, S. Bali, and J.E. Thomas, "Spatial Loading Dynamics of CO_2 Laser Traps," *Bulletin of the American Physical Society*, DAMOP2000, (2000).

K.M. O'Hara, M.E. Gehm, S.R. Granade, S. Bali, and J.E. Thomas, "Evaporative Cooling of Lithium Fermions in a Stable Optical Trap," *Bulletin of the American Physical Society*, SES99, (1999).

M.E. Gehm, K.M. O'Hara, T.A. Savard, and J.E. Thomas, "Noise-Induced Population Loss in Atom Traps," *Bulletin of the American Physical Society*, CENTENNIAL, (1999).

K.M. O'Hara, S.R. Granade, M.E. Gehm, T.A. Savard, S. Bali, and J.E. Thomas, "Ultrastable CO_2 Laser Trapping of Lithium Fermions," *Bulletin of the American Physical Society*, CENTENNIAL, (1999).

T.A. Savard, K.M. O'Hara, S.R. Granade, M.E. Gehm, and J.E. Thomas, "Raman-Induced Magnetic Resonance Imaging of Atoms in a MOT," *Bulletin of the American Physical Society*, DAMOP1998, (1998).